

# Imaging Topological Superconductivity in $\text{UTe}_2$

Joseph P. Carroll

A thesis presented for the degree of  
Doctor of Philosophy



**University College Cork, Ireland**  
Coláiste na hOllscoile Corcaigh

School of Physics  
University College Cork  
Ireland

Head of School: Prof. Paul Callanan  
Supervisor: Prof. J.C. Séamus Davis

2024

# Declaration

This is to certify that the work I am submitting is my own and has not been submitted for another degree, either at University College Cork or elsewhere. All external references and sources are clearly acknowledged and identified within the contents. I have read and understood the regulations of University College Cork concerning plagiarism and intellectual property.

Signature: *Joseph Carroll*

Date: 30<sup>th</sup> December 2024

In memory of my late grandfathers, Jerry and Sean

# Acknowledgments

First and foremost, I'd like to thank my supervisor, Prof. Séamus Davis. He is an inimitable scientist whose imagination, clarity, and tenacity have led him to great success. I have the utmost respect for his return to Ireland and his commitment to fostering a new generation of experts in the study of groundbreaking quantum materials.

Thanks to Prof. Davis, I have had the opportunity to collaborate with several teams of talented international researchers. A special thanks goes to the Prof. Dung-Hai Lee, for developing the SIP tunnelling model and explaining the subtleties of topological superconductivity to humble experimentalists, to Prof. Catherine Pepin, for leading the theoretical team who developed our  $UTe_2$  band structure model for QPI measurements, and to Prof. Johnpierre Paglione, whose team grew our  $UTe_2$  samples.

Within our own research group Shuqiu Wang and Qiangqiang Gu have been my closest collaborators and invaluable mentors. Without them none of this work on  $UTe_2$  would have been possible. Thanks also to the rest of the Cornell team, Kuanysh Zhussupbekov and Bin Hu who have continued using our Cornell STM, ARCHAOS to achieve amazing results.

Although most of the measurements presented in this thesis were performed at Cornell University, my home research group in UCC have been a huge source of support. Together they have built an internationally competitive research lab in our little city and for that they should be incredibly proud. A special thanks goes to Jonathan Ward, our unshakable lab manager whose expertise has informed every decision in the lab, and Catherine Dawson, our administrative manager whose support and day-to-day help is a much needed boost to morale.

Every time I've struggled with this research or with anything in my life, my family has been there to welcome me home and remind me of what's important. For that, I will always be grateful. Thanks goes first to my parents, Conor and

Ellen. They taught me to have an open mind, to be who I want to be, and to have a laugh all the while. Thanks especially to my younger sister Ciara. She might not know just how much she's helped me over the years but she's always made me laugh when I've needed it most. I've been so proud and impressed watching her grow up. Thanks to my grandmothers, the Marys, they are the heart and foundation of our family. Over the course of this PhD both of my grandfathers have passed away. It was my grandmothers who held us all up when things were too much. I am so grateful to all my grandparents, they are an inspiration. Thanks also to my aunts, Gemma and Olivia, and my uncles Jim and Brendan. They have always looked out for me and been there to talk.

Finally, thanks to my friends who've been there when I needed to calm down and get away from work. Thanks to Anthony, Shaun, James, Eibhlín, Hannah, and most of all to Jane, who's stuck with me despite all the ups and downs. I can't express how much I've needed this group of friends when things got tough.

# Abstract

Superconductivity has been a topic of significant interest to the physics community for over a century. However, despite persistent effort, there remain many unsolved problems and unmeasured phenomena. Although the physics of  $p$ -wave superconductivity was developed in the 1960s there have been little to no conclusive measurements of a  $p$ -wave superconductor. The subject of this thesis,  $\text{UTe}_2$ , has ignited a new wave of interest in  $p$ -wave superconducting states as it offers the exciting prospect of measuring unusual surface electronic states, such as zero-energy Andreev bound states, and helical or chiral topological surface states. The latter state being a prerequisite for non-Abelian fermion statistics and Majorana zero modes.

Low-temperature spectroscopic-imaging scanning tunnelling microscopy is an ideal experimental platform with which to study such a superconductor as it allows direct, high energy resolution measurement of the surface electronic states. Using this tool, we present research conducted over the last four years which, we hope, contributes to the understanding of this new material and outlines how one could search for the effects of  $p$ -wave superconductivity in other compounds.

In Chapter 1 we discuss the theoretical framework frequently used in superconductivity research. Where relevant, we highlight the differences between conventional  $s$ -wave superconductors and their  $p$ -wave counterparts. In Chapter 2 we explain the essential operating principles of a spectroscopic-imaging scanning tunnelling microscope (SI-STM) and the experimental techniques used to acquire the results presented herein. Chapter 3 provides an overview of the wealth of theoretical and experimental work which has taken place since the discovery of  $\text{UTe}_2$ 's superconducting properties. Taking these results with the experimental results presented in this thesis, there is strong support for the presence of a  $p$ -wave superconducting state in  $\text{UTe}_2$ .

Chapter 4 features the results of our first SI-STM research project which

---

makes use of a superconducting scan tip to enhance the spectroscopic resolution of our STM system. By measurement of the superconducting energy gap across a representative field of view we discover the presence of a spatially modulating superconducting state, a pair density wave (PDW) at the (0 -1 1) crystal surface. This is likely to be the first observation of a spatially modulating  $p$ -wave superconducting state, highlighting the ubiquity of such states in varying material systems. While performing superconducting scan tip measurements of this PDW, we discovered a zero-energy Andreev bound state at the (0 -1 1) surface. We discuss the theory of how such states come about and how they can be measured in Chapter 5. We also discuss the theory of topological superconductivity and the diverse classification scheme associated with it. Chapter 6 then presents direct measurement of the surface Andreev bound state supported by a newly developed  $s$ -wave - insulator -  $p$ -wave tunnelling model. Using this model and tip-sample dependent tunnelling measurements, we place restrictions on the form of superconducting order present in  $\text{UTe}_2$ . Finally, in Chapter 7 we present a detailed band structure model which reveals the electronic states responsible for low energy scattering at the surface of  $\text{UTe}_2$ . These measurements reveal unique scattering signatures of the quasiparticle surface band expected from a crystal whose superconducting order parameter transforms as the  $B_{3u}$  irreducible representation of the crystal point symmetry group  $D_{2h}$ .

# Contents

<b>1</b>	<b>Unconventional Superconductivity</b>	<b>13</b>
1.1	Introduction . . . . .	13
1.2	Cooper Pairs & the BCS Wavefunction . . . . .	14
1.3	The BCS Gap Equation . . . . .	17
1.4	Macroscopic Phase & Off-Diagonal Long Range Order . . . . .	22
1.5	Unconventional Pairing & d-Vector Representation . . . . .	24
1.6	Finite-momentum Pairing States . . . . .	29
1.6.1	Fulde-Ferrell and Larkin-Ovchinnikov (FFLO) States . . . . .	29
1.6.2	Pair Density Waves (PDWs) . . . . .	31
1.6.2.1	Ginzburg-Landau Theory . . . . .	31
1.6.2.2	Intertwined Orders . . . . .	33
<b>2</b>	<b>Spectroscopic Imaging Scanning Tunnelling Microscopy (SI-STM)</b>	<b>36</b>
2.1	Introduction . . . . .	36
2.2	Tunnelling Currents . . . . .	36
2.3	Topography . . . . .	40
2.4	Spectroscopy . . . . .	42
2.4.1	Single Particle Tunnelling . . . . .	42
2.4.2	Scanned Josephson Tunnelling Microscopy (SJTM) . . . . .	44
2.4.2.1	The Josephson Equations . . . . .	44
2.4.2.2	SJTM . . . . .	46
2.5	Quasiparticle Interference Imaging . . . . .	47
<b>3</b>	<b>UTe<sub>2</sub>: A Spin Triplet Superconductor</b>	<b>50</b>
3.1	Introduction . . . . .	50
3.2	Upper Critical Field & <i>P</i> -Wave Pairing Symmetry . . . . .	51

3.3	NMR Relaxation Rate and Knight Shift . . . . .	52
3.4	Specific Heat Capacity & Thermal Conductivity . . . . .	54
3.5	Magnetic Penetration Depth & Topological Surface State Conductivity . . . . .	56
3.6	Conclusions . . . . .	57
<b>4</b>	<b>Discovery of a Pair Density Wave in <math>UTe_2</math></b>	<b>60</b>
4.1	Normal Tip Measurements . . . . .	60
4.2	Superconducting Tip Characterisation . . . . .	61
4.3	Superconducting Tip Gap Map Analysis . . . . .	65
4.3.1	Shear Correction . . . . .	66
4.3.2	Phase Extraction & the Lock-In Method . . . . .	68
4.3.3	Lawler-Fujita Algorithm . . . . .	72
4.4	PDW Discovery & Phase Analysis . . . . .	74
4.4.1	PDW Discovery . . . . .	74
4.4.2	Interplay of CDW and PDW . . . . .	77
4.5	Parent Order & Triplet PDW . . . . .	77
<b>5</b>	<b>Andreev Reflection, Andreev Bound States, &amp; Topological Superconductivity</b>	<b>80</b>
5.1	Introduction . . . . .	80
5.2	Bogoliubov-deGennes Equations . . . . .	81
5.3	Andreev Reflection . . . . .	85
5.4	Andreev Bound States . . . . .	90
5.5	Andreev Bound State Topology . . . . .	93
<b>6</b>	<b>The Zero-Energy Surface State of <math>UTe_2</math></b>	<b>98</b>
6.1	Introduction . . . . .	98
6.2	Andreev Spectra . . . . .	98
6.3	$S$ -wave - Insulator - $P$ -wave (SIP) Model . . . . .	104
6.3.1	Topological Surface Band (TSB) Phenomenology . . . . .	104
6.3.2	SIP Model Details . . . . .	105
6.3.3	SIP Model Predictions and Experimental Verification . . . . .	108
<b>7</b>	<b>Quasiparticle Surface State Quasiparticle Interference (QSQPI)</b>	<b>113</b>
7.1	Introduction . . . . .	113

---

7.2	The $\text{UTe}_2$ Fermi Surface within QSQPI . . . . .	114
7.3	Fermi Surface Projection . . . . .	116
7.4	Normal State QPI . . . . .	117
7.5	Nodal Locations on the Fermi Surface . . . . .	119
7.6	Quasiparticle Surface Bands (QSBs) . . . . .	123
7.7	Final QSB QPI Simulations . . . . .	125
7.8	Normal State & QSB QPI Measurements . . . . .	129
7.9	QSB QPI Theory-Experiment Correspondence . . . . .	132
<b>8</b>	<b>Final Remarks</b>	<b>137</b>
<b>A</b>	<b>ARCHAOS</b>	<b>139</b>
A.1	Introduction . . . . .	139
A.2	Cryogenics . . . . .	139
A.3	Vibration Isolation . . . . .	140
A.4	STM Head . . . . .	142
A.5	Measurement & Control Electronics . . . . .	143
<b>B</b>	<b>PDW Fitting</b>	<b>145</b>
<b>C</b>	<b>Josephson versus Andreev Tunnelling</b>	<b>148</b>
<b>D</b>	<b>Phase Fluctuations in the SIP Model</b>	<b>151</b>
<b>E</b>	<b>Normal vs. Superconducting Tip QSB QPI Detection</b>	<b>153</b>
<b>F</b>	<b>QSB QPI Repeated Measurements</b>	<b>156</b>

# List of Figures

1.1	Coherence Factors and Quasiparticle States within BCS Theory	20
1.2	Density of States of a $d$ -wave and $p$ -wave Superconductor . . . .	22
1.3	The Superfluid Phases of $^3\text{He}$ . . . . .	26
1.4	Character Table of $D_{2h}$ . . . . .	28
1.5	Finite-momentum Pairing in the Presence of a Magnetic Field .	31
1.6	Free Energy Minima in the Normal and Superconducting State .	34
2.1	Example Topography on the (0 -1 1) Surface of $\text{UTe}_2$ . . . . .	41
2.2	Superconducting Density of States from $dI/dV$ . . . . .	44
2.3	Quasiparticle Scattering on the Surface of Cu (1 1 1) . . . . .	48
3.1	Crystal Structure of $\text{UTe}_2$ & The Superconducting Phases of $\text{UTe}_2$ under Magnetic Field . . . . .	52
3.2	The Knight Shift in Triplet Superconductors & Knight Shift Data from $\text{UTe}_2$ . . . . .	54
3.3	Surface Conductivity of $\text{UTe}_2$ in the Superconducting State . . .	58
4.1	Normal Tip Detection of PDWs in $\text{UTe}_2$ . . . . .	62
4.2	Normal Tip Spectroscopy at the (0 -1 1) Surface of $\text{UTe}_2$ . . . .	63
4.3	Dynes Fit of Nb Superconducting Scan Tip . . . . .	64
4.4	Combined $\text{UTe}_2$ -Nb Single Particle Spectrum . . . . .	65
4.5	Shear Correction of Gap Map Measurements . . . . .	69
4.6	Phase Map Produced by the Lock-In Method . . . . .	71
4.7	Lawler-Fujita Algorithm Applied to the $\text{UTe}_2$ (0 -1 1) Surface .	73
4.8	Topography & Coherence Peak Map Registration . . . . .	75
4.9	Pair Density Wave Detection from Gap Map $\delta\Delta(\mathbf{r})$ . . . . .	76
4.10	Phase Relationship between CDW and PDW Modulations . . . .	78

---

5.1	Schematic of Andreev Reflection at an Normal Metal - Insulator - Superconductor Junction . . . . .	86
5.2	Normalized Conductance for NIS and NIP Junction . . . . .	91
5.3	Andreev Bound States in SNS Contacts . . . . .	93
5.4	Atland-Zirnbauer (Ten Fold Way) Classification Scheme . . . . .	94
5.5	Topological Superconductor Surface State Dispersions . . . . .	97
6.1	Andreev Spectra on $UTe_2$ . . . . .	99
6.2	Zero-Energy States at the $UTe_2$ (0 -1 1) Surface . . . . .	100
6.3	Andreev Spectrum Dependence on $z$ . . . . .	101
6.4	Decay Constant of Andreev Spectra . . . . .	103
6.5	Fermi Arc TSB Phenomenology . . . . .	105
6.6	SIP Model Basics . . . . .	107
6.7	Illustration of Zero-Energy Andreev Reflection . . . . .	108
6.8	The Effect of Increased Tunnelling on Zero-Energy States . . . . .	110
6.9	TSB Characterisation by Tunnelling . . . . .	112
7.1	Fermi Surface Model for $UTe_2$ . . . . .	117
7.2	$UTe_2$ Crystal Structure, (0 0 1) Surface and (0 -1 1) Surface . . . . .	118
7.3	$f$ -electron Fermi Surface and Joint Density of States . . . . .	120
7.4	Nodal Positions on the $UTe_2$ Fermi Surface for $B_{1u}$ , $B_{2u}$ , and $B_{3u}$ . . . . .	121
7.5	High-Resolution, Low-Damping Bulk Spectral Functions . . . . .	123
7.6	Illustrative Projection of Bulk Nodes and QSB Scattering Wavevec- tors for $B_{2u}$ and $B_{3u}$ . . . . .	126
7.7	Low Damping Surface Spectral Functions and Joint Density of States for $B_{2u}$ and $B_{3u}$ . . . . .	127
7.8	$B_{2u}$ and $B_{3u}$ Surface Spectral Functions . . . . .	129
7.9	Normal State QPI Measurements at the (0 -1 1) Surface . . . . .	131
7.10	QSB QPI Measurements at the (0 -1 1) Surface . . . . .	133
7.11	QPI Theory-Experiment Comparison . . . . .	135
7.12	Spin Resolved $B_{3u}$ Surface Spectral Function . . . . .	136
A.1	ARCHAOS Design . . . . .	141
A.2	ARCHAOS Scan Head . . . . .	143
B.1	NIS vs. SIS Fitting Quality Comparison . . . . .	147

---

C.1	Josephson versus Andreev Tunnelling on the (0 -1 1) surface of UTe <sub>2</sub> . . . . .	150
D.1	Zero-Energy Peak Splitting for Realistic Phase Effects . . . . .	152
E.1	Normal versus Superconducting Tip QSB QPI Detection . . . . .	155
F.1	QSB QPI Repeated Measurements . . . . .	157

# Chapter 1

## Unconventional Superconductivity

### 1.1 Introduction

It has been a hundred years since the advent of quantum mechanics<sup>1</sup> and the subsequent discoveries of uniquely quantum properties such as superposition and entanglement. First discovered in the context of atomic theory, it was thought that quantum effects could only be observed on the scale of single atoms. However, it has since been shown that macroscopic systems may exhibit quantum effects and there are few better examples of macroscopic quantum systems than superfluid and superconducting condensates. The discovery of superconductivity by Heike Kamerlingh Onnes in 1911 stands out as the first observation of a macroscopic quantum condensate, predating the observation of Bose-Einstein condensation<sup>2</sup> or coherent laser light<sup>3</sup>.

While the conventional (*s*-wave) superconductors discovered by Onnes are now well understood there remains an enormous amount of research interest in the families of “high-temperature” superconductors, such as the iron-pnictides and the cuprates. The research presented in this thesis is focused on the exotic properties of a superconductor,  $\text{UTe}_2$ , whose transition temperature is only a few degrees above the absolute zero of temperature,  $T_c \approx 2$  K. The motivation for studying  $\text{UTe}_2$  comes from the growing scientific consensus that this material is a *p*-wave superconductor. Such superconductors are exceedingly rare and there are only a handful of candidate *p*-wave superconductors discovered thus far. These superconductors are expected to exhibit a plethora of unusual properties. As we’ll see below, during our team’s study of  $\text{UTe}_2$  we

encountered finite-momentum pairing states and a surface bound state whose characteristics give us some insight into the pairing symmetry of this unique material. Before we discuss this latest research we will provide some background into the phenomenon of superconductivity and those aspects relevant to the research below.

## 1.2 Cooper Pairs & the BCS Wavefunction

Fritz London was perhaps the first to identify the role of macroscopic quantum condensation in superconductivity and superfluidity<sup>4</sup>. Together with his brother Heinz they developed the first phenomenological theories of superconductivity in the form of the London equations.

$$\frac{\partial \mathbf{j}_s}{\partial t} = \frac{n_s e^2}{m} \mathbf{E} \quad (1.1)$$

$$\nabla \times \mathbf{j}_s = -\frac{n_s e^2}{m} \mathbf{h} \quad (1.2)$$

Here we assume that the charge carriers in a superconductor are composed of a superfluid and normal fluid fraction such that the total electron density is  $n = n_n + n_s$ . In the London equations, the  $\mathbf{j}_s$  term is the superfluid current density and  $\mathbf{h}$ , the local magnetic field. These two equations describe the essential characteristics of a superconductor, namely its resistanceless currents and expulsion of magnetic fields over a characteristic length scale, in this case the London penetration depth  $\lambda_L = \sqrt{\frac{mc^2}{4\pi n_s e^2}}$ .

While phenomenological, these equations are very successful in describing the macroscopic electrodynamics of superconductors but how such properties come about was very poorly understood at the time of the Londons. In the nearly 90 years since there has been significant progress. We now firmly understand the mechanism which underlies the superconductors studied by the Londons and so, to begin, we will discuss the theoretical framework derived to explain these conventional superconductors. In doing so we will find that it establishes a description of superconductivity which can be applied more generally.

We begin with Fröhlich, who was the first to suggest that, in conventional superconductors, lattice interactions may allow an attractive interaction between electrons resulting in bound pairs<sup>5</sup>. This was expanded upon by Cooper

for an individual pair<sup>6</sup> and by Bardeen, Cooper, and Schrieffer who together showed how such pairs condense<sup>7</sup>. We consider a general treatment and begin with the assumption that pairs of electrons, Cooper pairs, are the building blocks of the superconducting condensate and can thus be expressed by a pair creation operator

$$P_{\mathbf{k},\sigma_1,\sigma_2}^\dagger = c_{\mathbf{k},\uparrow}^\dagger c_{-\mathbf{k},\downarrow}^\dagger \quad (1.3)$$

Note that we will begin by describing a zero momentum spin-singlet superconducting state, one in which the pairs of fermions have opposite spin and momentum, and introduce the concept of spin triplet Cooper pairs and finite-momentum states later.

We then create a pair of fermions in orbital  $g(\mathbf{r}_1 - \mathbf{r}_2)$  such that

$$\tilde{a}^\dagger = \sum_{\mathbf{k}} g_{\mathbf{k}} P_{\mathbf{k}}^\dagger \quad (1.4)$$

For such paired fermion states to be considered truly bosons and to form a true Bose-Einstein condensate, these operators must observe the bosonic commutation relations

$$[\tilde{a}, \tilde{a}^\dagger] = 1 \quad (1.5)$$

However substitution of this pseudoboson operator  $\tilde{a}^\dagger$  into Eq. 1.5 yields

$$[\tilde{a}, \tilde{a}^\dagger] = \sum_{\mathbf{k},\mathbf{k}'} g_{\mathbf{k}'}^* g_{\mathbf{k}} \left[ c_{-\mathbf{k}',\downarrow} c_{\mathbf{k}',\uparrow}, c_{\mathbf{k},\uparrow}^\dagger c_{-\mathbf{k},\downarrow}^\dagger \right] = \sum_{\mathbf{k}} |g_{\mathbf{k}}|^2 (1 - n_{\mathbf{k},\uparrow} - n_{\mathbf{k},\downarrow}) \quad (1.6)$$

Thus suggesting that superconductivity is a special case of boson condensation which differs from that of a simple non interacting BEC at  $T = 0$ . We continue nonetheless with the concept of condensation as it remains applicable and look for a coherent state similar to that in a BEC

$$|\psi_{\text{BEC}}\rangle = e^{\alpha a^\dagger} |0\rangle \quad (1.7)$$

$$|\psi_{\text{BCS}}\rangle = e^{\alpha \sum_{\mathbf{k}} g_{\mathbf{k}} P_{\mathbf{k}}^\dagger} |0\rangle = e^{\alpha \sum_{\mathbf{k}} g_{\mathbf{k}} c_{\mathbf{k},\uparrow}^\dagger c_{-\mathbf{k},\downarrow}^\dagger} |0\rangle = \left[ \prod_{\mathbf{k}} e^{\alpha g_{\mathbf{k}} c_{\mathbf{k},\uparrow}^\dagger c_{-\mathbf{k},\downarrow}^\dagger} \right] |0\rangle \quad (1.8)$$

Thankfully the exponential terms allow us to turn the sum over  $k$  states to a product. Furthermore, our pseudo bosonic operator is actually composed of fermionic operators and we cannot put two such fermions in the same  $k$  state

as

$$(c_{\mathbf{k},\uparrow}^\dagger c_{-\mathbf{k},\downarrow}^\dagger)^2 = 0 \quad (1.9)$$

So we can expand the exponential term to just the zero-th and first order terms of the Taylor expansion as all other terms are zero.

$$e^{\alpha g_{\mathbf{k}} c_{\mathbf{k},\uparrow}^\dagger c_{-\mathbf{k},\downarrow}^\dagger} = 1 + \alpha g_{\mathbf{k}} c_{\mathbf{k},\uparrow}^\dagger c_{-\mathbf{k},\downarrow}^\dagger \quad (1.10)$$

After these expansions the wavefunction is then

$$|\psi_{\text{BCS}}\rangle = \prod_{\mathbf{k}} \left( 1 + \alpha g_{\mathbf{k}} c_{\mathbf{k},\uparrow}^\dagger c_{-\mathbf{k},\downarrow}^\dagger \right) |0\rangle \quad (1.11)$$

Currently, this wavefunction is not normalized. To do so, we consider a specific  $\mathbf{k}$  orbital such that  $|0_{\mathbf{k}}\rangle$  is the vacuum for that orbital. We then obtain the normalization constant

$$\langle \psi_{\text{BCS}} | \psi_{\text{BCS}} \rangle = \prod_{\mathbf{k}} (1 + |\alpha g_{\mathbf{k}}|^2) \quad (1.12)$$

Dividing  $|\psi_{\text{BCS}}\rangle$  by the square root of this constant we obtain

$$|\psi_{\text{BCS}}\rangle = \prod_{\mathbf{k}} \left( \frac{1}{\sqrt{1 + |\alpha g_{\mathbf{k}}|^2}} + \frac{\alpha g_{\mathbf{k}}}{\sqrt{1 + |\alpha g_{\mathbf{k}}|^2}} c_{\mathbf{k},\uparrow}^\dagger c_{-\mathbf{k},\downarrow}^\dagger \right) |0\rangle \quad (1.13)$$

Finally we define these prefactors to be

$$u_{\mathbf{k}} = \frac{1}{\sqrt{1 + |\alpha g_{\mathbf{k}}|^2}} \quad (1.14)$$

$$v_{\mathbf{k}} = \frac{|\alpha g_{\mathbf{k}}|^2}{\sqrt{1 + |\alpha g_{\mathbf{k}}|^2}} \quad (1.15)$$

And arrive at the following expression for the ground state wavefunction

$$|\psi_{\text{BCS}}\rangle = \prod_{\mathbf{k}} \left( u_{\mathbf{k}} + v_{\mathbf{k}} c_{\mathbf{k},\uparrow}^\dagger c_{-\mathbf{k},\downarrow}^\dagger \right) |0\rangle \quad (1.16)$$

Thus we find the general BCS wavefunction recognisable from many introductory textbooks to superconductivity<sup>8,9</sup>. However, we still know very little about this ground state wavefunction. Therefore we will go further and calculate the ground state energy, the quasiparticle excitations from this ground state, and then crucially we must extend this formalism to unconventional

superconducting states.

### 1.3 The BCS Gap Equation

In real materials the interaction term of the Hamiltonian, which binds fermions, is in general, a complicated function depending on the momentum of the fermionic states under consideration, as well as their individual spin. Such an interaction potential could arise from several sources including lattice interactions, ferromagnetic coupling, or anti-ferromagnetic coupling. In the case of  $s$ -wave superconductors the isotope effect<sup>10</sup> implicated the role of electron-phonon coupling allowing Cooper<sup>6</sup> to simplify the Hamiltonian to the form

$$H_{\text{BCS}} = \sum_{\mathbf{k},\sigma} \epsilon_{\mathbf{k},\sigma} c_{\mathbf{k},\sigma}^\dagger c_{\mathbf{k},\sigma} + \sum_{\mathbf{k},\mathbf{k}'} V_{\mathbf{k},\mathbf{k}'} c_{\mathbf{k},\uparrow}^\dagger c_{-\mathbf{k},\downarrow}^\dagger c_{-\mathbf{k}',\downarrow} c_{\mathbf{k}',\uparrow} \quad (1.17)$$

As we are concerned with a bulk, macroscopic superconducting state, the double creation and annihilation terms of the Hamiltonian have macroscopic occupation. We can then make use of the mean-field approximation to evaluate the energy of the BCS condensate. To do so, we replace both  $c_{\mathbf{k},\uparrow}^\dagger c_{-\mathbf{k},\downarrow}^\dagger$  and  $c_{-\mathbf{k}',\downarrow} c_{\mathbf{k}',\uparrow}$  by the following

$$c_{\mathbf{k},\uparrow}^\dagger c_{-\mathbf{k},\downarrow}^\dagger = \langle c_{\mathbf{k},\uparrow}^\dagger c_{-\mathbf{k},\downarrow}^\dagger \rangle + (c_{\mathbf{k},\uparrow}^\dagger c_{-\mathbf{k},\downarrow}^\dagger - \langle c_{\mathbf{k},\uparrow}^\dagger c_{-\mathbf{k},\downarrow}^\dagger \rangle) \quad (1.18)$$

$$c_{-\mathbf{k}',\downarrow} c_{\mathbf{k}',\uparrow} = \langle c_{-\mathbf{k}',\downarrow} c_{\mathbf{k}',\uparrow} \rangle + (c_{-\mathbf{k}',\downarrow} c_{\mathbf{k}',\uparrow} - \langle c_{-\mathbf{k}',\downarrow} c_{\mathbf{k}',\uparrow} \rangle) \quad (1.19)$$

As the term in brackets on the right-hand side is necessarily small we can neglect terms which are the product of both brackets resulting in the mean-field Hamiltonian

$$H_{\text{BCS}}^{\text{MF}} = \sum_{\mathbf{k},\sigma} \epsilon_{\mathbf{k}\sigma} c_{\mathbf{k},\sigma}^\dagger c_{\mathbf{k},\sigma} + \sum_{\mathbf{k},\mathbf{k}'} V_{\mathbf{k},\mathbf{k}'} \left( c_{\mathbf{k},\uparrow}^\dagger c_{-\mathbf{k},\downarrow}^\dagger \langle c_{-\mathbf{k}',\downarrow} c_{\mathbf{k}',\uparrow} \rangle + \langle c_{\mathbf{k},\uparrow}^\dagger c_{-\mathbf{k},\downarrow}^\dagger \rangle c_{-\mathbf{k}',\downarrow} c_{\mathbf{k},\uparrow} - \langle c_{\mathbf{k},\uparrow}^\dagger c_{-\mathbf{k},\downarrow}^\dagger \rangle \langle c_{-\mathbf{k}',\downarrow} c_{\mathbf{k}',\uparrow} \rangle \right) \quad (1.20)$$

To ensure energy is measured from the chemical potential we replace  $\epsilon_{\mathbf{k}}$  with  $\xi_{\mathbf{k}} = \epsilon_{\mathbf{k}} - \mu$  and furthermore we can define the order parameter such that

$$\Delta_{\mathbf{k}} = - \sum_{\mathbf{k}'} V_{\mathbf{k},\mathbf{k}'} \langle c_{-\mathbf{k}',\downarrow} c_{\mathbf{k}',\uparrow} \rangle \quad (1.21)$$

And arrive at a mean-field Hamiltonian of the form

$$H_{\text{BCS}}^{\text{MF}} = \sum_{\mathbf{k},\sigma} \xi_{\mathbf{k},\sigma} c_{\mathbf{k},\sigma}^\dagger c_{\mathbf{k},\sigma} - \sum_{\mathbf{k}} \left( \Delta_{\mathbf{k}} c_{\mathbf{k},\uparrow}^\dagger c_{-\mathbf{k},\downarrow}^\dagger + \Delta_{\mathbf{k}}^* c_{-\mathbf{k},\downarrow} c_{\mathbf{k},\uparrow} - \Delta_{\mathbf{k}} \langle c_{\mathbf{k},\uparrow}^\dagger c_{-\mathbf{k},\downarrow}^\dagger \rangle \right) \quad (1.22)$$

This Hamiltonian cannot be solved for its eigenvalues unless made diagonal, that is, expressed in terms of number operators of the form  $a_{\mathbf{k}}^\dagger a_{\mathbf{k}}$ . To diagonalize this mean-field Hamiltonian we turn to the approach taken by Nikolay Bogoliubov<sup>11</sup> and replace the normal state quasiparticle operators with new linear combinations of these operators, namely

$$\gamma_{\mathbf{k},\uparrow} = u_{\mathbf{k}}^* c_{\mathbf{k},\uparrow} + v_{\mathbf{k}}^* c_{-\mathbf{k},\downarrow}^\dagger \quad (1.23)$$

$$\gamma_{-\mathbf{k},\downarrow}^\dagger = u_{\mathbf{k}} c_{-\mathbf{k},\downarrow}^\dagger - v_{\mathbf{k}} c_{\mathbf{k},\uparrow} \quad (1.24)$$

These Bogoliubov operators are weighted superpositions of the initial electron-like and hole-like quasiparticle states and, as such, follow the fermionic commutation relations such that

$$\{\gamma_{\mathbf{k},\sigma}, \gamma_{\mathbf{k}',\sigma'}^\dagger\} = \delta_{\mathbf{k},\mathbf{k}'} \delta_{\sigma,\sigma'} \quad (1.25)$$

$$\{\gamma_{\mathbf{k},\sigma}, \gamma_{\mathbf{k}',\sigma'}\} = 0 \quad (1.26)$$

By use of these commutation relations the normal state operators may be written as a combination of Bogoliubov operators such that

$$c_{\mathbf{k},\uparrow} = u_{\mathbf{k}} \gamma_{\mathbf{k},\uparrow} - v_{\mathbf{k}}^* \gamma_{-\mathbf{k},\downarrow}^\dagger \quad (1.27)$$

$$c_{-\mathbf{k},\downarrow}^\dagger = u_{\mathbf{k}}^* \gamma_{-\mathbf{k},\downarrow}^\dagger + v_{\mathbf{k}} \gamma_{\mathbf{k},\uparrow} \quad (1.28)$$

After a good deal of algebra and through the use of the commutation relations above, we find that the off-diagonal coefficients, of the form  $\gamma_{-\mathbf{k},\downarrow} \gamma_{\mathbf{k},\uparrow}$ , will be zero when

$$2\xi_{\mathbf{k}} u_{\mathbf{k}} v_{\mathbf{k}} + \Delta_{\mathbf{k}} v_{\mathbf{k}}^2 - \Delta_{\mathbf{k}}^* u_{\mathbf{k}}^2 = 0 \quad (1.29)$$

Solutions of this equation are of the form

$$u_{\mathbf{k}} = |u_{\mathbf{k}}| e^{i\phi_{\mathbf{k}}/2} \quad v_{\mathbf{k}} = |v_{\mathbf{k}}| e^{-i\phi_{\mathbf{k}}/2} \quad \Delta_{\mathbf{k}} = |\Delta_{\mathbf{k}}| e^{i\phi_{\mathbf{k}}} \quad (1.30)$$

Notably, the phase  $\phi_{\mathbf{k}}$  of the order parameter defines the relative phase of these quasiparticle excitations. An *s*-wave superconductor exhibits a constant

phase in  $\mathbf{k}$ -space, however, interesting effects arrive for unconventional superconductors, in which the phase of the order parameter varies in  $\mathbf{k}$ -space. We will discuss the consequences of this momentum-dependent phase later. In any case, substitution of these equations into Eq. 1.29 allows us to derive expressions for  $|u_{\mathbf{k}}|^2$  and  $|v_{\mathbf{k}}|^2$  and, crucially, diagonalizes the Hamiltonian in Eq. 1.22.

$$|u_{\mathbf{k}}|^2 = \frac{1}{2} \left( 1 + \frac{\xi_{\mathbf{k}}}{\sqrt{\xi_{\mathbf{k}}^2 + |\Delta_{\mathbf{k}}|^2}} \right) \quad (1.31)$$

$$|v_{\mathbf{k}}|^2 = \frac{1}{2} \left( 1 - \frac{\xi_{\mathbf{k}}}{\sqrt{\xi_{\mathbf{k}}^2 + |\Delta_{\mathbf{k}}|^2}} \right) \quad (1.32)$$

Defining the term  $E_{\mathbf{k}} = \sqrt{\xi_{\mathbf{k}}^2 + |\Delta_{\mathbf{k}}|^2}$  and substituting these expressions into Eq. 1.22, in which the normal state quasiparticle operators have been replaced with Bogoliubov operators, yields the diagonalized Hamiltonian

$$H_{\text{BCS}}^{\text{MF}} = \sum_{\mathbf{k}} E_{\mathbf{k}} \left( \gamma_{\mathbf{k},\uparrow}^\dagger \gamma_{\mathbf{k},\uparrow} + \gamma_{-\mathbf{k},\downarrow}^\dagger \gamma_{-\mathbf{k},\downarrow} \right) + \sum_{\mathbf{k}} \left[ \xi_{\mathbf{k}} - E_{\mathbf{k}} + \Delta_{\mathbf{k}} \langle c_{\mathbf{k},\uparrow}^\dagger c_{-\mathbf{k},\downarrow}^\dagger \rangle \right] \quad (1.33)$$

Which is of the desired form

$$H_{\text{BCS}} = \sum_{\mathbf{k},\sigma} E_{\mathbf{k}} \gamma_{\mathbf{k},\sigma}^\dagger \gamma_{\mathbf{k},\sigma} + E_g \quad (1.34)$$

This new Hamiltonian includes the new Bogoliubov quasiparticles, or bogoliubons, which are superpositions of electron and hole states with the relative weight of electron-like and hole-like quasiparticles being controlled by  $|u_{\mathbf{k}}|$  and  $|v_{\mathbf{k}}|$ . Therefore, at energies far above the chemical potential, when  $\xi_{\mathbf{k}} \gg \Delta_{\mathbf{k}}$ , the bogoliubon operator  $\gamma_{\mathbf{k}}^\dagger$  becomes hole-like, while far below the chemical potential these new quasiparticles are almost entirely electron-like. Schematically the functions  $|v_{\mathbf{k}}|^2$  and  $|u_{\mathbf{k}}|^2$ , which define the electron-ness or hole-ness of the bogoliubons respectively, are plotted in Fig. 1.1a.

A consequence of the BCS theory, one which was crucial in its experimental verification<sup>12</sup>, is the formation of an energy gap in the density of quasiparticle states. This energy gap is clearly seen upon plotting the energy dispersion of Bogoliubov quasiparticles as shown in Fig. 1.1b. The gap value is defined relative to the chemical potential, therefore, the full gap is  $2|\Delta_{\mathbf{k}}|$ . The effect on the quasiparticle density of states can be found by relating the density of

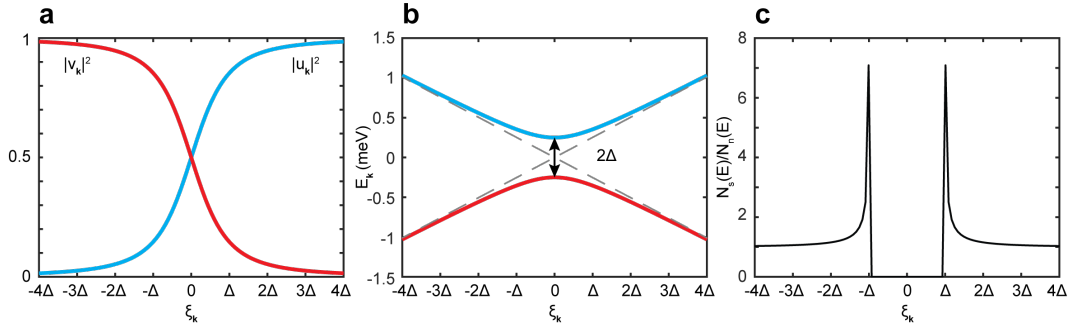


Figure 1.1: **a.** Distribution of weighting factors  $|v_{\mathbf{k}}|^2$  and  $|u_{\mathbf{k}}|^2$  as a function of energy  $\xi_{\mathbf{k}}$ . Far from the chemical potential  $\xi_{\mathbf{k}} \ll 0$  or  $\xi_{\mathbf{k}} \gg 0$  Bogoliubov quasiparticles are almost entirely electron-like or hole-like while exactly at the chemical potential Bogoliubov quasiparticles are equal superpositions of hole-like and electron-like quasiparticles. **b.** Bogoliubov quasiparticle dispersion  $E_{\mathbf{k}}$ . A clear gap of magnitude  $2|\Delta_{\mathbf{k}}| = 0.5\text{meV}$  is observed, the magnitude of the order parameter in all plots shown is defined to be  $|\Delta_{\mathbf{k}}| = 0.25\text{meV}$  in correspondence with that observed in  $\text{UTe}_2$ . The quasiparticle dispersion in the normal state  $E_{\mathbf{k}} = |\xi_{\mathbf{k}}|$  is indicated by grey dashed lines. **c.** Ratio of the density of quasiparticle states in the superconducting  $N_s(E)$  and normal state  $N_n(E)$ . Two sharp coherence peaks are formed around the energy gap  $\pm|\Delta_{\mathbf{k}}|$ .

states of Bogoliubov quasiparticles with those of the normal state such that

$$N_S(E)dE = N_n(\xi)d\xi \quad (1.35)$$

In all singlet superconductors, the energy gap is several milli-electronvolts in magnitude allowing us to make the approximation that the density of states (DOS) around the energy gap is similar to that at the Fermi level  $N_n(\xi) = N(0)$ . This allows us to write the simple relation for the modified DOS. Note that the states previously below  $\Delta$  are pushed up to the energy gap, forming coherence peaks. These DOS spectra are readily observed by  $dI/dV$  measurement in STM and will appear frequently later.

$$\frac{N_S(E)}{N(0)} = \frac{d\xi}{dE} = \begin{cases} \frac{E}{\sqrt{E^2 - \Delta^2}}, & E > \Delta \\ 0 & E < \Delta \end{cases} \quad (1.36)$$

In real materials the order parameter may be anisotropic and feature point or line nodes in momentum space. This anisotropy alters the DOS, as the gap function contribution features a sum/integral over momentum space. To see

this more clearly we assume the DOS is

$$N(E) = \frac{2}{\Omega} \sum_{\mathbf{k}} \delta(E_{\mathbf{k}} - E) \quad (1.37)$$

where  $\Omega$  is the 3D  $k$ -space volume considered. We then make use of the Bogoliubov quasiparticle dispersion

$$E_{\mathbf{k}} = \pm \sqrt{\xi_{\mathbf{k}}^2 + |\Delta_{\mathbf{k}}|^2} \quad (1.38)$$

Converting the sum over  $k$ -space to a 3D integral and considering a 2D gap function in the  $k_x - k_y$  plane we obtain

$$N(E) = N_0 \int \frac{d\Omega_{\mathbf{k}}}{4\pi} \int d\xi \delta(\sqrt{\xi^2 + |\Delta_0 g_{\mathbf{k}}|^2} - E) \quad (1.39)$$

$$= N_0 \int \frac{d\Omega_{\mathbf{k}}}{4\pi} \frac{E}{\sqrt{E^2 - |\Delta_0 g_{\mathbf{k}}|^2}} \quad (1.40)$$

For a  $d$ -wave superconductor with line nodes in the  $k_x - k_y$  plane, the order parameter is well described by  $\Delta_{\mathbf{k}} = \Delta_0 \cos(2\theta_{\mathbf{k}})$ , where  $\theta_{\mathbf{k}}$  is the angle in the  $k_x - k_y$  plane. By performing the substitution  $x = \cos(2\theta)$  we arrive at the expression<sup>13</sup>

$$N(E) = N_0 \frac{E}{\Delta_0} \int_{-1}^{+1} dx \operatorname{Re} \left\{ \frac{1}{\sqrt{(E/\Delta_0) - x^2}} \right\} \quad (1.41)$$

$$= N_0 \frac{E}{\Delta_0} \begin{cases} \frac{\pi}{4} & |E| < \Delta_0 \\ \frac{1}{2} \arcsin\left(\frac{\Delta_0}{E}\right) & |E| \geq \Delta_0 \end{cases} \quad (1.42)$$

We plot this function in Fig. 1.2a and immediately see some key differences between the DOS of  $d$ -wave and  $s$ -wave superconductors. In contrast to the  $s$ -wave DOS, which falls sharply at the gap edge (Fig. 1.1c), the DOS of a  $d$ -wave superconductor decreases linearly due to the presence of line nodes of normal state quasiparticles which remain excited at energies within the gap. However, at  $E = 0$  even these quasiparticles are completely gapped out and  $N(0) = 0$ . Even the coherence peaks which are prominent in the  $s$ -wave case are replaced by weaker kinks in the DOS at the gap edge. These features can be observed in  $d$ -wave superconducting samples however the exact shape of the spectrum depends strongly on the experimental setup, the presence of impurities, and the disorder of the samples<sup>14</sup>.

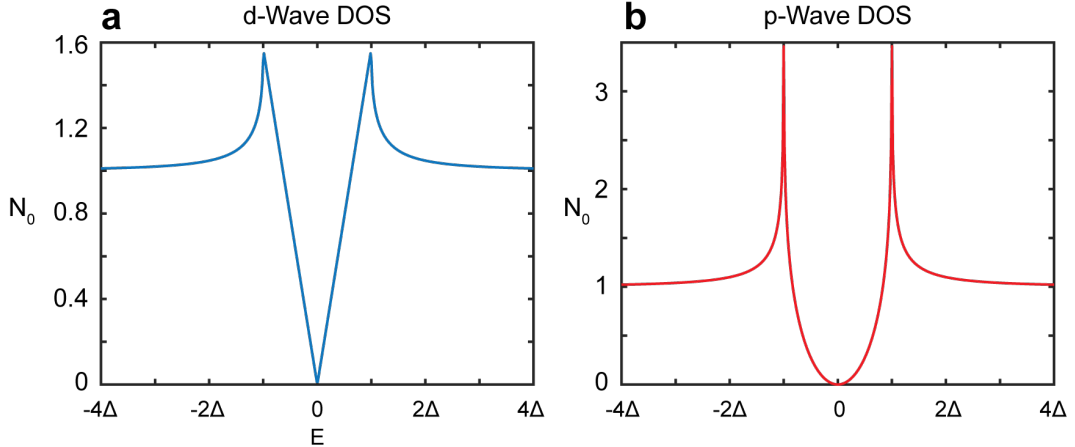


Figure 1.2: **a.** The density of states (DOS) of a  $d$ -wave superconductor with line nodes in the  $k_x - k_y$  plane, calculated by Eq. 1.41. **b.** The DOS of a  $p$ -wave superconductor with point nodes along the  $k_z$  axis calculated from Eq. 1.43. The in-gap DOS falls as  $N(E) \propto E^2$

Of particular relevance to this thesis is the physics of  $p$ -wave superconductivity. The DOS for such a state can be calculated in a similar way to the above however now we consider the order parameter  $|\Delta_{\mathbf{k}}| = \Delta_0 \sin(\theta_{\mathbf{k}})$  and use the substitution  $\sin(\theta_{\mathbf{k}}) = \sqrt{1 - x^2}$ <sup>13</sup>

$$N(E) = N_0 \frac{E}{\Delta_0} \int dx \operatorname{Re} \left\{ \frac{1}{\sqrt{(E/\Delta_0)^2 + x^2 - 1}} \right\} = N_0 \frac{E}{\Delta_0} \left| \frac{1 + \frac{E}{\Delta_0}}{1 - \frac{E}{\Delta_0}} \right| \quad (1.43)$$

From Fig. 1.2b we see that, similar to the  $d$ -wave case, the DOS within the superconducting gap does not fall drastically as in the  $s$ -wave superconductor. This  $p$ -wave order parameter also features nodes, however, these are point nodes rather than the line nodes of a  $d$ -wave superconductor. These point nodes are single, point-like excitations near zero energy and consequently do not contribute to the DOS as significantly as line nodes.

## 1.4 Macroscopic Phase & Off-Diagonal Long Range Order

Before moving forward to describe more diverse superconducting condensates we make some brief comments on the limits of the BEC picture of superconductivity and the source of the U(1) symmetry breaking which defines the macroscopic order parameter phase. We begin by understanding that Bose-Einstein

condensation is a case of a broader framework of macroscopic condensation, introduced by Oliver Penrose and Lars Onsager<sup>15</sup>, known as off-diagonal long-range order (ODLRO). This approach makes use of the single-particle and two-particle density matrix

$$\rho_1(\mathbf{r}_1, \mathbf{r}'_1) = N \int d\mathbf{r}_2 \int d\mathbf{r}_3 \dots \int d\mathbf{r}_N \Psi^*(\mathbf{r}_1, \mathbf{r}_2, \dots, \mathbf{r}_N) \Psi(\mathbf{r}'_1, \mathbf{r}_2, \dots, \mathbf{r}_N) \quad (1.44)$$

$$\rho_2(\mathbf{r}_1, \mathbf{r}_2, \mathbf{r}'_1, \mathbf{r}'_2) = N(N-1) \int d\mathbf{r}_3 \int d\mathbf{r}_4 \dots \int d\mathbf{r}_N \Psi^*(\mathbf{r}_1, \mathbf{r}_2, \dots, \mathbf{r}_N) \Psi(\mathbf{r}'_1, \mathbf{r}'_2, \dots, \mathbf{r}_N) \quad (1.45)$$

We may also define such a matrix at finite temperature by including the partition function  $Z = \sum_n e^{-\beta E_n}$  such that

$$\rho_1(\mathbf{r}_1, \mathbf{r}'_1) = \frac{N}{2} \sum_n e^{-\beta E_n} \int d\mathbf{r}_2 \int d\mathbf{r}_3 \dots \int d\mathbf{r}_N \Psi_n^*(\mathbf{r}_1, \mathbf{r}_2, \dots, \mathbf{r}_N) \Psi_n(\mathbf{r}'_1, \mathbf{r}_2, \dots, \mathbf{r}_N) \quad (1.46)$$

where  $E_n$  and  $\Psi_n$  are the  $n$ -th eigenenergy and eigenvector of the system respectively. This matrix is Hermitian and can be diagonalized so that the trace of the density matrix at a point,  $\mathbf{r}_1 = \mathbf{r}'_1$ , is the particle number  $\text{Tr}\rho_1 = \int d\mathbf{r} \rho_1(\mathbf{r}_1, \mathbf{r}_1) = N$  and  $\text{Tr}\rho_2 = \int d\mathbf{r} \rho_2(\mathbf{r}_1, \mathbf{r}_2, \mathbf{r}_1, \mathbf{r}_2) = N(N-1)$

If we consider spinless bosons whose  $\alpha$ -th eigenvalue of  $\rho_1$  is  $n_\alpha$  with eigenvector  $\chi_\alpha(\mathbf{r})$ , we can write

$$\rho_1(\mathbf{r}, \mathbf{r}') = \sum_\alpha n_\alpha \chi_\alpha^*(\mathbf{r}') \chi_\alpha(\mathbf{r}) \quad (1.47)$$

At  $T = 0$  non-interacting bosons condense to a single  $\mathbf{k} = 0$  eigenstate,  $\chi_0 = 1/\sqrt{V}$ , giving the simple expression for the density operator for any  $\mathbf{r}$  and  $\mathbf{r}'$

$$\rho_1(\mathbf{r}', \mathbf{r}) = \langle \hat{\psi}^\dagger(\mathbf{r}') \hat{\psi}(\mathbf{r}) \rangle = N \chi_0^*(\mathbf{r}') \chi_0(\mathbf{r}) = N/V \quad (1.48)$$

In general, for finite temperatures and interaction strengths the occupancy of this orbital  $\chi_0$  is not complete and the density matrix decreases to a constant value  $N < N_0$  for  $|\mathbf{r}' - \mathbf{r}|$  large, where  $N_0$  is the total particle number. Above the transition temperature this long-range correlation is not present and the

density matrix falls exponentially to zero for  $|\mathbf{r}' - \mathbf{r}| \rightarrow \infty$ . In superconductors, the pair terms on the right-hand side of the Hamiltonian Eq. 1.22 allow quasiparticles to scatter into and out of the condensate therefore, at finite temperature and with weak interactions between pairs, the density matrix  $\rho_2$  remains finite for  $|\mathbf{r}' - \mathbf{r}|$  large thus confirming that superconductivity falls under the category of ODLRO. From this interpretation the Meissner effect and flux quantisation is an expected property of superconductors as it is for that of a charged condensate with macroscopic occupation<sup>16</sup>. In fact, it is believed that the BCS ground state can be continuously tuned to a BEC ground state, this is referred to as the BCS-BEC crossover, and is an area of ongoing research in condensed matter and ultra-cold atom systems<sup>17</sup>.

In the mean-field treatment above we introduced a Hamiltonian which does not conserve particle number. As particle number is the conjugate of phase,  $i\frac{\partial}{\partial N} = \phi$ , we therefore expect superconductors to exhibit macroscopic phase coherence at  $T = 0$  however, it is possible to write down the BCS equations such that particle number is conserved. Phase coherence cannot then be considered a direct result of this convenient derivation of the BCS equations but rather a physical effect. In reality, the phase of the superconductor is the result of the degeneracy of the BCS ground state. In the thermodynamic limit, the difference in energy between a system with  $N$  or  $N + 1$  pairs is negligible and so there is large degeneracy to the ground state. These degenerate ground states can then be labelled by the phase field  $\phi$ . The choice of a particular ground state at  $T = 0$  is then a choice of a particular  $\phi$  and the breaking of local  $U(1)$  phase rotation symmetry<sup>18</sup>. For an  $s$ -wave superconductor this choice of phase is an isotropic value over all momentum space  $\phi_{\mathbf{k}} = \phi_{-\mathbf{k}} = \phi$  however, as we will now see, this is not true of the superconductors of recent interest.

## 1.5 Unconventional Pairing & d-Vector Representation

In our derivation of the BCS wavefunction, Eq. 1.16, we assumed that the pair potential, the interaction term which binds quasiparticles into Cooper pairs,  $g_{\mathbf{k}}$ , is isotropic. While this is mostly correct in the case of phonon-mediated Cooper pairing it is certainly not applicable to what are known as the unconventional superconductors. Such superconductors are at the forefront of

research and include the cuprates, iron-based, heavy-fermion, and organic superconductors<sup>19</sup>. To describe these superconducting states we must consider a broader classification of Cooper pairing which arises naturally when considering fermionic statistics. Two fermions at positions  $\mathbf{r}_1$  and  $\mathbf{r}_2$  and with spins  $\alpha$  and  $\beta$  must be odd parity under exchange of particles

$$\psi_\alpha^\dagger(\mathbf{r}_1)\psi_\beta^\dagger(\mathbf{r}_2) = -\psi_\beta^\dagger(\mathbf{r}_2)\psi_\alpha^\dagger(\mathbf{r}_1) \quad (1.49)$$

Consequently the Cooper pair wavefunction or the mean-field term responsible for ODLRO

$$b_{\mathbf{k},\alpha,\beta} = \langle c_{-\mathbf{k},\alpha}c_{\mathbf{k},\beta} \rangle \quad (1.50)$$

must also obey fermionic commutation relations under exchange of particles. As this term depends on the orbital and spin components of the two quasiparticle operators, we can express the mean-field operator as a product of orbital and spin dependent functions

$$b_{\mathbf{k},\alpha,\beta} = f(\mathbf{k})\chi_{\alpha,\beta} \quad (1.51)$$

From this we can see that two distinct pairing types are possible, a spin singlet pairing state and a spin triplet state whose corresponding orbital functions are even and odd-parity in momentum space respectively. More explicitly,

$$\begin{aligned} f(\mathbf{k}) = f(-\mathbf{k}) & \quad \chi_{\alpha,\beta} = \frac{1}{\sqrt{2}} (|\uparrow\downarrow\rangle - |\downarrow\uparrow\rangle) \\ f(\mathbf{k}) = -f(-\mathbf{k}) & \quad \chi_{\alpha,\beta} = \begin{cases} |\uparrow\uparrow\rangle \\ \frac{1}{\sqrt{2}} (|\uparrow\downarrow\rangle + |\downarrow\uparrow\rangle) \\ |\downarrow\downarrow\rangle \end{cases} \end{aligned}$$

This mean-field operator is very closely related to the superconducting order parameter, see Eq. 1.21, thus the order parameter obeys the same particle exchange relations and can be in a spin singlet or triplet form. As we are now considering the role of spin in Cooper pairing we adopt a useful notation which makes rotations of the order parameter much easier to calculate. We express the order parameter in terms of Pauli matrices, such that

$$\Delta_{\mathbf{k}} = \Delta_0(i\sigma_2) + i(\mathbf{d}(\mathbf{k}) \cdot \boldsymbol{\sigma})\sigma_2 \quad (1.52)$$

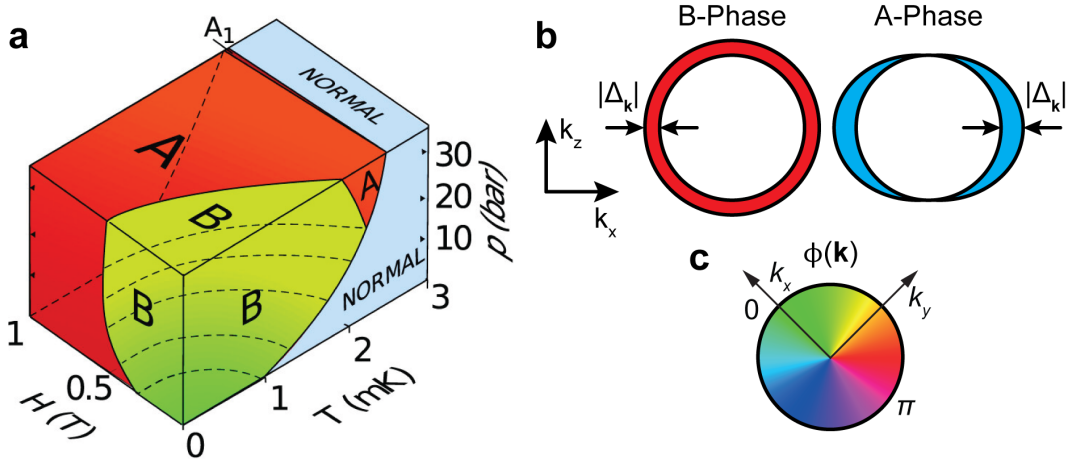


Figure 1.3: **a.** Phase diagram of superfluid  $^3\text{He}$  under applied pressure and magnetic field as a function of temperature sourced from Ref. [20]. **b.** The superconducting energy gap of the B- and A-Phase of  $^3\text{He}$  respectively. Substitution of the A-Phase d-vector, Eq. 1.56 into the dispersion Eq. 1.57 yields zeros/nodes in the superconducting energy gap wherever  $|\mathbf{d}(\mathbf{k})|^2 \pm |\mathbf{d}(\mathbf{k}) \times \mathbf{d}^*(\mathbf{k})| = 0$  **c.** Schematic of chiral order parameter phase winding in momentum space

where  $\Delta_0$  is a scalar constant and  $\mathbf{d}(\mathbf{k})$  is the d-vector which is the triplet order parameter required to capture anisotropic pairing. In terms of their individual components the above is then

$$\Delta_{\mathbf{k}} = \begin{pmatrix} \Delta_{\mathbf{k},\uparrow\uparrow} & \Delta_{\mathbf{k},\uparrow\downarrow} \\ \Delta_{\mathbf{k},\downarrow\uparrow} & \Delta_{\mathbf{k},\downarrow\downarrow} \end{pmatrix} = \begin{pmatrix} -d_x(\mathbf{k}) + id_y(\mathbf{k}) & \Delta_0 + d_z(\mathbf{k}) \\ -\Delta_0 + d_z(\mathbf{k}) & d_x(\mathbf{k}) + id_y(\mathbf{k}) \end{pmatrix} \quad (1.53)$$

This d-vector notation now allows us to classify superconducting states in many different materials. In superfluid He we conveniently have SO(3) symmetry and can express the d-vector in terms of the spherical harmonic functions such that

$$\mathbf{d}_i(\mathbf{k}) = \sum_{m=-l}^l \eta_{i,m}^l Y_{l,m}(\hat{\mathbf{k}}) \quad (1.54)$$

Since these spherical harmonic functions define the shape of the atomic orbitals we adopt a similar naming convention in superconductivity research such that we label  $l = 0$  states to be *s*-wave,  $l = 1$  *p*-wave,  $l = 2$  *d*-wave, etc. As an example we briefly introduce the pairing states of  $^3\text{He}$ , which is believed to be somewhat analogous to  $\text{UTe}_2$ . The phase diagram for this isotope is shown in Fig. 1.3 and displays three distinct superfluid phases, the A, A<sub>1</sub>, and B phase. It has been known for decades that these phases exhibit pairing in the

$l = 1$  or  $p$ -wave channel and from experiment the momentum dependence of the d-vector has been firmly established<sup>21</sup>. For the B phase, this d-vector is simply

$$\mathbf{d}^B(\mathbf{k}) \propto \begin{pmatrix} k_x \\ k_y \\ k_z \end{pmatrix} \quad (1.55)$$

While this is an example of  $p$ -wave pairing it's important to realize that this superfluid state is isotropic, or full-gapped, and exhibits odd-parity in momentum space (Fig. 1.3b). In comparison, the A phase of  $^3\text{He}$  is defined by the d-vector

$$\mathbf{d}^A(\mathbf{k}) \propto \begin{pmatrix} k_x + ik_y \\ 0 \\ 0 \end{pmatrix} \quad (1.56)$$

The anisotropy of the d-vector suggests an anisotropy in pair formation and consequently in the energy gap. For an unconventional superconductor, the quasiparticle dispersion relation  $E_{\mathbf{k}}$  is modified to include the triplet order parameter so that the complete dispersion relation is

$$E_{\mathbf{k}} = \sqrt{\xi_{\mathbf{k}}^2 + |\Delta_{\mathbf{k}}|^2} = \sqrt{\xi_{\mathbf{k}}^2 + \Delta^2(|\mathbf{d}(\mathbf{k})|^2 \pm |\mathbf{d}(\mathbf{k}) \times \mathbf{d}^*(\mathbf{k})|)} \quad (1.57)$$

where the d-vector has been normalized and  $\Delta$  controls the amplitude of the gap function. Substitution of the A phase d-vector then reveals points in k-space for which there is no change in the dispersion from the normal state, namely when  $k_x = 0$  and  $k_y = 0$ . These points in k-space are referred to as nodes or nodal points. Their presence alters many of the properties of the superconductor/superfluid including the density of states, electronic specific heat capacity, magnetic penetration depth, and many others. Of relevance to later discussions of  $\text{UTe}_2$  is that the A phase of  $^3\text{He}$  is a chiral superfluid phase. Such states are referred to as chiral in reference to the handedness of their momentum space phase winding. This phase winding is the result of the continuous  $\pi/2$  phase shift between the  $k_x$  and  $k_y$  components of the order parameter. The chirality of the phase winding is then determined by the choice of degenerate order parameters with opposite phase winding  $k_x \pm ik_y$  as  $e^{i\frac{\pi}{2}} = i$  while  $e^{-i\frac{\pi}{2}} = -i$ . Chiral superfluid/superconducting states are of significant importance in current research as they are expected to host exotic fractionalized quasiparticles with non-Abelian statistics known as Majorana

	E	$C_2(z)$	$C_2(y)$	$C_2(x)$	i	$\sigma(xy)$	$\sigma(xz)$	$\sigma(yz)$	linear, rotations	quadratic
<b>A<sub>g</sub></b>	1	1	1	1	1	1	1	1		$x^2, y^2, z^2$
<b>B<sub>1g</sub></b>	1	1	-1	-1	1	1	-1	-1	$R_z$	xy
<b>B<sub>2g</sub></b>	1	-1	1	-1	1	-1	1	-1	$R_y$	xz
<b>B<sub>3g</sub></b>	1	-1	-1	1	1	-1	-1	1	$R_x$	yz
<b>A<sub>u</sub></b>	1	1	1	1	-1	-1	-1	-1		
<b>B<sub>1u</sub></b>	1	1	-1	-1	-1	-1	1	1	z	
<b>B<sub>2u</sub></b>	1	-1	1	-1	-1	1	-1	1	y	
<b>B<sub>3u</sub></b>	1	-1	-1	1	-1	1	1	-1	x	

Figure 1.4: Character table for the point group symmetry  $D_{2h}$  outlining the irreducible representations of this group and the associated symmetries of these irreducible representations in Schoenflies notation<sup>23</sup>.  $E$  is the identity operator,  $C_n$  is a rotation through  $2\pi/n$ ,  $I$  is inversion symmetry,  $\sigma$  is a reflection in a specified plane

zero modes<sup>22</sup>.

While rotational symmetry,  $SO(3)$ , is conserved in a fluid this is not true of crystalline systems which host superconductivity. In crystalline systems, the symmetry of the lattice necessarily determines the symmetry of the superconducting order parameter. In the d-vector notation it is the d-vector which transforms as the irreducible representations  $\Gamma$  of the point symmetry group  $G$  of the crystal.

$$\mathbf{d}(\mathbf{k}) = \sum_{i=1}^{d_\Gamma} \eta_i \psi_i^\Gamma(\hat{\mathbf{k}}) \quad (1.58)$$

Here  $d_\Gamma$  is the dimensionality of the irreducible representation. These irreducible representations are classified by their parity such that order parameters which transform as even parity or gerade irreducible representations  $\Gamma_g$  are necessarily spin singlet, while those which transform as odd-parity or ungerade  $\Gamma_u$  are spin triplet. The crystal point symmetry group of  $UTe_2$  is  $D_{2h}$  and its irreducible representations are listed in Fig. 1.4. There are four even and four odd-parity irreducible representations in this group of which the  $A_g$  and  $A_u$  are fully gapped while the  $B_g$  or  $B_u$  states are nodal.

## 1.6 Finite-momentum Pairing States

As we've seen some key approximations were made in the derivation of the BCS relations in Section 1.3. Firstly, Cooper pairs were assumed to form singlet,  $s$ -wave states. We've now extended our system of classification to encompass states of higher orbital angular momentum such as  $p$ - and  $d$ -wave. The second assumption is that Cooper pairs form with zero centre of mass momentum. We will now see that this is also an oversimplification of real materials and that superconducting states with non-zero momentum are realizable.

### 1.6.1 Fulde-Ferrell and Larkin-Ovchinnikov (FFLO) States

The first suggestion of finite-momentum pairing states came from two separate reports, one by Fulde and Ferrell (FF)<sup>24</sup> and the other from Larkin and Ovchinnikov (LO)<sup>25</sup>. Combined, the states reported by these authors are referred to as the FFLO state and it has been sought after for decades. Only recently, in the heavy-fermion and organic superconductors has this state become realizable<sup>26,27</sup>. We briefly comment on the form of the FF and LO states as it is instructive to see how finite-momentum Cooper pairing may come about. For an  $s$ -wave superconductor whose Cooper pairs have zero net spin there are two ways in which a magnetic field may destroy Cooper pair condensation. These are orbital and paramagnetic pair-breaking effects. The presence of a magnetic field leads to the formation of Abrikosov vortices which thread Type-II superconductors. Around these vortices flows a supercurrent of Cooper pairs reducing the superconducting condensation energy and in their centre are unpaired, normal-state quasiparticles. Thus, at a certain critical field  $H_{c_2}^{\text{orb}} = \Phi_0/2\pi\xi^2$ <sup>13</sup>, the orbital limiting field, the cores of these vortices overlap destroying the Cooper pair condensate. Note that  $\Phi_0$  is the magnetic flux quantum, the unit of magnetic flux which passes through a single vortex  $\Phi_0 = h/2e$ , and  $\xi$  is the superconducting coherence length, a natural length scale for Cooper pairs.

The paramagnetic pair-breaking effect arises from the energy difference between spin-up and spin-down quasiparticles in the presence of a magnetic field. This Pauli paramagnetic effect causes pair breaking when the energy difference between polarized and unpolarized quasiparticles exceeds the Cooper pair binding energy. This Pauli paramagnetic limiting field is then  $H_{c_2}^{\text{para}} =$

$\sqrt{2}\Delta/g\mu_B$  where  $g$  is the Landé  $g$ -factor and  $\mu_B$  is the Bohr magneton. The ratio of these orbital and paramagnetic limiting fields gives the Maki parameter<sup>27</sup> which is instructive in searching for candidate materials for an FFLO state.

$$\alpha = \sqrt{2} \frac{H_{c_2}^{\text{orb}}}{H_{c_2}^{\text{para}}} \quad (1.59)$$

The insight from FFLO was the observation that the Pauli paramagnetic pair-breaking effect can be reduced by the formation of new Cooper pairs between the Zeeman split bands. This new Cooper pair has finite centre of mass momentum as it results from pairing between two spin-split bands now separated in  $k$ -space by the wavevector  $q$ , thus we have Cooper pairs of the form  $c_{\mathbf{k},\uparrow}^\dagger c_{-\mathbf{k}+\mathbf{q},\downarrow}^\dagger$  (Fig. 1.5a,b). Fulde and Ferrell<sup>24</sup> proposed a state in which this finite-momentum pairing occurs for just one half of the Zeeman split Fermi surfaces, this is shown in Fig. 1.5c. The order parameter for such a state is

$$\Delta_{\text{FF}}(\mathbf{r}) = \Delta e^{i\mathbf{q}\cdot\mathbf{r}} \quad (1.60)$$

and is spatially homogeneous but has phase varying in real space and breaks time-reversal symmetry. For a spin-split Fermi surface which does not experience depairing, the pairing states with  $q$  and  $-q$  are degenerate. The resulting state is that considered by Larkin and Ovchinnikov<sup>25</sup>

$$\Delta_{\text{LO}}(\mathbf{r}) = \Delta(e^{i\mathbf{q}\cdot\mathbf{r}} + e^{-i\mathbf{q}\cdot\mathbf{r}}) = 2\Delta \cos(\mathbf{q}\cdot\mathbf{r}) \quad (1.61)$$

and has a spatially varying magnitude for the order parameter of wavelength  $2\pi/q$ . In real materials several  $q$  vectors may have equivalent upper critical fields in which case the order parameter of the finite-momentum condensate is

$$\Delta_{\text{FFLO}}(\mathbf{r}) = \sum_{m=1}^M \Delta_m e^{i\mathbf{q}_m\cdot\mathbf{r}} \quad (1.62)$$

where  $M$  is the number of equivalent scattering wavevectors allowing Cooper pairing between the spin-split Fermi surface.

The difficulty in discovering the FFLO state in experiment is a result of the balance between orbital and pair breaking effects, which is expressed in the Maki parameter,  $\alpha$ . While the Pauli paramagnetic limiting field is increased by the formation of an FFLO state, it does nothing to increase the orbital limiting field as vortices are still formed by the condensate. Materials with large

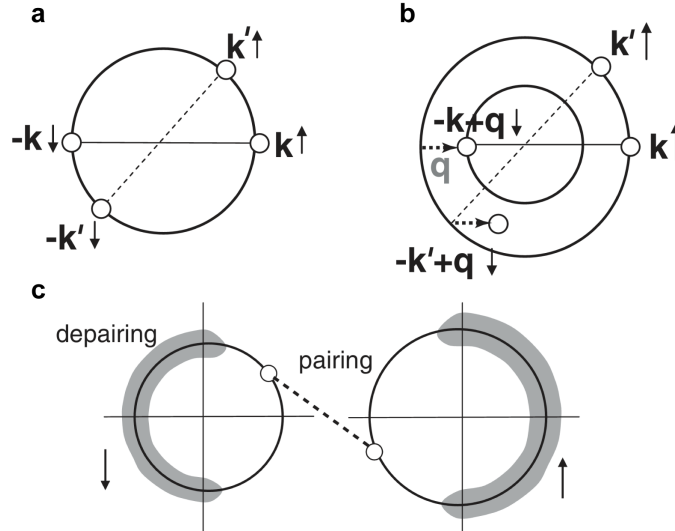


Figure 1.5: **a.** Zero momentum Cooper pairing for a single Fermi surface. **b.** Finite-momentum Cooper pairing in a Zeeman split Fermi surface. Cooper pairs form with centre of mass momentum  $q$ . **c.** Cooper pairing as considered by Fulde and Ferrell<sup>24</sup>. Pairs are formed between half of the spin-split Fermi surface giving rise to condensates with spatially varying phase. Figure reproduced from Ref. [27]

Maki parameters such as the heavy-fermion superconductors are some of the only materials which could stabilise such a state. In experiment, the applied magnetic field must also be aligned parallel to the superconductor surface with small misalignment providing flux for the formation of vortices thus limiting the formation of the FFLO state. While finite-momentum pairing was first discussed in the context of the FFLO state, current research has uncovered spatially modulating Cooper pair density and superconducting energy gaps which, while possibly related to the FFLO states, are not simply explained by the above theory.

## 1.6.2 Pair Density Waves (PDWs)

### 1.6.2.1 Ginzburg-Landau Theory

In recent years modulations in the superconducting energy gap and Cooper pair density have been discovered in a range of materials including  $s$ -wave<sup>28</sup>,  $d$ -wave<sup>29</sup>, and  $p$ -wave superconductors<sup>30</sup> despite no magnetic field being applied during these measurements. Without a detailed microscopic interpretation of these results these finite-momentum pairing states are referred to generally

as pair density waves (PDWs) and feature both/either spatial modulations in the order parameter magnitude and/or phase. It is worth noting that while the superconducting energy gap is related to the Cooper pair density in BCS theory, this is not necessarily true for all materials. A notable example of this is in the pseudogap phase of the cuprate superconductors. In fact the significant research interest in PDWs stems from their role in the superconducting, and possibly in the pseudogap phase, of the cuprates. In these systems the PDW phase has been hypothesized as the parent phase to the high-temperature superconductor<sup>31,32,33,34</sup>.

Although we do not have a microscopic mechanism for PDW formation, we can make use of a phenomenological theory of superconductivity introduced in 1950 by Ginzburg and Landau<sup>35</sup> and now commonly referred to as Ginzburg-Landau theory. This approach is based upon Landau's theory of second-order phase transitions which introduced the concept of an order parameter. This order parameter is zero in the high-temperature, disordered phase of the system but takes on a finite value after a certain symmetry of the Hamiltonian is no longer preserved. The most commonplace example of such an order parameter is the magnetic moment  $\mathbf{M}$  of a ferromagnet. In the paramagnetic, high-temperature phase  $\mathbf{M} = 0$ . Below the Curie temperature rotational symmetry is broken as the magnetic moments at each crystal site align generating a finite macroscopic moment  $\mathbf{M} > 0$ . The same concept can be applied to a superconductor however, now we use the superconducting energy gap, which we assume is proportional to the Cooper pair number density,  $\Delta \propto \sqrt{n_s}$ , to be the order parameter produced by the formation of Cooper pairs. Ginzburg and Landau's approach is based upon the difference in free energy between the normal and superconducting state. For a uniform superconductor in the absence of an applied magnetic field, this difference is simply a Taylor expansion of  $|\Delta|^2$  or in terms of the number density  $n_s$ . Here we keep only the first two terms assuming we are near  $T = T_c$

$$f_s - f_n = \alpha|\Delta|^2 + \beta|\Delta|^4 \quad (1.63)$$

Thermal equilibrium is achieved when the free energy is minimized thus  $\beta$  must be positive to ensure that such a minimum exists. The coefficient  $\alpha$  may take either positive or negative sign and these two cases correspond to the normal and superconducting state respectively. For  $\alpha > 0$  the free energy is minimised for  $|\Delta|^2 = 0$  as seen in Fig. 1.6a. However, for  $\alpha < 0$  the above

equation is minimised when  $|\Delta|^2 = -\frac{\alpha}{\beta}$  as in a bulk superconductor unaffected by screening currents or defects. We plot this form of the free energy in Fig. 1.6b. We can then assume some simple forms for  $\alpha$  and  $\beta$

$$\alpha(T) = \alpha'(T - T_c) \qquad \beta(T) \approx \beta(T_c) > 0 \qquad (1.64)$$

Thus below, but near  $T_C$ , the order parameter takes the form

$$|\Delta|^2 = -\frac{\alpha}{\beta} = \frac{\alpha'(T_c - T)}{\beta} = \frac{\alpha'(1 - T/T_c)}{\beta} \qquad (1.65)$$

Which is of the same form as the BCS expression for the magnitude of a conventional superconducting energy gap with temperature  $|\Delta| \propto (1 - T/T_c)^{1/2}$ .

From Fig. 1.6b we see that in the superconducting state the free energy is lowered so that minima now occur at  $f_s - f_n < 0$ . For a Type-I superconductor, the energy difference between the superconducting and normal state must be related to the critical field of the superconductor,  $H_c$ . By comparison with the full Gibbs free energy  $G(T, H) = F - \mathbf{HB}/4\pi$  these minima must have a depth of  $\mathbf{H}_c/8\pi$ , this magnitude is indicated schematically in Fig. 1.6b by double-headed yellow arrows.

Finally, we note that the Ginzburg-Landau order parameter is necessarily a complex function with a phase term  $\Delta e^{i\phi}$ . The free energy is then a Mexican hat type function with a ring of degenerate minima. The phase of the order parameter is then a specific point on this degenerate ring of minima. This is a key point in understanding the Anderson-Higgs mechanism and the associated Goldstone modes of a superconductor, however, we do not address this mechanism here.

### 1.6.2.2 Intertwined Orders

We now know that even without a microscopic interpretation of superconductivity, insights can be gained from this Ginzburg-Landau approach. This is particularly useful in systems with intertwined forms of electronic order such as superconductivity, pair density waves, charge density waves, spin density waves, etc.<sup>36</sup>. We focus then on the preserved and broken symmetries of the system in the presence of different order parameters. Considering charge density wave order of the form

$$\rho_{Q_i}(\mathbf{r}) = \rho(\mathbf{r})e^{i\mathbf{Q}_i \cdot \mathbf{r}} + \rho^*(\mathbf{r})e^{-i\mathbf{Q}_i \cdot \mathbf{r}} \qquad (1.66)$$

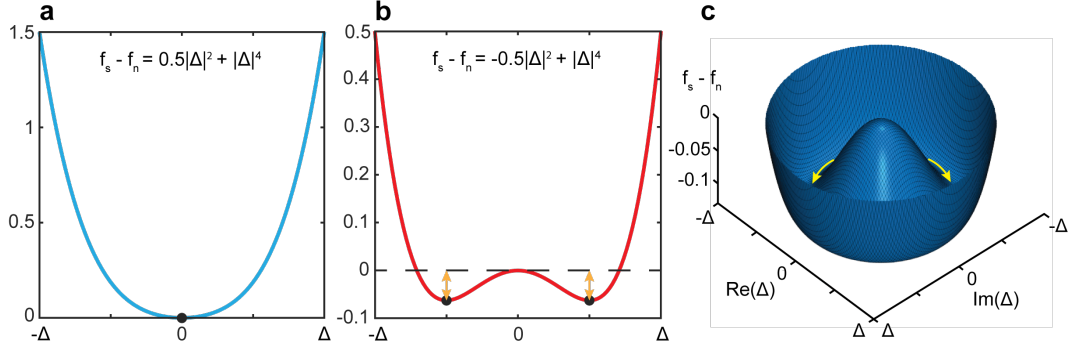


Figure 1.6: **a** Ginzburg-Landau free energy in the normal state with  $\alpha = 0.5 > 0$  and  $\beta = 1$ . A single minimum at  $|\Delta|^2 = 0$  is indicative of temperatures  $T > T_C$ . **b** Ginzburg-Landau free energy in the superconducting state with  $\alpha = -0.5 < 0$  and  $\beta = 1$ . Two minima occur at  $\mp \frac{\alpha}{\beta} = 0.5\Delta$ . The depth of these minima correspond to the energy of the upper critical field  $H_c/8\pi$ . This magnitude is indicated by double-headed yellow arrows. **c**. Ginzburg-Landau free energy in the superconducting state  $f_n - f_s = -0.5|\Delta|^2 + 0.5|\Delta|^4$  with a complex order parameter of the form  $\Delta e^{i\phi}$ . A ring of degenerate minima is indicated by yellow arrows.

and pair density wave order of the form

$$\Delta_{P_i} = \Delta_{P_i} e^{i\mathbf{P}_i \cdot \mathbf{r}} + \Delta_{-P_i}^* e^{-i\mathbf{P}_i \cdot \mathbf{r}} \quad (1.67)$$

Then both order parameters break translation symmetry, the first to do so when going from the disordered to ordered phase is the parent order. Furthermore, on entering the superconducting state local  $U(1)$  gauge symmetry is also broken so that the superconducting order parameter acquires a finite phase

$$|\Delta| = 0 \rightarrow |\Delta| = \Delta e^{i\phi} \quad (1.68)$$

In the presence of all three forms of order; CDW, PDW, and uniform superconductivity we can write the Ginzburg-Landau free energy functional as a sum of the individual orders, their linear coupling, and higher order coupling terms (H.O.C.T)

$$\mathcal{F} = \mathcal{F}_S + \mathcal{F}_C + \mathcal{F}_P + \sum_i (\lambda_i^* \rho_{Q_i} \Delta_S^* \Delta_{P_i} + \lambda_i \rho_{-Q_i}^* \Delta_S \Delta_{-P_i}^*) + \text{H.O.C.T} \quad (1.69)$$

Here  $\mathcal{F}_S$ ,  $\mathcal{F}_C$ ,  $\mathcal{F}_P$  are the free energy densities of the uniform superconductor, CDW, and PDW respectively. Clearly either spatial modulations of the charge

or Cooper pairs may couple to the uniform superconductor. To lowest order there are then two parent-child relationships possible: (1) if  $\Delta_S(\mathbf{r})$  and  $\Delta_P(\mathbf{r})$  are the dominant orders, they generate charge modulations with the same wavevector  $\mathbf{P}_i$ ,  $\rho(\mathbf{r}) \propto \Delta_S^* \Delta_P + \Delta_{-P_i}^* \Delta_S$ , and at twice this wavevector  $2\mathbf{P}_i$ ,  $\rho_{2P_i} \propto \Delta_{-P_i}^* \Delta_P$ ; (2) if  $\Delta_S(\mathbf{r})$  and  $\rho_{Q_i}(\mathbf{r})$  are the dominant orders, then they may generate a PDW at wavevector  $\mathbf{Q}_i$ ,  $\Delta_{Q_i} \propto \Delta_S^* \rho_{Q_i}$ . The coupling between these order parameters makes determining their exact relationship incredibly difficult. Determining the parent-child relationship between PDW and CDW order is critically important in the cuprates as these phases are likely connected to the formation of the high-temperature superconductor<sup>29</sup>. However, these interactions are quite universal and these forms of intertwined order may occur in any strongly correlated superconducting material.

While this analysis gives intuition regarding the wavevector of the induced/parent order, it does nothing to tell us about the phase relationship between these orders. For this a microscopic model of the specific system is required which has not been derived for  $\text{UTe}_2$  and is beyond the scope of this thesis.

## Chapter 2

# Spectroscopic Imaging Scanning Tunnelling Microscopy (SI-STM)

### 2.1 Introduction

The invention of the scanning tunnelling microscope (STM) in 1982<sup>37</sup> signalled the beginning of atomic manipulation and measurement. Since then it has become a canonical probe of condensed matter systems due its unprecedented spatial and energy resolution. Excitingly, the limits of this experimental tool are frequently expanded with modern techniques such as scanned-Josephson tunnelling microscopy<sup>29</sup>, electronic shot noise spectroscopy<sup>38</sup>, spin-polarized tunnelling microscopy<sup>39</sup>, and many others. All of the experimental work presented in this thesis was measured using an STM so we will now discuss the basic operating principles of such machines and outline the range of experimental techniques relevant to this thesis.

### 2.2 Tunnelling Currents

While cryogenic and vacuum systems may vary from machine to machine the core component of the STM is the scan head. Here is housed two electrodes, a sharp scan tip and the sample material to be studied. When kept at incredibly small separations ( $10^{-10}\text{m} = 1\text{\AA}$ ) their electronic wavefunctions overlap to allow a measurable tunnelling current to pass across the insulating barrier. To begin then, we discuss the details of tunnelling current measurements and how

they can be used to reveal surface topography and electronic structure.

The standard theoretical description of such an experimental configuration is that provided by Bardeen<sup>40</sup>. In the description outlined below we follow the assumptions and approach of Bardeen as outlined in Ref.[41] and Ref.[42].

We first consider solving the stationary Schrödinger equation for two subsystems, which in this case are the STM tip and the sample under study. We then calculate the transmission rate for electrons using time-dependent perturbation theory. In three dimensions the Schrödinger equation of the sample is

$$\left(-\frac{\hbar^2}{2m}\nabla^2 + U_S\right)\psi_\mu = E_\mu\psi_\mu \quad (2.1)$$

and for the STM tip

$$\left(-\frac{\hbar^2}{2m}\nabla^2 + U_T\right)\chi_\nu = E_\nu\chi_\nu \quad (2.2)$$

The eigenfunctions of these equations describe the spatial dependence of more general time-dependent stationary states, which are themselves solutions of separate time-dependent Schrödinger equations for these systems. Such that

$$\Psi_\mu = \psi_\mu e^{-iE_\mu t/\hbar} \quad (2.3)$$

is a solution of

$$i\hbar\frac{\partial\Psi_\mu}{\partial t} = \left[-\frac{\hbar^2}{2m}\nabla^2 + U_S\right] \quad (2.4)$$

and a solution of the same form can be written for  $\chi_\nu$ . By reducing the tip-sample distance, the two states are no longer independent and the combined Schrodinger equation must be solved. To do so, we make the key approximation that the two wavefunctions are approximately orthogonal

$$\int \psi_\mu^* \chi_\nu d^3\mathbf{r} \approx 0 \quad (2.5)$$

and in doing so we can assume a solution to the combined Schrödinger equation

$$i\hbar\frac{\partial\Psi}{\partial t} = \left[-\frac{\hbar^2}{2m}\nabla^2 + U_S + U_T\right] \Psi \quad (2.6)$$

of the form

$$\Psi = a_\mu(t)\psi_\mu e^{-iE_\mu t/\hbar} + \sum_{\nu=1}^{\infty} c_\nu(t)\chi_\nu e^{-iE_\nu t/\hbar} \quad (2.7)$$

The prefactors,  $a_\mu(t)$  and  $c_\nu(t)$ , describe the probability of electron transfer as a function of time. Thus as  $t \rightarrow -\infty$ ,  $a_\mu(-\infty) = 1$  and  $c_\nu(-\infty) = 0$  however as the tip-sample distance is reduced these states evolve due to the time dependence of  $U_T$ . Because electron dynamics occur with a time constant of the order of femtoseconds ( $10^{-15}$  s) we can consider adiabatic changes in  $U_T$  as the time needed to move the tip is of the order of seconds.

$$U_T(t) = e^{\eta t/\hbar} U_{T,\eta} > 0 \quad (2.8)$$

Now inserting Eq.2.7 into Eq.2.6, projecting onto the state  $\chi_\nu$ , and considering only the first order perturbation theory contributions we obtain

$$i\hbar \frac{dc_\nu(t)}{dt} = \langle \chi_\nu | U_T | \psi_\mu \rangle e^{-i(E_\lambda - E_\nu + i\eta)t/\hbar} \quad (2.9)$$

This projection of sample states to tip states is the key concept of tunnelling and is often expressed using the tunnelling matrix element

$$M_{\mu\nu} = \langle \psi_\mu | U_T | \chi_\nu \rangle \quad (2.10)$$

Using this notation and integrating over time we arrive at the expression

$$c_\nu(t) = M_{\mu\nu} \frac{e^{-i(E_\mu - E_\nu + i\eta)t/\hbar}}{E_\mu - E_\nu + i\eta} \quad (2.11)$$

The magnitude of this expression,  $|c_\nu(t)|^2$  per unit time, or  $\frac{d|c_\nu(t)|^2}{dt}$  gives the tunnelling probability per unit time,  $P_{\mu\nu}(t)$

$$P_{\mu\nu}(t) = |M_{\mu\nu}|^2 \frac{2\eta}{\hbar [(E_\mu - E_\nu)^2 + \eta^2]} \quad (2.12)$$

Taking the limit of  $\eta \rightarrow 0$  we obtain

$$P_{\mu\nu}(t) = \frac{2\pi}{\hbar} \delta(E_\mu - E_\nu) |M_{\mu\nu}|^2 \quad (2.13)$$

This is the same expression as that obtained by Dirac<sup>43</sup> but which is more commonly referred to as Fermi's Golden Rule. The tunnelling current  $I$  is then proportional to  $eP_{\mu\nu}$  and by including finite temperature effects and introducing a factor of 2 for electron spin states we obtain the following expression for

the net tunnelling current

$$I = \frac{4\pi e}{\hbar} \sum_{\nu\mu} [f(E_\mu - E_F^S) - f(E_\nu - E_F^T)] |M_{\mu\nu}|^2 \delta(E_\nu - E_\mu - eV) \quad (2.14)$$

Converting the discrete sum of states to an integral over the density of states (DOS) for the tip and sample,  $n^T$  and  $n^S$  respectively we obtain

$$I = \frac{4\pi e}{\hbar} \int_0^{eV} [f(E_F^T - eV + \epsilon) - f(E_F^S + \epsilon)] \quad (2.15)$$

$$\times n^T(E_F^T - eV + \epsilon) n^S(E_F^S + \epsilon) |M(E_F^S + \epsilon, E_F^T - eV + \epsilon)|^2 d\epsilon \quad (2.16)$$

Thus, by providing a bias voltage  $V$  we shift the electron occupancy in the tip or sample allowing the transfer of electrons/holes from occupied to unoccupied states or vice versa via tunnelling.

Finally, we must address the structure of the tunnelling matrix elements. This term depends strongly on the spatial configuration of the tunnelling electron states which, as in atomic physics, are frequently expanded in terms of spherical harmonic functions. A tip wavefunction  $\chi(\mathbf{r})$  is then expressed as

$$\chi(\mathbf{r}) = \sum_{l,m} C_{l,m} f_{l,m}(\kappa\rho) Y_{l,m}(\theta, \phi) \quad (2.17)$$

where  $\rho = |\mathbf{r} - \mathbf{r}_0|$ ,  $\kappa = \frac{\sqrt{2m\phi}}{\hbar}$  is the decay constant which depends on the work function  $\phi$ , and  $r_0$  is the center of the apex atom of the tip. The same expansion can also be used for the sample states  $\psi(\mathbf{r})$ . We assume some separation plane between the tip and sample, at which point the wavefunction of both tip and sample is negligible. For states near the Fermi level we can then write the following Schrödinger equation

$$\nabla^2 \chi(\mathbf{r}) = \kappa^2 \chi(\mathbf{r}) \quad (2.18)$$

Inserting Eq.2.17 into Eq.2.18 we obtain the following differential equation for the radial component, in which  $u = \kappa\rho$ .

$$\frac{d}{du} \left( u^2 \frac{df(u)}{du} \right) - [u^2 + l(l+1)] f(u) = 0 \quad (2.19)$$

The solutions for such equations are the spherical modified Bessel functions, particularly,  $k_l(u)$  satisfies the appropriate boundary conditions. These func-

tions always contain a  $e^{-u} = e^{-\kappa\rho}$  term. This explains a crucial working principle of STM, the tunnelling current observes a decaying exponential dependence on tip-sample distance. While the exact form of this dependence varies depending on tip and sample wavefunctions, this decaying exponential is always observed and can be directly measured in experiment.

In fact, this exponential dependence on tip-sample distance is a key result which helps to explain the ability of STM scan tips to resolve individual atomic sites on the sample surface. However such resolution is not guaranteed as tip preparation techniques such as electrochemical etching or controlled crashing are nearly always needed to achieve high resolution tips.

## 2.3 Topography

After developing an understanding of the main observable in STM, the tunnelling current, we can now investigate the varying operational modes of such instruments. The most straightforward of which is topographic imaging. Using a PID feedback system, we can control the STM tip to maintain a constant tunnelling current while scanning the sample surface. As such measurements are typically carried out within a small energy range around the Fermi level, typically in the meV-eV range, we can assume that the tip DOS is constant and that the tunnelling matrix elements do not change appreciably. Furthermore, all measurements reported herein are performed at  $T < 4.2\text{K}$ , at such temperatures we can assume a near step-like Fermi distribution. Thus we can express the simplified tunnelling current as

$$I(\mathbf{r}, V) = C e^{-\frac{T(\mathbf{r})}{T_0}} \int_0^{eV} n_S(\mathbf{r}, E) dE \quad (2.20)$$

where  $E$  is measured in reference to the Fermi energy  $E_F$  and the constant  $C$  absorbs the constants associated with a flat tip DOS and constant tunnelling matrix element amplitude. By establishing a constant setup current for the feedback system,  $I_s$  and with a constant bias voltage,  $V_b$  we can measure a topographic image which mathematically is expressed as

$$T(\mathbf{r}, V_b) = T_0 \ln \left[ \frac{I_s}{\int_0^{eV_b} n_S(\mathbf{r}, E) dE} \right] + \text{const.} \quad (2.21)$$

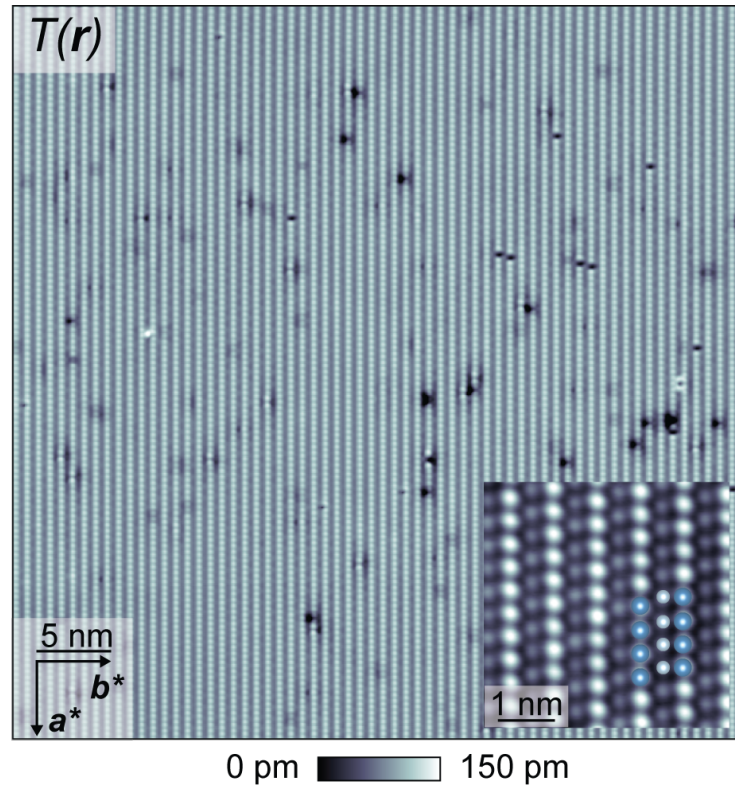


Figure 2.1: Example topographic image recorded at the  $(0 -1 1)$  surface of  $\text{UTe}_2$  revealing chains of tellurium atoms which run along the crystal  $a$  direction ( $V_b = 30$  mV,  $I_s = 500$  pA). The inset is recorded in a 4 nm square FOV. The presence of two inequivalent tellurium sites is clearly resolved thus demonstrating atomic resolution ( $V_b = 5$  mV,  $I_s = 3$  nA).

The measured topographs can be thought of as a relief map of the crystal surface. In reality, it is of course a measure of the integrated DOS, however, the measurement's dependence on tip-sample distance typically exceeds variations in the DOS. Topographs are therefore presented in units of distance, where the vertical distance has been calibrated using step edges of known height. An example of such a topographic image, recorded on the  $(0 -1 1)$  cleave surface of  $\text{UTe}_2$ , is shown in Fig. 2.1 and its inset. Here, chains of tellurium atoms fill the field of view (FOV), with crystal vacancies visible as dark regions. The inset exemplifies the high spatial resolution of STM as two sets of Te atoms are clearly visible. The height difference between these sites is the result of different inter-bond distances with the subsurface uranium atoms.

## 2.4 Spectroscopy

### 2.4.1 Single Particle Tunnelling

As shown in Eq.2.15 and the simplified Eq.2.20, the tunnelling current allows access to the DOS of the sample under study. However, a more direct measure of the DOS is differential conductance or  $\frac{dI}{dV}$  measurement, this is the most utilized operational procedure in quantum materials studies by STM and will be frequently referred to throughout. By substitution of Eq.2.21 into the voltage derivative of Eq.2.20 we obtain a simple expression for the differential conductance,  $\frac{dI}{dV}(\mathbf{r}, V)$ , or  $g(\mathbf{r}, V)$

$$g(\mathbf{r}, V) = \frac{eI_s n_S(\mathbf{r}, V)}{\int_0^{eV_b} n_S(\mathbf{r}, V) dE} \quad (2.22)$$

which reveals that such measurements are proportional to the local DOS,  $n_S(\mathbf{r}, E)$ . In superconductors with a large energy gap, like the cuprate superconductors, the integral in the denominator of the topographic expression Eq.2.21 is non-negligible and must be compensated for to allow direct measure of  $n_S$ . By choosing  $V_b$  such that  $T(\mathbf{r}, V_b)$  is homogeneous the denominator can be expressed as a constant and  $\frac{dI}{dV}(\mathbf{r}, V)$  is a direct measure of the local DOS. If  $T(\mathbf{r}, V)$  is heterogeneous and if  $n_S(\mathbf{r}, E)$  is particle-hole symmetric up to the setpoint voltage, then calculation of  $\frac{g(\mathbf{r}, +V)}{g(\mathbf{r}, -V)}$  may also reveal variations in the local DOS. In our case the superconducting energy gap of UTe<sub>2</sub> is very small  $|\Delta| \sim 0.3$  meV and the contribution from the integral in the denominator of Eq. 2.22 is negligible, thus no corrections are needed to account for this “setup effect”.

While measurements of the tunnelling current and subsequent numerical differentiation can be used to measure  $n_S(\mathbf{r}, E)$ , this method is very sensitive to electronic and vibrational noise. To circumvent such issues and improve the signal-to-noise ratio (SNR) of measurement we employ a lock-in amplifier to apply a sinusoidal modulating voltage of magnitude  $\sim 50$ - $150$   $\mu$ V and measure the resulting modulation in the tunnelling current. We therefore outline the procedure for lock-in measurements of  $\frac{dI}{dV}$  below.

As in typical STM junctions, we apply a DC bias voltage,  $V_0$  to the tip-sample junction but now add a modulating voltage of the form  $V_m(t) = V_m \cos(\omega t + \phi)$ . The tunnelling current response, expanded in Taylor series,

is then

$$I(V_0 + V_m(t)) = I(V_0) + \frac{dI}{dV}|_{V_0} V_m \cos(\omega t + \phi) + \frac{1}{2} \frac{d^2 I}{dV^2}|_{V_0} V_m^2 \cos^2(\omega t + \phi) + \dots \quad (2.23)$$

A high pass filter is then used to remove the DC component of this current signal, leaving only the AC terms of the current

$$I(V_0 + V_m(t))_{\text{filtered}} = \frac{dI}{dV}|_{V_0} \cos(\omega t + \phi) + \dots \quad (2.24)$$

Lock-in amplifiers then multiply this filtered signal by a reference signal produced at the same frequency as the AC input. This reference signal is a complex function of the form

$$V_r(t) = e^{-i\omega_r t} = \cos(\omega_r t) - i \sin(\omega_r t) \quad (2.25)$$

The mixed signal contains two parts, one modulating at frequency  $\omega - \omega_r$  and another at  $\omega + \omega_r$

$$Z(t) = \frac{dI}{dV}|_{V_b} [e^{i[(\omega - \omega_r)t + \phi]} + e^{-i[(\omega + \omega_r)t + \phi]}] + \dots \quad (2.26)$$

Should the reference and signal frequency exactly match then we get a pure DC component in the mixed signal. In any case, the  $\omega - \omega_r$  term is small and subsequent low-pass filtering removes higher frequency terms and extracts this first-order term of the modulating current to be read as the output of the lock-in. This output is the differential conductance measurement which, as shown above, is directly proportional to the local DOS,  $n_S(\mathbf{r}, E)$ .

In experiment, this lock-in detection technique is performed once a tunnel junction with setpoint current and voltage,  $I_s$  and  $V_b$  is established. The scan tip feedback is then disabled and the tunnel junction voltage is adjusted to  $V_0$ , with  $V_0 < V_b$ . The lock-in provides the voltage modulation and reference signal to extract the  $\frac{dI}{dV}$  measurement and the tunnel junction voltage  $V_0$  is adjusted to the next value, determined by the STM operator. Performed at a single point in space above the sample, we then extract the local DOS as a function of energy  $\frac{dI}{dV}(V) \propto n_S(E)$ . An example of such a measurement using a superconducting tip on a superconducting Nb crystal is featured in Fig.2.2 and reveals the typical DOS for an s-wave superconductor as in Fig. 1.1c.

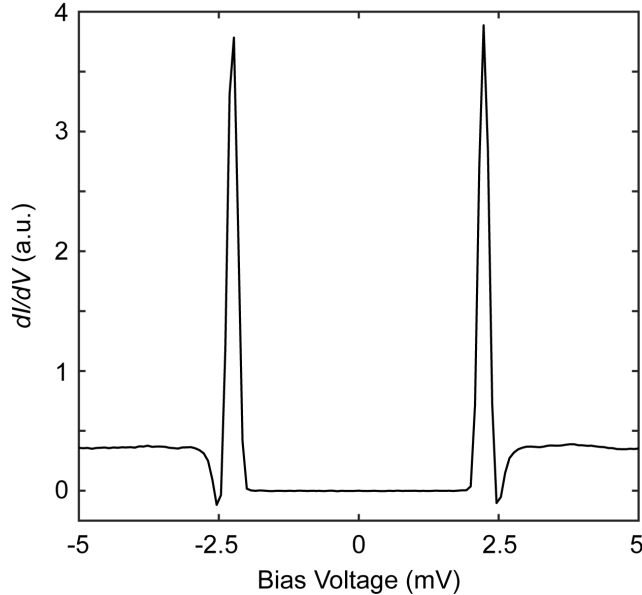


Figure 2.2: Differential conductance,  $\frac{dI}{dV}$  spectrum obtained using a superconducting Nb tip on a superconducting Nb crystal at  $T = 0.3$  K. The bias voltage during  $\frac{dI}{dV}$  operation ranges from  $-5$  mV to  $+5$  mV and includes 131 voltage steps. The junction setup parameters are  $V_b = 5$  mV and  $I_s = 500$  pA. Superconducting coherence peaks of the combined  $s$ -wave energy gaps are clearly seen at energies  $\Delta = \pm 2.23$  meV.

## 2.4.2 Scanned Josephson Tunnelling Microscopy (SJTM)

### 2.4.2.1 The Josephson Equations

The operating modes of SI-STM discussed thus far feature only single-particle states, that is, single holes/electrons are transported via the tunnelling process. However, by leveraging the properties of Cooper pair condensates, other tunnelling processes are possible. In particular, scanned Josephson tunnelling microscopy (SJTM) provides a direct measure of Cooper pair density on the surface of a superconductor. This process is made possible by the Josephson effect<sup>44</sup> which describes Cooper pair tunnelling as the result of the phase difference between two Cooper pair condensates.

At zero temperature the Josephson AC and DC Josephson effects can be derived by considering the coupling between the condensate wavefunctions of two connected superconductors. We consider for our wavefunctions

$$\psi_1 = \sqrt{N_1} e^{i\phi_1} \quad (2.27)$$

$$\psi_2 = \sqrt{N_2} e^{i\phi_2} \quad (2.28)$$

where  $N_{1,2}$  and  $\phi_{1,2}$  are the number of Cooper pairs and the macroscopic phase of each superconductor respectively. If a finite voltage is applied across the superconductor junction and there exists some coupling  $-K$  between the two, then one can write a set of two coupled Schrödinger equations

$$i\hbar \frac{\partial \psi_1}{\partial t} = (E_1 + eV) \psi_1 - K \psi_2 \quad (2.29)$$

$$i\hbar \frac{\partial \psi_2}{\partial t} = (E_2 - eV) \psi_2 - K \psi_1 \quad (2.30)$$

Inserting Eq. 2.27 into the above equations and separating into real and imaginary parts, we obtain

$$\hbar \frac{dN_1}{dt} = -2K \sqrt{N_1 N_2} \sin(\phi_2 - \phi_1) \quad (2.31)$$

$$\hbar \frac{dN_2}{dt} = 2K \sqrt{N_1 N_2} \sin(\phi_2 - \phi_1) \quad (2.32)$$

$$\hbar N_1 \frac{d\phi_1}{dt} = -eV N_1 + K \sqrt{N_1 N_2} \cos(\phi_2 - \phi_1) \quad (2.33)$$

$$\hbar N_2 \frac{d\phi_2}{dt} = eV N_2 + K \sqrt{N_1 N_2} \cos(\phi_2 - \phi_1) \quad (2.34)$$

Subtracting the two imaginary parts, Eq. 2.33 gives us an expression of charge conservation between the superconductors. Defining the supercurrent between them to be  $I_s = -2e \frac{dN_1}{dt} = 2e \frac{dN_2}{dt}$ , the phase difference between them to be  $\Phi = \phi_2 - \phi_1$ , and the Josephson critical current as  $I_C = 4eK \sqrt{N_1 N_2} / \hbar$  then gives the familiar expression for the DC Josephson effect

$$I_s = I_C \sin(\Phi) \quad (2.35)$$

From this we see that a flow of Cooper pairs can be transferred between superconductors with zero voltage between them. Furthermore, by subtracting the real parts, Eq. 2.34, and realizing that the particular phase of each superconductor plays no role we can relabel  $\phi_2 = \Phi/2$  and  $\phi_1 = -\Phi/2$  and obtain the AC Josephson equation

$$\hbar \frac{d\Phi}{dt} = 2eV \quad (2.36)$$

Finite voltage therefore changes the phase difference between two superconductors over time. While modifications to these equations are required for finite temperature and real circuits, the Josephson effect is a general property

of superconductors and occurs for systems connected to a superconductor by a weak link. It is through this effect that the surface of metals can become superconducting by the proximity effect, and it is fundamental to the operation of superconducting quantum interference devices (SQUIDs), which are some of the most sensitive magnetometers in operation.

#### 2.4.2.2 SJTM

In STM tunnel junctions finite temperature excitations ( $k_B T \sim 25 \mu\text{eV}$ ) frequently exceed the characteristic Josephson energy  $E_J = \frac{\hbar I_c}{2e} \sim 3 \mu\text{eV}$  thus, in this phase diffusive regime, the maximum pair current occurs at finite voltage<sup>45</sup>.

$$I_P(V) = \frac{I_J^2 V Z}{2(V^2 + V_C^2)} \quad (2.37)$$

Where  $I_J$  is the DC Josephson current,  $V_C$  is the voltage at which the maximum phase-diffusive current is observed, and  $Z$  is the effective impedance associated with re-trapping of the diffusive phase. The maximum current in this case is then

$$I_m = \frac{I_J^2 Z}{4V_C} \quad (2.38)$$

Using the first derivative of Eq.2.37, we can find a simple form for the differential conductance at zero voltage bias

$$g(V = 0) = \left. \frac{dI_P}{dV} \right|_{V=0} = \frac{I_J^2 Z}{2V_C} = \frac{2I_m}{V_C} \quad (2.39)$$

Finally, we make use of the key relationship that the product  $I_C R_N$  is proportional to the superconducting order parameter amplitude and hence the Cooper pair density  $\rho_S$ .

$$\rho_S(\mathbf{r}) \propto (I_J(\mathbf{r}) R_N(\mathbf{r}))^2 \propto g(0, \mathbf{r}) R_N^2(\mathbf{r}) \quad (2.40)$$

We now have two measurable quantities from STM,  $g(0, \mathbf{r})$  and  $R_N(\mathbf{r})$ , which can be used to image the Cooper pair condensate directly. This imaging method has been used to discover Cooper pair density waves in the cuprate superconductor,  $\text{Bi}_2\text{Sr}_2\text{CaCu}_2\text{O}_{8+x}$ <sup>29</sup>, and more recently in the superconducting transition metal dichalcogenide  $\text{NbSe}_2$ <sup>46</sup>.

## 2.5 Quasiparticle Interference Imaging

In his PhD thesis, Louis de Broglie aimed to reconcile the wave nature of light with the corpuscular theory shown by Einstein to explain the photoelectric effect. In doing so he hypothesized that all matter has a wave-like nature associated with it and derived the simple relation for the de Broglie wavelength,  $\lambda = \frac{h}{p}$  where  $p$  is the particle momentum.

The wave nature of electrons is critical in the application of quasiparticle interference imaging (QPI) and thus the results presented in this thesis. In a perfect metal, devoid of impurities or vacancies, the periodic potential of the crystal lattice results in Bloch solutions to the Schrödinger equation of the form

$$\psi_{\mathbf{k}}(\mathbf{r}) = e^{i\mathbf{k}\cdot\mathbf{r}}u_{\mathbf{k}}(\mathbf{r}) \quad (2.41)$$

where  $u_{\mathbf{k}}(\mathbf{r})$  is a periodic function with the same period as the lattice potential. As discussed in Section 2.4.1, SI-STM can probe the local DOS  $n_S(\mathbf{r}, E)$  however this quantity provides no k-space information in a pure crystal as

$$n_S(\mathbf{r}, E) \propto \sum_{\mathbf{k}} |\psi_{\mathbf{k}}(\mathbf{r})|^2 \delta(E - \epsilon(\mathbf{k})) = \sum_{\mathbf{k}} |u_{\mathbf{k}}(\mathbf{r})|^2 \quad (2.42)$$

In experiment, no crystal structure is perfect; they feature vacancies, step edges, impurities, and many other types of disorder. All of these features result in elastic quasiparticle scattering which mixes eigenstates of the same energy  $\epsilon(\mathbf{k})$  but different wavevector  $\mathbf{k}$ . Considering only scattering between two Bloch states

$$n_S(\mathbf{r}, E) \propto |\psi_{\mathbf{k}_1}(\mathbf{r}) + \psi_{\mathbf{k}_2}(\mathbf{r})|^2 \delta(E - \epsilon(\mathbf{k})) = \quad (2.43)$$

$$|a_1 e^{i\mathbf{k}_1 \cdot \mathbf{r}} u_{\mathbf{k}_1}(\mathbf{r})|^2 + |a_2 e^{i\mathbf{k}_2 \cdot \mathbf{r}} u_{\mathbf{k}_2}(\mathbf{r})|^2 + (a_1 a_2^* u_{\mathbf{k}_1}(\mathbf{r}) u_{\mathbf{k}_2}^*(\mathbf{r}) e^{i(\mathbf{k}_1 - \mathbf{k}_2) \cdot \mathbf{r}} + \text{c.c.}) \quad (2.44)$$

we find that the local DOS features a dependence on the k-space wavevectors,  $\mathbf{q} = \mathbf{k}_1 - \mathbf{k}_2$  and  $\mathbf{q}^* = \mathbf{k}_2 - \mathbf{k}_1$ . Quasiparticle scattering then introduces standing waves in the real space  $n_S(\mathbf{r}, E)$ , known as Friedel oscillations, with wavelength  $\lambda = \frac{2\pi}{|q|}$ . These oscillations can be clearly measured on crystal surfaces via differential conductance maps or even in topography, as shown in Fig. 2.3.

Inferring the scattering wavevectors and their energy dependence from real

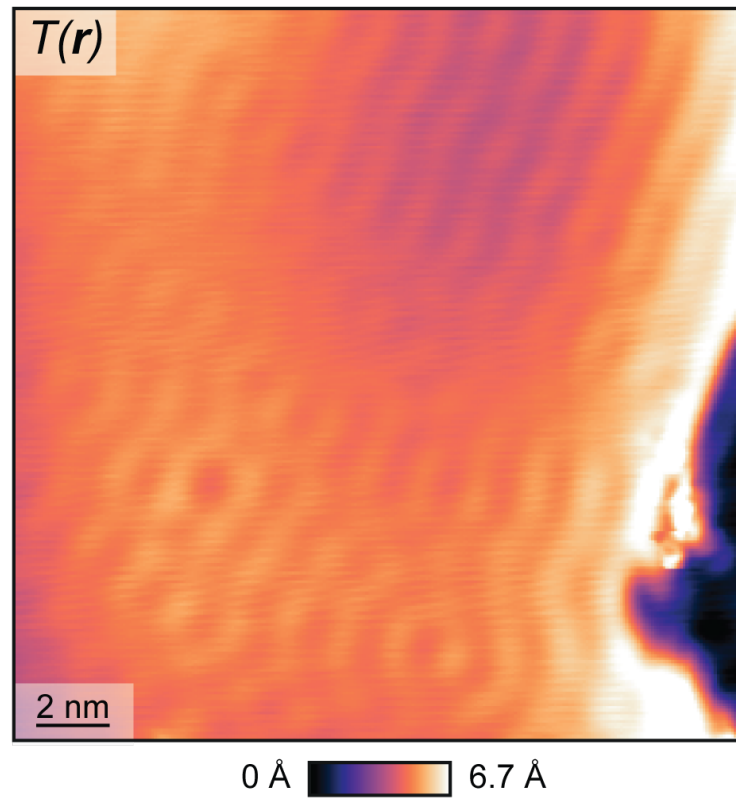


Figure 2.3: Topographic image of the Cu (1 1 1) surface prepared by annealing and sputtering and obtained using a Nb scan tip. The step edge induces standing waves of the local DOS which run parallel to its edge. Point defects cause isotropic modulations at the metallic surface. ( $V_b = 10$  mV,  $I_s = 200$  pA)

space images is impractical. However, Fourier transform of  $n_S(\mathbf{r}, E)$  measured by differential conductance can reveal the periodicity of  $n_S(\mathbf{r}, E)$  modulations resulting from the periodicity of the crystal (these are the surface reciprocal lattice vectors  $|q_{\text{Bragg}}| = \frac{2\pi}{a}$  where  $a$  is a lattice vector), from inter-band scattering, and from charge density waves.

# Chapter 3

## UTe<sub>2</sub>: A Spin Triplet Superconductor

### 3.1 Introduction

We now turn to the subject of this thesis, uranium ditelluride, UTe<sub>2</sub>, which is a member of the family of heavy-fermion superconductors. First developed in the late 1970s and throughout the 1980s, these compounds are premier examples of strongly correlated electronic materials. While some exhibit properties of a renormalized, heavy-fermion Fermi liquid, others are strongly affected by the interplay of magnetism, originating from the magnetic moment of heavy elements and conduction electrons which together produce Kondo lattice systems<sup>47</sup>.

Many heavy-fermion systems are also host to unconventional superconducting states, likely resulting from the nearby presence of magnetic order in their phase diagrams. Among these heavy-fermion superconductors, UTe<sub>2</sub> stands out as a leading example of odd-parity  $p$ -wave superconductivity with a somewhat accessible superconducting transition temperature,  $T_c \sim 1.6 - 2.2$  K. The discovery of a superconductor with odd-parity symmetry promises analogous discoveries to those made studying the exotic physics of superfluid <sup>3</sup>He. We therefore take time to discuss several key experimental measurements to better understand the complex physics of  $p$ -wave superconductivity.

## 3.2 Upper Critical Field & *P*-Wave Pairing Symmetry

The first indications of spin triplet superconductivity in  $\text{UTe}_2$  featured in the paper announcing superconductivity in this system<sup>48</sup>. In all three crystallographic directions (Fig. 3.1) the upper critical field  $H_{c2}(T)$  exceeds that possible for singlet superconductors as the BCS paramagnetic limit is  $\sim H_{\text{para.}} = 1.86T_c = 4 \text{ T}$ <sup>49</sup>. In the years since, the phase diagram of this compound under magnetic field has been experimentally measured up to 60T and has revealed several superconducting phases including a re-entrant phase for fields aligned between the  $b$  and  $c$  crystal axes. The low-field, low-temperature phase, SC1 in Fig. 3.1, persists up to at least 15 T for fields along the  $b$  axis and may continue further. Whether SC2 is a separate superconducting phase remains undetermined. Such a large  $H_{c2}/T_c$  ratio is strongly suggestive of spin triplet Cooper pairing thus the outstanding question remains - exactly what is the symmetry and form of this spin triplet superconducting state?

As outlined in Chapter 1, the symmetry of the superconducting order parameter is related to the irreducible representations of the crystal point symmetry group.  $\text{UTe}_2$ 's unit cell is body-centred orthorhombic and is of the point group  $D_{2h}$ . The irreducible representations of this group are featured in Fig. 1.4. Although even parity symmetries are possible, namely  $A_{1g}$ ,  $B_{1g}$ ,  $B_{2g}$ , and  $B_{3g}$ , these states do not explain the high upper critical field nor the experiments described below. Thus, we focus on the odd-parity irreducible representations,  $A_u$ ,  $B_{1u}$ ,  $B_{2u}$ , and  $B_{3u}$ . Superconducting states which transform as these irreducible representations are either fully gapped ( $A_u$ ) or feature point nodes in momentum space aligned with one of the three orthogonal crystal axes  $c$ ,  $b$ , or  $a$  for  $B_{1u}$ ,  $B_{2u}$ , and  $B_{3u}$  respectively. The question of fundamental importance in characterizing the low-field, low-temperature superconducting state is therefore where on the Fermi surface do these nodes appear? Gaining insight into the nodal locations has proven extraordinarily difficult, with many groups reaching different conclusions. Below we outline a small fraction of experiments which seek to answer this question while keeping in mind that, to this point, there is little agreement in the literature.

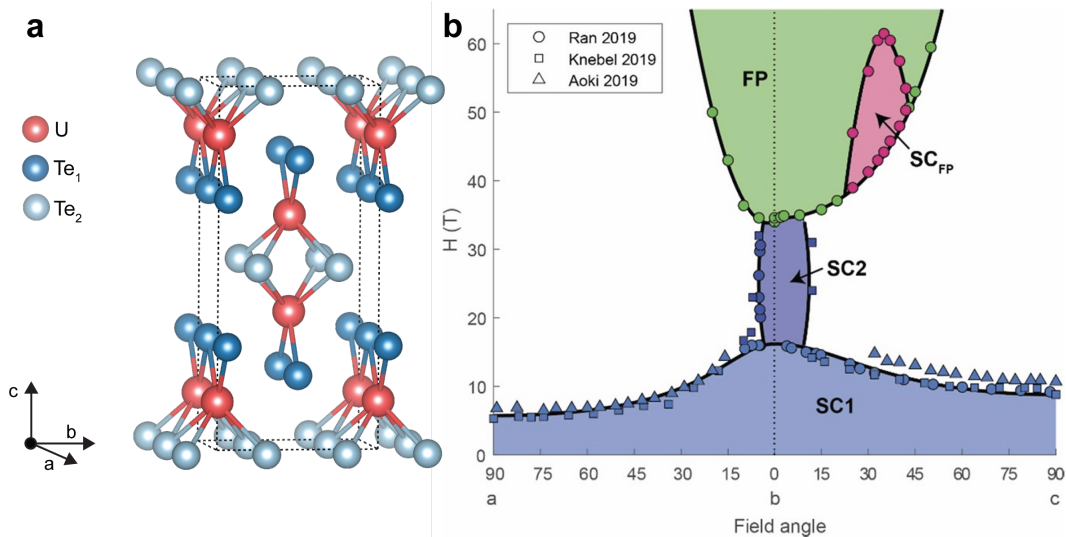


Figure 3.1: **a.** Schematic crystal structure of  $UTe_2$ . Its body-centred orthorhombic unit cell is indicated by black dashed lines. **b.** Superconducting phase diagram under applied magnetic field. The low field, low temperature SC1 phase is the subject of this report. A non-superconducting field-polarized (FP) phase is observed at high fields directed around the crystal b axis. Figure reproduced from Ref. [50].

### 3.3 NMR Relaxation Rate and Knight Shift

Nuclear magnetic resonance (NMR) is a direct probe of a material's nuclear spin interactions with the surrounding environment. Its development has been crucial to a wide range of fields. Notably, it is the key principle of magnetic resonance imaging (MRI), and has also been instrumental in the verification of BCS theory<sup>51</sup> and the unconventional superconducting properties of  $^3\text{He}$ <sup>52</sup>.

The lack of coherence peaks in the spin lattice relaxation rate,  $1/T_1$ , has been taken as strong evidence of unconventional pairing in several superconducting compounds, including the cuprates<sup>53</sup>. Coherence peaks in  $1/T_1T$  are also absent in  $UTe_2$  suggesting an unconventional superconducting state<sup>54</sup>. Furthermore, early  $^{125}\text{Te}$ -NMR measurements found a plateau in  $1/T_1T$  which was proposed as evidence of a multicomponent superconducting order parameter. In fact many reports following the discovery of superconductivity in this system argued evidence for a multicomponent, time-reversal symmetry breaking, chiral order parameter<sup>55</sup> like those discussed for the A phase of superfluid  $^3\text{He}$  in Section 1.5. In such a scenario, the order parameter should transform as a linear combination of  $D_{2h}$  irreducible representations such as  $A_u + iB_{3u}$ . As we will find later, a multicomponent order parameter in the low temperature,

low field phase now appears unlikely (see Chapter 6).

Further insights from NMR come from Knight shift measurements. The Knight shift is the relative shift in NMR frequency which results from the presence of conduction electrons surrounding nuclear sites. This shift is the result of the hyperfine coupling between conduction electrons and nuclei and is therefore altered upon entering the superconducting state. In cooling an s-wave superconductor the Knight shift falls at  $T_c$  and decreases to zero as conduction electrons around the Fermi surface form spin zero Cooper pairs<sup>56</sup>. Spin triplet Cooper pairs have even parity spin wavefunctions and thus unity spin,  $S = 1$ . For d-vectors fixed to a crystal axis, the Cooper pair spin is perpendicular to this axis and thus the d-vector. The NMR Knight shift is therefore expected to be unchanged for  $\mathbf{H} \perp \mathbf{d}$  and decrease at the onset of superconductivity for  $\mathbf{H} \parallel \mathbf{d}$ . Knight shift measurements of superconductors are therefore taken to provide information regarding the d-vector orientation and hence the pairing symmetry. In Ref. [57], the Knight shift of  $\text{UTe}_2$  is measured across  $T_c$ , as seen in Fig. 3.2b uncoloured, the Knight shift decreases for fields aligned to the  $b$  and  $c$  axes but shows no appreciable decrease for fields aligned to the  $a$  axis. This is strongly suggestive of a d-vector constrained to the y-z plane which transforms as the  $B_{3u}$  irreducible representation.

Up to 2022, all  $\text{UTe}_2$  samples were grown by the chemical vapour transport (CVT) method, creating samples with  $T_c \sim 1.6$  K. However, a new generation of samples grown by the molten salt flux (MSF) method<sup>59</sup> are of increased purity, with residual-resistivity ratios (RRR) as high as 800<sup>60</sup>. These MSF crystals exhibit a  $T_c \sim 2$  K and have altered the conclusions of several experimental measurements such as specific heat  $C/T$ <sup>61</sup> and NMR Knight shift. In Ref. [58], now using a  $T_c = 2$  K sample, the Knight shift is found to decrease for fields aligned along any crystal axis, see Fig. 3.2b coloured. However, the lack of coherence peaks in the spin-lattice relaxation rate  $1/T_1$  and the presence of a finite spin susceptibility in the superconducting state remain indicative of an unconventional pairing state. A simple explanation for Knight shift reduction in all directions is the fully gapped  $A_u$  state for which the d-vector has finite components in each crystal axis. This NMR study further highlights the difficulties associated with pairing symmetry determination by Knight shift. As previously discussed the d-vector is pinned to a crystal axis by spin-orbit coupling, however, external magnetic fields may overwhelm the spin-orbit effects and allow d-vector rotation as discussed for  $\text{UTe}_2$  in Refs.

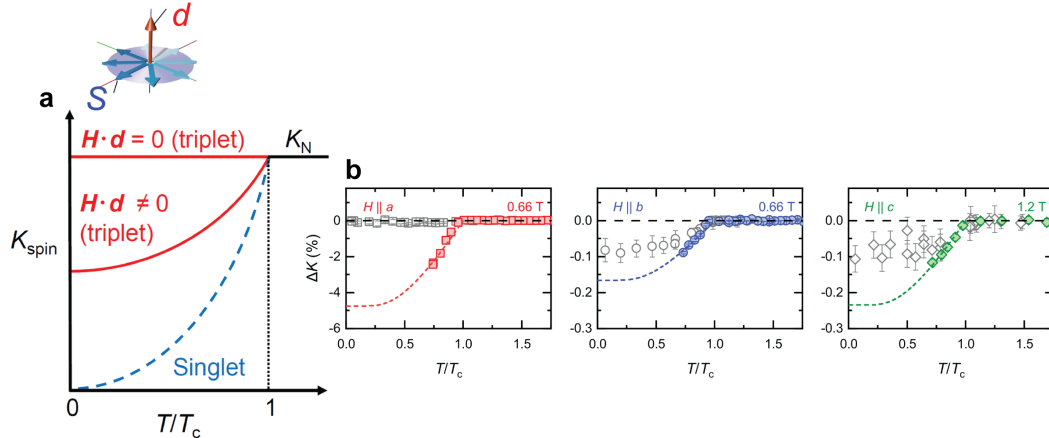


Figure 3.2: **a.** The spin triplet order parameter, the  $d$ -vector is defined orthogonal to the  $S = 1$  spin of the Cooper pair. Upon cooling through  $T_c$  the NMR Knight shift drops to zero for a singlet superconductor. For a triplet superconductor the Knight shift is expected to decrease for fields aligned with the  $d$ -vector and is unaffected for fields aligned orthogonal to the  $d$ -vector. **b.** This plot is reproduced from Ref. [58] whose authors find a reduction in the NMR Knight shift for fields aligned to any of the MSF-grown  $\text{UTe}_2$  crystal axes. Coloured plot markers are Knight shift data recorded using MSF-grown samples. Empty plot markers are obtained from CVT-grown samples.

[62],[63]. In these reports, the Knight shift was found to depend on the applied external magnetic field, indicating  $d$ -vector rotation and shedding light on the intermediate field phase SC2 in Fig. 3.1. While exact determination of superconducting pair symmetry has proven difficult in NMR studies of  $\text{UTe}_2$ , there is agreement on the presence of a  $p$ -wave superconducting state with either nodal  $B_{3u}$  or fully-gapped  $A_u$  symmetry.

### 3.4 Specific Heat Capacity & Thermal Conductivity

Specific heat capacity measurements are a canonical probe of condensed matter systems because, at low temperatures, the phononic contribution to specific heat  $C \propto T^3$  can be subtracted to reveal the electronic contribution which is proportional to the density of electronic states. Furthermore, the experimental value of  $C/T$  extrapolated to  $T \rightarrow 0$  is the Sommerfeld coefficient. For a second-order phase transition there is necessarily a discontinuity in the specific heat capacity and this is observed in all superconductors, including  $\text{UTe}_2$ . The

magnitude of this jump divided by the normal state Sommerfeld coefficient  $\Delta C/\gamma_N T_c$  for UTe<sub>2</sub> measurements is universally measured to be larger than that expected for weak-coupling BCS theory,  $\Delta C/\gamma_N T_c = 1.43$ , indicative of superconductivity in the strong coupling regime<sup>48</sup>.

The peak in specific heat when cooling through  $T_c$  results from the introduction of a finite order parameter  $\Delta_{\mathbf{k}}$ . The presence of a non-degenerate, multi-component order parameter should produce a second peak in  $C_e$ . This was observed for CVT grown samples of UTe<sub>2</sub> and taken as evidence of a chiral  $p$ -wave order parameter. Notably, the presence of a finite zero temperature Sommerfeld coefficient  $\gamma_0 \sim \gamma_N/2$  in early studies of UTe<sub>2</sub>, has indicated the presence of unpaired quasiparticle states possibly resulting from a chiral equal-spin pairing state<sup>48</sup>. However, the two peaks in specific heat were found to move together under pressure, suggesting an extrinsic origin<sup>64</sup>. Furthermore, the introduction of high-purity MSF samples has confirmed the intrinsic superconducting transition manifests as a single peak in  $\Delta C_e$ . MSF samples also show a significant reduction of  $\gamma_0 \sim 23$  mJ/mol K<sup>261</sup> for samples displaying highest RRR. There is therefore little remaining evidence for a chiral order parameter from specific heat capacity measurements.

Both specific heat and thermal transport measurements support the presence of point nodes in the low temperature, low field phase of UTe<sub>2</sub> supporting an order parameter which transforms as either  $B_{1u}$ ,  $B_{2u}$ , or  $B_{3u}$ . In Ref. [65] the specific heat capacity was measured under various field orientations. A dip feature was observed at intermediate fields oriented along the  $a$  axis and, upon rotating this field towards the  $b$  axis,  $C_e/T$  was found to exhibit peaks which converge at high fields. These features are indicative of nodal points along the  $a$  axis, thus suggesting an order parameter with symmetry  $B_{3u}$ . Evidence for nodal superconductivity also comes from thermal transport measurements  $\kappa/T$ <sup>66</sup>, in which the field dependence of the residual thermal conductivity  $\kappa_0$  is found to be similar to that observed in other nodal superconductors and dissimilar to the expected field dependence of a fully gapped state such as  $A_u$ . However, more recent thermal transport measurements performed on MSF grown samples<sup>67</sup> have found a weak dependence of  $\kappa/T$  for magnetic fields aligned along the  $a$  and  $c$  axes thus suggesting a fully gapped pairing state as nodal quasiparticles are easily excited and should contribute to thermal transport at low temperatures and under magnetic field.

Specific heat capacity and thermal transport measurements, like many

studies of  $\text{UTe}_2$ , have reached several different conclusions. However, as with the NMR studies discussed above, there is agreement that a chiral superconducting state is unlikely to be present in this compound.

### 3.5 Magnetic Penetration Depth & Topological Surface State Conductivity

We now turn to another experimental technique which has, to this point, been taken as strong evidence of nodal superconductivity in  $\text{UTe}_2$ , the magnetic penetration depth. The magnetic penetration depth in the superconducting state is intimately related to the normalized superfluid density along the  $i$  axis,  $n_S^i(T)$  through the relation

$$n_S^i(T) = \left( \frac{\lambda_i(0)}{\lambda_i(T)} \right)^2 \quad (3.1)$$

Fitting to either this quantity or the effective magnetic penetration depth  $\lambda_{\text{eff}}(T)$  can reveal the presence of nodal excitations, such as point or line nodes in the superconducting state. This has been used in several studies to argue for the presence of point nodes in the low-temperature phase of  $\text{UTe}_2$ . In Ref. [66] the change in effective penetration depth versus temperature  $\Delta\lambda_{\text{eff}}(T)$  was measured on CVT grown samples of  $\text{UTe}_2$  and fit to a power law of the form  $aT^n + b$  yielding  $n$  values around 2, indicative of point nodes which lie in the  $a$ - $b$  plane of the crystal. These measurements were performed for fields applied along the  $c$  axis, however, new measurements with  $\mathbf{H}$  along  $a$ ,  $b$ , and  $c$  and using both CVT and MSF crystals have measured the same exponent to be between 1.76 and 2.11 for several different samples and field orientations<sup>68</sup>. This is unexpected for a superconducting order parameter featuring point nodes, as fields aligned along the nodal direction should exhibit  $\Delta\lambda_{\text{eff}}(T) \propto T^4$ . These authors thus conclude that a chiral order parameter such as  $B_{3u} + i\epsilon A_u$  best explains their results. Such a superconducting state should feature nodal points off the high-symmetry axes whose momentum space position is tuned by the magnitude of  $\epsilon$ . From scanning SQUID measurements the magnetic penetration depth and superfluid density may also be extracted by measuring the local susceptibility. This is carried out in Ref. [69], and by fitting the superfluid density using a cylindrical Fermi surface the results are found to be consistent with point nodes along the  $a$  axis indicative of single component order pa-

parameter with  $B_{3u}$  symmetry or a chiral state  $B_{3u} + i\epsilon A_u$  for sufficiently small  $\epsilon$ .

Finally, we highlight the microwave surface impedance measurements of Ref. [70]. This technique probes the surface impedance of the sample and can be used to extract the complex conductivity  $\tilde{\sigma} = \sigma_1 - i\sigma_2$ . The imaginary component of which is related to the effective magnetic penetration depth and hence the superfluid density. For fields aligned along the crystal  $c$  axis the authors find the temperature dependence of the superfluid density  $n^S(T)$  to follow the expected behaviour of a nodal superconductor with nodes in the  $a$ - $b$  plane. Critically, this report also finds anomalous behaviour of  $\sigma_1(T)$  which increases monotonically with decreasing temperature. As seen in Fig. 3.3 this behaviour stands in stark contrast to both conventional ( $s$ -wave) and even-parity unconventional ( $d$ -wave) superconducting systems in which the normal quasiparticle states are rapidly depleted at the onset of superconductivity; so that  $\frac{\sigma_1(0)}{\sigma_1(T_c)} = 0$  for an  $s$ -wave superconductor and  $\frac{\sigma_1(0)}{\sigma_1(T_c)} = 0.1 - 0.3$  for a line nodal  $d_{x^2-y^2}$  superconductor. The same value for  $\text{UTe}_2$  is 2.3, thus suggesting residual quasiparticle states despite measurements from specific heat<sup>61</sup> which rule out bulk unpaired states. While pair breaking processes are expected to be important for a  $p$ -wave superconductor<sup>71</sup> in which Anderson's theorem no longer holds<sup>72</sup>, the authors of Ref. [70] fit a modified function for  $n^S(T)$  taking into account bulk scattering rates. In doing so, they find that scattering cannot explain the unusually large  $\sigma_1$ . This large  $\sigma_1(0)/\sigma_1(T_c)$  is therefore attributed to the presence of topological surface states resulting from a chiral or helical superconducting state.

### 3.6 Conclusions

While the research outlined above is not exhaustive, we hope it conveys the flurry of research carried out and ongoing in studies of  $\text{UTe}_2$  and, most importantly, conveys the difficulties in characterization of unconventional superconductors. What should now seem clear, is that  $\text{UTe}_2$  is a leading candidate material to host  $p$ -wave superconductivity, a state which has only been conclusively identified in the superfluid phases of  $^3\text{He}$ . While a chiral superconducting state remains possible, the conclusions derived from measurement have been altered by the development of high-purity MSF grown samples, and as we will see below, such a state is incompatible with our STM measurements (See

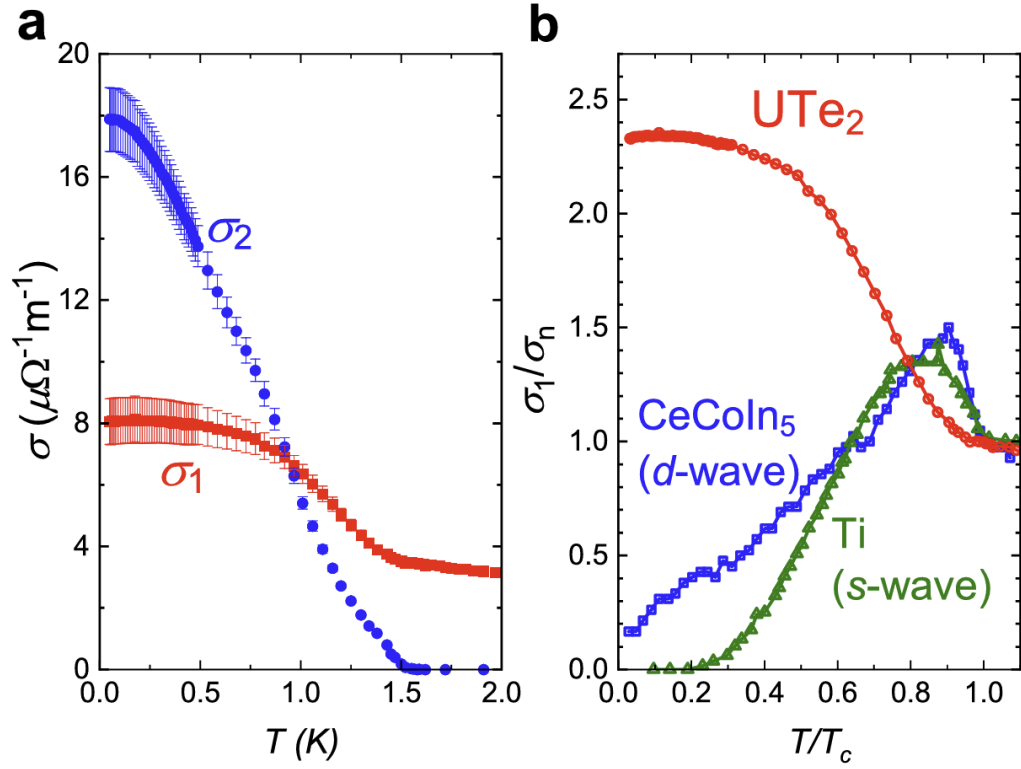


Figure 3.3: **a.** Components of the complex surface conductivity  $\tilde{\sigma}(T) = \sigma_1(T) - i\sigma_2(T)$ .  $\sigma_2(T)$  as the magnetic penetration depth decreases at the onset of a coherent superconducting state. **b.** The anomalous increase in  $\sigma_1(0)/\sigma_1(T_c)$  is compared to conventional (s-wave) and unconventional (d-wave) superconducting samples. The observed monotonic increase is unexpected for bulk superconducting states but may be explained by the development of topological surface states. Figure reproduced from Ref. [70]

Chapter 6). The superconducting order parameter therefore likely transforms as a single IR of  $D_{2h}$  however, whether this state is fully-gapped ( $A_u$ ) or nodal ( $B_{1u}, B_{2u}, B_{3u}$ ) remains to be answered. What remains incontrovertible, is the place of  $\text{UTe}_2$  in condensed matter, it has and will remain a material of significant interest for years to come.

# Chapter 4

## Discovery of a Pair Density Wave in UTe<sub>2</sub>

### 4.1 Normal Tip Measurements

The discovery of incommensurate charge density waves in UTe<sub>2</sub> by SI-STM signalled the first observation of unusual charge order in this system<sup>73</sup>. By Fourier transform of  $\frac{dI}{dV}(\mathbf{r}, V)$  maps the intensity of these three incommensurate CDWs, ( $\mathbf{Q}_1, \mathbf{Q}_2, \mathbf{Q}_3$ ), are suppressed under an applied magnetic field similar to H<sub>c2</sub> for this system. The authors thus proposed the existence of a parent spin triplet PDW state whose coupling with the background superconductor produces these unconventional CDWs.

As outlined in Sections 1.6 and 2.4.2, there are two methods to detect PDW modulations by SI-STM. Firstly by employing SJTM, the Cooper pair density at the sample surface can be directly visualized, thus modulations in the Cooper pair density associated with PDWs can be detected directly. Another method of PDW detection is to track modulations in the superconducting energy gap across the crystal surface. This energy gap is defined by the energy separation between the Fermi level and the energy of the superconducting coherence peaks ( $E = \pm|\Delta_{\mathbf{k}}|$ ). Mapping this energy modulation across a crystal surface thus produces a superconducting gap map, henceforth referred to simply as a gap map. Given that, to this point, no Josephson signal has been detected by tunnelling experiments in this system, gap map measurements remain the only method of PDW detection.

With a strategy for PDW detection and motivated by the presence of unusual charge order and the possible discovery of a spin triplet PDW we used

ARCHAOS (Appendix A) to cryogenically cleave a CVT-grown sample of  $\text{UTe}_2$  revealing its (0 -1 1) cleave surface. After selecting a target FOV, shown in Fig. 4.1a, a gap map was obtained by measurement of  $\frac{dI}{dV}(\mathbf{r}, \Delta_{\pm})$ . An example  $\frac{dI}{dV}(V)$  spectrum is presented in Fig. 4.1b with blue arrows highlighting the weak superconducting coherence peaks. By fitting a second-order polynomial function to the positive ( $\Delta_+$ ) and negative ( $\Delta_-$ ) coherence peaks, modulations of the superconducting energy gap, defined as  $\Delta_{\text{UTe}_2} = \frac{\Delta_+ - \Delta_-}{2}$ , can be visualized across the target FOV. The resulting gap map,  $\Delta_{\text{UTe}_2}(\mathbf{r})$  is presented in Fig. 4.1c. The Fourier transform of this gap map (Fig. 4.1d), reveals three PDW peaks ( $\mathbf{P}_1, \mathbf{P}_2, \mathbf{P}_3$ ) with the same incommensurate wavevectors as the normal state CDW in this system.

While three PDW peaks can be observed in the gap map Fourier transform, their intensity is very similar to background noise levels. The reason for such a poor signal-to-noise ratio (SNR) is the difficulty associated with fitting the unexpectedly weak coherence peaks measured universally on the (0 -1 1) surface of  $\text{UTe}_2$ . Fig.4.2 (black) features an example  $\frac{dI}{dV}(V)$  spectrum recorded at 4.2 K, when  $\text{UTe}_2$  is in the normal state, and at 0.28 K, in the superconducting state (red). Well below its transition temperature ( $T_c = 1.6\text{K}$ ) the zero-energy conductance is reduced by only  $\sim 10\%$ . While initial samples grown by the CVT method exhibited a large residual Sommerfeld coefficient improvements in this sample growth technique, and the advent of MSF-grown crystals, have shown that this residual DOS is sample dependent<sup>74</sup> and no superconducting samples grown to date have exhibited the bulk residual DOS suggested in SI-STM measurements. The source of the residual DOS is therefore still unclear. Both pair breaking processes<sup>75</sup> and topological surface states are expected to be important for odd-parity superconducting states and could both produce finite DOS at surface terminations.

## 4.2 Superconducting Tip Characterisation

As discussed above, the shallow coherence peaks of  $\text{UTe}_2$  make fitting procedures exceptionally difficult and result in poor SNR. To circumvent this issue, Nb superconducting scan tips were prepared by field emission on a Nb crystal. The use of such tips is a well-established method of enhancing spectroscopic energy resolution beyond thermal broadening<sup>76,77</sup>. To determine the energy gap of the Nb tip used for measurement,  $\frac{dI}{dV}|_{\text{SIN}}(V)$  spectra were recorded at

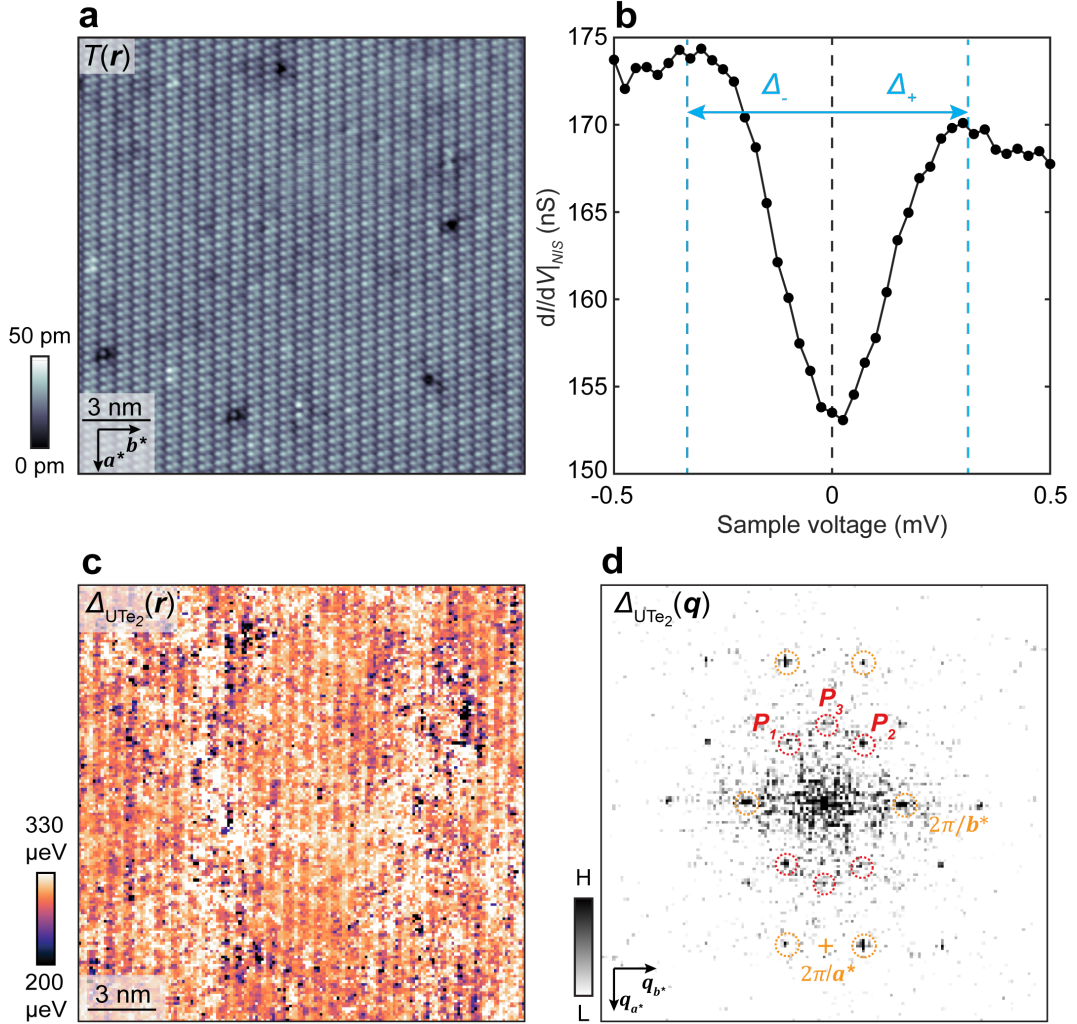


Figure 4.1: (a) Topography of target FOV shown in c. (b) Typical normal tip  $\frac{dI}{dV}$  spectrum on the (0 -1 1) surface of  $\text{UTe}_2$ . The energy of the fitted coherence peak is indicated by blue dashed arrows. (c) Superconducting energy gap modulations  $\Delta_{\text{UTe}_2}(\mathbf{r})$  found by fitting to coherence peaks as in b. (d) Fourier transform of the gap map presented in c,  $\Delta_{\text{UTe}_2}(\mathbf{q})$ . Surface reciprocal lattice peaks are highlighted by orange dashed circles. Incommensurate PDW modulations ( $\mathbf{P}_1, \mathbf{P}_2, \mathbf{P}_3$ ) are highlighted in red dashed circles

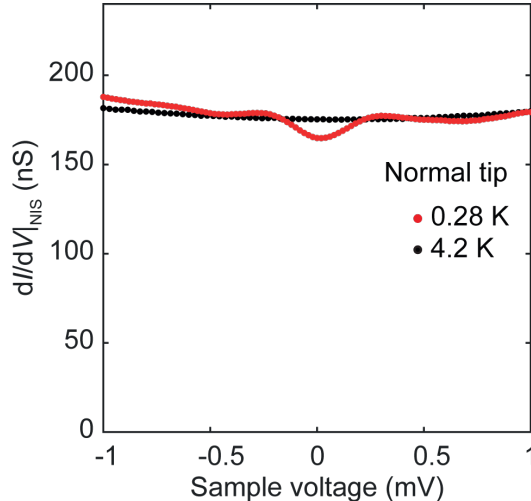


Figure 4.2: Metallic tip  $\frac{dI}{dV}|_{\text{NIS}}$  measurements on the (0 -1 1) cleave surface. Measurements performed at 4 K, in the normal state, are plotted with black points. Measurements performed at 0.28 K, in the superconducting state, are plotted in red

the cleave surface of  $\text{UTe}_2$  at  $T = 1.5$  K. At this temperature, the superconducting gap of  $\text{UTe}_2$  is closed. An example spectrum is presented in Fig. 4.3. This spectrum is fitted to the phenomenological Dynes model, Eq. 4.1, which captures pair-breaking processes associated with finite temperature by introducing a quasiparticle broadening parameter  $\Gamma$ .

$$N(E) = N_0 \text{Re} \left[ \frac{E + i\Gamma}{\sqrt{(E + i\Gamma)^2 - \bar{\Delta}^2}} \right] \quad (4.1)$$

Here  $N_0$  is the normal state DOS at the Fermi level and  $\bar{\Delta}$  is the zero-temperature superconducting energy gap. The experimentally obtained spectrum at 1.5 K is well fitted by Eq. 4.1 and we determine  $|\Delta| = 1.38$  meV and  $\Gamma = 0.11$  meV.

Now using our Nb superconducting tip we can lower the temperature of our SI-STM system to  $T = 0.28$  K. In Eq. 2.15 we found that the tunnelling current in an STM junction is proportional to the convolution of the tip and sample DOS. In previous sections we assumed that the tip DOS is flat in the region surrounding the Fermi level  $E_F$  however, now using a superconducting scan tip, this is no longer valid as there is a superconducting energy gap around  $E_F$ . The effect of this energy gap on measurement is to push the states of the sample which were previously within the energy range of the tip gap  $|\Delta| =$

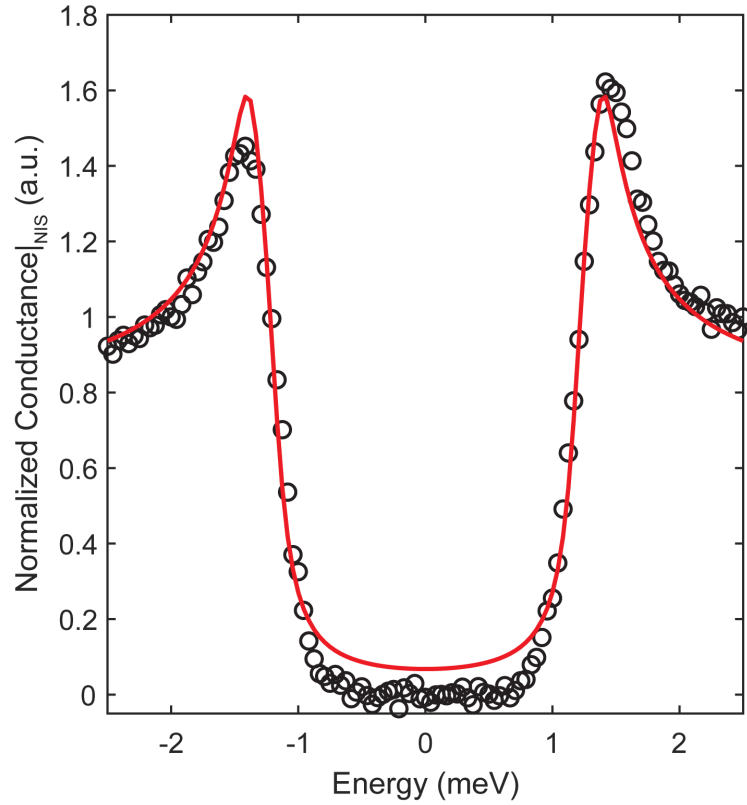


Figure 4.3: A typical spectrum measured on the  $\text{UTe}_2$  (0 -1 1) surface using a superconducting Nb tip at 1.5K ( $I_s = 100$  pA,  $V_b = 4$  mV). At this temperature, the  $\text{UTe}_2$  gap is closed, thus the spectrum is a convolution of the nearly flat DOS of normal  $\text{UTe}_2$  and the superconducting gap of the Nb tip. The spectrum is well fit using the Dynes model with a very weakly anisotropic energy gap, integrated around  $k$ -space, of the form  $\Delta(\theta_{\mathbf{k}}) = 1.38(0.93 + 0.07 \cos(4\theta_{\mathbf{k}}))$  in units meV. The fitting parameters of the Dynes model are  $\Gamma = 0.11$  meV,  $|\bar{\Delta}| = 1.38$  meV. To estimate the quality of the fit we calculate the  $R^2$  coefficient, as defined in Appendix Eq. B.2, and find  $R^2 = 0.98$

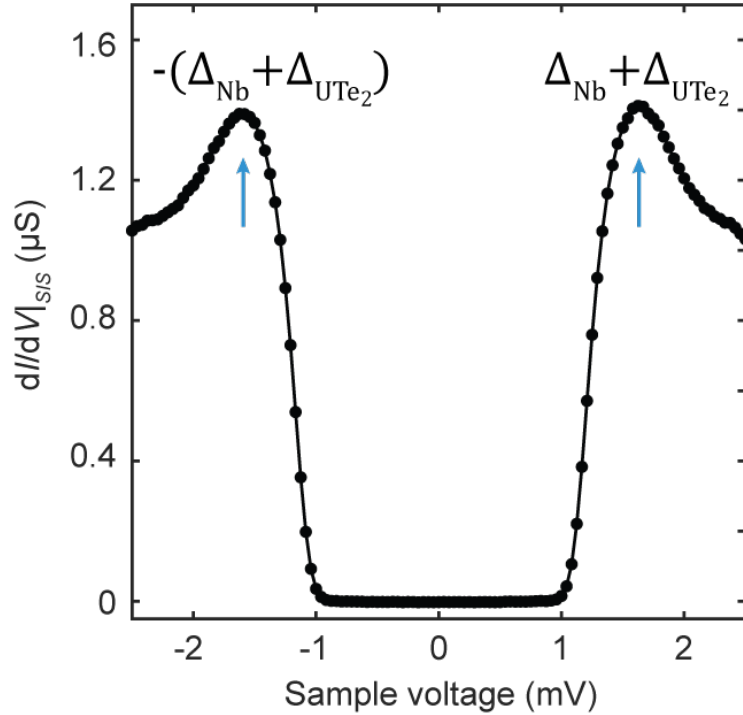


Figure 4.4: Measured  $\frac{dI}{dV}|_{\text{SIS}}$  spectrum obtained using a superconducting Nb tip on the  $\text{UTe}_2$  (0 -1 1) crystal surface. Combined coherence peaks  $\pm(\Delta_{\text{Nb}} + \Delta_{\text{UTe}_2})$  indicated with blue arrows

1.38 meV to the combined gap edge. At  $T = 0.28$  K the superconducting  $\text{UTe}_2$  DOS becomes convoluted with the scan tip DOS thus combined Nb- $\text{UTe}_2$  coherence peaks appear at energies  $|\Delta_{\text{Nb}}| + |\Delta_{\text{UTe}_2}|$ . An example of the resulting tunnelling spectra is featured in Fig. 4.4. The superconducting energy gap of the Nb tip is a previously measured constant therefore subtracting this value from the overall spectrum reveals modulations in the energy gap of  $\text{UTe}_2$ . Doing so for the example spectrum in Fig. 4.4 yields a superconducting energy gap of  $\sim 245 \mu\text{eV}$  in good agreement with normal tip measurements as in Fig. 4.2.

### 4.3 Superconducting Tip Gap Map Analysis

The Nb superconducting scan tip permits higher energy resolution measurements, however, due to the enhanced gap size in  $\frac{dI}{dV}(V)$  measurements, the combined coherence peaks, whose modulations we wish to track, are now separated in energy by  $\sim 3\text{meV}$ . At the low junction parameters required for accurate gap map measurements ( $V_b = 3\text{meV}$ ,  $I_s = 2.5\text{nA}$ ) the scan tip is

made unstable when sweeping the bias from the negative to the positive coherence peak or vice versa. To resolve this issue, two separate gap maps were measured at energies around the coherence peaks. To create a complete gap map we must combine these individual maps. We first match the real space FOVs. To do so, we will discuss several analysis techniques which rectify distortions associated with STM measurements at finite temperature.

### 4.3.1 Shear Correction

An intrinsic issue associated with differential conductance measurements is that these maps require several days to carry out and some drift of the STM tip due to temperature variation or vibrations is inevitable over such long periods. An example of the kind of distortions resulting from this drift can be seen in the topograph shown in Fig. 4.6a. Clearly the effect of drift in the scan head is a sheared image of the crystal lattice, in this case the (0 -1 1) surface of  $\text{UTe}_2$ . This surface is defined by the lattice vectors  $\mathbf{c}^*$  and  $\mathbf{a}$  in the horizontal and vertical direction respectively. For now, we refer to the horizontal and vertical axes in this plane as the  $y$  and  $x$  axes respectively. A shear of  $p$  in the horizontal  $y$  direction, as in Fig. 4.6a, modifies the  $y$  coordinates to be  $y - px$ . Considering a perfect lattice in 2D of the form

$$f(x, y) = \text{Re}(e^{i(Q_x x + Q_y y)}) \quad (4.2)$$

then the effect of a shear of magnitude  $p$  produces an image of the form

$$f_s(x, y) = \text{Re}(e^{i(Q_x x + Q_y (y - px))}) = \text{Re}(e^{i(x(Q_x - pQ_y) + yQ_y)}) \quad (4.3)$$

Thus, the horizontal  $y$  components of our wavevectors remain unchanged, while the  $x$  components are moved by an amount  $-pQ_y$ . This has the effect of shifting the reciprocal wavevectors in the  $x$  direction. This effect can be clearly in the topograph,  $T_S(\mathbf{r})$  recorded simultaneously with the positive energy coherence peak map in Fig. 4.5a. By performing corrections to the simultaneously obtained topograph we have the benefit of viewing the corrections we make to the data on the atomic lattice. We can then apply the exact same transformations to the spectroscopic measurements. The simultaneous topograph in Fig 4.5 features tellurium chains which are clearly sheared and distorted instead of running in straight lines vertically. Furthermore by Fourier transform of

$T_S(\mathbf{r})$  we obtain  $T_S(\mathbf{q})$  in Fig. 4.5b. Here the reciprocal lattice wavevectors are highlighted by dashed orange circles and connected via a dashed red line to indicate the degree of shear. To unshear our image we note we can express a shear like that above by the matrix

$$S(p) = \begin{pmatrix} 1 & 0 \\ p & 1 \end{pmatrix} \quad (4.4)$$

To shear at an arbitrary angle  $\theta$ , defined anticlockwise from the horizontal  $y$  axis, we can make use of the rotation matrix to align these wavevectors to the  $y$  axis, shear, then rotate back. Thus a shear acting on an ideal, unsheared lattice wavevector  $\mathbf{r}_1$  is defined as

$$S(p, \theta) = R^{-1}(\theta)S(p)R(\theta)\mathbf{r}_1 = \mathbf{r}_2 \quad (4.5)$$

Using the rotation matrix

$$R(\theta) = \begin{pmatrix} \cos(\theta) & -\sin(\theta) \\ \sin(\theta) & \cos(\theta) \end{pmatrix} \quad (4.6)$$

We obtain the shear matrix

$$S(p, \theta) = \begin{pmatrix} 1 - p \cos(\theta) \sin(\theta) & p \sin^2(\theta) \\ -p \cos^2(\theta) & 1 + p \cos(\theta) \sin(\theta) \end{pmatrix} \quad (4.7)$$

To correct our shear we just perform the opposite operation. Rotate our data to the  $y$  axis, unshear, and rotate back by the same angle  $\theta$ . Our original wavevector  $\mathbf{r}_1$  is recovered by the operation  $R^{-1}(\theta)S^{-1}(p)R(\theta)\mathbf{r}_2$  where  $\mathbf{r}_2$  is the wavevector of our sheared or experimental data.

For a distorted triangular lattice, like that of the (0 -1 1) surface of  $\text{UTe}_2$ , we write the reciprocal lattice vector coordinates as below

$$\mathbf{Q} = \begin{pmatrix} \mathbf{Q}_1 \\ \mathbf{Q}_2 \\ \mathbf{Q}_3 \end{pmatrix} = \begin{pmatrix} q_0 \cos(\alpha) \\ q_0 \sin(\alpha) \\ 1.9q_0 \cos(\alpha + 74^\circ) \\ 1.9q_0 \sin(\alpha + 74^\circ) \\ 1.9q_0 \cos(\alpha + 106^\circ) \\ 1.9q_0 \sin(\alpha + 106^\circ) \end{pmatrix} \quad (4.8)$$

Reversing the shear involves finding the roots of the below equations in which we have set the coordinates of the sheared reciprocal lattice wavevectors to the average reciprocal lattice wavevector,  $\langle q_0 \rangle = \frac{\sqrt{\sum_{i=1-3} \mathbf{Q}_i^2}}{3}$ . By solving these equations for just two of our reciprocal lattice peaks we can correct the entire image as the shear is a global transformation.

$$\tilde{\mathbf{Q}}_1 = \begin{pmatrix} q_0 \cos(\alpha) + pq_0 \sin(\theta) \cos(\theta - \alpha) \\ q_0 \sin(\alpha) - pq_0 \cos(\theta) \cos(\theta - \alpha) \end{pmatrix} = \langle q_0 \rangle \quad (4.9)$$

$$\tilde{\mathbf{Q}}_2 = \begin{pmatrix} 1.9q_0 \cos(\alpha + 74^\circ) + 1.9pq_0 \sin(\theta) \cos(\theta - \alpha - 74^\circ) \\ 1.9q_0 \sin(\alpha + 74^\circ) - 1.9pq_0 \cos(\theta) \cos(\theta - \alpha - 74^\circ) \end{pmatrix} = \langle q_0 \rangle \quad (4.10)$$

This is a system of four equations with four unknowns,  $q_0$ ,  $p$ ,  $\theta$ , and  $\alpha$  which can be solved for numerically. Performing this procedure on the topograph featured in Fig. 4.5a yields  $T_{SC}(\mathbf{r})$  in Fig. 4.5c. Now we see that the rows of tellurium atoms are arranged vertically, and from Fourier transform of this topograph  $T_{SC}(\mathbf{q})$ , we find the reciprocal lattice peaks are unsheared (Fig. 4.5d). While shear correction is an incredibly useful technique in correcting distortions, it is a global transformation applied to the entire image. To correct local distortions we must learn to extract the phase of our peaks in the Fourier transform.

### 4.3.2 Phase Extraction & the Lock-In Method

After shear correction of our STM data we are still unable to exactly match our coherence peak map field of views. To do so will require the use of the LF algorithm which, as we see from previous studies, see Ref.[28], have made use of Fourier analysis to compare the real space phase of CDWs and PDWs. We aim to do the same and thus require some method of extracting the phase of individual signals from our data. To do so we make use of the principles of lock-in detection as outlined in Section 2.4.1, however, we now apply these same principles numerically to extract the phase information of our signal. To begin we model the desired signal as an arbitrary real space modulation of magnitude  $A$

$$f(\mathbf{r}) = A \cos(\mathbf{Q} \cdot \mathbf{r} + \phi) \quad (4.11)$$

where the added phase term  $\phi$  acts to offset the crest of the wave by  $\phi/Q$  towards the  $-\mathbf{Q}$  direction. We consider a simple one-dimensional model first

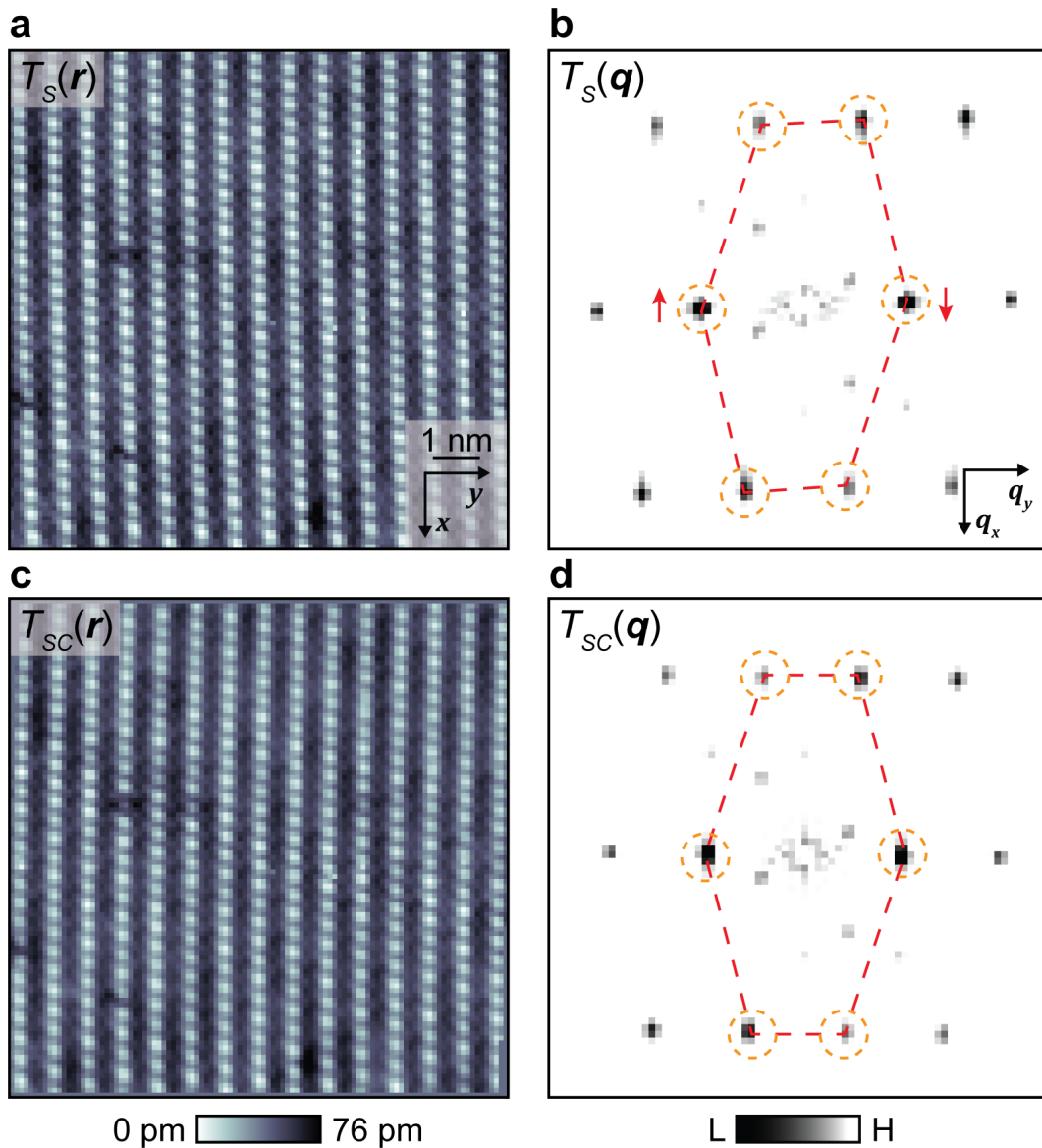


Figure 4.5: **a.** Topograph  $T_S(\mathbf{r})$  obtained simultaneously with the positive coherence peak map (Fig. 4.9). **b.** Fourier transform of a,  $T_S(\mathbf{q})$ . Six reciprocal lattice wavevectors are highlighted in dashed orange circles. The degree of shear is indicated by red dashed lines. Reversing this shear moves the reciprocal lattice wavevectors in the direction indicated by red arrows. **c.** Shear corrected topograph  $T_{SC}(\mathbf{r})$ . **d.** Fourier transform of the shear corrected topograph  $T_{SC}(\mathbf{q})$ . Red dashed lines connect highest intensity pixels of the reciprocal lattice wavevectors. That these peaks are now level indicates that the image has been unsheared.

and multiply this one-dimensional signal by a reference signal of the same periodicity. Finally we integrate the result over the real space length  $-L/2$  to  $L/2$ .

$$A_q = \int_{-L/2}^{L/2} f(x)e^{iqx} dx \quad (4.12)$$

$$= \int_{-L/2}^{L/2} A \cos(qx + \phi)e^{iqx} dx \quad (4.13)$$

$$= A \int_{-L/2}^{L/2} [e^{i(qx+\phi)} + e^{-i(qx+\phi)}] e^{iqx} dx \quad (4.14)$$

$$= \frac{AL}{2} e^{i\phi} \quad (4.15)$$

As the left hand term above is a quickly oscillating, symmetric function over the integration limits, this term goes to zero leaving only the phase term of the input signal. Thus, the phase component of the input signal can be found by  $\phi = \tan^{-1} \left( \frac{\text{Im}(A_q)}{\text{Re}(A_q)} \right)$ . Note also that we can extract the amplitude,  $A$  of our input signal allowing us to extract amplitude and phase maps for arbitrary wavevectors. In two dimensions we can replace the integration limits by a Gaussian centred on  $\mathbf{r}$ , so that we perform the following

$$A_{\mathbf{Q}}(\mathbf{r}) = \int A(\mathbf{r}) \cos(\mathbf{Q} \cdot \mathbf{r} + \phi(\mathbf{r})) e^{-i\mathbf{Q} \cdot \mathbf{R}} e^{-\frac{(\mathbf{r}-\mathbf{R})^2}{2\sigma^2}} d\mathbf{R} \quad (4.16)$$

Here we use the variables  $\mathbf{R}$  and  $\mathbf{r}$  to differentiate between the integration window and real space location respectively. In order to improve the computational time required for the filtering procedure, we carry out these operations in q-space by Fourier transforming the product of input and reference signals

$$A_{\mathbf{Q}}(\mathbf{q}) = \int f(\mathbf{R}) e^{i\mathbf{Q} \cdot \mathbf{R}} e^{i\mathbf{q} \cdot \mathbf{r}} e^{-\frac{(\mathbf{r}-\mathbf{R})^2}{2\sigma^2}} d\mathbf{r} d\mathbf{R} \quad (4.17)$$

Rearranging this equation and substituting  $\mathbf{x} = \mathbf{r} - \mathbf{R}$  we arrive at

$$A_{\mathbf{Q}}(\mathbf{q}) = \int f(\mathbf{R}) e^{i\mathbf{Q} \cdot \mathbf{r}} e^{-i\mathbf{q} \cdot \mathbf{R}} d\mathbf{R} \int e^{-i\mathbf{q} \cdot \mathbf{x}} e^{-\frac{x^2}{2\sigma^2}} d\mathbf{x} \quad (4.18)$$

The left term of the above is simply the Fourier transform of our input signal multiplied by the reference signal. This shifts the desired  $\mathbf{Q}$  component to the origin of q-space. This is then filtered by the Fourier transform of the Gaussian as seen in the right-hand integral. The filter width in this q-space represen-

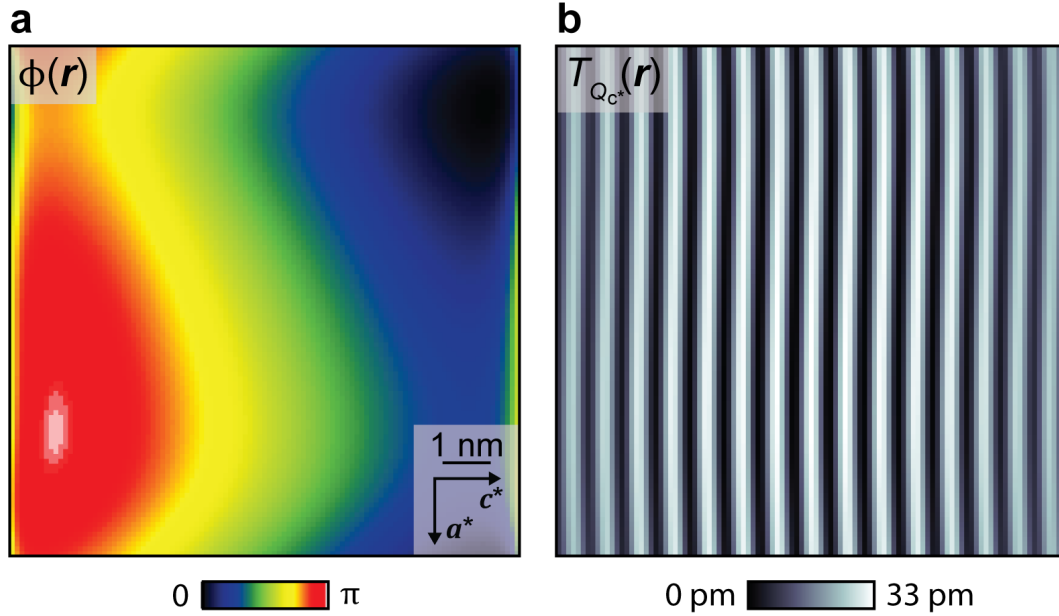


Figure 4.6: **a.** Phase map  $\phi(\mathbf{r})$  of the horizontal reciprocal lattice wavevector  $(0, \frac{2\pi}{c^*})$ . **b.** Real part of the horizontal reciprocal lattice wavevector,  $T_{Q_{c^*}}(\mathbf{r})$ . Horizontally aligned rows of intensity are indicative of the tellurium chain periodicity on the (0 -1 1) surface of  $\text{UTe}_2$ .

tation,  $\sigma$  is related to the real space filter width by,  $\sigma_{\mathbf{q}} \propto 1/\sigma_{\mathbf{r}}$ . This filter width plays a critical role in inverse Fourier filtration, too large and unwanted wavevectors are captured in the filtration, too small and we lose important information from the real space signal. Correct filtering thus requires a degree of trial and error to capture the real space behaviour.

To best illustrate these procedures, we take  $T_{SC}(\mathbf{r})$  above, after shear correction. Using the above lock-in algorithm, we select the horizontal reciprocal lattice peak at  $(0, \frac{2\pi}{c^*})$  and, using a Gaussian filter of real space radius  $\sigma_r = 1.3$  nm, we can inverse Fourier filter this reciprocal lattice peak. Fig. 4.6a shows the phase map  $\phi(\mathbf{r})$  produced using this process while Fig. 4.6b is the real part of the inverse Fourier filtered signal. Comparing Fig. 4.5b with Fig. 4.6b one can see the periodicity of the tellurium chains is captured by the maxima of the inverse Fourier filtered signal  $T_{Q_{c^*}}(\mathbf{r})$ .

### 4.3.3 Lawler-Fujita Algorithm

The final step required to match our two data sets is to apply the Lawler-Fujita (LF) algorithm. This algorithm, which was introduced in Ref [78] to extract intra-unit cell phase information in  $\text{Bi}_2\text{Sr}_2\text{CaCu}_2\text{O}_{8+\delta}$ , is extremely useful when registering multiple data sets recorded in the same FOV. High spatial and energy resolution,  $g(\mathbf{r}, V)$  maps can take up to 3 days of continuous measurement. During this time, mechanical noise or temperature variations can cause distortions in the resulting image which do not reflect the atomic structure and which cannot be corrected for via a global transformation, like that used in shear correction. These distortions manifest themselves as smearing of the reciprocal lattice wavevectors in  $q$ -space. Continuing the procedure above, we consider applying this algorithm to the shear corrected topograph  $T_{SC}(\mathbf{r})$  obtained simultaneously with the positive coherence peak map. To understand the LF algorithm we start with a lattice of the form

$$T = \sum_{j=1}^n T_j \cos(\mathbf{Q}_j \cdot [\mathbf{r} + \mathbf{u}_j(\mathbf{r})]) \quad (4.19)$$

$$= \sum_{j=1}^n T_j \cos(\mathbf{Q}_j \cdot \mathbf{r} + \theta_j(\mathbf{r})) \quad (4.20)$$

where  $j$  sums over the number of reciprocal lattice wavevectors to be considered,  $\mathbf{Q}_j$  are the magnitude of these wavevectors, and the vector field  $\mathbf{u}_j(\mathbf{r})$  represents the distortion field. Thus, for a perfect lattice,  $\mathbf{u}_j$  and  $\theta_j$  are constant. We consider the distorted lattice to be the same as the perfect one with a change of coordinates so that

$$\mathbf{Q}_j \cdot \mathbf{r} + \theta_j(\mathbf{r}) = \mathbf{Q}_j \cdot \tilde{\mathbf{r}} + \bar{\theta}_j(\mathbf{r}) \quad (4.21)$$

where  $\tilde{\mathbf{r}} = \mathbf{r} - \mathbf{u}(\mathbf{r})$ . From this, we can derive an expression for the displacement field using

$$\mathbf{u}(\mathbf{r}) = \mathbf{Q}^{-1}(\bar{\theta}(\mathbf{r}) - \theta\mathbf{r}) \quad (4.22)$$

The right-hand side of this equation can be derived solely from the input topograph/map as  $\mathbf{Q} = \begin{pmatrix} \mathbf{Q}_1^T \\ \mathbf{Q}_2^T \\ \mathbf{Q}_3^T \end{pmatrix}$  is simply the magnitude of the reciprocal

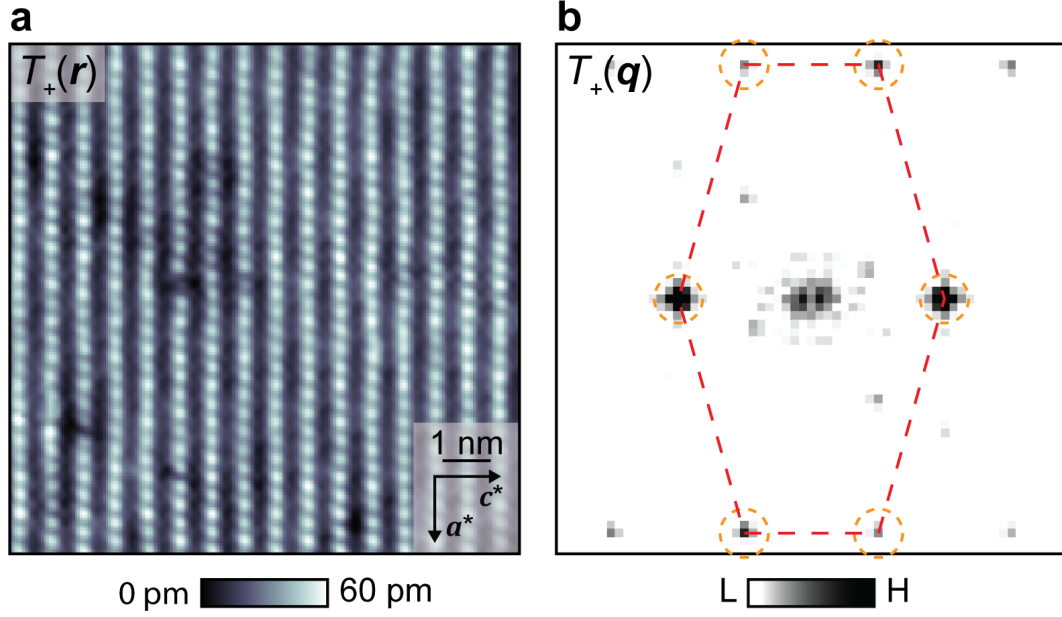


Figure 4.7: **a.** Topograph  $T_+(\mathbf{r})$  of the  $\text{UTe}_2$  (0 -1 1) surface after shear correction, LF correction, and interpolation. **b.** Fourier transform of **a**,  $T_+(\mathbf{q})$ . Surface reciprocal lattice wavevectors are indicated by dashed orange circles. Dashed red lines indicate the absence of shears and distortions previously seen in the untreated data (Fig. 4.5a)

lattice wavevectors in  $\mathbf{q}$ -space,  $\bar{\theta}(\mathbf{r}) = \begin{pmatrix} \bar{\theta}_1^T(\mathbf{r}) \\ \bar{\theta}_2^T(\mathbf{r}) \\ \bar{\theta}_3^T(\mathbf{r}) \end{pmatrix}$  is the corrected phase, and

$\theta(\mathbf{r}) = \begin{pmatrix} \theta_1^T(\mathbf{r}) \\ \theta_2^T(\mathbf{r}) \\ \theta_3^T(\mathbf{r}) \end{pmatrix}$  is the initial phase of the topograph/map's reciprocal lattice

wavevectors and can be extracted by the lock-in technique described above. Finally, the image is corrected using the GRIDDATA function of Matlab which fits the distortion field  $u(\mathbf{r})$  to the data and interpolates it to produce the undistorted image.

To demonstrate the effect of the LF algorithm, we continue to use the topograph seen in Fig. 4.6a. The topograph after applying the LF algorithm and interpolated for clarity is featured as,  $T_+(\mathbf{r})$  in Fig. 4.7a. From comparison with Fig. 4.5b we can see that the image after shear and LF correction is much more ordered. From the topograph's Fourier transform  $T_+(\mathbf{q})$ , we see that the reciprocal lattice wavevectors are less disperse than the initial image and connecting these peaks forms a distorted hexagon, as expected for  $\text{UTe}_2$ .

## 4.4 PDW Discovery & Phase Analysis

### 4.4.1 PDW Discovery

Now that we can correct experiment-related distortions from our data, we can match the FOV of our two coherence peak maps and generate a complete gap map. In Fig. 4.8a and b we present the distortion corrected topographs,  $T_+(\mathbf{r})$ ,  $T_-(\mathbf{r})$ , recorded with the coherence peak differential conductance maps. These topographs have been shear and LF corrected then cropped so that their FOV matches very closely. We can check how closely by calculating the cross correlation (XCORR) between them. For two images  $I_1$  and  $I_2$  the XCORR is

$$X(\mathbf{r}, I_1, I_2) = \frac{\int I_1^*(\mathbf{r}_1) I_2(\mathbf{r} + \mathbf{r}_1) d\mathbf{r}_1}{\sqrt{\int |I_1(\mathbf{r}_1)|^2 d\mathbf{r}_1 \int |I_2(\mathbf{r}_2)|^2 d\mathbf{r}_2}} \quad (4.23)$$

where the denominator normalizes the function so that two identical images  $I_1$  and  $I_2$  produce a peak, at the centre of  $X(\mathbf{r}, I_1, I_2)$ , of magnitude one. Upon calculating XCORR for our two topographs we obtain a single pixel peak centred at (0,0) of magnitude 0.93, indicative of registration to within one pixel or approximately 58 pm.

Now that we have matched the FOVs of the simultaneously recorded topographs we can apply the same distortion corrections and transformations to the coherence peak data set. The resulting coherence peak maps,  $E_+(\mathbf{r})$  and  $E_-(\mathbf{r})$ , show clearly that the coherence peak maxima occur between tellurium chains. Subtracting the tip gap from both coherence peak maps generates maps of the  $\text{UTe}_2$  coherence peaks,  $\Delta_{\pm}(\mathbf{r}) = |E_{\pm}(\mathbf{r})| - |\Delta_{\text{tip}}|$ . As the superconducting energy gap is defined in reference to the Fermi level we calculate  $\Delta_{\text{UTe}_2} = \frac{|\Delta_+(\mathbf{r})| - |\Delta_-(\mathbf{r})|}{2}$  and finally, by subtracting the average gap value over the FOV, we obtain our gap map image  $\delta\Delta(\mathbf{r}) = \Delta_{\text{UTe}_2} - \langle \Delta_{\text{UTe}_2}(\mathbf{r}) \rangle$ . This gap map,  $\delta\Delta(\mathbf{r})$  is presented in Fig. 4.9a and its Fourier transform,  $\delta\Delta(\mathbf{q})$  is presented in Fig. 4.9b. Three peaks, highlighted by dashed red circles, are observed at the same incommensurate q-space locations as the CDW in Ref. [73] and the PDW in Fig. 4.1d. Crucially, the use of the superconducting tip data ensures that the PDW peaks observed exhibit an enhanced signal-to-noise ratio owing to the better fit quality of superconducting tip gap maps (Appendix B). This map therefore represents the first detection of PDWs in this system.

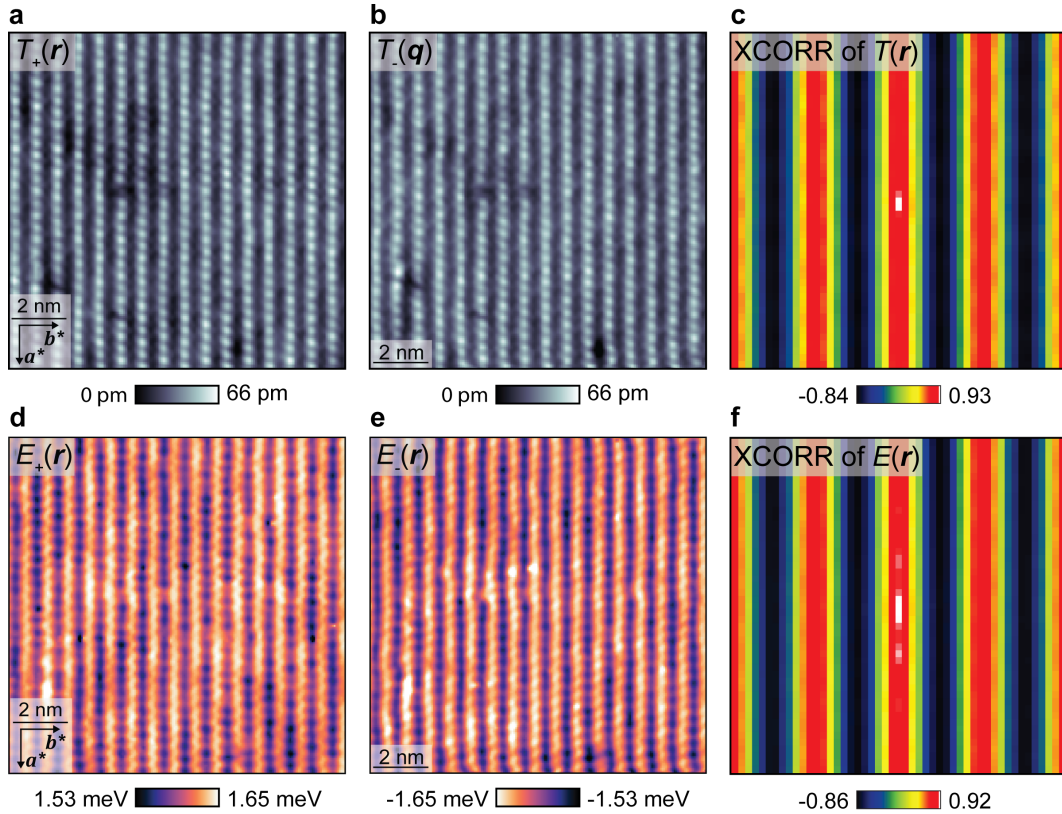


Figure 4.8: **a**. Topograph recorded simultaneously with the positive energy coherence peak map,  $T_+(\mathbf{r})$ . **b**. Topograph recorded with the negative energy coherence peak map,  $T_-(\mathbf{r})$ . **c**. Cross-correlation function evaluated for  $T_+(\mathbf{r})$  and  $T_-(\mathbf{r})$ . A maxima of 0.93 at (0,0) is only a single pixel wide indicative of closely matched FOVs in  $T_+(\mathbf{r})$  and  $T_-(\mathbf{r})$ . **d**. Positive energy coherence peak map obtained by parabolic fitting,  $E_+(\mathbf{r})$ . **e**. Negative energy coherence peak map,  $E_-(\mathbf{r})$ . **f**. Cross correlation of coherence peak maps  $E_{\pm}(\mathbf{r})$ . A single-pixel wide maximum of 0.92 is observed at (0,0)

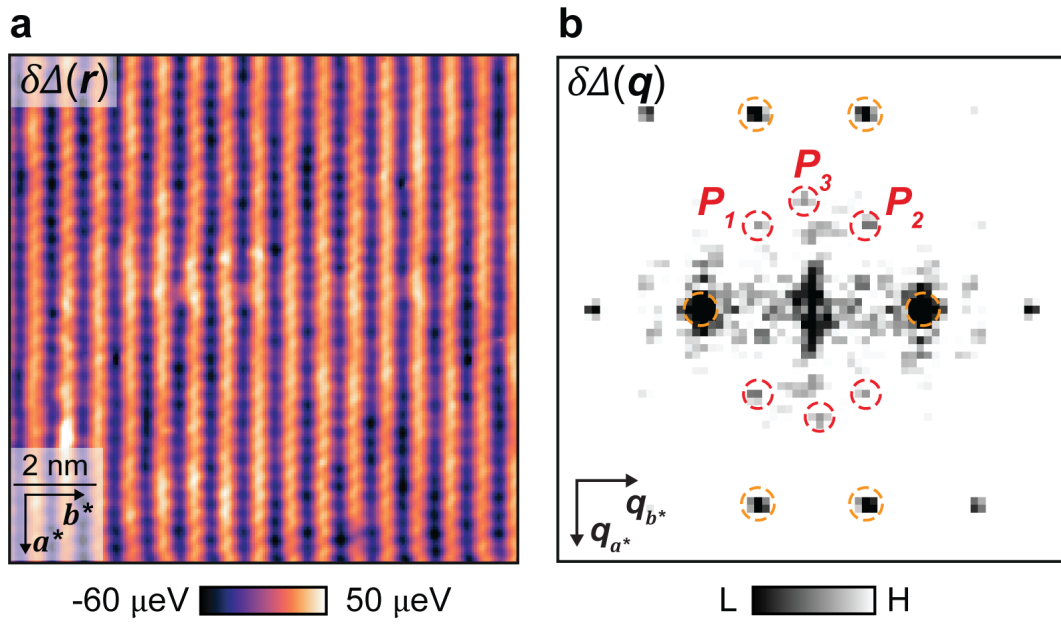


Figure 4.9: **a**. Gap map  $\delta\Delta(\mathbf{r})$  of the  $\text{UTe}_2$  (0 -1 1) surface obtained after distortion correction, interpolation, and image registration. **b**.  $\delta\Delta(\mathbf{q})$ , the Fourier transform of  $\delta\Delta(\mathbf{r})$ . Dashed orange circles highlight the surface reciprocal lattice wavevectors. Dashed red circles highlight the newly discovered PDW wavevectors, labelled  $\mathbf{P}_1$ ,  $\mathbf{P}_2$ ,  $\mathbf{P}_3$ .

### 4.4.2 Interplay of CDW and PDW

Now, equipped with tools allowing exact registration and phase extraction of differential conductance images, we can study the interplay of the CDW phase with that of the PDW. To do so we record a CDW map at  $T = 4\text{K}$  in an overlapping FOV to Fig. 4.8a above and apply shear correction and the LF algorithm so that we can register the CDW map to our new gap map. The resulting map  $g(\mathbf{r}, -9\text{mV})$  is shown in Fig. 4.10a and its Fourier transform,  $g(\mathbf{q}, -9\text{mV})$  is shown in Fig. 4.10b revealing the three CDW wavevectors in blue dashed circles.

Next, using the lock-in method, we select just the CDW peaks from our CDW map and the PDW peaks from our gap map and extract the real component of the signal and its phase. The CDW peaks ( $\mathbf{Q}_1, \mathbf{Q}_2, \mathbf{Q}_3$ ) are highlighted in blue dashed circles in Fig. 4.10b and the inverse Fourier filtration is performed with a filter width  $\sigma_r = 1.14\text{ nm}$ . The same filter width is also used to extract information from the PDW peaks ( $\mathbf{P}_1, \mathbf{P}_2, \mathbf{P}_3$ ) in Fig. 4.8b. After extracting the individual real components of the inverse Fourier transform for each CDW/PDW wavevector the real space maps of  $\mathbf{Q}_1, \mathbf{Q}_2,$  and  $\mathbf{Q}_3$  are added together to produce the CDW/PDW maps shown in Fig. 4.10c and Fig. 4.10d respectively. We label the CDW map,  $g_Q(\mathbf{r}, -9\text{meV})$  and the PDW map,  $\delta\Delta_P(\mathbf{r})$ . We note that these density waves appear to be approximately negative images of each other, suggesting that there is a substantial phase difference between them. To better understand this phase relationship, we extract the phase map of each CDW/PDW component and calculate the phase difference between them  $|\delta\phi_i(\mathbf{r})| = |\phi_i^P(\mathbf{r}) - \phi_i^C(\mathbf{r})|$ . We can then plot this phase difference in histogram format and find a distribution of phase differences. This distribution is shown in Fig. 4.10e and clearly demonstrates that the CDW and PDW are approximately  $\pi$  out of phase with  $\delta\Delta_{RMS}(\mathbf{r}) = 0.96\pi$ .

## 4.5 Parent Order & Triplet PDW

In Section 4.1 we motivated the search for a PDW in  $\text{UTe}_2$  by the opportunity to observe a PDW whose coupling to the bulk order parameter should induce a CDW. We refer to such a PDW as the parent form of order and the subsequent CDW as the daughter order. While we have no definitive conclusion regarding this parent-daughter relationship we can speculate from the observed facts. While Ref. [73] proposes parent PDW order to explain the

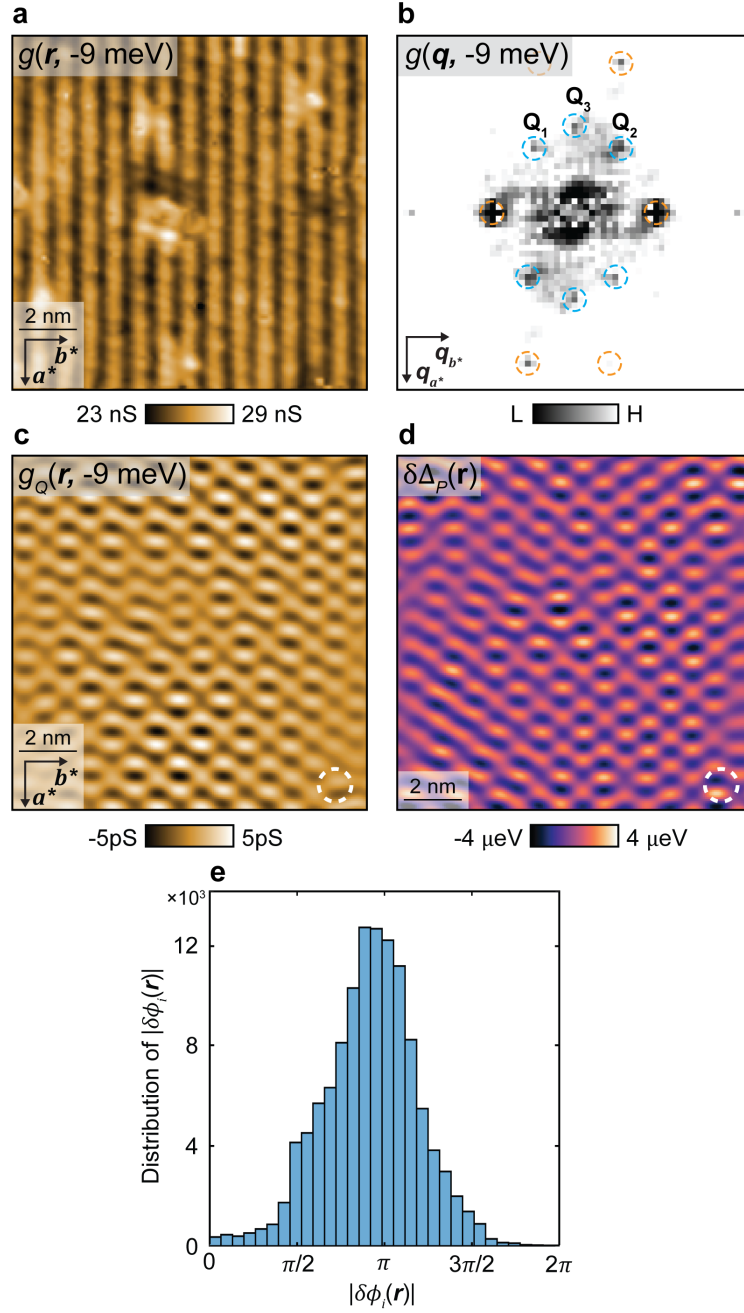


Figure 4.10: **a.** Differential conductance map,  $g(\mathbf{r}, -9 \text{ meV})$ , recorded at  $T = 4$  K and registered to the gap map FOV. **b.** Fourier transform of **a**,  $g(\mathbf{q}, -9 \text{ meV})$ . The three CDW peaks to be inverse Fourier filtered are  $\mathbf{Q}_1, \mathbf{Q}_2, \mathbf{Q}_3$  highlighted in blue dashed circles. **c.** Real part of the inverse Fourier transform of  $\mathbf{Q}_1 + \mathbf{Q}_2 + \mathbf{Q}_3$ ,  $g_Q(\mathbf{r}, -9 \text{ meV})$ . A filter width of  $\sigma_r = 1.14$  nm is used in filtration. **d.** Real part of the inverse Fourier transform of  $\delta\Delta(\mathbf{r})$  featuring  $\mathbf{P}_1 + \mathbf{P}_2 + \mathbf{P}_3$ . **e.** Histogram counting the phase difference between CDW and PDW modulations at each pixel in the FOV. Phase difference at position  $\mathbf{r}$  is defined as  $|\delta\phi_i(\mathbf{r})| = |\phi_i^P(\mathbf{r}) - \phi_i^C(\mathbf{r})|$

---

magnetic field dependence of the CDW it is not clear how such a PDW, forming below  $T_c = 1.6\text{K}$  may induce a CDW whose onset temperature is between 4.5 K and 10 K. Furthermore the PDW modulations reported herein are of magnitude  $10\mu\text{eV}$  while the CDW modulations can be detected up to 25 meV. The most plausible mechanism connecting these two orders is therefore one in which superconductivity emerges in the presence of a normal state CDW thereby inducing PDW modulations at the same wavevectors. Such a scenario is at odds with the proposal of Ref. [73] however, as pointed out in Section 1.6.2.2, it is a natural consequence of the interaction between a pre-existing CDW and bulk superconductivity.

Even if the phenomena discovered in Ref. [30] and Ref. [73] are, in fact, produced by the interplay of uniform superconductivity and charge order they remain important in the broader context of PDW detection. As we discussed extensively in Chapter 3,  $\text{UTe}_2$  is, in all likelihood, a  $p$ -wave superconductor. Thus formation of a PDW within a uniform  $p$ -wave superconducting state suggests the exciting possibility that such a PDW is composed of spin triplet Cooper pairs. Thus Ref. [30] extends the surprising conclusion inferred from previous reports, such as Refs. [29], [28], and [79], that PDWs are a ubiquitous phase of superconducting order in real material systems.

# Chapter 5

## Andreev Reflection, Andreev Bound States, & Topological Superconductivity

### 5.1 Introduction

The use of superconducting scan tips to measure the surface electronic structure of  $\text{UTe}_2$  helped greatly in discovering the presence of a weak PDW on the  $(0 -1 1)$  surface. In Chapters 6 and 7 we will see that the superconducting scan tip encourages Andreev transport of low-energy quasiparticle states. These Andreev effects are a direct consequence of particle-hole hybridization made possible by the superconducting pair potential. This hybridization was alluded to in our discussion of the Bogoliubov transformation in Section 1.3. We will now discuss this transformation again, this time in greater depth, as it is critical in deriving the Bogoliubov-de Gennes equations. We will then see how a single Andreev reflection can take place at the surface of a superconductor. Where appropriate, we make modifications to our  $s$ -wave formalism to model some properties of  $p$ -wave superconductors, including the conductance between a normal metal and  $p$ -wave superconductor separated by an insulating barrier, as well as discussion of Andreev bound states (ABSs). These bound states have been observed in several superconducting systems including the cuprate superconductors<sup>80</sup> but are especially relevant to  $p$ -wave superconductors where they should be present on almost all crystal surfaces. These states

have a close relationship to topological surface states, proposed to exist on the surfaces of  $p$ -wave superconductors with non-trivial band topology. We therefore conclude with a brief overview of topological classification methods for superconductors as there is extensive literature discussing the non-trivial topology of  $\text{UTe}_2$ .

## 5.2 Bogoliubov-deGennes Equations

The Bogoliubov-de Gennes (BdG) equations have been powerful tools in understanding the behaviour of single-particle excitations in superconductors. Upon entering the superconducting state the hybridization of electrons and holes modifies the electronic band structure around the Fermi level making descriptions of the new Bogoliubov quasiparticle dynamics difficult, particularly in the case of an inhomogeneous system. In experiment, there are many ways a superconductor may be inhomogeneous; there are inevitably impurities throughout the crystal which can cause resonant scattering of Bogoliubov quasiparticles at low energies<sup>81</sup>, in the presence of a magnetic field Abrikosov vortices locally suppress superconductivity and form a lattice of normal-state vortex cores<sup>82</sup>, and even the crystal surface should modify the single-particle excitation spectrum<sup>83</sup>. In all these cases, the BdG equations and the associated theoretical framework are the best tools condensed matter physicists have in describing these effects. We begin, as in Section 1.3 by studying the BCS mean-field Hamiltonian which we now write in real space as

$$\begin{aligned}
 H_{\text{MF}} = & \int d\mathbf{r} \sum_{\alpha,\beta} \psi_{\beta}^{\dagger}(\mathbf{r}) \xi(\mathbf{r}) \psi_{\alpha}(\mathbf{r}) \\
 & + \int \int d\mathbf{r} d\mathbf{r}' \psi_{\uparrow}^{\dagger}(\mathbf{r}) \Delta(\mathbf{r}, \mathbf{r}') \psi_{\downarrow}^{\dagger}(\mathbf{r}') + \psi_{\downarrow}(\mathbf{r}) \Delta^{*}(\mathbf{r}, \mathbf{r}') \psi_{\uparrow}(\mathbf{r}') \quad (5.1) \\
 & + \int \int d\mathbf{r} d\mathbf{r}' \sum_{\alpha,\beta} \Delta_{\alpha,\beta}(\mathbf{r}, \mathbf{r}') \langle \psi_{\alpha}^{\dagger}(\mathbf{r}) \psi_{\beta}^{\dagger}(\mathbf{r}') \rangle
 \end{aligned}$$

Where we define  $\xi(\mathbf{r}) = -\frac{\hbar^2}{2m} \nabla_{\mathbf{r}}^2 - E_F$  as the normal state kinetic energy and  $\Delta_{\alpha,\beta}(\mathbf{r}, \mathbf{r}') = -g(\mathbf{r} - \mathbf{r}') \langle \psi_{\alpha}(\mathbf{r}') \psi_{\beta}(\mathbf{r}) \rangle$  as the superconducting pair potential with  $g(\mathbf{r} - \mathbf{r}')$  acting as the attractive interaction<sup>84</sup>. Note also that these quasiparticle wavefunctions are related to the operator  $c_{\mathbf{k},\alpha}$  used in Section 1.3 by  $\psi_{\alpha}(\mathbf{r}) = \sum_{\mathbf{k}} e^{i\mathbf{k}\cdot\mathbf{r}} c_{\mathbf{k},\alpha}$ . Key to the Bogoliubov-de Gennes approach is that we can introduce some redundancy into the mean-field Hamiltonian by separating

the mean-field Hamiltonian,  $H_{\text{MF}}$ , into particle and hole sectors. Using the anti-commutation relation for fermions,  $\{\psi_\sigma(\mathbf{r}), \psi_{\sigma'}^\dagger(\mathbf{r}')\} = \delta(\mathbf{r} - \mathbf{r}')\delta_{\alpha\beta}$ , on the normal state part of the Hamiltonian  $H_0$ , we get

$$\begin{aligned} H_0 &= \int d\mathbf{r} \sum_{\alpha,\beta} \psi_\alpha^\dagger(\mathbf{r}) \xi_{\alpha,\beta}(\mathbf{r}) \psi_\beta(\mathbf{r}) \\ &= \frac{1}{2} \int d\mathbf{r} \sum_{\alpha,\beta} \left[ \psi_\alpha^\dagger(\mathbf{r}) \xi_{\alpha,\beta}(\mathbf{r}) \psi_\beta(\mathbf{r}) - \psi_\alpha(\mathbf{r}) \xi_{\alpha,\beta}^*(\mathbf{r}) \psi_\beta^\dagger(\mathbf{r}) \right] + \frac{1}{2} \sum_{\alpha,\beta} \int d\mathbf{r} \xi_{\alpha,\beta}(\mathbf{r}) \end{aligned} \quad (5.2)$$

The third line of Eq. 5.1 is made up of expectation values and we therefore ignore it for now. Taking the second line of  $H_{\text{MF}}$ , which we refer to as  $H_S$ , and using the anti-commutation relation,  $\{\psi_\sigma^\dagger(\mathbf{r}), \psi_{\sigma'}^\dagger(\mathbf{r}')\} = 0$  we obtain the following

$$\begin{aligned} H_S &= \frac{1}{2} \left[ \int d\mathbf{r} \psi_\uparrow^\dagger(\mathbf{r}) \Delta(\mathbf{r}) \psi_\downarrow^\dagger(\mathbf{r}) - \psi_\downarrow^\dagger(\mathbf{r}) \Delta(\mathbf{r}) \psi_\uparrow^\dagger(\mathbf{r}) \right. \\ &\quad \left. + \psi_\downarrow(\mathbf{r}) \Delta^*(\mathbf{r}) \psi_\uparrow(\mathbf{r}) - \psi_\uparrow(\mathbf{r}) \Delta^*(\mathbf{r}) \psi_\downarrow(\mathbf{r}) \right] \end{aligned} \quad (5.3)$$

This separation then allows us to easily write the mean-field Hamiltonian in matrix form by making use of a four-component spinor so that we write

$$H_{\text{MF}} = \frac{1}{2} \int d\mathbf{r} \begin{bmatrix} \psi_\uparrow^\dagger(\mathbf{r}) & \psi_\downarrow^\dagger(\mathbf{r}) & \psi_\uparrow(\mathbf{r}) & \psi_\downarrow(\mathbf{r}) \end{bmatrix} H_{\text{BdG}}(\mathbf{r}) \begin{bmatrix} \psi_\uparrow(\mathbf{r}) \\ \psi_\downarrow(\mathbf{r}) \\ \psi_\uparrow^\dagger(\mathbf{r}) \\ \psi_\downarrow^\dagger(\mathbf{r}) \end{bmatrix} + K \quad (5.4)$$

We have several constants now, the third line of Eq. 5.1 and the rightmost term of Eq. 5.2. These constants only act to modify the ground state energy so we absorb them into the variable  $K$  above and, from now on, will ignore these terms. This new Hamiltonian  $H_{\text{BdG}}$  is the Bogoliubov-de Gennes Hamiltonian and it is a  $4 \times 4$  matrix due to the spin and electron-hole degrees of freedom. We write it explicitly below making use of the Pauli matrices  $\sigma_i$  where we define  $\sigma_0$  as the two-by-two identity matrix  $\sigma_0 = I_{2 \times 2}$ .

$$H_{\text{BdG}}(\mathbf{r}) = \begin{bmatrix} \xi(\mathbf{r})\sigma_0 & \Delta(\mathbf{r})i\sigma_2 \\ -\Delta^*(\mathbf{r})i\sigma_2 & -\xi^*(\mathbf{r})\sigma_0 \end{bmatrix} \quad (5.5)$$

This Hamiltonian is clearly not diagonalized but it conveniently separates our electron and hole states. To diagonalize this Hamiltonian we must find some unitary matrix  $U$  such that

$$U^\dagger H_{\text{BdG}} U = \begin{bmatrix} E_n & 0 & 0 & 0 \\ 0 & E_n & 0 & 0 \\ 0 & 0 & -E_n & 0 \\ 0 & 0 & 0 & -E_n \end{bmatrix} \quad (5.6)$$

Here  $E_n$  are the new energy eigenvalues of the single-particle or Bogoliubov quasiparticle states. This unitary matrix is just the Bogoliubov transformation we saw previously, written in matrix form. It transforms the normal state quasiparticle spinor to a spinor of Bogoliubov quasiparticles

$$\begin{bmatrix} \psi_\uparrow(\mathbf{r}) \\ \psi_\downarrow(\mathbf{r}) \\ \psi_\uparrow^\dagger(\mathbf{r}) \\ \psi_\downarrow^\dagger(\mathbf{r}) \end{bmatrix} = U \begin{bmatrix} \gamma_n \\ \gamma_n \\ \gamma_n^\dagger \\ \gamma_n^\dagger \end{bmatrix} = \sum_{n>0} \begin{bmatrix} u_\uparrow^n & 0 & 0 & -v_\uparrow^{n*} \\ 0 & u_\downarrow^n & v_\downarrow^{n*} & 0 \\ 0 & -v_\uparrow^n & u_\uparrow^{n*} & 0 \\ v_\downarrow^n & 0 & 0 & u_\downarrow^{n*} \end{bmatrix} \begin{bmatrix} \gamma_n \\ \gamma_n \\ \gamma_n^\dagger \\ \gamma_n^\dagger \end{bmatrix} \quad (5.7)$$

Applying this transformation to the mean-field Hamiltonian gets us to the desired form for the effective Hamiltonian

$$H_{\text{eff.}} = \sum_n E_n \gamma_n^\dagger \gamma_n + E_g \quad (5.8)$$

where  $E_g$  is the ground state energy. This is the same result as we derived in Eq. 1.34. While previously we saw that Eq. 1.29 fixed the form of our weighting functions, now we look in more depth at how this diagonalization fixes the relationship between the weighting functions. This relationship then determines the Bogoliubov-de Gennes equations. To see this explicitly we first calculate the commutator of the mean-field Hamiltonian with the normal state

quasiparticle operators.

$$[\psi_{\uparrow}(\mathbf{r}), H_{\text{MF}}] = \int d\mathbf{r} \xi_{\uparrow}(\mathbf{r}) \psi_{\uparrow}(\mathbf{r}) + \int d\mathbf{r}' \Delta(\mathbf{r}, \mathbf{r}') \psi_{\downarrow}^{\dagger}(\mathbf{r}') \quad (5.9a)$$

$$[\psi_{\downarrow}(\mathbf{r}), H_{\text{MF}}] = \int d\mathbf{r} \xi_{\downarrow}(\mathbf{r}) \psi_{\downarrow}(\mathbf{r}) - \int d\mathbf{r}' \Delta(\mathbf{r}', \mathbf{r}) \psi_{\uparrow}^{\dagger}(\mathbf{r}') \quad (5.9b)$$

$$[\psi_{\uparrow}^{\dagger}(\mathbf{r}), H_{\text{MF}}] = - \int d\mathbf{r} \xi_{\uparrow}^*(\mathbf{r}) \psi_{\uparrow}^{\dagger}(\mathbf{r}) - \int d\mathbf{r}' \Delta^*(\mathbf{r}, \mathbf{r}') \psi_{\downarrow}(\mathbf{r}') \quad (5.9c)$$

$$[\psi_{\downarrow}^{\dagger}(\mathbf{r}), H_{\text{MF}}] = - \int d\mathbf{r} \xi_{\downarrow}^*(\mathbf{r}) \psi_{\downarrow}^{\dagger}(\mathbf{r}) + \int d\mathbf{r}' \Delta^*(\mathbf{r}', \mathbf{r}) \psi_{\uparrow}(\mathbf{r}') \quad (5.9d)$$

We can calculate the same quantities by replacing the normal state operators by Eq. 5.7, calculating  $[\psi_{\alpha}(\mathbf{r}), H_{\text{eff}}]$  and  $[\psi_{\alpha}^{\dagger}(\mathbf{r}), H_{\text{eff}}]$ .

$$[\psi_{\uparrow}(\mathbf{r}), E_n \gamma_n^{\dagger} \gamma_n + E_g] = E_n u_{\uparrow}^n \gamma_n - E_n v_{\uparrow}^{n*} \gamma_n^{\dagger} \quad (5.10a)$$

$$[\psi_{\downarrow}(\mathbf{r}), E_n \gamma_n^{\dagger} \gamma_n + E_g] = E_n u_{\downarrow}^n \gamma_n - E_n v_{\downarrow}^{n*} \gamma_n^{\dagger} \quad (5.10b)$$

$$[\psi_{\uparrow}^{\dagger}(\mathbf{r}), E_n \gamma_n^{\dagger} \gamma_n + E_g] = -E_n u_{\uparrow}^{n*} \gamma_n^{\dagger} - E_n v_{\uparrow}^n \gamma_n \quad (5.10c)$$

$$[\psi_{\downarrow}^{\dagger}(\mathbf{r}), E_n \gamma_n^{\dagger} \gamma_n + E_g] = -E_n u_{\downarrow}^{n*} \gamma_n^{\dagger} + E_n v_{\downarrow}^n \gamma_n \quad (5.10d)$$

Upon substitution of Eq. 5.7 into Eq. 5.9 and by comparison with Eq. 5.10 we arrive at the Bogoliubov-de Gennes (BdG) equations

$$\int d\mathbf{r} \xi_{\uparrow}(\mathbf{r}) u_{\uparrow}^n(\mathbf{r}) + \int d\mathbf{r}' \Delta(\mathbf{r}, \mathbf{r}') v_{\downarrow}^n(\mathbf{r}') = E_n u_{\uparrow}^n(\mathbf{r}) \quad (5.11a)$$

$$\int d\mathbf{r} \xi_{\downarrow}(\mathbf{r}) u_{\downarrow}^n(\mathbf{r}) + \int d\mathbf{r}' \Delta(\mathbf{r}', \mathbf{r}) v_{\uparrow}^n(\mathbf{r}') = E_n u_{\downarrow}^n(\mathbf{r}) \quad (5.11b)$$

$$\int d\mathbf{r}' \Delta^*(\mathbf{r}, \mathbf{r}') u_{\downarrow}^n(\mathbf{r}') - \int d\mathbf{r} \xi_{\uparrow}^*(\mathbf{r}) v_{\uparrow}^n(\mathbf{r}) = E_n v_{\uparrow}^n(\mathbf{r}) \quad (5.11c)$$

$$\int d\mathbf{r}' \Delta^*(\mathbf{r}', \mathbf{r}) u_{\uparrow}^n(\mathbf{r}') - \int d\mathbf{r} \xi_{\downarrow}^*(\mathbf{r}) v_{\downarrow}^n(\mathbf{r}) = E_n v_{\downarrow}^n(\mathbf{r}) \quad (5.11d)$$

We see clearly that the electron-like coefficients,  $u^n$  are coupled to the hole-like coefficients,  $v^n$  and vice versa, indicating the hybridization which results from the superconducting pair potential. We can then finally write these equations in matrix form

$$\sum_{n>0} H_{\text{BdG}} \Psi^n = \sum_{n>0} E_n \Psi^n \quad (5.12)$$

where  $\Psi^n = (u_{\uparrow}^n(\mathbf{r}), u_{\downarrow}^n(\mathbf{r}), v_{\uparrow}^n(\mathbf{r}), v_{\downarrow}^n(\mathbf{r}))^T$  is the spinor of these weighting factors. Thus, we have derived an eigenequation in which the eigenvector de-

scribes the dynamics of Bogoliubov quasiparticles. Notably Eq. 5.11 features only the positive energy solutions. In reality, we derive eight BdG equations through the method above however, due to the strict particle-hole symmetry which we have introduced, the positive and negative energy solutions are related. If  $\Psi_1^n$  is an eigenvector of Eq. 5.12 with eigenvalue  $E_n$  then the eigenvector  $\Psi_2^n = (-v_\uparrow^{n*}, v_\downarrow^{n*}, -u_\uparrow^{n*}, u_\downarrow^{n*})^T$ , when used in Eq. 5.12, has eigenvalues  $-E_n$ .

### 5.3 Andreev Reflection

It should now seem clear that the superconducting pair potential certainly mixes electron- and hole-like quasiparticles around the superconducting energy gap within a bulk superconductor. At the same time, a gap forms at the Fermi surface which, one would expect, prevents incoming electrons from entering into the superconductor for energies  $E < |\Delta(\mathbf{r})|$ . In reality, the condensate of Cooper pairs, has a finite phase  $\phi$ . The incoming electron or electron-like quasiparticle, encountering the pair potential at the interface acquires phase  $\phi$  and finds a partner within the metal with the same phase. These two in-phase particles then condense in the bulk superconductor. While this process occurs, the partner quasiparticle's empty state is sent backwards into the normal metal as a hole.

Now let's consider a concrete example of this mechanism. We proceed using the approach of BTK<sup>85</sup> and consider the boundary conditions of the quasiparticle wavefunctions  $u^n$  and  $v^n$  from the BdG equations. We consider a simple scenario, presented in Fig. 5.1, in which quasiparticles of a normal metal are moving to the right, in the positive direction, with wavevector  $k_N = (k_N^+ \cos \theta, k_N^+ \sin \theta) = (k_{Nx}^+, k_{Ny}^+)$  and approach the specular surface of a superconductor at an angle  $\theta$  with the surface normal. We assume there is some potential barrier between the metal and superconductor and treat it as a delta function

$$V(x) = I\delta(x) \tag{5.13}$$

In the metal, there are then three possible states, the incident electron-like quasiparticle (ELQ) with wavevector  $k_N^+ = (-k_{Nx}^+, k_{Ny}^+)$ , a reflected ELQ with wavevector  $k_N^+ = (-k_{Nx}^+, k_{Ny}^+)$ , and an Andreev reflected hole-like quasiparticle (HLQ) with wavevector  $k_N^- = (k_{Nx}^-, k_{Ny}^-)$ . We write the wavefunction in the

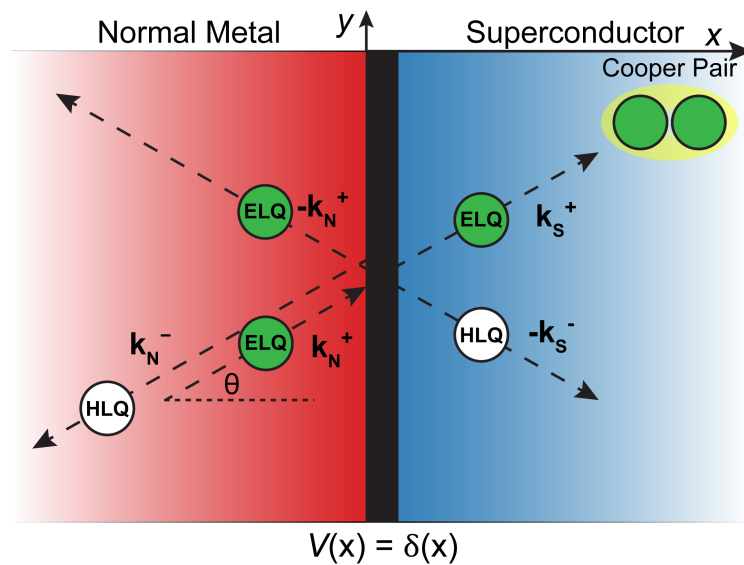


Figure 5.1: Quasiclassical trajectory of an electron-like quasiparticle (ELQ) incident to the surface of a superconductor with a potential barrier  $V(x) = \delta(x)$  between the two materials. The incident ELQ approaches the surface with momentum  $k_N^+$  it may reflect from the surface as an ELQ or HLQ with the former referring to normal reflection and the latter Andreev reflection. Transmission into the superconductor by Andreev reflection contributes a Cooper pair into the superconducting condensate.

metal, which we consider to be on the left or in the space  $x < 0$ , as

$$\begin{bmatrix} u(r) \\ v(r) \end{bmatrix}_L = \begin{bmatrix} 1 \\ 0 \end{bmatrix} e^{ik_N^+ r} + a(E, \theta) \begin{bmatrix} 0 \\ 1 \end{bmatrix} e^{ik_N^- r} + b(E, \theta) \begin{bmatrix} 1 \\ 0 \end{bmatrix} e^{-k_N^+ r} \quad (5.14)$$

where  $a(E, \theta)$  and  $b(E, \theta)$  weight the probability of the reflected ELQ and HLQ respectively. Here the wavevector of the incoming and reflected quasiparticle is determined from the energy dispersion in the material. For the normal metal, we then have the following, where the positive sign is associated with electrons and the negative sign with holes.

$$k_N^\pm = k_F \pm \frac{mE}{\hbar^2 k_F} \quad (5.15)$$

It's important to note that the group velocity of holes is opposite to that of electrons for the same wavevector  $k$ , it is therefore negative in the x-direction for any  $k > 0$ .

In the superconductor we have only two possible states, the quasiparticle is transmitted with either electron-like or hole-like character. In the right hand space,  $x > 0$  we therefore have

$$\begin{bmatrix} u(r) \\ v(r) \end{bmatrix}_R = c(E, \theta) \begin{bmatrix} u_+ e^{i\phi_+} \\ v_+ \end{bmatrix} e^{ik_S^+ r} + d(E, \theta) \begin{bmatrix} v_- e^{i\phi_-} \\ u_- \end{bmatrix} e^{-ik_S^- r} \quad (5.16)$$

Here the phase term  $\phi$  is the phase of the superconducting order parameter which we divide into the phase in the positive and negative directions  $\phi_\pm$  to prepare for unconventional pairing. Again the wavevectors of these eigenvectors are modified from the Fermi wavevector this time using the superconducting dispersion

$$k_S^\pm = k_F \pm \frac{m\sqrt{E^2 - |\Delta(\mathbf{k}_\pm)|^2}}{\hbar^2 k_F} \quad (5.17)$$

In reality, the energy of these quasiparticles is very close to the Fermi energy as the gap forms in a small range around the Fermi level,  $E_F \gg E$ . The incident angles are therefore all approximately equal  $k_{Nx}^+ \approx k_{Nx}^- \approx k_{Nx}^+ \approx k_{Sx}^+ \approx k_{Sx}^- \approx k_F \cos \theta$ . This has important consequences, mainly that the Andreev reflected HLQ follows the incident path of the metal's ELQ. This behaviour is referred to as retro-reflectivity. We also note that the coherence factors themselves  $u_\pm$

and  $v_{\pm}$  are defined using the superconducting dispersion

$$u_{\pm}^2 = \frac{1}{2} \left( 1 + \frac{\sqrt{E^2 - |\Delta(\mathbf{k})_{\pm}|^2}}{E} \right) \quad (5.18a)$$

$$v_{\pm}^2 = \frac{1}{2} \left( 1 - \frac{\sqrt{E^2 - |\Delta(\mathbf{k})_{\pm}|^2}}{E} \right) \quad (5.18b)$$

Solutions to the BdG equations must then obey the boundary conditions of the quasiparticle wavefunctions at the interface  $x = 0$ , particularly they must be continuous

$$\begin{bmatrix} u(r) \\ v(r) \end{bmatrix}_{x=0}^L = \begin{bmatrix} u(r) \\ v(r) \end{bmatrix}_{x=0}^R \quad (5.19)$$

and their derivatives in the incident direction,  $\partial u(r)/\partial x = u'(r)$  and  $\partial v(r)/\partial x = v'(r)$  must satisfy

$$\begin{bmatrix} u'(r) \\ v'(r) \end{bmatrix}_{x=0}^R - \begin{bmatrix} u'(r) \\ v'(r) \end{bmatrix}_{x=0}^L = \frac{2mI}{\hbar^2} \begin{bmatrix} u(r) \\ v(r) \end{bmatrix}_{x=0} \quad (5.20)$$

Defining a measure of the junction impedance  $Z = \frac{mI}{\hbar^2 k_F \cos \theta}$  and solving the above equations given the constraints leads to expressions for the reflection and transmission coefficients<sup>86</sup>

$$a(E, \theta) = \frac{(e^{-i\phi_+})u_-v_+}{(1 + Z^2)u_+u_- - Z^2v_+v_-e^{(i\phi_- - i\phi_+)}} \quad (5.21a)$$

$$b(E, \theta) = \frac{Z(i + Z)[v_+v_-e^{(i\phi_- - i\phi_+)} - u_+u_-]}{(1 + Z^2)u_+u_- - Z^2v_+v_-e^{(i\phi_- - i\phi_+)}} \quad (5.21b)$$

$$c(E, \theta) = \frac{(1 - iZ)u_-}{(1 + Z^2)u_+u_- - Z^2v_+v_-e^{(i\phi_- - i\phi_+)}} \quad (5.21c)$$

$$d(E, \theta) = \frac{e^{(i\phi_- - i\phi_+)}iZv_+}{(1 + Z^2)u_+u_-e^{(i\phi_- - i\phi_+)}} \quad (5.21d)$$

Now that we have these coefficients we can study the effects on the tunnelling conductance, an important variable for STM. Once again we follow the approach of BTK<sup>85</sup> and express the conductance using these transmission and reflection amplitudes. For a single tunnelling channel, in the absence of scattering, the conductance is quantized in units  $2e^2/\hbar$ , as per Landauer<sup>87</sup>. We will consider the normalized conductance, in which we study the variation

in the conductance from the normal state, we therefore exclude this unit of conductance from the below. We can derive the conductance spectrum from the reflection and transmission coefficients as

$$\sigma(E, \theta) = \frac{\sigma_S(E, \theta)}{\sigma_N} = \frac{1 + R_a(E, \theta) - R_b(E, \theta)}{\sigma_N} \quad (5.22)$$

This conductance is increased by Andreev reflection  $R_a(E, \theta)$  and decreased by normal reflection  $R_b(E, \theta)$  as expected. These  $R(E, \theta)$  come directly from the transmission and reflection coefficients

$$R_a(E, \theta) = |a(E, \theta)|^2 = \frac{\sigma_N^2 |\Gamma_+|^2}{|1 + (\sigma_N - 1)\Gamma_+\Gamma_- e^{i\phi_- - i\phi_+}|^2} \quad (5.23a)$$

$$R_b(E, \theta) = |b(E, \theta)|^2 = \frac{(1 - \sigma_N)|1 - \Gamma_+\Gamma_- e^{i\phi_- - i\phi_+}|^2}{|1 + (\sigma_N - 1)\Gamma_+\Gamma_- e^{i\phi_- - i\phi_+}|^2} \quad (5.23b)$$

$$\Gamma_{\pm} = \frac{E - \Omega_{\pm}}{|\Delta_{\pm}|} \quad \sigma_N = \frac{1}{1 + Z}$$

The normalized conductance  $\sigma(E, \theta)$  is then given by

$$\sigma(E, \theta) = \frac{1 + \sigma_N |\Gamma_+|^2 + (\sigma_N - 1) |\Gamma_- \Gamma_+|^2}{|1 + (\sigma_N - 1)\Gamma_+\Gamma_- e^{i\phi_- - i\phi_+}|^2} \quad (5.24)$$

With the large number of variables present we will fix the incident angle at  $\theta = 0$  and study the effect of finite barrier strengths  $Z$  and order parameter phase  $\phi$ . We first consider the case of an  $s$ -wave superconductor, so that  $\phi_+ = \phi_- = \phi_0$ ,  $\Delta_+ = \Delta_- = \Delta_0$  and we arbitrarily set the barrier strength  $Z$  to be  $Z = 0, 1, 5$ . We then plot Eq. 5.24 in Fig. 5.2a for these values of  $Z$ . The first thing to notice is that, for both Fig. 5.2a and b, the normalized conductance  $\sigma(E) = \sigma_S(E)/\sigma_N$  approaches one for energies  $E > \Delta_0$  as expected. Increasing the barrier strength corresponds to increasing the junction resistance of the NIS junction. For a transparent junction  $Z = 0$  we observe perfect Andreev reflection, indicated by a normalized conductance of  $\sigma(E < \Delta_0) = 2$  at energies within the superconducting gap. Increasing  $Z$ , or decreasing the junction resistance, decreases the sub-gap conductance until it reaches zero for large  $Z$ . Under the same conditions, coherence peaks develop at the gap edge due to resonant Andreev tunnelling resulting from the divergence of  $E^2 - |\Delta_0|^2$  terms in the transmission coefficient. The conductance spectrum then closely

resembles the BCS DOS as seen in Fig. 1.1c.

In our derivation, we made clear the distinction between the superconducting order parameter and phase in the positive and negative directions. We did so to capture the effects of unconventional pairing, that is an order parameter whose phase and/or magnitude is dependent on direction.  $\text{UTe}_2$  is considered to be a  $p$ -wave superconductor which is necessarily odd-parity in the orbital part of its wavefunction, thus for any direction, which is not directly aligned with its nodes, the phase difference between the positive and negative direction is  $\pi$ . We manually implement this phase difference in Fig. 5.2b by setting  $\phi_+ = 0$  and  $\phi_- = \pi$  and  $\Delta_+ = -\Delta_-$ . Thus we model a normal metal - insulator -  $p$ -wave superconductor (NIP) junction. The resulting conductance spectrum is drastically different to the NIS case. For  $Z = 0$ , we once again observe perfect Andreev reflection within the superconducting energy gap. However, for finite  $Z$  we obtain smaller and smaller terms in the denominator of Eq. 5.24 around zero energy. The result corresponds to a bound state formed from constructive interference of Bogoliubov quasiparticles at the interface between the insulator and  $p$ -wave superconductor. Andreev tunnelling to this bound state from the normal metal side is a resonant process thus a zero-bias conductance peak (ZBCP) appears for large junction resistance or large potential barrier  $Z$ .

## 5.4 Andreev Bound States

Despite over 50 years of research<sup>88</sup> Andreev bound states (ABSs) remain highly relevant in modern condensed matter research due to their presence on certain surfaces of  $d$ -wave superconductors<sup>89</sup>, their connection with the topological surface states of topological superconductors<sup>90</sup>, and the formation of Majorana zero modes. As we've seen, they can be identified by the appearance of a ZBCP which can be measured even with large potential barriers to transport. We will now see that ABSs are not only obtained by transport between two or more materials, but an intrinsic feature of an odd-parity superconductor which exists independently of transport phenomena. Kulik was the first to solve the problem of Andreev transport in a superconductor - normal metal - superconductor (SNS) junction and thus the first to discover the mechanism which forms an ABS<sup>88</sup>. In Fig. 5.3a we see how a cycle of Andreev reflections may produce an ABS between two  $s$ -wave superconductors. The incident ELQ

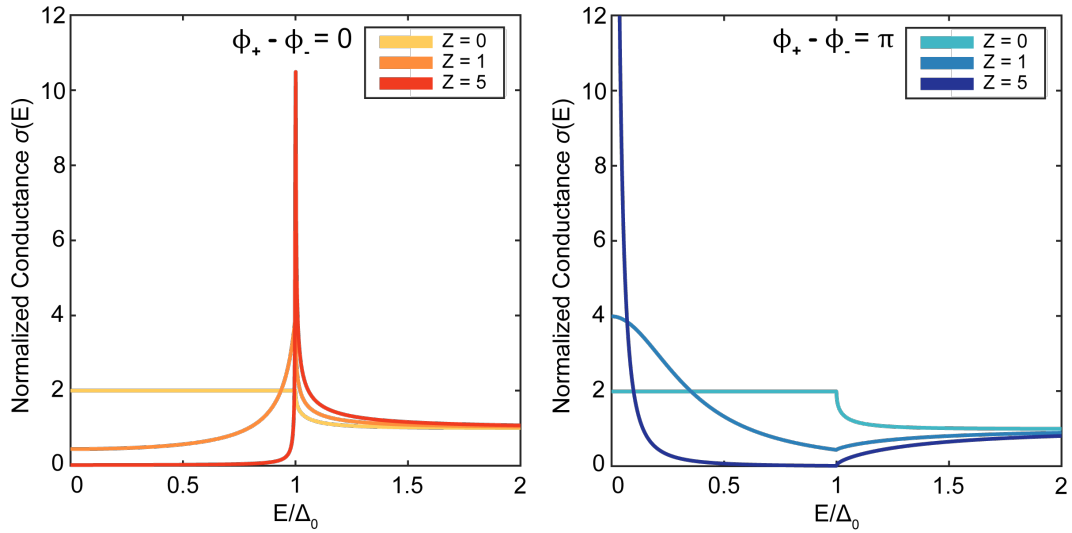


Figure 5.2: **a.** Normalized conductance  $\sigma(E)$  from Eq. 5.24 in a normal metal - insulator -  $s$ -wave superconductor (NIS). For any  $Z$  the conductance for energies outside the gap,  $E \gg \Delta_0$ , tends to the normal state conductance  $\sigma(E) = \sigma_S(E)/\sigma_N = 1$ . For  $Z = 0$ , the insulating barrier is turned off and there is perfect Andreev reflection in the superconducting gap  $\sigma(E < \Delta_0) = 2$ . For finite  $Z$ , coherence peaks are observed at  $E = \Delta_0$  and the in-gap conductance is reduced to zero for large potential barriers. **b.** Normalized conductance  $\sigma(E)$  from Eq. 5.24 in an  $p$ -wave superconductor - insulator - normal metal junction. For  $Z = 0$ , we observe perfect Andreev reflection within the energy gap as before. However, for finite  $Z$ , a zero-bias conductance peak (ZBCP) is universally observed. This ZBCP is the result of the formation of a bound state at the surface layer of the  $p$ -wave superconductor. This bound state is formed at zero energy  $E_b = 0$ , consequently tunnelling electrons flow, via the bound state, in a process of resonant Andreev tunnelling

from the metal strikes the superconductor on the right and retro-reflects as a HLQ. The HLQ traverses the normal metal, strikes the left superconductor and is retro-reflected as an ELQ. At each of these reflections the quasiparticle “picks up” some phase from the reflection process but also from the bulk superconductor. If the phase difference between these superconductors is just right one can see how constructive interference of these cyclically reflected quasiparticles may produce a bound state at energies  $E < |\Delta|$ . The condition required to generate an ABS in this setup is analogous to Bohr’s quantum condition for atomic orbits, the phase shift along this closed path of reflections must be a multiple of  $2\pi$ <sup>86</sup>.

$$-\arctan\left(\frac{\sqrt{|\Delta_R|^2 - E_b^2}}{E_b}\right) - \arctan\left(\frac{\sqrt{|\Delta_L|^2 - E_b^2}}{E_b}\right) \pm \phi + \frac{2d_N E}{\hbar v_F} = 2n\pi \quad (5.25)$$

Here  $|\Delta_{L/R}|$  is the energy gap of the left and right superconductor,  $E_b$  is the energy of the bound state,  $\phi = \phi_L - \phi_R$  is the phase difference between the two superconductors, and  $n$  is an integer. The term  $\frac{d_N E}{\hbar v_F}$  is the phase acquired moving in one direction through the metal, where  $d_N$  is the thickness of the metal layer and  $v_F$  is the Fermi velocity. Thus, the above expression is a sum of the phase change due to Andreev reflections (the first two terms), the phase change from the pair potential, and the phase acquired in the normal metal region. In Fig 5.3b we plot the bound state energy versus the phase difference between the left and right superconductors. Similar to the zero energy state we observed in the previous section we find a zero energy bound state for phase difference  $\phi = \phi_L - \phi_R = \pi$ .

To see that these bound states are independent of transport phenomena we consider the junction of a normal metal and superconductor. Again, we can consider the process of cyclic Andreev reflections at the interface, these cyclic reflections produce a bound state at energy  $E_b$  as long as the below condition is satisfied.

$$1 - \exp\left(\frac{2id_N}{\hbar v_F}\right) \Gamma_{+|E=E_b} \Gamma_{-|E=E_b} \exp(\pm i(\phi_- - \phi_+)) = 0 \quad (5.26)$$

Where we set  $\Gamma_{\pm} = \frac{E_b - \sqrt{E_b^2 - |\Delta_{\pm}|^2}}{|\Delta_{\pm}|}$ . We can then see that a bound state can be formed even when the thickness of the normal metal is zero,  $d_N = 0$ . Thus the

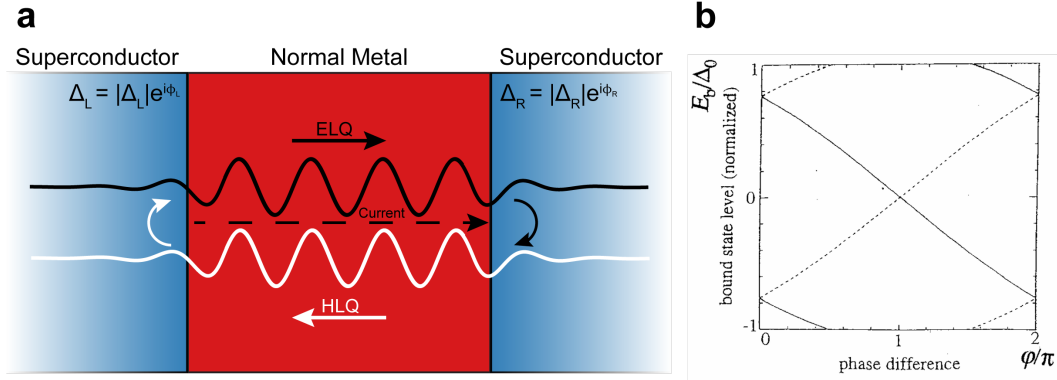


Figure 5.3: **a.** Illustration of the resonant reflection process producing an Andreev bound state in a superconductor - normal metal - superconductor (SNS) junction. **b.** Andreev bound state energy versus phase for an SNS junction with two *s*-wave superconductors. A zero-energy bound state is observed whenever the phase difference between the superconductors  $\phi = \phi_L - \phi_R = \pi$ . Figure reproduced from Ref. [86]

bound state condition becomes

$$\Gamma_+|_{E=E_b}\Gamma_-|_{E=E_b}\exp(\pm i(\phi_- - \phi_+)) = 0 \quad (5.27)$$

Which is fulfilled for any pair potential which changes sign by  $\pi$  in the direction perpendicular to its surface. Thus this process of cyclic Andreev reflections produces a bound state independent of an adjacent material, it is intrinsic to the surface of an odd-parity superconductor.

## 5.5 Andreev Bound State Topology

In recent decades the study of topological phases of matter, materials supporting edge/surface states protected by topological invariants, has expanded enormously. While initially applied to the study of the quantum Hall effect<sup>91</sup>, the field has since grown to include topological insulators<sup>92</sup>, topological semi-metals<sup>93</sup>, and even topological superconductors<sup>94</sup>. Topological insulators are now widely classified and readily grown in labs around the world. While the study of topological semi-metals is more recent there are many compounds which host their topologically non-trivial surface states<sup>95</sup>. However, despite the significant demand for topological superconductors we have only a handful of promising candidates. The superfluid phases of <sup>3</sup>He are the only firmly established examples of topologically non-trivial Cooper pair condensates<sup>96</sup>.

		TRS	PHS	SLS	$d=1$	$d=2$	$d=3$
Standard (Wigner-Dyson)	A (unitary)	0	0	0	-	$\mathbb{Z}$	-
	AI (orthogonal)	+1	0	0	-	-	-
	AII (symplectic)	-1	0	0	-	$\mathbb{Z}_2$	$\mathbb{Z}_2$
Chiral (sublattice)	AIII (chiral unitary)	0	0	1	$\mathbb{Z}$	-	$\mathbb{Z}$
	BDI (chiral orthogonal)	+1	+1	1	$\mathbb{Z}$	-	-
	CII (chiral symplectic)	-1	-1	1	$\mathbb{Z}$	-	$\mathbb{Z}_2$
BdG	D	0	+1	0	$\mathbb{Z}_2$	$\mathbb{Z}$	-
	C	0	-1	0	-	$\mathbb{Z}$	-
	DIII	-1	+1	1	$\mathbb{Z}_2$	$\mathbb{Z}_2$	$\mathbb{Z}$
	CI	+1	-1	1	-	-	$\mathbb{Z}$

Figure 5.4: The Atland-Zirnbauer (AZ) (Ten Fold Way) classification scheme for random matrices<sup>99,100</sup> which defines topological classes based upon fundamental symmetries of the bulk Hamiltonian including time-reversal symmetry (TRS), particle-hole symmetry (PHS), and chiral or sublattice symmetry (SLS). The absence of symmetries is denoted by 0 and the presence of symmetries is denoted by +1 or -1 depending on whether the symmetry operator squares to +1 or -1. The symbol  $\mathbb{Z}$  is the integer topological number related to the number of edge/surface states. The symbol  $\mathbb{Z}_2$  is the topological index in time-reversal conserving systems and coincides with the parity of the spin Chern number<sup>94</sup>.

A necessary ingredient for topological superconductivity is the complex phase winding of the superconducting order parameter in momentum space which is, most simply, realized in odd-parity  $p$ -wave pairing as that in superfluid  $^3\text{He}$ . Our subject of study  $\text{UTe}_2$  is therefore a prime candidate to host topological superconductivity.

The defining characteristic of these topological phases of matter is the appearance of edge/surface states expected from the discontinuity of the topological invariant at the edge/surface, this is the so-called bulk-boundary correspondence<sup>97</sup>. In several instances these edge/surface states can be very exotic, as is the case for the fractionalized charge measured in the fractional quantum Hall effect<sup>98</sup>. In superconductors, these surface states are zero-energy Bogoliubov quasiparticles confined in Andreev bound states. These bound states can have various forms of dispersion which derive from the various topological numbers used for their classification.

The topological invariants used in all topological systems depend upon critical symmetries of the bulk band structure and, in the case of topological su-

perconductors, the structure of the order parameter<sup>96</sup>. A general classification system exists, the Atland-Zimbauer scheme otherwise known as the ten-fold way<sup>100</sup>. In this scheme superconductors are classified by time-reversal symmetry (TRS), particle-hole symmetry (PHS), and chiral symmetry (a combination of TRS and PHS). There are then ten possible ways that the BdG Hamiltonian  $H_{\text{BdG}}$  of a superconductor can be classified.  $H_{\text{BdG}}$  could lack TRS or PHS (denoted by 0 in Table 5.4), or the TRS and PHS operators could square to +1 or -1. There are then 9 ways  $H_{\text{BdG}}$  could transform under TRS and PHS, the tenth is that  $H_{\text{BdG}}$  may lack TRS or PHS but maintain chiral symmetry  $\Gamma = i\mathcal{TC}$ . Here the symmetry operator for PHS is defined as  $\mathcal{C} = \tau_x K$  such that  $\mathcal{C}^2 = 1$  and where  $\tau_x$  is the first Pauli matrix acting on particle-hole space and  $K$  is the complex conjugate operator. A similar expression can be used for the TRS symmetry operator  $\mathcal{T} = i\sigma_y K$  so that  $\mathcal{T}^2 = -1$  where  $\sigma_y$  acts on the spin space. A  $H_{\text{BdG}}$  which preserves PHS is then one which acts as

$$\mathcal{C}H_{\text{BdG}}(\mathbf{k})\mathcal{C}^{-1} = -H_{\text{BdG}}(-\mathbf{k}) \quad (5.28)$$

and one which preserves TRS is

$$\mathcal{T}H_{\text{BdG}}(\mathbf{k})\mathcal{T}^{-1} = H_{\text{BdG}}(-\mathbf{k}) \quad (5.29)$$

Notably superconductors and superfluids generally preserve PHS in the vicinity of the gap due to the particle-hole mixing which results from the pair potential.

This ten fold way classification system works exceptionally well for “strong” topological superconductors, that is superconductors which are fully gapped with an odd-parity gap function. Such states fulfill the definition of a topological phase, that it is disconnected from any other gapped phase. This ensures that the gap must close in order to change the topological properties of the phase. An example of such a topological superfluid phase is that of the B phase of  $^3\text{He}$  which has a d-vector of the form  $d(\mathbf{k}) \propto (k_x, k_y, k_z)$ <sup>96</sup>. This state has TRS (-1) and PHS (+1) and thus has chiral symmetry.  $H_{\text{BdG}}(\mathbf{k})$  anti-commutes with the chiral operator  $\{\Gamma, H_{\text{BdG}}(\mathbf{k})\} = 0$ . This state is therefore categorized in the DIII classification of Table 5.4 and has an associated 3D topological winding number  $w_{3D}$  which guarantees the presence of Andreev bound states on all surfaces. Such a state is similar to the proposed  $A_u$  state of  $\text{UTe}_2$  if it hosts a spherical Fermi surface component. The Andreev bound states associated with these topological surface states have linear, Dirac-like

dispersion and vanishing density of states at zero-energy. An illustration of this dispersion is shown in Fig. 5.5a.

Nodal topological superconductors are possible however these states not fully gapped and are therefore considered “weak” topological superconductors. Again, we can look to the superfluid phases of  $^3\text{He}$  for guidance in topological classification. The A-phase of this superfluid has a d-vector of the form  $d(\mathbf{k}) \propto (k_x + ik_y, 0, 0)$ . It conserves PHS but breaks TRS. Such a topological superfluid/superconducting state is generally referred to as a chiral superfluid/superconductor and in this case  $^3\text{He-A}$  is a Weyl superconductor, hosting zero energy Weyl surface states<sup>96</sup>. Classifying such a state then requires reducing the dimensions of the Brillouin zone (BZ) by the dimension of the nodal points. For the case of the A-phase we consider the topological classification with co-dimension  $p = d_{BZ} - 1$ . Thus, for a superfluid phase with nodes aligned along the  $k_z$  axis we consider the Hamiltonian  $H_{\text{BdG}}(\mathbf{k}_{\parallel}, k_z)$  and integrate the Berry curvature  $\mathbf{F}(\mathbf{k}) = \nabla_{\mathbf{k}} \times \mathbf{A}(\mathbf{k})$  at each two-dimensional (2D) slice

$$N_{k_z} = \frac{1}{2\pi} \int dk_x dk_y F_z(\mathbf{k}) \quad (5.30)$$

where the Berry curvature is the curl of the Berry connection or Berry vector potential  $\mathbf{A}(\mathbf{k}) = i\langle u_n(\mathbf{k}) | \nabla_{\mathbf{k}} u_n(\mathbf{k}) \rangle$ . This number  $N_{k_z}$  is the first topological invariant, the TKKN number or first Chern number. This number can only be defined for a three-dimensional nodal system by carrying out this dimensional reduction, this is why we refer to this topological phase as “weak”. Carrying out this integral we obtain  $N_{k_z} = +1$  for  $|k_z| < k_F$  and  $N_{k_z} = 0$  for any  $|k_z| > k_F$ . Each slice in the topologically non-trivial region of momentum space can then be considered a 2D fully gapped chiral superconductor with a topological surface state forming within this gap. The resulting surface state of the A-phase then has a one-dimensional arc state with flat dispersion. It is made up of the zero energy states of each slice connecting the nodes as they project to the 2D surface BZ. Fig. 5.5b presents the zero energy arc states for a TRS conserving, topological, nodal superconductor. It features two degenerate, linearly dispersing, surface bands. A chiral superconductor/superfluid, like  $^3\text{He-A}$ , would host only one of these surface states on a given surface due to the broken TRS. These flat Andreev bound states provide a large contribution to the density of states (DOS) at zero energy. This large DOS can then produce a ZBCP in tunnelling spectroscopy. A superconducting state similar to the A-phase of  $^3\text{He}$  is also possible in  $\text{UTe}_2$  depending on the Fermi surface

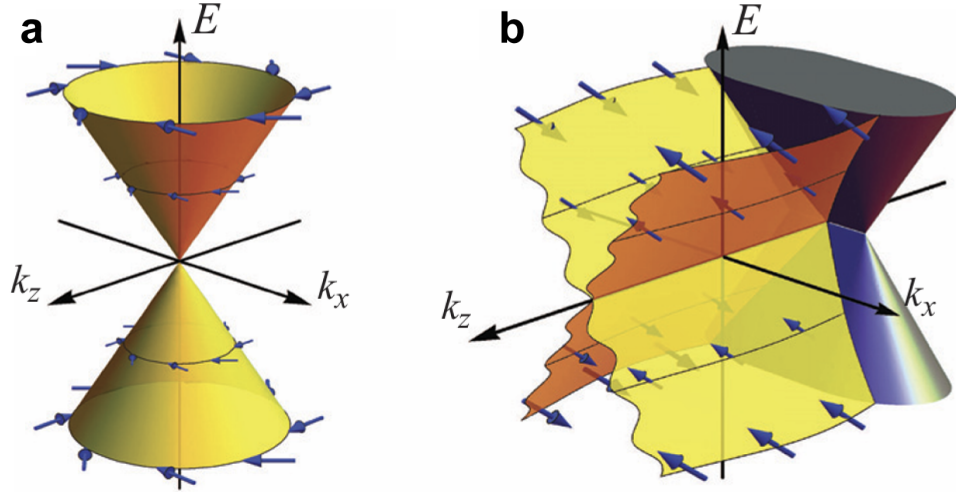


Figure 5.5: **a.** The Dirac-like dispersion of topological surface states seen in fully-gapped topological superconducting systems. The zero-energy states are Majorana-like due to the particle-hole hybridization of Bogoliubov quasiparticles<sup>22</sup>. **b.** The arc-like dispersion of topological surface states seen in nodal topological superconducting systems. The flat band of zero-energy states links the projection of the nodal points to the surface Brillouin zone. Figures reproduced from Ref. [101].

geometry and whether two or more irreducible representations are accidentally degenerate.

Owing to the size of the field of topological condensed matter there is a wealth of topological classifications. Mirror and rotational symmetries of the bulk crystal can be combined with the ten fold way to define higher order topological phases in what is called topological crystalline superconductivity<sup>102,103</sup>. In this case the mirror and rotational symmetries, conserved or broken, on a particular crystal surface may impact the presence or absence of topological surface states in nodal superconductors. Similar to the states above, these higher order topological phases feature zero-energy flat bands or hinge states connecting the projection of the bulk nodes to the 2D surface momentum space<sup>102</sup>.

# Chapter 6

## The Zero-Energy Surface State of UTe<sub>2</sub>

### 6.1 Introduction

One of the clearest paths to topologically non-trivial superconductivity is the presence of odd-parity, spin-triplet superconductivity and, as discussed in Chapter 3, such a superconducting state is likely present in UTe<sub>2</sub>. We therefore turn to our recent STM measurements which reveal the presence of an Andreev bound state at the (0 -1 1) cleave surface of UTe<sub>2</sub> and clarify the possible order parameter symmetries of this potential topological superconductor.

### 6.2 Andreev Spectra

As pointed out in Chapter 4, finite zero-energy conductance is consistently detected when using a normal metal tip in STM while UTe<sub>2</sub> is in the superconducting state i.e. for  $T < T_c = 1.6$  K. It is this finite DOS and the low SNR obtained by coherence peak fitting which motivated the use of superconducting scan tips in PDW detection. The use of superconducting Nb tips not only enhances the energy resolution of the coherence peaks but also allows Andreev reflection processes within the combined energy gap  $|\Delta_{\text{Nb+UTe}_2}| = |\Delta_{\text{Nb}}| + |\Delta_{\text{UTe}_2}|$ . In Fig. 6.1 we present a  $dI/dV(V)$  spectrum recorded at  $T = 0.28$  K using a superconducting tip. The region inside the combined energy gap features finite-energy, in-gap peaks and a sharp zero-energy peak. These in-gap states are dependent on the tip configuration, changing in intensity with different tip geometries and sometimes featuring

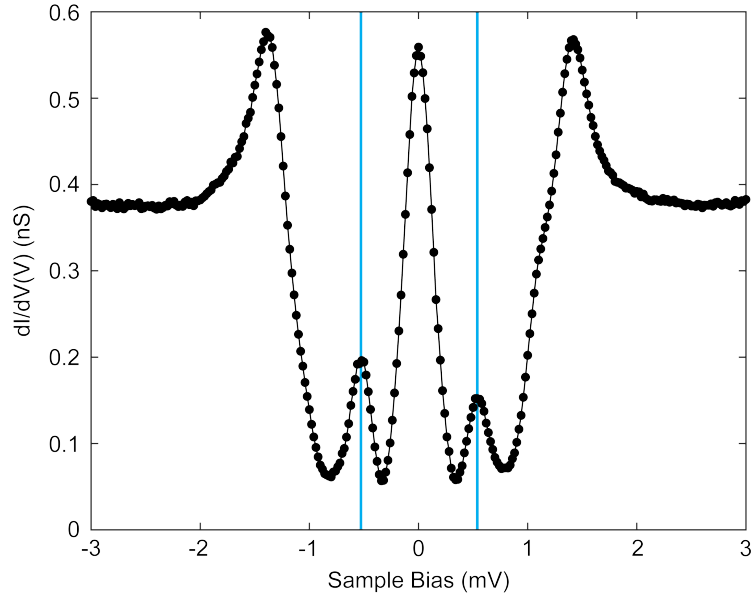


Figure 6.1:  $dI/dV(E)$  measurement on the  $(0 -1 1)$  surface of  $\text{UTe}_2$  using a superconducting Nb tip. Tunnel junction bias voltage  $V_b = 3$  mV and setpoint current  $I_s = 1$  nA. Blue lines indicate the energy of in-gap peaks likely resulting from multiple Andreev reflections.

two or four finite-energy in-gap peaks. These spectra are therefore a challenge to interpret, however, we can derive some essential facts through measurement.

Most importantly, we must confirm that the in-gap states are only a feature of the superconducting sample. Finite-energy in-gap states can be a feature of a superconducting tip with an embedded magnetic impurity<sup>104</sup>. To confirm that this is not the case for the Nb tips used here we record a  $dI/dV(V)$  line scan across a adsorbed metallic cluster of Nb atoms (Fig. 6.2a). In Fig. 6.2b (red) we see that spectra recorded on the superconducting surface feature four finite-energy in-gap peaks and the prominent zero-energy peak. Measurements performed on (6.2b black) and along (6.2c) the metallic Nb cluster show only the superconducting energy gap associated with our scan tip. The in-gap states are therefore unique to tunnelling between the superconducting tip and the  $\text{UTe}_2$   $(0 -1 1)$  surface.

If all this in-gap conductance does not result from impurity states of the tip then the question remains - how can in-gap states arise in this tunnelling setup? We first note from the blue lines in Fig. 6.1, that the sub-gap peaks appear at energies  $A_+ = 0.54$  meV and  $A_- = 0.52$  meV. In superconductor-insulator-superconductor tunnel junctions multiple Andreev reflection (MAR) processes are possible and should depend significantly on the tunnel junction

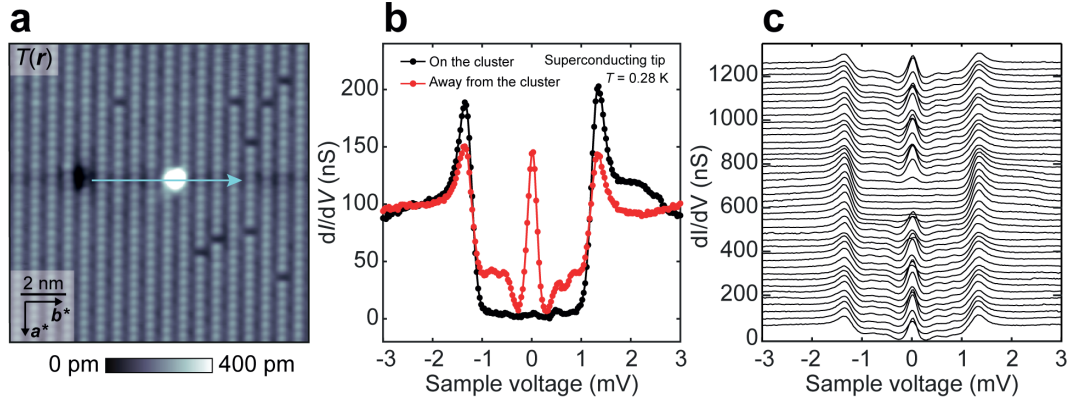


Figure 6.2: **a.** Topography in a  $13 \text{ nm}^2$  FOV on the  $(0 -1 1)$  cleave surface of  $\text{UTe}_2$  with an adsorbed impurity cluster likely composed of metallic Nb from the scan tip ( $V_S = 7 \text{ mV}$ ,  $I_S = 200 \text{ pA}$ ). **b.**  $dI/dV$  spectra recorded off (red) and on (black) the impurity cluster. The sub gap features present on the  $\text{UTe}_2$  surface fall to zero at the adsorbed cluster. **c.**  $dI/dV$  linescan across the impurity cluster indicated by the blue arrow in **a.**

structure<sup>105</sup>. This transport mechanism consists of a series of Andreev reflections in which the reflected particle gains energy  $eV$  with each subsequent reflection. These reflections can have very complex energy dependence even for symmetric superconducting energy gaps<sup>106</sup>. For asymmetric energy gaps as in our experimental setup  $|\Delta_{\text{UTe}_2}|/|\Delta_{\text{Nb}}| \approx 0.2$ , MAR processes can produce peaks at energies  $(|\Delta_{\text{Nb}}| + |\Delta_{\text{UTe}_2}|)/3 \approx 0.54 \text{ meV}$ . This is consistent with the finite-energy peaks marked by blue lines in Fig. 6.1. We therefore expect MAR processes to be the source of these finite-energy in-gap states.

We can gain further insights into the origin of these peaks by studying their dependence on tunnelling distance  $z(m)$ . In Fig. 6.3 we plot  $dI/dV(V)$  recorded at increasing tunnel current setpoints and thus decreasing tip-sample distance or  $z$  values. The in-gap states seen in Fig. 6.1 are recorded at each junction setup thus allowing us to track these peaks' conductance dependence on the tip-sample distance or  $dI/dV(V, z)$ . By doing so, we can compare the behaviour of normal state quasiparticle tunnelling against that of in-gap Bogoliubov quasiparticle transport. As described in Section 2.4.1, normal state tunnelling currents and consequently differential conductance exhibits an exponential dependence on tip-sample  $dI/dV(V, z) \propto Ae^{-\kappa z}$ . Normalizing this  $\kappa$  value by the normal state tunnelling constant  $\kappa_N$  provides information regarding the tunnelling process<sup>107,108</sup>. As we saw in Section 5.3, for a transparent barrier  $Z = 0$  Andreev conductance is twice that of normal state conductance

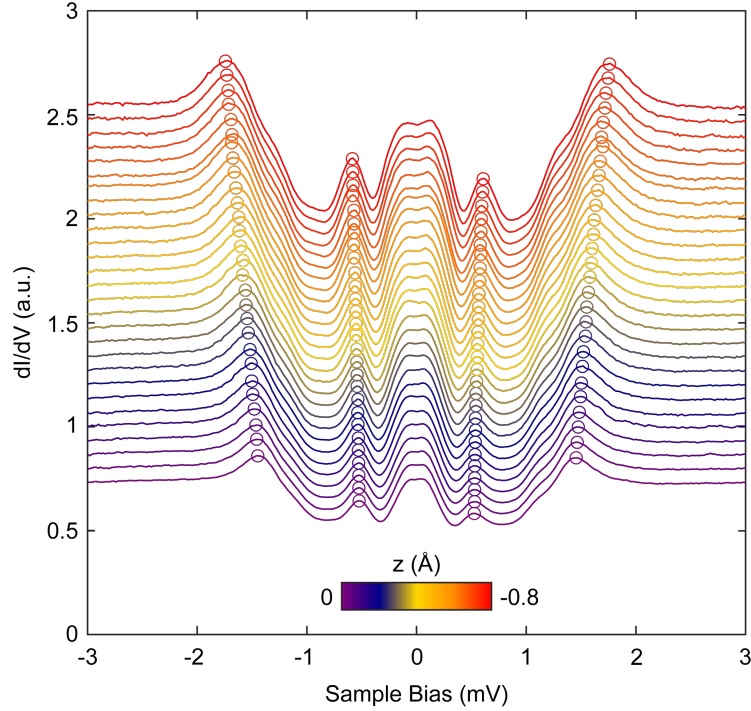


Figure 6.3:  $dI/dV(E)$  spectra recorded with junction bias voltage  $V_b = 3$  mV and varying setpoint currents from  $I_s = 1.4$  nA to 4 nA. At these low junction resistances the zero-energy peak shown in Fig. 6.1 splits to finite-energy maxima. As the junction resistance decreases the coherence peaks and MAR peaks move to higher energy. The reason for this divergence is not well understood. From second-order polynomial fitting to the multiple Andreev reflection (MAR) and coherence peaks, maxima in  $dI/dV(E)$  were identified and are indicated by coloured circles.

owing to the fact that it is a two particle process. Hence peaks resulting from Andreev reflection have normalized tunnelling constant  $\kappa_{AR}/\kappa_N > 1^{108}$ . On the other hand, resonant Andreev transport to bound states or coherence peaks should exhibit  $\kappa_{Res}/\kappa_N < 1$ .

In Fig 6.3, we present a series of spectra recorded with bias voltage  $V_b = 3$  mV and setpoint current  $I_s$  ranging from 1.4 nA to 4 nA. To increase the setpoint current by this amount the tip is moved a total distance of  $\delta z \approx 0.8$  Å towards the sample. High setpoint currents/low tip-sample distances were recorded to maximize the signal-to-noise ratio of the spectra however, these low junction resistance measurements typically split the zero-energy peak. We will discuss this phenomenon in more detail later, as it is crucial to understanding the pairing state of  $UTe_2$ , but for now, we study the evolution of these spectra's differential conductance peaks with varying tunnelling distance  $z$ . To derive

a normal state tunnelling constant  $\kappa_N$  we fit  $dI/dV(V, z)$  spectra at  $V = -3$  mV with an exponential function. The data with its exponential fit overlaid (blue) is shown in Fig. 6.4a. From this fit we derive  $\kappa_N = 1.23\text{\AA}^{-1}$  for the single particle decay constant. In Fig. 6.4a we also plot the differential conductance of the positive and negative coherence peaks (red and orange) whose maxima are derived by second order polynomial fitting. While the conductance at the coherence peaks is larger than that at  $V = -3$  mV, it exhibits a weaker dependence on tip-sample distance. From fitting an exponential to the coherence peak conductance we derive the normalized decay constant  $\kappa/\kappa_N$ , which is 0.83 and 0.84 for the positive and negative peaks, respectively. This confirms that resonant Andreev tunnelling contributes to the tunnelling current at these energies<sup>108</sup>. By contrast, in Fig. 6.4b we present the conductance of the finite-energy, sub-gap peaks (purple and pink) obtained by second-order polynomial fitting to these peaks at varying  $z$  alongside the normal state conductance (blue). Again, we can derive the decay constant for these suspected MAR peaks. Doing so, we find that the positive and negative MAR peaks have normalized decay constants 1.32 and 1.01, respectively indicative of higher order tunnelling processes, such as Andreev reflection. Although the normalized decay constant for these peaks does not reach the full Andreev reflection value of 2 this is expected in the tunnelling regime. We therefore attribute these finite-energy sub-gap peaks to MAR processes. Finally, we study the decay constant at and around zero-energy to gain insight into the tunnelling process responsible for the large zero-energy conductance. To do so, we average the differential conductance within  $40\mu\text{eV}$  around zero-energy, fit to an exponential function, and compare against the normal state decay constant  $\kappa_N$ . In Fig. 6.4c we compare  $dI/dV(V = \pm 20\mu\text{V})$  (green) with the single-particle  $dI/dV(V = -3\text{mV})$  (blue). Similar to the coherence peak conductance the zero-energy conductance exhibits a weaker dependence on tip-sample distance than the normal state tunnelling channel. Extracting the normalized decay constant we obtain  $\kappa_{\text{ZBP}}/\kappa_N = 0.83$  indicative of resonant Andreev tunnelling, expected for tunnelling to an Andreev bound state<sup>86</sup>.

Although it now seems clear that the zero-energy peak is the result of tunnelling to an Andreev bound state, we note that zero-energy peaks in differential conductance are often attributed to the Josephson effect, discussed in Section 2.4.2. However, Josephson tunnelling always features a decay constant  $\kappa_J/\kappa_N > 1$ , owing to the two-particle tunnelling process<sup>108</sup> and furthermore the

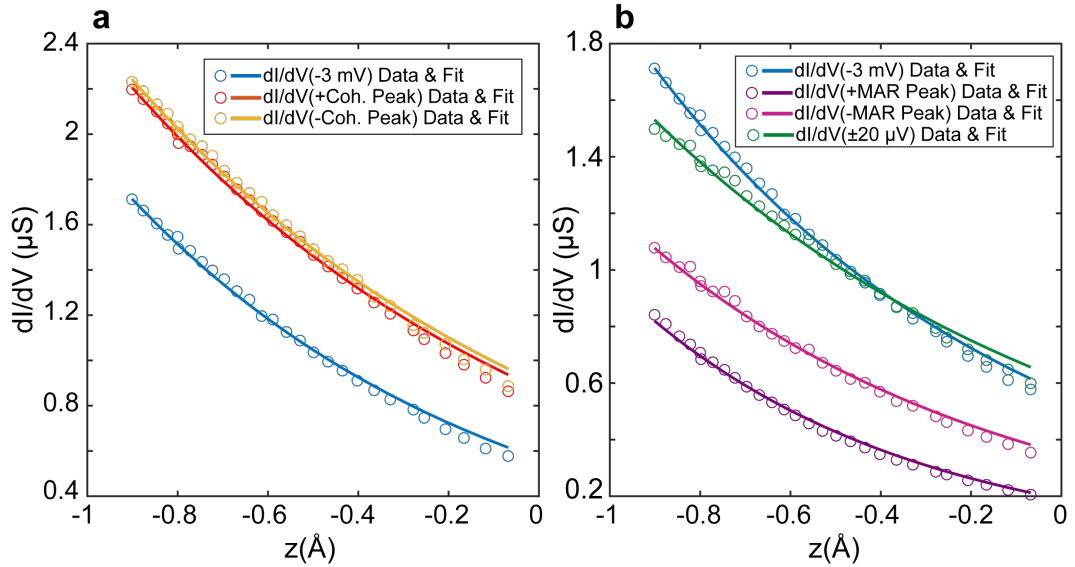


Figure 6.4: **a**. Differential conductance recorded at 3 mV (blue) and at coherence peak energies determined by second-order polynomial fitting. Positive and negative energy coherence peak conductance are represented by red and orange, respectively. The coherence peaks' weaker dependence on tip-sample distance is indicative of resonant Andreev tunnelling. **b**. Normal, single-particle differential conductance (blue), differential conductance of positive and negative multiple Andreev reflection (MAR) peaks, and averaged differential conductance within  $40\mu\text{V}$  around zero-energy. MAR peaks show a strong dependence on tip-sample distance due to higher order tunnelling processes while zero-energy conductance depends weakly on tip-sample distance due to resonant tunnelling processes.

magnitude of the zero-energy peak is significantly larger than that expected for an  $s$ -wave to  $p$ -wave Josephson effect. In Appendix C we compare Josephson and Andreev tunnelling more directly and conclusively rule out the Josephson effect in these measurements.

We have now firm evidence that the zero-energy peak measured on the (0 -1 1) surface of  $\text{UTe}_2$  is the product of a zero-energy Andreev bound state however, why this state is present and what are its properties remains unclear. To answer these questions we turn to a theoretical model, developed for Ref. [109], which models tunnelling between an  $s$ -wave superconductor and a  $p$ -wave superconductor whose gap function we can control exactly.

## 6.3 $S$ -wave - Insulator - $P$ -wave (SIP) Model

### 6.3.1 Topological Surface Band (TSB) Phenomenology

Whether the Andreev bound state at the surface of  $\text{UTe}_2$  is topologically trivial or non-trivial depends strongly on the normal state Fermi surface and superconducting order parameter. Following many of the early reports on the Fermi surface of  $\text{UTe}_2$  we assume the presence of a closed Fermi surface around the  $\Gamma$  point of the Brillouin zone<sup>110,111,112</sup>. For such a Fermi surface, the presence of a  $p$ -wave order parameter ensures that Andreev bound states (ABS) are topologically non-trivial and of either  $\mathbb{Z}$  or  $\mathbb{Z}_2$  topological classification (see Fig. 5.4). The associated topologically non-trivial ABSs then consist of either, a Majorana-Dirac cone or a flat Majorana/Fermi arc as shown in Fig. 5.5.

In Chapter 3, we discussed how the presence or absence of chiral superconductivity is of particular importance in determining the pairing symmetry of this  $p$ -wave superconductor as several experimental and theoretical reports have concluded a chiral, TRS breaking, order parameter. We therefore begin our theoretical modelling by calculating the density of states (DOS) for a chiral and non-chiral order parameter in  $\text{UTe}_2$ . As our example chiral order parameter we choose a complex linear combination of two irreducible representations of  $D_{2h}$ ,  $A_u + iB_{3u}$ . The dispersion of the resulting chiral surface state in the  $k_x - k_y$  plane is presented in the Fig. 6.5a. It features only a single, TRS-breaking band. By contrast, in Fig. 6.5b we plot the dispersion of a TRS-conserving surface state resulting from a non-chiral order parameter of  $B_{3u}$  symmetry. To understand how these flat TSB states contribute to the

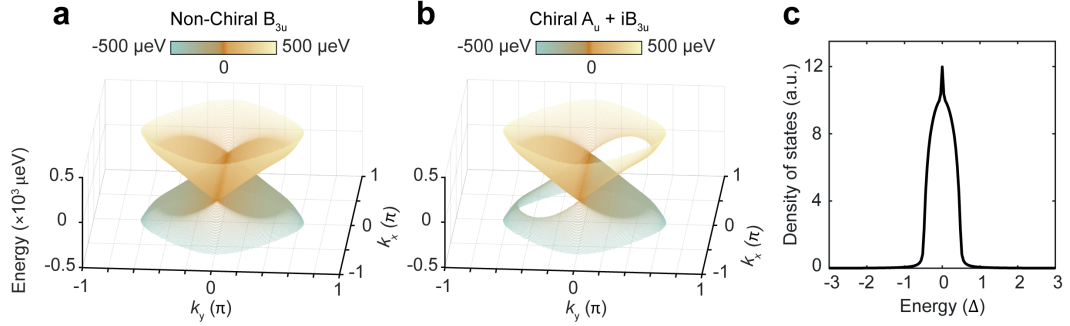


Figure 6.5: **a.** 3D band dispersion for a  $B_{3u}$  topological surface state in the  $k_x - k_y$  plane. **b.** The same as in b for a time-reversal symmetry breaking, chiral state  $A_u + iB_{3u}$ . Topological surface states merge with bulk bands at the superconducting energy gap  $|\Delta_{\text{UTe}_2}| = 0.25$  meV. **c.** Density of states (DOS) obtained using Eq. 6.1 resulting from topological surface states presented in a and b. Both TSBs feature a flat Fermi arc which produces a sharp peak around the Fermi level with a broad maximum and extending to the  $\text{UTe}_2$  energy gap.

DOS we make use of the simple relation

$$N(E) = \sum_{k_{x,y}} \frac{\Gamma/\pi}{(E - E_{\text{TSB}}(k_x, k_y))^2 + \Gamma^2} \quad (6.1)$$

where  $\Gamma$  is a momentum independent quasiparticle broadening parameter. The result of this summation is presented in Fig. 6.5c with  $\Gamma = 5\mu\text{eV}$ . The resulting DOS is identical for both TSB states, chiral and non-chiral, producing a sharp zero-energy peak. The zero-energy peak in our  $dI/dV(V)$  spectra (Fig. 6.1) therefore cannot distinguish a chiral from a non-chiral state in the large junction resistance limit. We then seek tunnelling characteristics which may help distinguish these two proposed topological surface states. To do so, we model tunnelling between an  $s$ -wave superconducting tip (S), through vacuum (I), to a  $p$ -wave superconductor (P) of appropriate pairing symmetry.

### 6.3.2 SIP Model Details

The unknown geometry of STM scan tips makes exact modelling of tunnelling conductance extremely difficult, we therefore use a planar tunnelling model, which as we will see later, captures the essential experimental facts. An illustration of the model is shown in Fig. 6.6a. We begin by writing the general

four component Bogliubov-de Gennes Hamiltonian for a superconductor

$$H = \sum_{\mathbf{k}} \psi^\dagger(\mathbf{k}) H(\mathbf{k}) \psi(\mathbf{k}) = (c_{\mathbf{k},\uparrow}, c_{\mathbf{k},\downarrow}, c_{-\mathbf{k},\uparrow}^\dagger, c_{-\mathbf{k},\downarrow}^\dagger)^T \quad (6.2)$$

We then introduce the Nb tip by first writing the Hamiltonian for an  $s$ -wave superconductor as

$$H_{\text{Nb}}(\mathbf{k}) = \begin{pmatrix} \epsilon(\mathbf{k})\sigma_0 & \Delta_{\text{Nb}}(i\sigma_2) \\ \Delta_{\text{Nb}}^*(-i\sigma_2) & -\epsilon(-\mathbf{k})\sigma_0 \end{pmatrix} \quad (6.3)$$

where  $\sigma_{1,2,3}$  are the Pauli matrices and  $\sigma_0$  is the  $2 \times 2$  identity matrix  $I_{2 \times 2}$ .  $\Delta_{\text{Nb}}$  is the momentum independent superconducting order parameter for the Nb tip. To model the normal state band structures,  $\epsilon_{\text{Nb}}(\mathbf{k})$  and  $\epsilon_{\text{UTe}_2}(\mathbf{k})$ , we consider a simple, nearest-neighbour, tight-binding dispersion in a cubic lattice, of the form  $\cos(k_x) + \cos(k_y) + \cos(k_z) - 2$  in units of meV. The Hamiltonian used for  $\text{UTe}_2$  is

$$H_{\text{UTe}_2}(\mathbf{k}) = \begin{pmatrix} \epsilon_{\text{UTe}_2}(\mathbf{k})\sigma_0 & \Delta_{\text{UTe}_2}(\mathbf{k}) \\ \Delta_{\text{UTe}_2}^*(\mathbf{k}) & -\epsilon_{\text{UTe}_2}(-\mathbf{k})\sigma_0 \end{pmatrix} \quad (6.4)$$

where the  $p$ -wave order parameter is defined by the d-vector  $\Delta_{\text{UTe}_2}(\mathbf{k}) \equiv \Delta_{\text{UTe}_2} i(\mathbf{d} \cdot \boldsymbol{\sigma})\sigma_2$ . Changing the order parameter symmetry of the  $p$ -wave superconductor thus requires change of d-vector. For a non-chiral  $B_{3u}$ ,  $p$ -wave state this d-vector is

$$\mathbf{d} = (0, \sin(k_z c), \sin(k_y b)) \quad (6.5)$$

and the resulting gap function is

$$\Delta_{\mathbf{k}} \propto \begin{pmatrix} i \sin(k_z c) & \sin(k_y b) \\ \sin(k_y b) & i \sin(k_z c) \end{pmatrix} \quad (6.6)$$

while for a chiral  $A_U + iB_{3u}$  state the d-vector is

$$\mathbf{d} = (0, \sin(k_y b) + i \sin(k_z c), \sin(k_z c) + i \sin(k_y b)) \quad (6.7)$$

giving rise to the gap function

$$\Delta_{\mathbf{k}} \propto \begin{pmatrix} -\sin(k_z c) + i \sin(k_y b) & \sin(k_z c) + i \sin(k_y b) \\ \sin(k_z c) + i \sin(k_y b) & -\sin(k_z c) + i \sin(k_y b) \end{pmatrix} \quad (6.8)$$

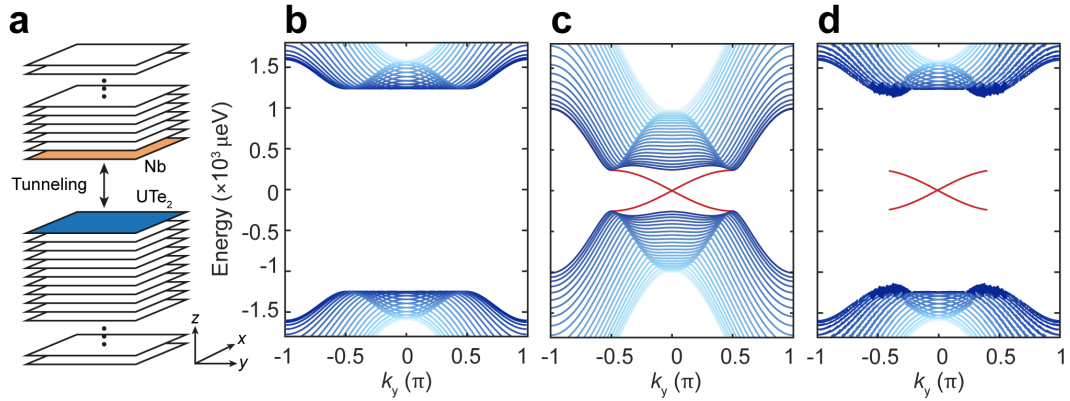


Figure 6.6: **a.** Illustration of SIP model framework for calculation. Twenty layers of Nb are stacked in the  $c$  direction adjacent to fifty layers of UTe<sub>2</sub> with tunnelling between the surface layers. **b.** Surface band dispersion of Nb (orange layer) featuring a superconducting energy gap of  $|\Delta| = 1.25$  meV when  $|M| = 0$ . **c.** Surface band dispersion of UTe<sub>2</sub> (blue layer) with a superconducting energy gap  $|\Delta| = 0.25$  meV while  $|M| = 0$ . Red in-gap states correspond to the time-reversal symmetry preserving TSB of a  $B_{3u}$  order parameter. **d.** SIP model calculation of the surface band dispersion of Nb with finite tunnelling matrix element,  $|M| = 0.2$  meV. UTe<sub>2</sub> bulk states are forbidden from tunnelling to the Nb tip because of the superconducting energy gap. TSB states exhibit enhanced tunnelling due to resonant Andreev reflection of TSB quasiparticles. The zero-energy Fermi arc produces a peak in the UTe<sub>2</sub> DOS which is measured by the Nb tip as a peak around  $E = 0$

Lastly, tunnelling of electronic states between the Nb tip and UTe<sub>2</sub> sample is introduced via the tunnelling Hamiltonian

$$H_T = -|M| \sum_{\mathbf{k}_{\parallel}} \left[ \psi_{\text{Nb}, \mathbf{k}_{\parallel}}^{\dagger} \tau_3 \otimes \sigma_0 \psi_{\text{UTe}_2, \mathbf{k}_{\parallel}} + \text{h.c.} \right] \quad (6.9)$$

Here  $\mathbf{k}_{\parallel} = (k_x, k_y, 0)$  is the in-plane quasiparticle momentum at the interface. The model then consists of twenty Nb layers adjacent to fifty UTe<sub>2</sub> layers stacked in the  $\hat{c}$  direction with tunnelling at the surface layer of each superconductor (Fig. 6.6a). The combined Hamiltonian  $H = H_{\text{Nb}} + H_{\text{UTe}_2} + H_T$  is then solved for its eigenvalues and eigenvectors. Eigenenergies at the surface layers whose wavefunction weight exceeds a lower bound ( $10^{-3}$  in this case) are kept to produce the plots shown.

By setting the tunnelling matrix elements to zero,  $|M| = 0$ , the combined Hamiltonian can be solved at the Nb and UTe<sub>2</sub> surfaces respectively. For Nb, this simply reveals the superconducting energy gap around the Fermi level

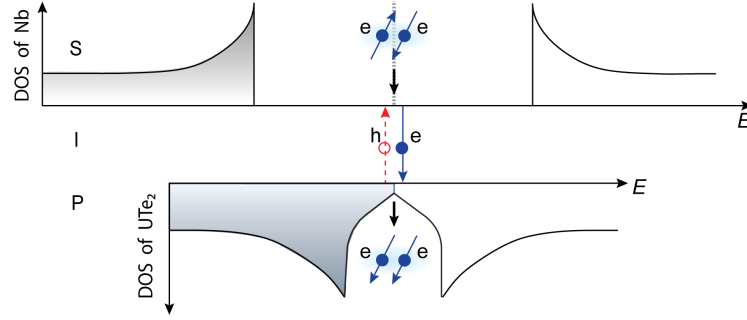


Figure 6.7: Schematic of Andreev reflection between the  $s$ -wave Nb tip and the TSB of  $p$ -wave  $\text{UTe}_2$  with an insulating barrier between them

(Fig. 6.6b) however, for  $\text{UTe}_2$  this clearly demonstrates the presence of in-gap topological surface states, evidenced by the red bands crossing the Fermi level, here we have used the TRS conserving  $B_{3u}$  order parameter. Furthermore, by setting the magnitude of the tunnelling matrix element to be small  $|M| = 0.2$  meV, and by calculating the band dispersion at the Nb interface, we find that the bulk states of  $\text{UTe}_2$  do not contribute to the in-gap states measured by the Nb tip. In contrast, the TSB of  $\text{UTe}_2$  can tunnel, via resonant Andreev reflections, to the Nb tip thus demonstrating  $s$ -wave tip selection of TSB quasiparticles. Henceforth, we refer to conductance around zero-energy as Andreev conductance  $dI/dV(\mathbf{r}, V)|_{V=0} = a(\mathbf{r}, V)$  (Fig. 6.7).

While normal tip measurements could, in principle, detect this zero-energy state they instead measure finite DOS at zero-energy (Fig. 4.2). The zero-energy peak is likely masked by the conductance contribution of broken Cooper pairs which are expected to be formed by both magnetic and non-magnetic impurities in a  $p$ -wave superconductor<sup>75</sup>. These broken Cooper pairs experience scattering which overcomes the superconducting pair potential and thus do not contribute to Andreev reflection as they are no longer coherent Bogoliubov quasiparticles.

### 6.3.3 SIP Model Predictions and Experimental Verification

From both theory and experiment, we have now confirmed that our superconducting tip can detect zero-energy TSB quasiparticles via resonant Andreev tunnelling. The remaining question is whether the SIP model may distinguish between these two forms of superconducting pairing. A simple variable of the

experiment can be mimicked in this tunnelling model. The magnitude of the tunnelling matrix  $|M|$  can be varied and this variable should be related to the tip-sample distance, although the exact dependency cannot be predicted *a priori*. By increasing the magnitude of the tunnelling matrix, or equivalently by reducing the tip-sample distance, these two forms of topological superconductivity become distinguishable. As shown in Fig. 6.8 the chiral,  $A_u + iB_{3u}$  TSB splits in momentum space but maintains a zero-energy Fermi arc. As the magnitude of the tunnelling matrix element is increased, the zero-energy peak in the DOS remains unaffected by changes in tip-sample distance. By contrast, the TSB of a time-reversal symmetry conserving  $B_{3u}$  state becomes gapped in energy as the tunnelling matrix is increased or tip-sample distance decreased. This gap in band dispersion manifests as a split in the zero-energy DOS, and consequently, in the zero-energy Andreev conductance. Although specific examples,  $B_{3u}$  and  $A_u + iB_{3u}$ , are chosen for Fig. 6.8 this phenomenology is consistent for all possible chiral and non-chiral states of the  $D_{2h}$  point symmetry group.

An important element in the interpretation of these results is the role of the macroscopic superconducting phase of both the  $s$ -wave tip and  $p$ -wave sample, as well as the protection symmetries of the TSBs. As discussed in Section 2.4.2, phase interactions between superconductors can be crucial in the interpretation of tunnelling current measurements. In the SIP model, while the tip and sample are far apart ( $|M| \rightarrow 0$ ) they each have an arbitrary, and independent phase, however as the distance between these electrodes is reduced  $|M| > 0$  there are phase interactions between them resulting in a finite relative phase difference. To minimize the electronic energy of the system, this relative phase difference evolves with decreasing tip-sample distance to be  $\delta\phi = \pi/2$ . Such a phase difference breaks time-reversal symmetry, as  $e^{i\delta\phi} = i \rightarrow e^{-i\delta\phi} = -i$ . For a chiral superconducting state, this symmetry is already broken and the TSB does not require this protection symmetry to maintain its gaplessness. By contrast, the TSB of a non-chiral state is protected by time-reversal symmetry and the breaking of this symmetry destroys the in-gap TSB. A clear demonstration of this TSB splitting is shown in Appendix Fig. D.1.

To verify the SIP model predictions, and distinguish between a chiral and non-chiral order parameter in  $\text{UTe}_2$ , we perform  $dI/dV(V)$  or Andreev spectroscopy  $a(V)$  measurements as a function of junction resistance at  $T = 280$

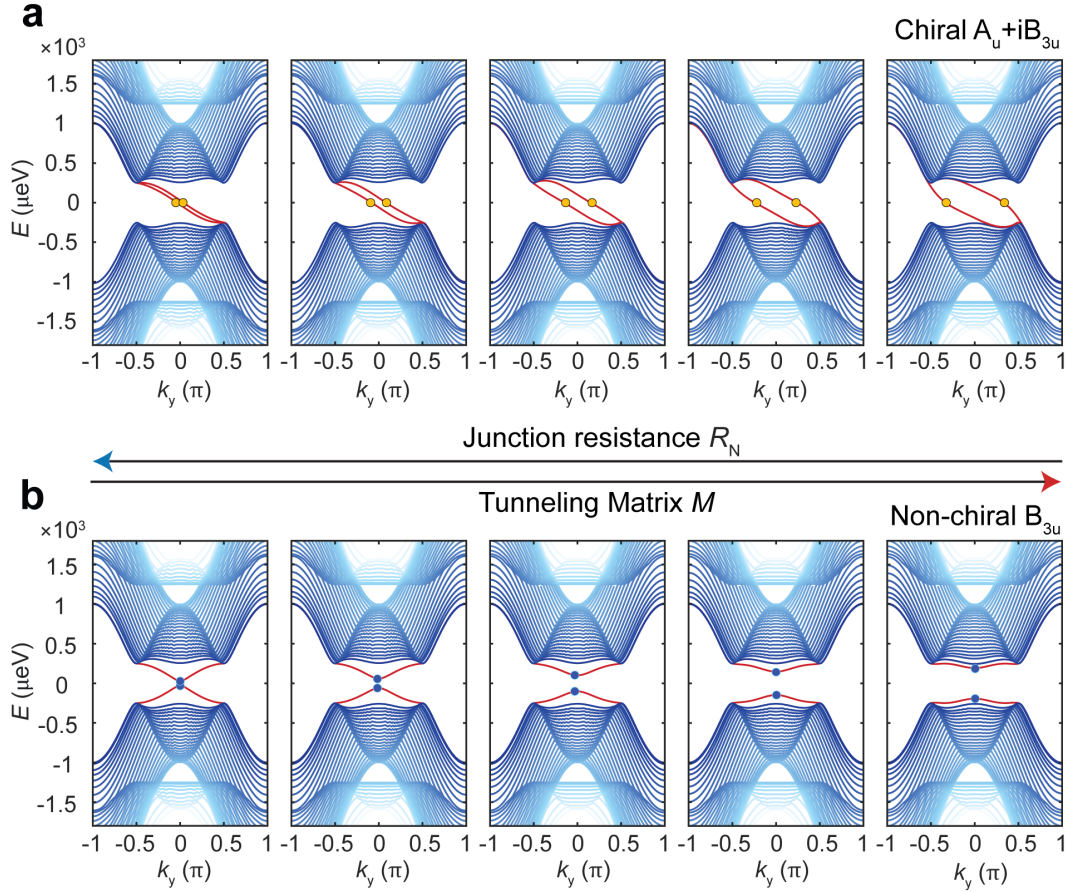


Figure 6.8: **a**. Calculated quasiparticle dispersion within the SIP interface with relative phase difference  $\delta\phi = \pi/2$  as a function of tunnelling matrix element  $|M|$ . Calculations are carried out for a chiral  $A_u + iB_{3u}$  order parameter and reveal that with decreasing junction resistance the chiral TSB splits in momentum, but maintains zero-energy crossings. The zero-energy DOS is therefore unchanged by the introduction of the  $s$ -wave scan tip. **b**. The same plot as in **a** for a non-chiral superconductor with  $B_{3u}$  symmetry. Increased tunnelling to an  $s$ -wave tip splits the TSB in energy thus generating, two particle-hole symmetric Andreev conductance maxima.

---

mK. Figure 6.9a shows clearly that the zero-energy peak first broadens, and then splits, at small junction resistance. This definitively rules out the possibility of a chiral superconducting state and suggests a non-chiral pairing state consistent with much of the evidence outlined in Chapter 3. We can also now compare the rate of TSB splitting obtained by experiment to that predicted from the SIP model. While the exact relationship between  $|M|$  and  $R_N$  is unknown, a qualitative comparison can be made. The experimentally determined splitting is presented in Fig. 6.8b and the SIP prediction in Fig. 6.8c. Qualitatively we find a close match between theory and experiment for  $|M| \propto 1/R_N$ .

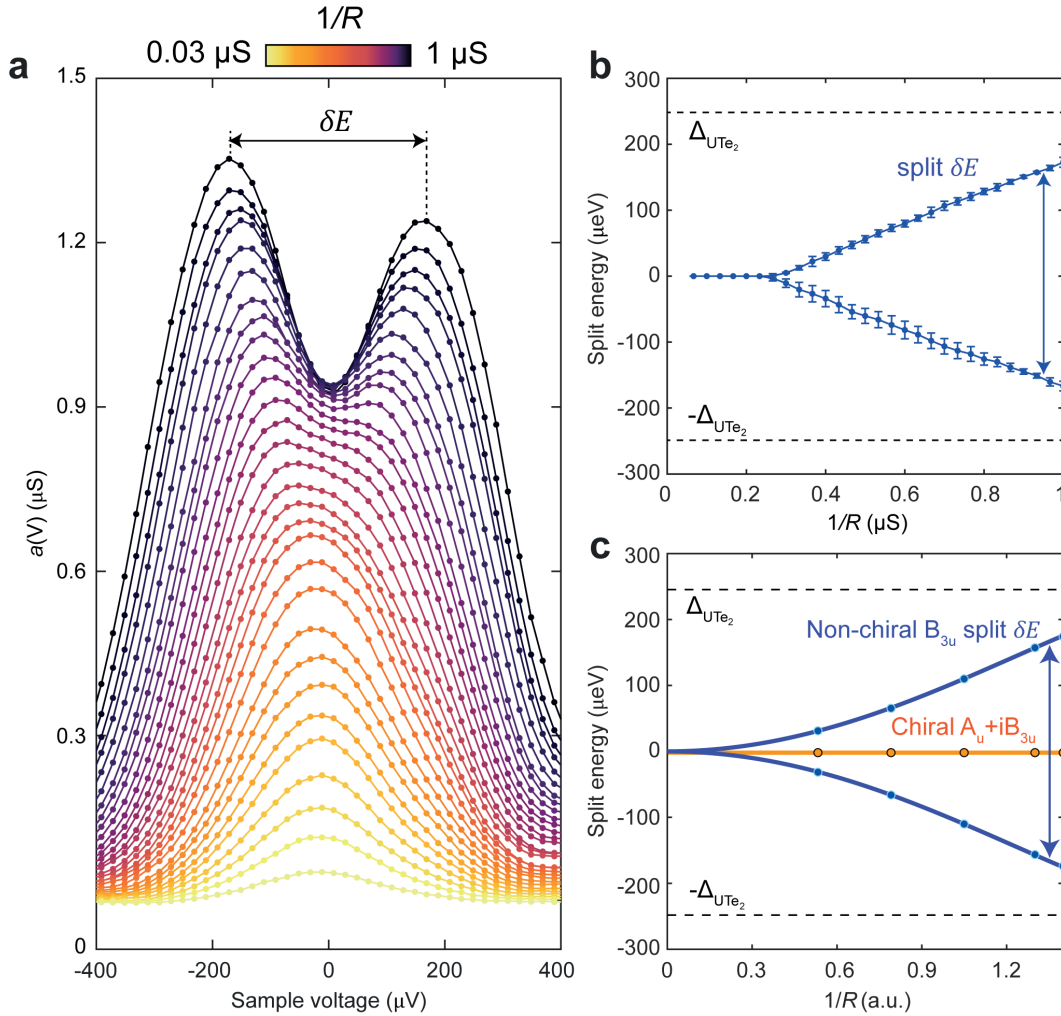


Figure 6.9: **a.** Measured evolution of Andreev conductance  $a(V) \equiv dI/dV|_{\text{SIP}}$  at  $T = 280 \text{ mK}$  on the  $(0 -1 1)$  surface of  $\text{UTe}_2$  as a function of decreasing junction resistance  $R_N$ . The  $a(V)$  spectra begin to split at  $R_N \sim 5 \text{ M}\Omega$ . This splitting behaviour is indicative of a non-chiral, time-reversal symmetry preserving superconducting state. **b.** Measured energy splitting of Andreev conductance  $a(V)$  maxima as a function of decreasing junction resistance  $R_N$ . The superconducting energy gap of  $\text{UTe}_2$ ,  $|\Delta_{\text{UTe}_2}|$  is indicated by black dashed lines. **c.** Calculated energy splitting of TSB states as a function of increased tunnelling matrix amplitude  $|M| \propto 1/R_N$ . TSB energy splitting expected for a chiral TSB are represented by orange circles and that expected for a non-chiral TSB are shown in blue circles. Comparison between experiment and calculation reveal an approximate relationship between junction resistance and tunnelling matrix element  $|M| \propto 1/R_N$ .

# Chapter 7

## Quasiparticle Surface State Quasiparticle Interference (QSQPI)

### 7.1 Introduction

The discovery of the large, zero-energy conductance peak, mediated by Andreev transport of in-gap quasiparticles, has indicated the presence of a topological surface band at the (0 -1 1) surface of  $\text{UTe}_2$ . Such a state is expected for an odd-parity  $p$ -wave superconductor however the observation of zero-energy state splitting limits the possible bulk order parameter symmetries to the single component  $B_{1u}$ ,  $B_{2u}$ , and  $B_{3u}$ . More exact determination of the order parameter requires moving beyond individual  $dI/dV(V)$  analysis, and instead studying its spatial variations  $dI/dV(\mathbf{r}, V)$ . Bogoliubov quasiparticle interference (QPI) has been used to identify the superconducting gap structure of many unconventional superconductors<sup>113,114</sup> and is therefore a natural technique to employ in studying  $\text{UTe}_2$ . Such measurements have added complications for  $\text{UTe}_2$ . Firstly, the presence of an Andreev bound state/quasiparticle surface band (QSB) at the (0 -1 1) surface should contribute to scattering, as these exotic in-gap Bogoliubov quasiparticles have their own dispersion  $\mathbf{k}_\sigma(E)$ . Secondly, QPI measurements are performed on the (0 -1 1) plane and the Fermi surface geometry at this plane must be deduced to understand the scattering wavevectors. And thirdly, the Fermi surface geometry of  $\text{UTe}_2$  remains poorly understood. We will therefore have to address each of these points as we proceed in interpreting our QPI measurements.

## 7.2 The UTe<sub>2</sub> Fermi Surface within QSQPI

As discussed in Chapter 3, there are many outstanding issues in studies of UTe<sub>2</sub>. Perhaps chief among the controversies is the topology of the Fermi surface (FS). Measurements of the FS have reached broad agreement regarding the existence of two cylindrical, quasi-2D bands, one is hole-type and centred around the  $X$  point of the Brillouin zone and the other is electron-type and centred around the  $Y$  point<sup>111,115</sup>. However, there is debate surrounding the existence of a 3D component to the FS, possibly related to  $f$ -electron correlations and the Kondo effect. While angle-resolved photoemission spectroscopy (ARPES) has found spherical intensity around the  $\Gamma$  and  $Z$  points of the Brillouin zone<sup>110,111</sup>, these conclusions have been complicated by the advent of De Haas-Van Alphen/Quantum Oscillation (QO) experiments on clean,  $T_c = 2K$  samples which find no evidence for a closed, three-dimensional (3D) component to the FS<sup>116,115,117</sup>. Despite these new measurements, several theoretical works have proposed that some 3D component of the FS should exist for this strongly correlated system. Calculations employing density functional theory (DFT) introduce an on-site Coulomb repulsion term  $U$  to describe  $f$ -electron correlations<sup>118</sup>. Tuning this variable from 1 eV to 2 eV results in a Lifshitz transition of the FS at  $U \sim 1.6$  eV. An intermediate value of  $U$  produces both the quasi-2D Fermi surface sheets and a pocket which encloses the  $Z$  point, consistent with ARPES measurements. An intermediate value for  $U$  reflects more itinerant  $f$ -electrons expected for the Kondo effect at low temperature. Furthermore, both tight-binding and DFT+DMFT (dynamical mean field theory) calculations of the FS reproduce some 3D FS component at low temperature and ambient pressure<sup>119,120</sup>. Therefore, theoretical studies of UTe<sub>2</sub> suggest that its FS is dominated by 2D bands but features some 3D components associated with heavy-electron physics.

To generate a model for the QPI of QSB states we therefore consider a 4-band tight-binding model which reproduces the cylindrical FS while featuring some 3D undulations near the  $Z$  point of the Brillouin zone to achieve maximum consistency between quantum oscillation measurements, ARPES, and theoretical calculations. The characteristic features are assumed to arise from the hybridization between two quasi-one-dimensional chains, one originating from the Te(2) 5p orbitals, and the other from the U 6d orbitals. The lattice constants are taken to be  $a = 0.41$  nm,  $b = 0.61$  nm,  $c = 1.39$  nm. The coupling between the two uranium orbitals is modelled by the following Bloch

Hamiltonian

$$H_{U-U} = \begin{pmatrix} U_{1,1} & U_{1,2} \\ U_{2,1} & U_{2,2} \end{pmatrix} \quad (7.1)$$

$$U_{1,1} = U_{2,2} = \mu_U - 2t_U \cos(k_x a) - 2t_{ch,U} \cos(k_y b) \quad (7.2)$$

$$U_{1,2} = U_{2,1}^* = -\Delta_U - 2t'_U \cos(k_x a) - 2t_{ch,U} \cos(k_y b) - 4t_{z,U} e^{-ik_z c/2} \cos\left(k_x \frac{a}{2}\right) \cos\left(k_y \frac{b}{2}\right) \quad (7.3)$$

Here the tight-binding parameters are, the chemical potential  $\mu_U$ , the intra-dimer overlap  $\Delta_U$ , the hopping  $2t_U$  along the uranium chain in the  $a$  direction, the hopping  $t'_U$  to other uranium in the dimer along the chain direction, the hoppings  $t_{ch,U}$  and  $t'_{ch,U}$  between chains in the  $a$ - $b$  plane, and the hopping  $t_{z,U}$  between chains along the  $c$  axis. Similarly, the coupling between the two tellurium orbitals is given by

$$H_{Te-Te} = \begin{pmatrix} Te_{1,1} & Te_{1,2} \\ Te_{2,1} & Te_{2,2} \end{pmatrix} \quad (7.4)$$

$$Te_{1,1} = Te_{2,2} = \mu_{Te} - 2t_{ch,Te} \cos(k_x a) \quad (7.5)$$

$$Te_{1,2} = Te_{2,1}^* = \Delta_{Te} - t_{Te} e^{-ik_y b} - 2t_{z,Te} \cos\left(k_z \frac{c}{2}\right) \cos\left(k_x \frac{a}{2}\right) \cos\left(k_y \frac{b}{2}\right) \quad (7.6)$$

Where the tellurium tight-binding parameters are, the chemical potential  $\mu_{Te}$ , the intra-unit cell overlap  $\Delta_{Te}$  between the two Te(2) atoms along the chain direction, the hopping  $t_{Te}$  along the Te(2) chain in the  $b$  direction, the hopping  $t_{ch,Te}$  between chains in the  $a$  direction, and the hopping  $t_{z,Te}$  between chains along the  $c$  axis. We then model hybridization between the uranium and tellurium orbitals as

$$H_{U-Te} = \begin{pmatrix} \delta_1 & \delta_2 \\ \delta_2 & \delta_1 \end{pmatrix} \quad (7.7)$$

And finally the normal state tight-binding Hamiltonian can be written using the above parts

$$H_{U_{Te_2}} = \begin{pmatrix} H_{U-U} & H_{U-Te} \\ H_{U-Te}^\dagger & H_{Te-Te} \end{pmatrix} \quad (7.8)$$

Eigenstates of this electronic structure are then expressed

$$\psi^\dagger(\mathbf{k}) = \left( c_{U_1, \mathbf{k}, \sigma}^\dagger, c_{U_2, \mathbf{k}, \sigma}^\dagger, c_{\text{Te}_1, \mathbf{k}, \sigma}^\dagger, c_{\text{Te}_2, \mathbf{k}, \sigma}^\dagger, \right. \\ \left. c_{U_1, -\mathbf{k}, \bar{\sigma}}, c_{U_2, -\mathbf{k}, \bar{\sigma}}, c_{\text{Te}_1, -\mathbf{k}, \bar{\sigma}}, c_{\text{Te}_2, -\mathbf{k}, \bar{\sigma}} \right) \quad (7.9)$$

with

$$c_{\alpha, \mathbf{k}, \sigma}^\dagger = (c_{\alpha, \mathbf{k}, \uparrow}^\dagger, c_{\alpha, \mathbf{k}, \downarrow}^\dagger) \quad c_{\alpha, \mathbf{k}, \bar{\sigma}} = (c_{\alpha, \mathbf{k}, \downarrow}, c_{\alpha, \mathbf{k}, \uparrow}) \quad (7.10)$$

In all calculations below we then use the following values for the tight-binding model, where all values are expressed in units  $eV$ :  $\mu_U = -0.355$ ,  $t_{\text{ch}, U} = 0.015$ ,  $t'_{\text{ch}, U} = 0.01$ ,  $t_{z, U} = -0.0375$ ,  $\mu_{\text{Te}} = -2.25$ ,  $\Delta_{\text{Te}} = -1.4$ ,  $t_{\text{Te}} = -1.5$ ,  $t_{\text{ch}, \text{Te}} = 0$ ,  $t_{z, \text{Te}} = -0.05$ ,  $\delta_1 = 0.13$ ,  $\delta_2 = 0$ . Solving this tight-binding Hamiltonian for its zero-energy eigenvectors then determines the FS of this  $\text{UTe}_2$  model. Note that we have made use of a primitive unit cell Brillouin zone rather than the full body-centred, orthorhombic Brillouin zone for ease of calculation however, reciprocal space dimensions of the unit cell remain the same. In Fig. 7.1a we plot a 2D cut of this Fermi surface at the  $k_z = 0$  plane. Consistent with recent measurements<sup>116</sup> it consists of two cylindrical-like bands, a hole-like band centred around the  $X$  point and an electron-like band around the  $Y$  point. In Fig. 7.1b we plot the same FS in 3D revealing how these FS cylinders undulate in the  $k_z$  direction. Crucially all measurements were performed at the  $(0 -1 1)$  cleave surface of  $\text{UTe}_2$  thus requiring an understanding of the 2D projection of this FS to the  $(0 -1 1)$  reciprocal plane.

### 7.3 Fermi Surface Projection

The dimensions of the 1st Brillouin zone are defined by the periodicity of the crystal structure. In Fig. 7.2a we present two unit cells of  $\text{UTe}_2$  with the  $(0 -1 1)$  cleave plane indicated by the grey shaded plane. Looking down from the  $(0 0 1)$  direction, in Fig. 7.2b, we see that the structure is defined by stacks of uranium and tellurium atoms and has an x-axis periodicity,  $a = 0.41$  nm and y-axis periodicity  $b = 0.61$  nm. The subsequent Brillouin zone therefore has periodicity  $\pi/a = 7.66$  nm<sup>-1</sup> in the x-direction and  $\pi/b = 5.15$  nm<sup>-1</sup> in the y-direction. Rotating our point of view to the  $(0 -1 1)$  cleave surface, presented in Fig. 7.2c, we see that the x-axis periodicity remains the same however the horizontal direction is now defined by an inter-tellurium chain

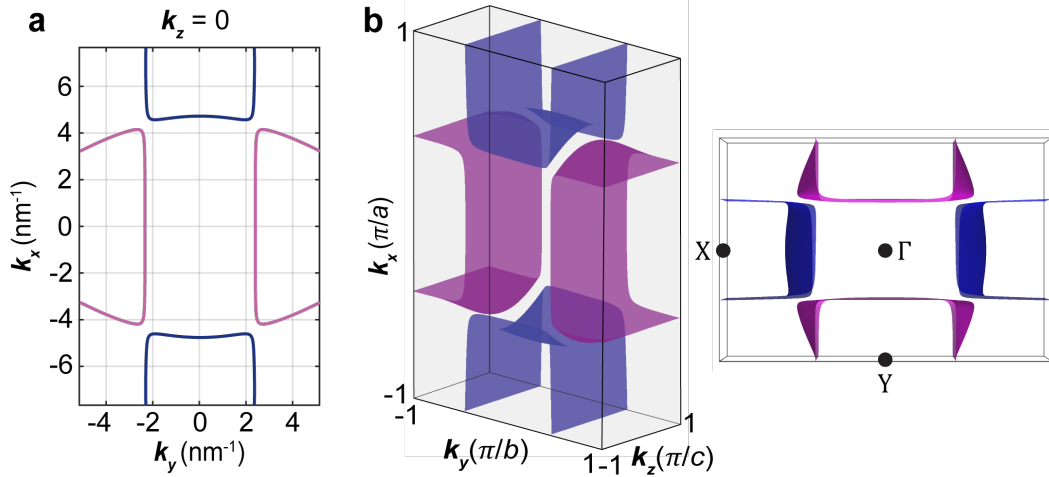


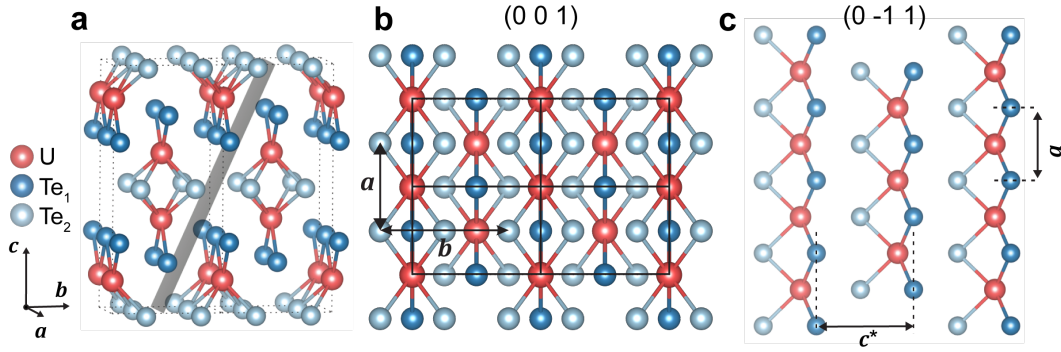
Figure 7.1: **a.** 2D Fermi surface (FS) cut at the  $\mathbf{k}_z = 0$  plane. Blue and pink FS sheets correspond to the hole- and electron-type Fermi surfaces respectively. **b.** 3D plot of the FS used in all subsequent calculations. Colours of the FS cylinders are the same as a. **c.** Schematic 2D projection of the 3D FS viewed perpendicular to the (0 -1 1) plane.

distance  $c^* = 0.76$  which, in turn defines the limits of the (0 -1 1) surface Brillouin zone (SBZ). We thus use this periodicity in discussing the horizontal scale in momentum space.

For scattering wavevectors connecting points of the Fermi surface, rotation from the (0 0 1) plane to the (0 -1 1) plane results in a change of  $k$ -space basis, defined by the translation vectors  $\mathbf{e}_a = (1, 0, 0)$  and  $\mathbf{e}_{c^*} = (0, \sin \theta, \cos \theta)$  where  $\theta = 23.7^\circ$ . A  $k_z = 0$  wavevector viewed from the (0 0 1) plane  $(a, b, 0)$  when projected to the (0 -1 1) plane becomes  $((a, b, 0) \cdot \mathbf{e}_a, (a, b, 0) \cdot \mathbf{e}_{c^*}) = (a, 0.4b)$ .

## 7.4 Normal State QPI

We can see how this  $k$ -space rotation works in practice by studying some expected scattering wavevectors of the normal state FS. While in theory we could connect any arbitrary points of the FS and propose this as a scattering wavevector, in reality we can take information gained from other research to guide our choice of wavevector. UTe<sub>2</sub> is one of many heavy-fermion superconductors<sup>121</sup> and thus experiences heavy  $f$ -electron hybridization at low temperature. The effects of this hybridization and the role of heavy fermion physics in UTe<sub>2</sub> is a matter of ongoing study, however, recent quantum oscillation experiments have pointed towards regions of the normal state band structure where the



$f$ -electron contribution is largest<sup>122</sup>. Heuristically, we can simulate this orbital contribution by increasing the intensity of these regions of our model FS. The resulting weighted FS is presented in Fig. 7.3a. These hybridized parts of the band structure are expected to contribute significantly to the low temperature density of states and thus should contribute most to scattering. From this we predict several scattering wavevectors  $\mathbf{p}_i$ ,  $i = 1 - 6$  which we plot as coloured arrows in Fig. 7.3a. To simulate the QPI with this simple model, we calculate the joint density of states (JDOS),  $J(\mathbf{q}, E)$ , which is defined using the spectral function  $A(\mathbf{k}, E)$  as below

$$J(\mathbf{q}, E) = \int A(\mathbf{k} + \mathbf{q}, E)A(\mathbf{k}, E)d\mathbf{k} \quad (7.11)$$

To quickly carry out this simulation using our model, in Fig. 7.3, we calculate the normalized autocorrelation using the Wiener-Khinchin theorem so that

$$\mathcal{A}(\mathbf{k}, E) = \text{FFT}[A(\mathbf{k}, E)] \quad (7.12)$$

$$J(\mathbf{q}, E) = |\text{IFFT}[\mathcal{A}(\mathbf{k}, E) \cdot \mathcal{A}^*(\mathbf{k}, E)]| \quad (7.13)$$

where the spectral function  $A(\mathbf{k}, E = 0)$  is the FS of Fig. 7.3a with spectral weight between zero and one. The resulting  $J(\mathbf{q}, E = 0)$  for this weighted FS viewed from the  $(0\ 0\ 1)$  plane is presented in Fig. 7.3b. Our proposed

scattering wavevectors  $\mathbf{p}_i$  produce high intensity peaks which we highlight by coloured arrows. The same QPI pattern viewed from the (0 -1 1) plane would have reduced y-axis components as outlined above.  $J(\mathbf{q}, E = 0)$  at this cleave plane is then presented in Fig. 7.3c. It features the full sextet of scattering wavevectors derived from the weighted FS, however, we now label these peaks  $\mathbf{q}_i$  to distinguish them from wavevectors of the (0 0 1) plane. At this new surface the coordinates of our normal state scattering wavevectors are  $\mathbf{q}_1 = (0.29\frac{2\pi}{a}, 0)$ ,  $\mathbf{q}_2 = (0.43\frac{2\pi}{a}, \frac{\pi}{c^*})$ ,  $\mathbf{q}_3 = (0.29\frac{2\pi}{a}, \frac{2\pi}{c^*})$ ,  $\mathbf{q}_4 = (0, \frac{2\pi}{c^*})$ ,  $\mathbf{q}_5 = (-0.14\frac{2\pi}{a}, \frac{\pi}{c^*})$ ,  $\mathbf{q}_6 = (0.57\frac{2\pi}{a}, 0)$ .

In Chapter 4 we discussed the charge density waves (CDWs) and pair density waves (PDWs) on the (0 -1 1) surface and saw several QPI maps obtained by FT[ $dI/dV(\mathbf{r}, V)$ ]. The wavevectors of the ordered phases detected in those experiments,  $(\mathbf{Q}_1, \mathbf{Q}_2, \mathbf{Q}_3)$  and  $(\mathbf{P}_1, \mathbf{P}_2, \mathbf{P}_3)$  respectively are the same as the scattering wavevectors discussed above, that is,  $|\mathbf{q}_2| = |\mathbf{Q}_1| = |\mathbf{Q}_2| = |\mathbf{P}_1| = |\mathbf{P}_2|$  and  $|\mathbf{q}_6| = |\mathbf{Q}_3| = |\mathbf{P}_3|$ . Whatever the source of the charge and subsequent superconducting orders, it appears likely that these heavy  $f$ -electron regions of the FS are involved in their formation. Of the remaining sextet of scattering wavevectors, the wavevector  $\mathbf{q}_4$  is a Bragg peak of the crystal structure, and wavevectors  $\mathbf{q}_1$ ,  $\mathbf{q}_3$ , and  $\mathbf{q}_5$  while expected from this naive scattering model, have yet to be seen in the presented measurements. These wavevectors are particularly relevant to QPI in the superconducting state, where they help characterize the superconducting order parameter. To see how, we must consider the effect of various  $p$ -wave order parameters on our tight-binding FS model.

## 7.5 Nodal Locations on the Fermi Surface

In Section 1.5 we found the dispersion relation for Bogoliubov quasiparticles is given by Eq. 1.57. The same equation defines the nodes or zeros of the superconducting order parameter, those regions of the FS which are ungapped by the superconducting pair potential. Their location is defined as anywhere on the FS for which  $\Delta^2(|\mathbf{d}(\mathbf{k})|^2 \pm |\mathbf{d}(\mathbf{k}) \times \mathbf{d}^*(\mathbf{k})|) = 0$ . For a  $B_{1u}$  state with  $\mathbf{d} \propto (\sin(k_y b), \sin(k_x a), 0)$  these nodes occur at the points  $k_y = (0, \pm\pi/b)$ ,  $k_x = (0, \pm\pi/a)$ . For  $B_{2u}$  we have  $\mathbf{d} \propto (\sin(k_z c), 0, \sin(k_x a))$  and nodes occur at  $k_z = (0, \pm\pi/c)$ ,  $k_x = (0, \pm\pi/a)$  and for  $B_{3u}$ ,  $\mathbf{d} \propto (0, \sin(k_z c), \sin(k_y b))$  and nodes are found at  $k_z = (0, \pm\pi/c)$  and  $k_y = (0 \pm \pi/b)$ . By plotting the

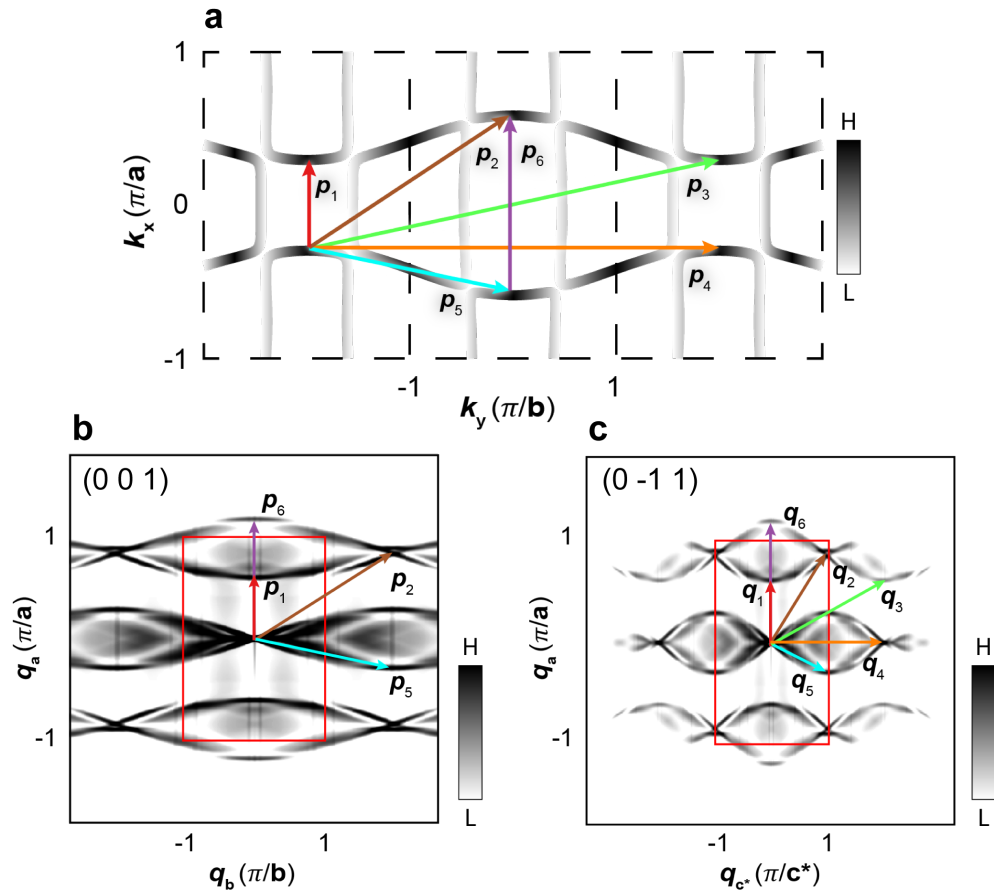


Figure 7.3: **a.** QSQPI Fermi Surface (FS) model, as seen from the  $(0\ 0\ 1)$  direction, with  $f$ -electron spectral weight, estimated from Ref. [122], indicated by black shading. A sextet  $\mathbf{p}_i$ ,  $i = 1 - 6$ , of scattering wavevectors connecting these hybridized regions of the FS are highlighted using coloured arrows. **b.** The joint density of states,  $J(\mathbf{q}, 0)$  of the weighted  $f$ -electron FS in a viewed from the  $(0\ 0\ 1)$  direction. The 1st Brillouin zone is outlined in red. **c.**  $J(\mathbf{q}, 0)$  from b projected to the  $(0\ -1\ 1)$  surface. The y-component of  $(0\ 0\ 1)$  scattering wavevectors are transformed to  $\mathbf{q}_y = \mathbf{p}_y \sin(\theta)$  where  $\theta = 23.7^\circ$ . The 1st  $(0\ -1\ 1)$  surface Brillouin zone is outlined in red.

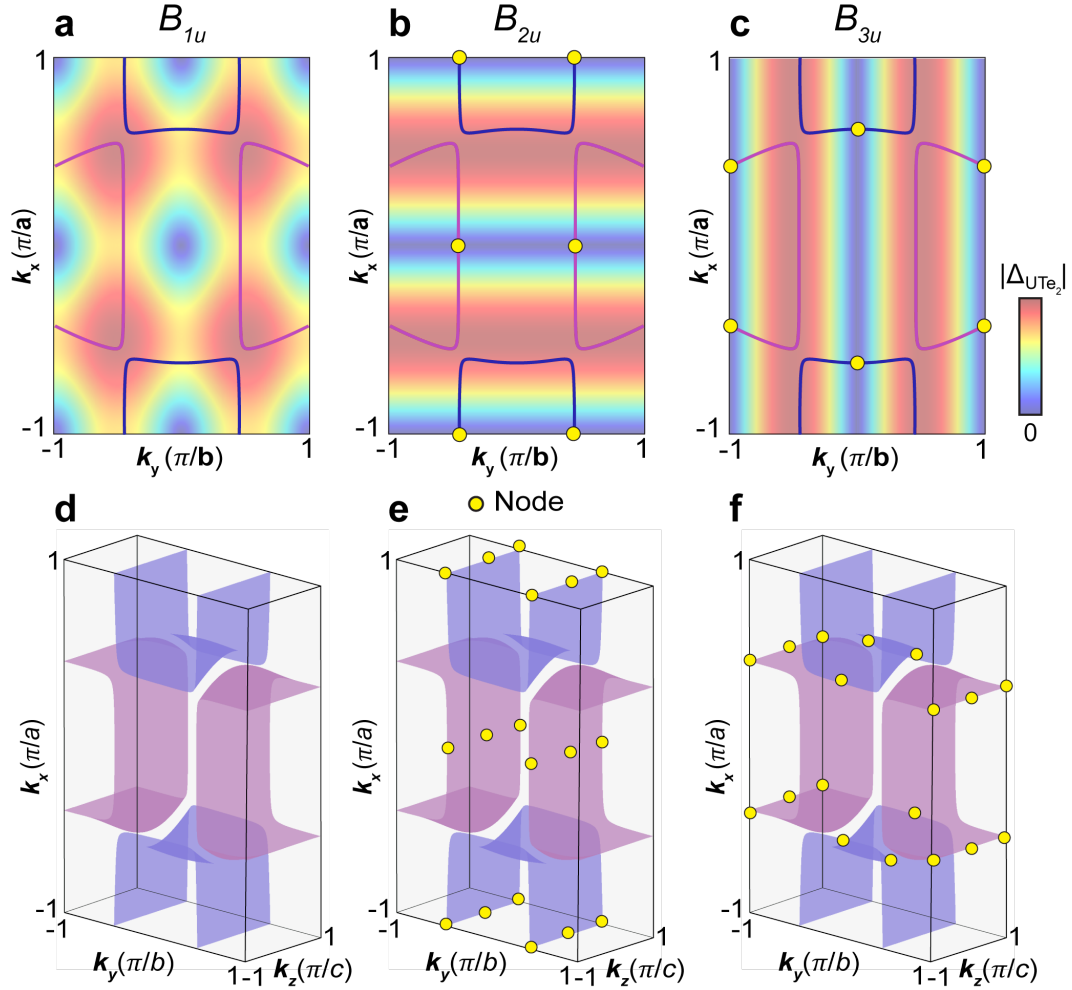


Figure 7.4: **a.** Superconducting gap function of symmetry  $B_{1u}$  on the  $\text{UTe}_2$  tight-binding Fermi surface defined above. The FS is cut at  $\mathbf{k}_z = 0$ . **b.** Superconducting gap function of symmetry  $B_{2u}$  on the  $\text{UTe}_2$  FS. **c.** The same as a and c for a superconducting order parameter with symmetry  $B_{3u}$

energy gap magnitude  $|\Delta_{\mathbf{k}}|$  for each order parameter throughout  $k_z = 0$ , as in Fig. 7.4, we see that nodes occur wherever the dark blue regions ( $|\Delta_{\mathbf{k}}| \rightarrow 0$ ) intersect the FS. Clearly from Fig. 7.4a the minima of a  $B_{1u}$  gap function do not intersect the FS in this model, consequently such a state would have no nodes and no QSB. In all future discussions we then focus primarily on the  $B_{2u}$  or  $B_{3u}$  states.

From the nodal locations derived above, in Fig. 7.4d-f, we present the 3D QSQPI FS model with theoretically predicted nodes indicated by yellow circles. The  $B_{1u}$  FS features no nodes in this model however, the  $B_{2u}$  and  $B_{3u}$  have nodal patterns reflecting their contrasting symmetries with nodes occurring at

the high-symmetry lines of the  $y$ - and  $x$ -axis respectively. The projection of these contrasting FS symmetries to the  $(0 -1 1)$  plane should result in starkly different nodal patterns.

To accurately simulate the FS projection, projected nodal patterns, and ultimately the superconducting QPI we implement the three candidate order parameters into our FS model by making use of the Bogoliubov-de Gennes Hamiltonian once again.

$$H(\mathbf{k}) = \begin{pmatrix} H_{\text{UTe}_2}(\mathbf{k}) \otimes I_2 & \Delta(\mathbf{k}) \otimes I_4 \\ \Delta^\dagger(\mathbf{k}) \otimes I_4 & -H_{\text{UTe}_2}^*(-\mathbf{k}) \otimes I_2 \end{pmatrix} \quad (7.14)$$

where  $H_{\text{UTe}_2}(\mathbf{k})$  is the Hamiltonian of our tight-binding model and the spin triplet order parameter  $\Delta(\mathbf{k}) = \Delta_0(\mathbf{d} \cdot \boldsymbol{\sigma})i\sigma_2$  with  $\Delta_0 = 1$ . The variables  $I_2$  and  $I_4$  are unit matrices of dimension  $2 \times 2$  and  $4 \times 4$ , respectively. To implement order parameters of  $B_{2u}$  and  $B_{3u}$  symmetry we use the following d-vectors

$$\mathbf{d}_{B_{2u}} = (C_1 \sin(k_z c), C_0 \sin(k_x a) \sin(k_y b) \sin(k_z c), C_3 \sin(k_x a)) \quad (7.15)$$

$$\mathbf{d}_{B_{3u}} = (C_0 \sin(k_x a) \sin(k_y b) \sin(k_z c), C_2 \sin(k_z c), C_3 \sin(k_y b)) \quad (7.16)$$

where  $a, b, c$  are lattice constants and  $C_0 = 0$ ,  $C_1 = 300\mu\text{eV}$ ,  $C_2 = 300\mu\text{eV}$ , and  $C_3 = 300\mu\text{eV}$ . The unperturbed bulk Green's function is then

$$G_0(\mathbf{k}, E) = [(E + i\eta)I - H(\mathbf{k})]^{-1} \quad (7.17)$$

where  $\eta$  is the quasiparticle broadening parameter. The corresponding unperturbed spectral function is

$$A_0(\mathbf{k}, E) = -1/\pi \text{Im}\{\text{Tr}(G_0(\mathbf{k}, E))\} \quad (7.18)$$

We can project these bulk spectral functions to the  $(0 -1 1)$  plane by integrating  $A_0(\mathbf{k}, E)$  along the normal to the  $(0 -1 1)$  plane. Performing this kind of calculation allows us to understand the projected band structure at this plane. Fig. 7.5a is the projected  $A_0(\mathbf{k}, E = 0)$  for  $\text{UTe}_2$  in the normal state. The primary contribution from the Fermi surface at this plane stems from the regions of the FS with 3D character. By implementing the  $B_{1u}$ ,  $B_{2u}$ , and  $B_{3u}$  gap functions into this model we can also calculate the projected  $A_0(\mathbf{k}, E = 0)$  in the superconducting state and use this to guide our understanding of the nodal pattern of these geometrically different  $p$ -wave order parameters. To do

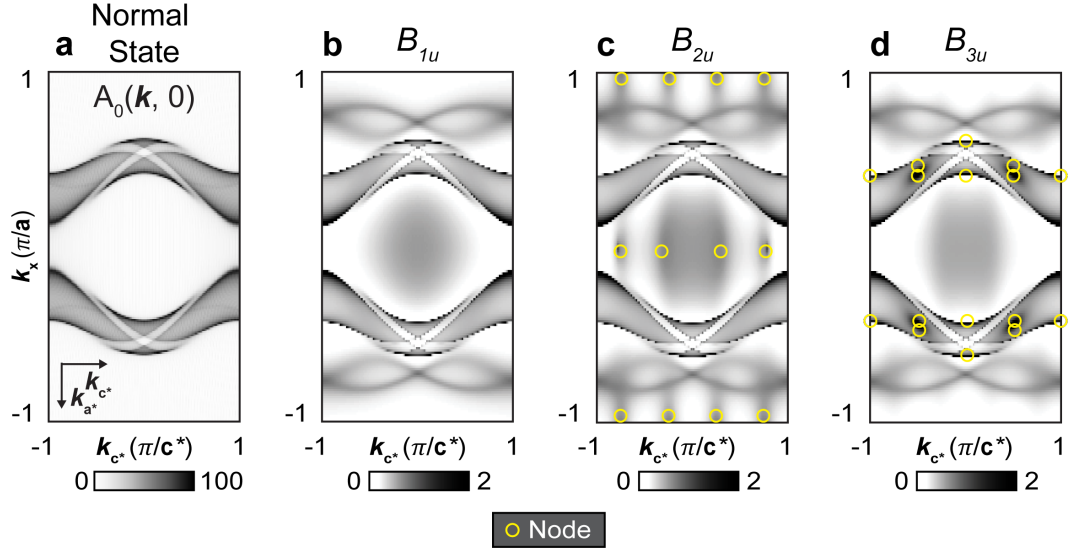


Figure 7.5: **a.** Bulk quasiparticle spectral function  $A_0(\mathbf{k}, E = 0)$  for the (0 -1 1) surface of  $\text{UTe}_2$  in the normal state. Bulk contributions are dominated by the projected components of the Fermi surface (FS) with 3D character. **b.**  $A_0(\mathbf{k}, E = 0)$  calculated in the superconducting state for an order parameter of  $B_{1u}$  symmetry. No nodes are seen for  $B_{1u}$  in this model as zeros of the pair potential do not cross the FS. **c.**  $A_0(\mathbf{k}, E = 0)$  calculated for an order parameter of  $B_{2u}$  symmetry. Nodes at  $k_z = (0, \pm\pi/c)$  and  $k_x = (0, \pm\pi/a)$  are projected to the (0 -1 1) surface forming lines of nodes which are highlighted by yellow circles. **d.**  $A_0(\mathbf{k}, E = 0)$  for an order parameter of  $B_{3u}$  symmetry. Nodes lie on the regions of the normal state FS which contribute most to the projected spectral function.

so we must use sufficiently low damping  $\eta = 10\mu\text{eV}$  and extremely high out of plane k-space sampling rate  $P_{N_k} = 500,000$ . Fig. 7.5b-d are the projected bulk spectral functions at the (0 -1 1) plane for  $B_{1u}$ ,  $B_{2u}$ , and  $B_{3u}$ . Once again the spectral function mostly consists of the the projected 3D sections of the FS which even at  $E = 0$  contributes because of the weak  $p$ -wave gap and finite thermal broadening. In Fig. 7.5c and d we highlight the regions of increased intensity with yellow circles. These are the expected point nodes of the  $B_{2u}$  and  $B_{3u}$  gap functions and their location in momentum space determines the position and intensity of the QSB at this cleave surface.

## 7.6 Quasiparticle Surface Bands (QSBs)

While the projection of the bulk spectral function can give us some insights into the nodal locations and bulk scattering, it cannot account for states ex-

isting only at the surface and their contribution to the spectral weight at the (0 -1 1) cleave plane. As we discussed in Chapter 5, there are many ways of topologically classifying a material however without the presence of a closed FS pocket the topological classification of UTe<sub>2</sub> cannot be considered a straightforward nodal, weak topological superconductor. However, a literature exists which succeeds in defining topological invariants for UTe<sub>2</sub> with a cylindrical band structure similar to that considered herein<sup>123,124</sup>. These weak topological phases are dependent on the usual global symmetries and also on crystal symmetries making UTe<sub>2</sub> a topological crystalline superconductor. Constructing similar crystalline topological invariants for our QSQPI band structure is a future research goal. As we will see, our surface spectral function simulations suggest that flat bands of zero-energy surface states exist on the (0 -1 1) surface. Whether these states are protected by topological invariants remains to be seen. We therefore distinguish the zero-energy states discussed in this QPI project by referring to them as quasiparticle surface bands (QSBs) in contrast to the previous chapter which features TSBs due to the topological protection guaranteed by the spherical FS. What remains clear regardless of theory, is that a zero-energy Andreev bound state is present at the (0 -1 1) surface of UTe<sub>2</sub> and is likely the result of *p*-wave superconductivity in bulk.

The unique physics of these *p*-wave and potentially topological surface states then envisages the bulk nodes playing a central role in any QSB<sup>125</sup>. Theory predicts that their *k*-space locations are projected onto the surface Brillouin zone (SBZ) and, moreover, that a contour of zero-energy QSB states (Fermi arc) connects pairs of projected nodal wavevectors<sup>97</sup>. In Fig. 7.6a and c we present the projection of the  $B_{2u}$  and  $B_{3u}$  point nodes to the (0 -1 1) plane as derived from Fig. 7.5. It is then expected that QSB scattering should be dominated by regions between nodes which we illustrate schematically in Fig. 7.6a,c by coloured scattering wavevectors connecting red inter-nodal regions. We thus derive a nonad of scattering wavevectors for the  $B_{2u}$  order parameter,  $\mathbf{q}_i^{B_{2u}}, i = 1 - 9$  and a sextet of scattering wavevectors  $\mathbf{q}_i^{B_{3u}}, i = 1 - 6$  for a  $B_{3u}$  order parameter which should dominate low energy ( $E < |\Delta_{\mathbf{k}}|$ ) scattering. This  $B_{3u}$  sextet of wavevectors is in fact quantitatively very similar to that derived from the weighted FS model above however at zero-energy we now observe scattering between QSB states on the projected FS. We overlay both sets of scattering wavevectors onto a larger *q*-space FOV in Fig. 7.6b,d to view the expected QPI wavevectors for each order parameter. This simple analysis

makes clear the geometric differences intrinsic to the projection of the nodes from the  $B_{2u}$  and  $B_{3u}$  order parameters and how this geometry effects the anticipated QSB.

To capture these geometric differences in our simulation we once again make use of low damping ( $\eta = 10\mu\text{eV}$ ) and high k-space sampling ( $P_{N_{\mathbf{k}}} = 500,000$ ) to simulate the bulk spectral function  $A_0(\mathbf{k}, E)$  and then derive the surface spectral function  $A_s(\mathbf{k}, E)$ . While obtaining the bulk unperturbed Green's function  $G_0(\mathbf{k}, E)$  is straightforward, calculating the surface Green's function,  $G_s(\mathbf{k}, E)$  and spectral function  $A_s(\mathbf{k}, E)$  requires introducing a strong planar impurity potential using the T-matrix technique as in Ref. [126]. In the limit of an infinite impurity potential the surface Green's function can be found exactly. From this, we acquire the surface spectral function

$$A_s(k_x, k_{c^*}, E) = -\frac{1}{\pi} \text{Im}\{\text{Tr}[G_s(k_x, k_{c^*}, E)]\} \quad (7.19)$$

In Fig. 7.7a,c we plot the surface spectral function derived for  $\text{UTe}_2$  with  $B_{2u}$  and  $B_{3u}$  symmetry. We highlight the projection of the bulk nodal locations, derived from  $A_0(\mathbf{k}, 0)$ , using yellow circles. Just like our prediction in Fig. 7.6, we find that QSB states occupy regions of momentum space connecting the projection of the bulk nodes. In Fig. 7.7b,d we present the JDOS, calculated as above using our  $A_s(\mathbf{k}, 0)$  images. Here we plot the q-space region  $k_x = \pm\pi/b$ ,  $k_{c^*} = \pm\pi/c^*$  as this is the main region of interest for our QSB scattering. In Fig. 7.7b,d we overlay the wavevectors of the nonad and sextet which feature in this q-space field of view (FOV). It is important to note the similarities between Fig. 7.7d and Fig. 7.3c, the JDOS derived from the  $f$ -electron regions of the FS and rotated to the (0 -1 1) plane. The features within the red box of Fig. 7.3c are strikingly similar to that obtained by the JDOS of the  $B_{3u}$  QSB spectral function. This is because the nodes and subsequent QSB of  $B_{3u}$  form on regions of the FS which contribute significantly to normal state scattering.

## 7.7 Final QSB QPI Simulations

From the above analysis it appears that the QPI patterns produced from the  $B_{2u}$  and  $B_{3u}$  order parameters should be clearly distinguishable in QPI measurements however, to now, we've focused on an unrealistic limit of our model, one in which quasiparticle damping is low, k-space sampling rates are imprac-

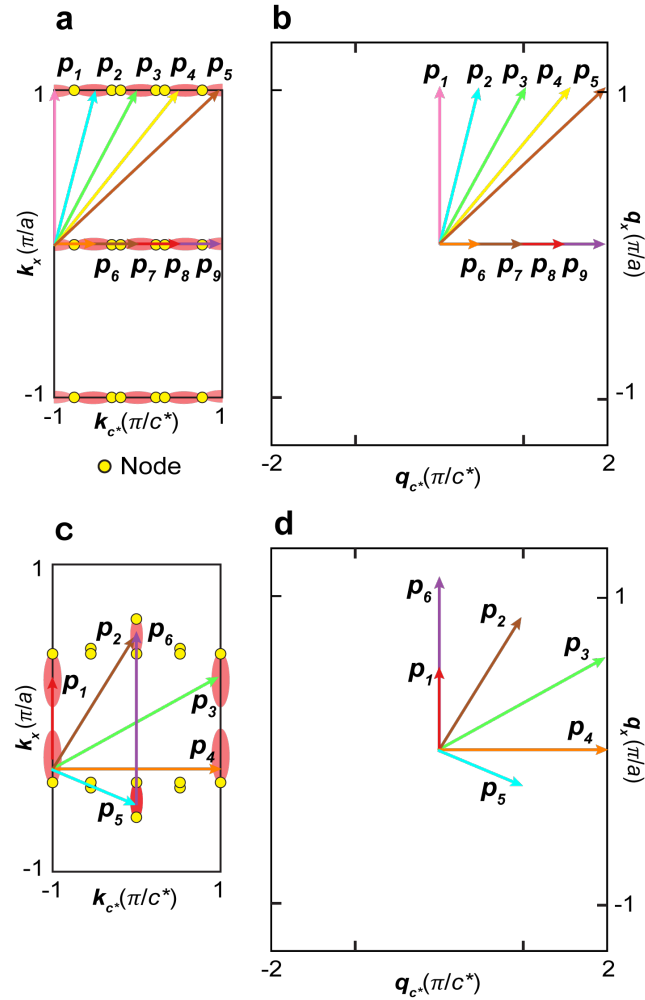


Figure 7.6: **a.** Projection of the bulk  $B_{2u}$  nodes to the SBZ. An illustration of QSB occupation is indicated using red intensity. A nonad of scattering wavevectors  $\mathbf{p}_i, i = 1 - 9$  connect these regions and should contribute strongly to scattering near zero-energy. **b.** Nonad of expected QPI scattering wavevectors for a  $B_{2u}$  order parameter. **c.** Projection of the bulk  $B_{3u}$  nodes to the SBZ featuring illustrative, red QSB intensity. A sextet of scattering wavevectors connects regions of maximum QSB intensity **d.** Sextet of expected QPI scattering wavevectors for a  $B_{3u}$  order parameter.

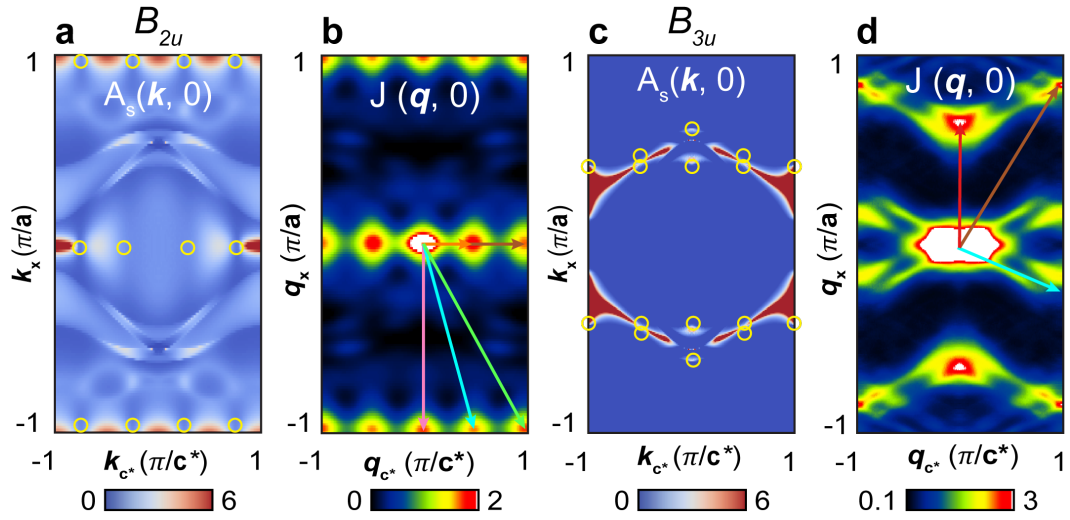


Figure 7.7: **a.** Surface spectral function  $A_s(\mathbf{k}, 0)$  calculated using an order parameter of  $B_{2u}$  symmetry. The location of nodes as derived from Fig. 7.5 are indicated by yellow circles. **b.** The joint density of states  $J(\mathbf{q}, 0)$  of  $B_{2u}$   $A_s(\mathbf{k}, 0)$ . Peaks from the nonad of wavevectors  $\mathbf{q}_i$ ,  $i = 1 - 9$  are presented as coloured arrows. **c.**  $A_s(\mathbf{k}, 0)$  calculated using an order parameter of  $B_{3u}$  symmetry. A strong QSB forms between the projection of the bulk nodes to the  $(0 -1 1)$  surface. **d.**  $J(\mathbf{q}, 0)$  calculated using  $A_s(\mathbf{k}, 0)$  of  $B_{3u}$ . Three peaks from the  $B_{3u}$  sextet are indicated with coloured arrows. This joint density of states calculation is similar to that in Fig. 7.3c due to the unique position of  $B_{3u}$  point nodes on the  $\text{UTe}_2$  Fermi surface.

tically high, and scattering is between all spin states. We've discussed these simulations because they confirm our understanding of the nodal pattern and subsequent QSB expected for these two odd-parity order parameters. However, we will now see that in a realistic model the low-energy scattering in the superconducting state can still feature significant contributions from the normal state FS making order parameter identification significantly more difficult.

To perform measurements in the superconducting state of  $\text{UTe}_2$  our STM head is cooled to  $T = 0.28\text{K}$ . Thermal fluctuations at this temperature limit the energy resolution of our measurements as they contribute energy of the order  $k_B T$  to the system, where  $k_B$  is Boltzmann's constant. At  $T = 0.28\text{K}$  these fluctuations are then  $k_B T \sim 25\mu\text{eV}$ . For experimental comparison, we increase the quasiparticle broadening parameter in our calculations to  $\eta = 30\mu\text{eV}$ . Critical to this final analysis is that we now calculate the correction to the local density of states (LDOS)  $\delta\rho(\mathbf{k}, E) = \int d\mathbf{r} \delta\rho(\mathbf{r}, E) e^{-i\mathbf{k}\cdot\mathbf{r}}$  rather than the joint density of states  $J(\mathbf{q}, E)$ . This correction to the LDOS is a more accurate technique in simulating QPI results as it takes into account not only the magnitude of the spectral function (as used in JDOS calculations) but the full structure of the T-matrix, which includes spin selection rules and both constructive and destructive quasiparticle interference. Furthermore, STM is a probe of the LDOS and by Fourier transform of this quantity one observes the correction to the LDOS from the QPI patterns,  $dI/dV(\mathbf{q}, E)$ . We define  $\delta\rho(\mathbf{q}, E)$  from the perturbed generalized Green's function where

$$\delta\rho(\mathbf{q}, E) = \frac{i}{2\pi} \int \frac{d^2\mathbf{q}}{S_{\text{BZ}}} \text{Tr}[g(\mathbf{q}, \mathbf{k}, E)] \quad (7.20)$$

where the perturbed generalized Green's function is

$$g(\mathbf{q}, \mathbf{k}, E) = G_s(\mathbf{q}, E)T(E)G_s(\mathbf{q} - \mathbf{k}, E) - G_s^*(\mathbf{q} - \mathbf{k}, E)T^*(E)G_s^*(\mathbf{q}, E) \quad (7.21)$$

Because  $\delta\rho(\mathbf{q}, E)$  is, in general, a complex quantity, all simulations presented herein are  $|\delta\rho(\mathbf{q}, E)|$ . The energy resolved surface spectral function  $A_s(\mathbf{k}, E)$  for our model with  $B_{2u}$  and  $B_{3u}$  order parameter symmetries is featured in Fig. 7.8a and b respectively. Clearly, the  $B_{3u}$  results are almost unchanged with these new parameters, however, the  $B_{2u}$  spectral function is significantly different. Its nodal pattern lies almost entirely on parts of the FS which contribute weakly to the surface spectral function. The resulting QSB is therefore weakened significantly with increasing damping. We can then expect the QPI

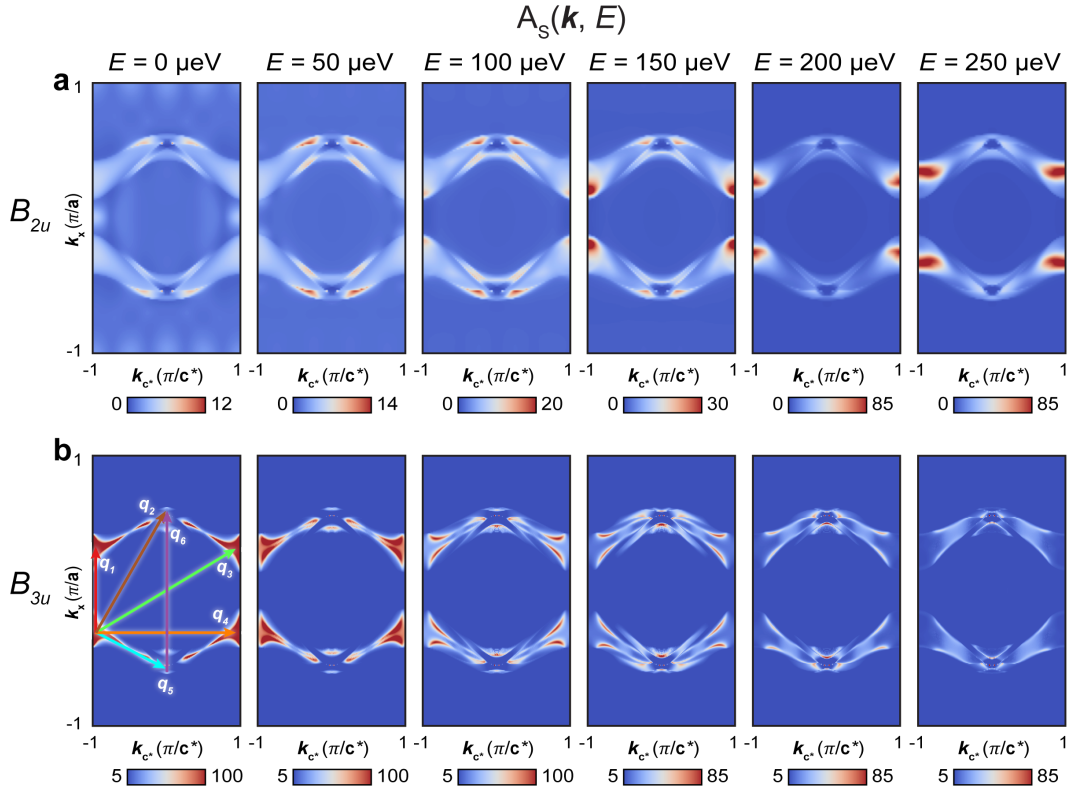


Figure 7.8: **a.** Surface spectral function  $A_s(\mathbf{k}, E)$  for a  $B_{2u}$  order parameter at energies  $E = 0, 50\mu\text{eV}, 100\mu\text{eV}, 150\mu\text{eV}, 200\mu\text{eV}, 250\mu\text{eV}$ . With more reasonable thermal broadening the nodal contribution to the surface spectral function is small and at zero-energy only weak contributions from the  $B_{2u}$  QSB are observed. **b.**  $A_s(\mathbf{k}, E)$  at energies  $E = 0, 50\mu\text{eV}, 100\mu\text{eV}, 150\mu\text{eV}, 200\mu\text{eV}, 250\mu\text{eV}$  for a  $B_{3u}$  order parameter. The nodes residing on the 3D components of the Fermi surface generate a QSB which dominates low-energy scattering up to the superconducting gap edge.

of a FS with  $B_{2u}$  order parameter symmetry to be largely the same as that from the normal state and, as we've seen in Fig. 7.7d the QPI expected of a FS with  $B_{3u}$  symmetry is geometrically similar to the bulk band structure scattering.

## 7.8 Normal State & QSB QPI Measurements

Our low-energy scattering calculations, both in the normal and superconducting state, have revealed that the signatures of the order parameter symmetry should be difficult to distinguish from the normal state FS contributions. The difference in scattering between the normal and superconducting states can be

directly studied by measuring  $dI/dV(\mathbf{r}, V) \equiv g(\mathbf{r}, V)$  within the same FOV at  $T = 4.2\text{K}$  and  $T = 0.28\text{K}$ . In Fig. 7.9a we present normal state differential conductance  $g(\mathbf{r}, E = 0)$  recorded in a 66nm FOV under tunnelling setpoint conditions  $V_b = 3\text{mV}$ ,  $I_s = 200\text{pA}$ . This data has been sheared and LF corrected to allow exact registration with our superconducting state measurements. In Fig. 7.9b we present the Fourier transform of a,  $g(\mathbf{q}, E = 0)$ . As we noted previously,  $\mathbf{q}_2$  and  $\mathbf{q}_6$  are the normal state CDW wavevectors and in the superconducting state PDW modulations are induced at the same wavevectors. We note that  $\mathbf{q}_6$  is weaker in this measurement than in previous  $g(\mathbf{q}, E)$  figures because these measurements make use of a tip condition which appears more sensitive to short wavevectors.  $\mathbf{q}_4$  is a result of the lattice periodicity and occurs at the point  $(0, \frac{2\pi}{c^*})$ . The short wavevectors are of particular interest in this study and in the normal state we observe arc-like intensity which links  $\mathbf{q} = 0$  with  $\mathbf{q}_5$ . In the normal state this intensity is the result of scattering between the hole-like FS of adjacent  $\text{UTe}_2$  Brillouin zones. For  $\text{UTe}_2$ , they are stacked in the  $k_z$  direction with an offset of  $\delta k_z = \pi/c$  between them allowing the  $\mathbf{q}_5$  wavevector to trace out the contours of the band around the  $X$  point. Our heuristic model of  $f$ -electron scattering appears consistent with these  $T = 4.2\text{K}$  measurements (see Fig. 7.3a). However, in contrast to Fig. 7.3c, we do not observe  $\mathbf{q}_1$  nor the higher order peak  $\mathbf{q}_3$  in these normal state measurements. The  $\mathbf{q}_1$  peak in particular will prove important, however, we must first compare these experimentally derived normal state scattering wavevectors with those in the superconducting state.

Cooling down our STM system to  $T = 0.28\text{K}$ , we perform the same measurements as above while  $\text{UTe}_2$  is in the superconducting state. A notable difference between these measurements is that, in the superconducting state, the in-gap tunnelling mechanism is not normal single particle tunnelling but instead, resonant Andreev tunnelling. In Chapter 6 we established the use of superconducting tips as direct probes of QSB quasiparticles however, we can study the differences between these normal and superconducting tip measurements by directly comparing the resulting Fourier transform of their differential conductance maps. This is done in Appendix E. Particularly, in Appendix Fig. E.1b we plot  $g(\mathbf{q}, 0)$  acquired using a normal metal tip and in Appendix Fig. E.1d we plot the Fourier transform of this Andreev conductance  $a(\mathbf{q}, 0)$ , acquired using a superconducting tip. There are several common characteristics including the arc-like feature connecting  $\mathbf{q} = 0$  and  $\mathbf{q}_5$  and the peaks

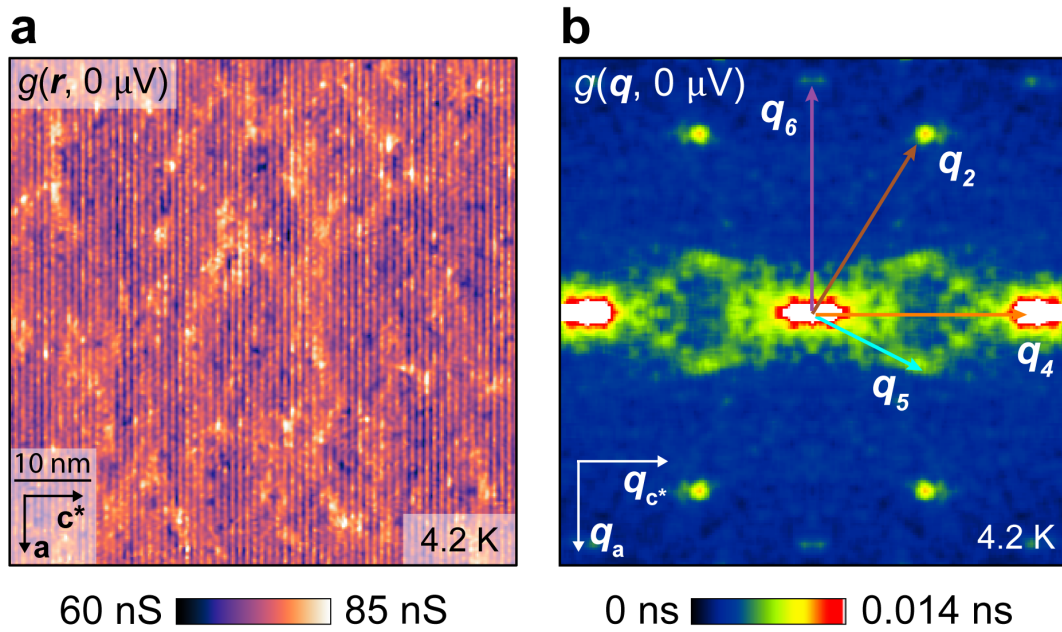


Figure 7.9: **a.**  $g(\mathbf{r}, E = 0)$  measured at  $T = 4.2\text{K}$  in the normal state of  $\text{UTe}_2$ . Measurements are performed in a  $66\text{nm}$  FOV with tunnelling bias voltage  $V_b = 3\text{mV}$  and setpoint current  $I_s = 200\text{pA}$ . **b.** The Fourier transform of **a**,  $g(\mathbf{q}, 0)$ . Four of the sextet of scattering wavevectors introduced above are observed in the normal state at the  $(0 -1 1)$  surface. These are highlighted using coloured arrows

at  $\mathbf{q}_2$ , however, the scattering features are strongly enhanced by the use of the superconducting tip. This is expected if we assume that the zero-energy Andreev conductance is proportional to the amplitude of QSB wavefunctions. Then spatial interference of QSB wavefunctions should manifest themselves as spatial variations in  $a(\mathbf{r}, E)$ , and subsequent Fourier transform of this quantity,  $a(\mathbf{q}, E)$  should allow high signal-to-noise measurements of QSB QPI at the surface of  $\text{UTe}_2$ .

Now in Fig. 7.10a we plot the measured Andreev differential conductance  $a(\mathbf{r}, E)$ , recorded at  $T = 0.28\text{K}$  in the same FOV as Fig. 7.9a above under exactly the same junction conditions  $V_b = 3\text{mV}$ ,  $I_s = 200\text{pA}$ . Fig. 7.10b reveals the high signal-to-noise scattering measurements made possible by the superconducting tip. This zero-energy QPI image,  $a(\mathbf{q}, 0)$ , reveals the complete sextet  $\mathbf{q}_i$ ,  $i = 1 - 6$  derived now from several considerations of the pairing symmetry and band structure. To make clear the shift in the relative intensity of these scattering wavevectors, in Fig. 7.10c we plot the normalized intensities of  $g(\mathbf{q}, 0)$  (orange) and  $a(\mathbf{q}, 0)$  (blue) taken along horizontal linecuts indicated in Fig. 7.10b by the white arrows. We normalize the scattering intensity of both QPI maps by setting regions of background (BG) noise to  $g(\mathbf{q}_{\text{BG}}, 0) = 1$  and  $a(\mathbf{q}_{\text{BG}}, 0) = 1$ . Clearly all peaks, except for  $\mathbf{q}_2$ , are enhanced at  $T = 0.28\text{K}$  however we note that, in general,  $\mathbf{q}_6$  is only weakly enhanced at these temperatures and appears unrelated to superconductivity. By contrast, features at small wavevectors are strongly enhanced at these temperatures with clear peaks appearing at  $\mathbf{q}_5$  and enhanced scattering connecting  $\mathbf{q} = 0$  and  $\mathbf{q}_5$ . Most notable is the appearance of  $\mathbf{q}_1$  which exists only at these temperatures and for energies within the bulk gap of  $\text{UTe}_2$  i.e. for  $V < 300\mu\text{V}$ . These QPI features are typical for  $a(\mathbf{q}, 0)$  and we include repeated measurements of this sextet, recorded at  $T = 0.28\text{K}$ , in Appendix F.

## 7.9 QSB QPI Theory-Experiment Correspondence

With our realistic band structure and surface spectral function projection methods, we now present the energy-resolved QPI patterns  $\delta\rho(\mathbf{q}, E)$ , calculated using the T-matrix method outlined in Section 7.7 and explained in detail in Ref. [126]. In Fig. 7.11a, we present  $\delta\rho(\mathbf{q}, E)$  for an order parameter of  $B_{2u}$  symmetry calculated using the surface spectral functions seen in Fig.

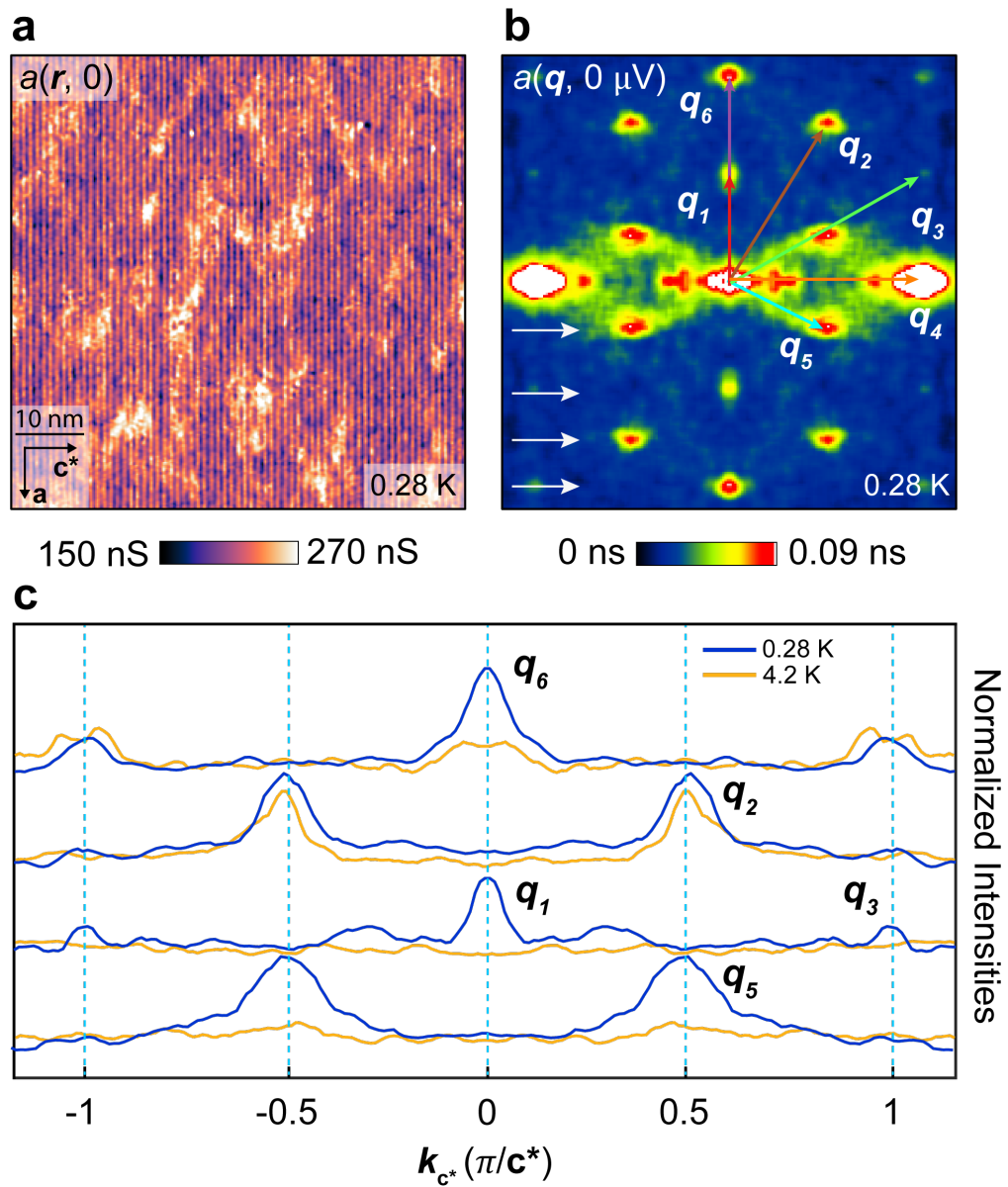


Figure 7.10: **a.** Andreev differential conductance  $a(\mathbf{r}, 0)$  recorded at  $T = 0.28$  K in a 66 nm FOV. The setpoint bias voltage is  $V_b = 3$  mV and the setpoint current is  $I_s = 200$  pA. This map has been shear and LF corrected to allow accurate registration between corresponding measurements at  $T = 4.2$  K as presented in Fig. 7.9. **b.** Fourier transformed Andreev conductance map  $a(\mathbf{q}, 0)$  revealing a sextet of scattering wavevectors indicated by coloured arrows. **c.** QPI linecuts recorded along the horizontal lines indicated with white arrows in **b**. Intensities are normalized using background noise levels of their corresponding QPI maps,  $g(\mathbf{q}, 0)$  and  $a(\mathbf{q}, 0)$ . Several wavevectors are enhanced in the superconducting state, particularly  $\mathbf{q}_5$ . The wavevector  $\mathbf{q}_1$  appears only in the superconducting state and for energies within the superconducting energy gap

7.8. We focus on the  $\mathbf{q}$ -space region  $(\pm\pi/a, \pm\pi/c^*)$ . Clearly, the QPI pattern closely resembles the normal state scattering observed at  $T = 4.2\text{K}$  in Fig. 7.9b, with peaks at  $\mathbf{q}_2$  and weak arc-like intensity connecting  $\mathbf{q} = 0$  and  $\mathbf{q}_5$ . The distinctive nonad of  $B_{2u}$  scattering wavevectors  $\mathbf{q}_i, i = 1-9$  we anticipated from the low damping spectral function are not seen in this calculation as the normal state FS dominates the low-energy scattering. This simulation can also be compared to the QPI in the superconducting state,  $a(\mathbf{q}, E)$  presented in Fig. 7.11c. There are numerous similarities between  $a(\mathbf{q}, E)$  and these  $B_{2u}$  QPI simulations, however, these common features are inherited from the normal state band structure as evidenced by our QPI measurements at  $T = 4.2\text{K}$ . There are no distinct QSB scattering features in this  $B_{2u}$  simulation, however, even if its QSB were relevant, its nonad of wavevectors would be easily recognized in our measurements.

In Fig. 7.11b we present  $\delta\rho(\mathbf{q}, E)$  for our  $\text{UTe}_2$  band structure in the presence of an order parameter with  $B_{3u}$  symmetry. Its sharp features are the result of the prominent QSB spectral weight near zero-energy which we saw in Fig. 7.8. The results of QSB scattering are then the enhancement of scattering features, in particular, more dominant scattering in the region connecting  $\mathbf{q} = 0$  and  $\mathbf{q}_5$  at zero-energy. The  $B_{3u}$  QSB forms near those nodes on the  $k_y = 0$  line of the hole-like band surrounding the X point of the Brillouin zone which, as we outlined in our simple  $f$ -electron scattering model, produces this arc-like scattering. Notably in neither the  $B_{2u}$  nor the  $B_{3u}$  calculations do we see a distinct peak at  $\mathbf{q}_5$ . This particular peak is only seen at low temperatures  $T = 0.28\text{K}$  but also appears at energies outside of the superconducting gap thus suggesting it is a normal state feature, enhanced at low temperatures, and possibly related to the CDW mechanism at this surface. Finally, the peak at  $\mathbf{q}_1$  is the most important of our superconducting state scattering features. It appears only in the superconducting state and only within the superconducting energy gap of  $\text{UTe}_2$ . While it is a natural scattering wavevector in our naive band structure JDOS, as in Fig. 7.3, in a more detailed model, like that used for our QPI calculations here, scattering at this wavevector is not allowed due to spin scattering rules included in the T-matrix. From our detailed theory calculations we only find this peak when considering an order parameter of  $B_{3u}$  symmetry. The uniqueness of  $\mathbf{q}_1$  in this superconducting phase is a result of spin-momentum locking of the QSB eigenstates. In Fig. 7.12 we present the spin and energy resolved surface spectral function for the  $B_{3u}$  QSB. Due

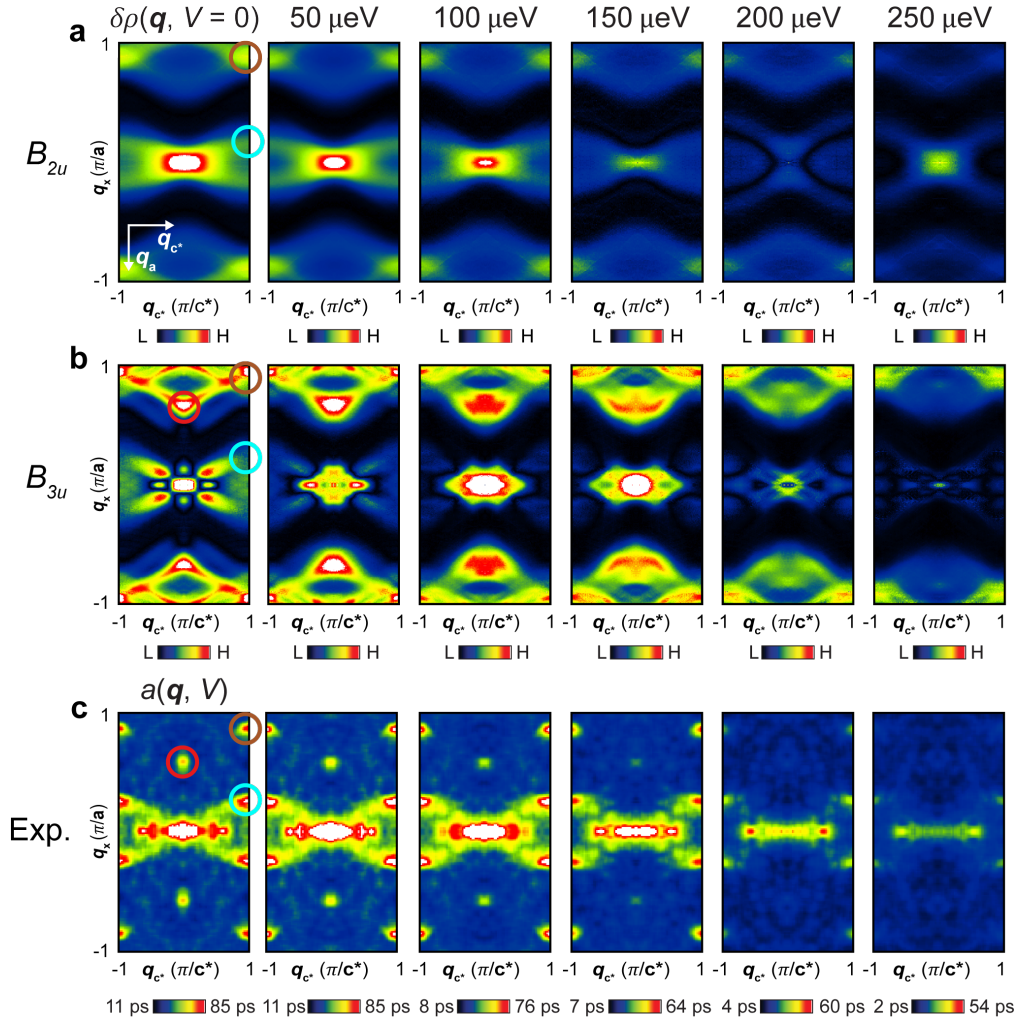


Figure 7.11: **a.** Predicted QPI patterns,  $\delta\rho(\mathbf{q}, V)$  for a  $\text{UTe}_2$  band structure model with  $p$ -wave order parameter symmetry  $B_{2u}$ . Contributions from the bulk band structure make QPI with this order parameter symmetry similar to the normal state QPI observed in Fig. 7.9. **b.**  $\delta\rho(\mathbf{q}, V)$  for a  $\text{UTe}_2$  band structure model with order parameter symmetry  $B_{3u}$ . Several scattering features are unique to this order parameter symmetry including enhanced scattering between  $\mathbf{q} = 0$  and  $\mathbf{q}_5$  at zero-energy and, most critically, the presence of scattering wavevector  $\mathbf{q}_1$ . **c.** Experimentally measured QPI  $a(\mathbf{q}, V)$  cropped from the same dataset as seen in Fig. 7.10. The wavevector  $\mathbf{q}_1$  appears only in the superconducting state for energies within the superconducting energy gap.

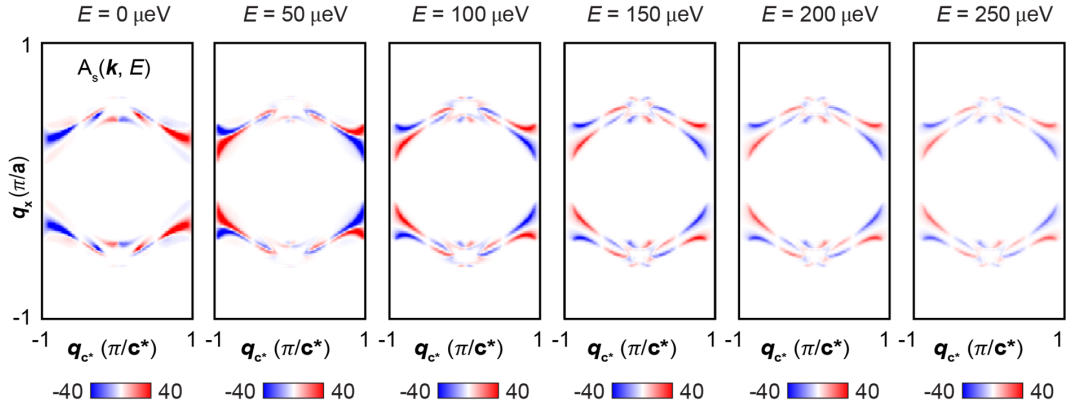


Figure 7.12: The surface spectral function  $A_s(\mathbf{k}, E)$  for a  $B_{3u}$  QSB where spin aligned along the  $x$  direction is coloured blue and spin in the  $-x$  direction is shown in red. Only  $B_{3u}$  allows spin conserved scattering in the  $x$  direction producing the wavevector  $\mathbf{q}_1$  near zero-energy.

to  $B_{3u}$ 's unique dependence on the  $z$  and  $y$  coordinates, eigenstates of the QSB have the same spin at  $+\mathbf{q}_a$  and at  $-\mathbf{q}_a$  thus allowing spin-conserved scattering in the  $x$  direction. Neither  $B_{1u}$  nor  $B_{2u}$  exhibits this symmetry and therefore, do not allow scattering to appear at  $\mathbf{q}_1$ . Based on this series of theoretical calculations and experimental results we therefore conclude that the zero-pressure, zero-field, low-temperature superconducting phase of  $\text{UTe}_2$  is one with  $B_{3u}$  symmetry.

# Chapter 8

## Final Remarks

The results of this thesis can largely be divided into two parts; the discovery of a spatially modulating superconducting order parameter or pair density wave (PDW) at the surface of  $\text{UTe}_2$ , and the detection and characterization of the zero-energy surface state by spectroscopy and quasiparticle interference. Both research projects are based on the observation of unusual superconducting states and it is this which defines the overall focus of this thesis.

The detection of PDWs on the surface of  $\text{UTe}_2$  is now one of many recent reports of modulating energy gaps and Cooper pair density in unconventional superconducting systems<sup>29,28,79</sup>. In the time since publication of Ref. [30] there has been further investigation into the behaviour of the CDW and PDW in this system. The CDW has since been found to melt with increasing magnetic field via the generation of phase dislocations or topological defects<sup>127</sup> pointing to the importance of magnetic field interactions with the CDW. By cycling temperature and magnetic field Ref. [128] find that the CDW develops in the same local regions of the surface despite melting and reforming. The same report hypothesizes the onset of magnetic order or short-range magnetic correlations as the driving mechanism for the CDW. As shown in Fig. 7.3a, normal state scattering features appear to be related to the  $f$ -electron hybridization of the Fermi surface. The CDW and induced PDW therefore appear related to the heavy fermion nature of  $\text{UTe}_2$ , a subject in need of further study. Of particular importance in understanding the mechanism responsible for this CDW is the recent observation that the CDW is confined only to the (0 -1 1) surface<sup>129,130,131</sup>. Owing to the local character of the CDW, PDW, and magnetic interactions SI-STM remains an ideal probe for further investigation into these ordered phases.

---

Of particular importance to this thesis is the role of the superconducting niobium scan tip used for PDW and zero-energy state detection. The discovery that such  $s$ -wave tips permit resonant Andreev tunnelling to Andreev bound states opens the way to direct tunnelling measurement of surface states in other unconventional superconductors and especially in other  $p$ -wave candidates. Furthermore, the conclusions derived from tunnelling dependent measurements are quite general and could be of further use in distinguishing chiral from non-chiral superconducting states in other materials. Again, it is because of the superconducting scan tip that high-resolution, low-energy QPI measurements have become possible for  $\text{UTe}_2$ . Our resulting study of  $\text{UTe}_2$ 's normal and superconducting state QPI pattern revealed that the appearance of low  $\mathbf{q}$  scattering wavevectors around  $\mathbf{q}_5$  and at  $\mathbf{q}_1$  are indicative of an odd parity superconducting state with the symmetry  $B_{3u}$  of the crystal point group  $D_{2h}$ . The combined theoretical and experimental approach of these investigations can be applied to the any of the known  $p$ -wave candidates thus providing an avenue for future SI-STM measurements which may help greatly in classifying the odd parity order parameters of these materials.

While the study of  $p$ -wave superconducting condensates enters its sixth decade we hope that the discovery of  $\text{UTe}_2$ 's superconducting properties signals the arrival of more candidate odd parity materials. Should these materials be developed, researchers must be ready with a combined theoretical and experimental framework for their classification. We hope that the research presented herein provides a robust framework with which to detect these unusual superconducting states by SI-STM researchers in the future.

# Appendix A

## ARCHAOS

### A.1 Introduction

Almost all measurements presented in this thesis were carried out in Cornell University using the old, yet extremely productive  $^3\text{He}$  SI-STM system there, ARCHAOS. We therefore briefly introduce the key components of this STM which have allowed it to successfully probe many forms of quantum matter using stable  $dI/dV$  mapping over several days.

### A.2 Cryogenics

Measurements of all superconductors require cryogenic temperatures, the highest  $T_c$  among superconducting systems at ambient pressure is that achieved by  $\text{Hg}_{0.8}\text{Tl}_{0.2}\text{Ba}_2\text{Ca}_2\text{Cu}_3\text{O}_{8+\delta}$  with  $T_c = 138$  K [132]. The family of heavy-fermion superconductors have much lower transition temperatures, for the  $\text{UTe}_2$  samples studied herein the transition temperature is  $T_c \sim 1.6$  K therefore, sub-Kelvin temperatures are required to study this material deep in the superconducting regime.

To achieve such temperatures, the STM and its cryogenic insert (Fig. A.1) are kept inside a cryogenic storage dewar. In order to cool from room temperature,  $\sim 100$  litres of liquid nitrogen ( $\text{LN}_2$ ) are pushed into the STM dewar from a transfer storage dewar until a stable base temperature of 77 K is achieved. Subsequently, the  $\text{LN}_2$  is pushed out using  $^4\text{He}$  gas and  $\sim 100$  L of liquid  $^4\text{He}$ , obtained from the Clark Hall helium liquefaction facility, is transferred to the experimental dewar. Once this process is complete the cryogenic insert and STM scan head are thermally equilibrated to  $\sim 4.2$  K. This is still nearly three

times the transition temperature of  $\text{UTe}_2$  thus further cooling is required.

By taking advantage of evaporative cooling, by pumping on  $^4\text{He}$  for example, the temperature of the STM cryogenic insert can be lowered further as the vapour pressure of a gas is strongly dependent on temperature  $P_{\text{vap.}} \propto e^{-\frac{L}{RT}}$ . This evaporative cooling is eventually balanced by the inflow of heat from the surrounding environment however, temperatures as low as  $T \sim 1.5$  K, while pumping on liquid  $^4\text{He}$ , and  $T \sim 0.28$  K for  $^3\text{He}$  can be achieved via this method. This approach is the one taken in ARCHAOS. By adding  $^4\text{He}$  gas to the “1K pot” it becomes liquified as the ambient temperature of the insert is 4.2 K. Pumping on this liquified helium then cools the 1K plate of the insert to  $\sim 1.5$  K. During this process  $^3\text{He}$  gas contained within the  $^3\text{He}$  line condenses in the  $^3\text{He}$  pot. By lowering a canister containing activated charcoal to the 4 K plate the, now evaporating,  $^3\text{He}$  adsorbs to the large surface area of the charcoal granules thus reducing the vapour pressure and cooling the surrounding environment. Through this method the STM head can reach temperatures of  $T \sim 0.28$  K, well within the superconducting state of  $\text{UTe}_2$ .

Lastly, we note that cryogenic temperatures are also critically important in maintaining a vacuum environment. While the insert is pumped to a pressure of  $\sim 10^{-6}$  mbar by a turbomolecular (turbo) pump, this pump is subsequently turned off during measurement at which point the STM head has been cooled to  $T \sim 0.28$  K. At such temperatures, free atoms or molecules adsorb to the cold interior surfaces of the insert and vacuum can. Furthermore, the vapour pressure of all gases at such temperatures is order of magnitudes lower than can be achieved by room temperature pumping alone thereby safeguarding the sample from environmental impurities.

### A.3 Vibration Isolation

As outlined in Chapter 2, the tunnelling current, the key observable in STM, is exponentially dependent on the tip-sample distance. This current is therefore very sensitive to vibrational noise, particularly noise acting in the direction perpendicular to the sample surface. All SI-STMs therefore require vibration isolation. The isolation measures employed for ARCHAOS are presented in Fig. A.1a. The STM insert and its dewar are bolted to a room temperature plate at which the vacuum and gas systems connect. This plate is then floated on air springs supplied with compressed nitrogen gas. The STM room is elec-

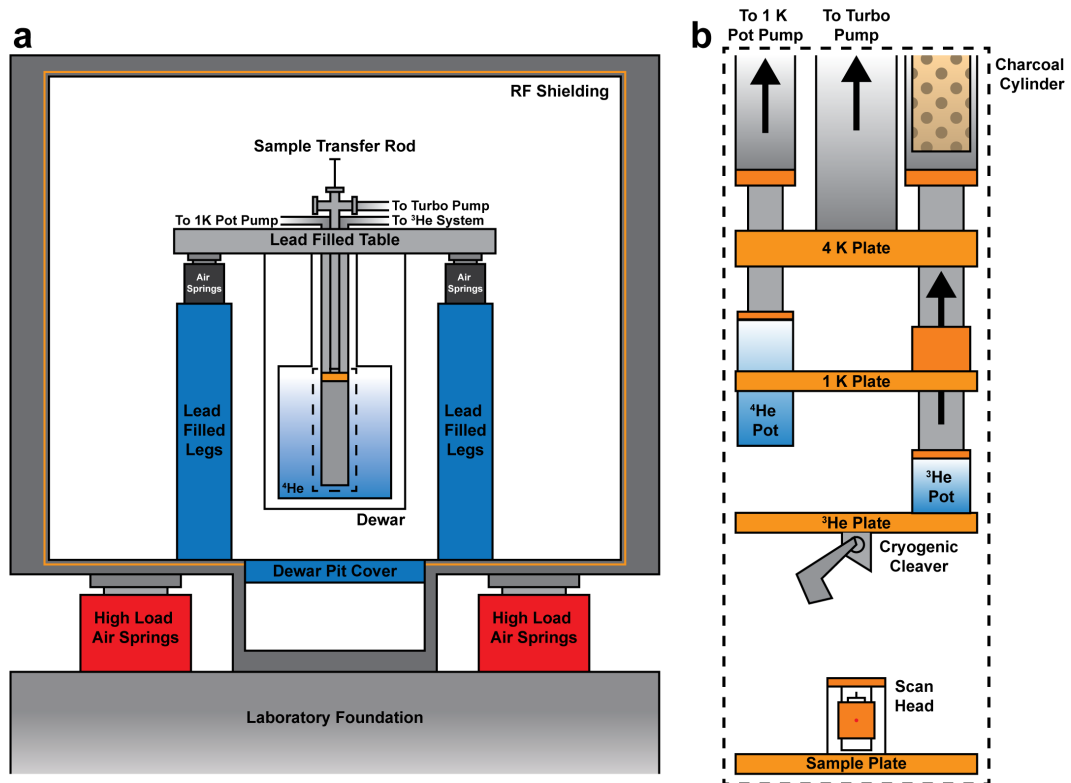


Figure A.1: **a.** Schematic of ARCHAOS vibration isolation systems. The table and legs supporting the STM dewar and insert are filled with lead to increase mass and dampen high frequency vibrations. Air springs further isolate the STM room and table from external vibrations intrinsic to the laboratory building. **b.** Schematic of the internal cryogenic systems indicated in b by the dashed black box. These illustrations are not to scale.

tromagnetically shielded from the surrounding environment via a metal cage and its entrance is sealed by acoustic doors. Furthermore, the STM room is built upon a concrete block supported on the Clark Hall basement foundations by large air springs further isolating the experiment from environmental noise.

## A.4 STM Head

The immense infrastructure required for an STM is all in support of stable operation of the STM scan head. The scan head used in ARCHAOS is of a similar design to that featured in Ref. [133]. It consists of a macor body inside which is the walker, a central sapphire prism firmly pressed against six stacks of piezoelectric crystals. Supplying a voltage slowly to these coarse motor stacks in sequence causes them to expand, moving the prism upwards, removing this voltage quickly and simultaneously allows the stacks to slip back to their neutral position while keeping the prism in place. This process allows large ( $\sim 100$  nm) steps in the  $z$  direction. The fine  $x$ - $y$  and  $z$  motion is performed by the scan tube which runs through the centre of the prism. This scan tube is a thin cylinder of piezoelectric material with four external electrodes. When voltage is applied to any one of the electrodes the tube bends towards the applied voltage. By applying voltage to an inner electrode all the piezo electrodes expand together allowing fine vertical motion of  $\sim 30$  nm. Measurements therefore require tens of thousands of coarse motor steps to near tunnelling current distances from full walker withdrawal, following this the scan tube is extended slowly until a setpoint tunnelling current is measured.

Samples to be inserted to the STM are initially glued to a brass sample stage using electrically and thermally conductive epoxy. An aluminium cleave rod, approximately the same diameter as the surface, is then glued to the easy cleave surface of the sample. The sample stage is then attached to the end of a transfer rod and inserted to the vacuum sealed upper chamber of the insert. This chamber is then evacuated and the transfer rod is pushed down through the insert, halting at each stage to thermalize with the surrounding environment. Upon passing through the  $^3\text{He}$  stage the cleaver is activated, sweeping the cleave rod from the sample and collecting it in a stainless steel bucket (Fig. A.1b). Finally the sample stage is pressed into the OFHC copper plate at the top of the STM head and secured by rotating its copper arms into slots in the head. A labelled photo of the ARCHAOS STM head is featured

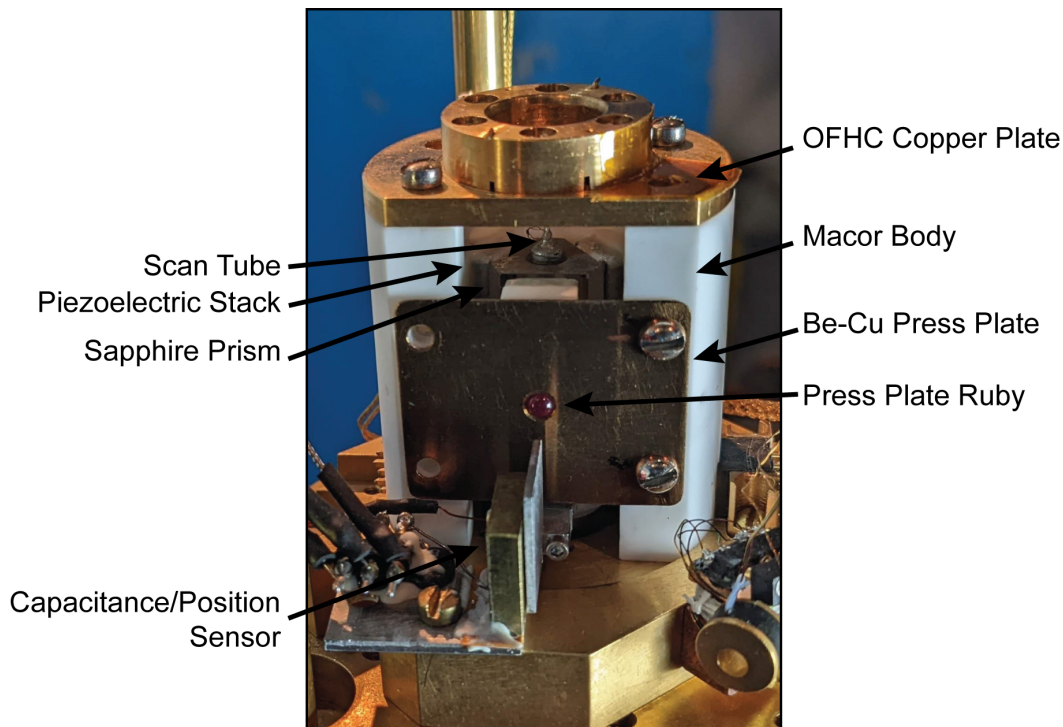


Figure A.2: Labelled photo of ARCHAOS STM scan head in position at the sample plate of the cryogenic insert

in Fig. A.2.

## A.5 Measurement & Control Electronics

Tunnelling current between the scan tip and sample under study can be as low as several hundred femto-amperes. Measurement of this current is therefore subject to electronic noise. To isolate this signal from the surrounding environment, the current is transferred through NbTi coaxial cable to a commercial current to voltage pre-amplifier (DL Instruments Model 1211) of gain  $10^{-9}$  A/V. Crucially, the noise level of this pre-amplifier is very low,  $\sim 5 \text{ fA}/\sqrt{\text{Hz}}$ . The resulting voltage is then converted to a digital signal via the Nanonis signal conversion interface (SC5) from SPECS. Furthermore the SC5 allows digital signals from the measurement computer to be converted to analog, thus allowing control of the bias voltage and scan tube piezos. Topographic imaging,  $dI/dV$  mapping, and other STM operations rely upon PID control of the piezo scan tube and this is carried out via software control from the measurement computer and Nanonis real-time controller (RC5) which houses the Nanonis CPU. The signal is then amplified using the Nanonis high-voltage

amplifier (HVA4). This commercial suite of nano positioning circuitry and software allows precise control of the STM scan tip allowing atomic resolution of superconducting samples.

# Appendix B

## PDW Fitting

We have made the claim that the use of superconducting scan tips in STM can improve the energy resolution of gap map measurements considerably. To better support this conclusion we describe the fitting procedure used to determine the energy of coherence peak maxima for both normal and superconducting tips. As the superconducting energy gap of  $\text{UTe}_2$  is approximately  $300 \mu\text{eV}$ , normal tip gap map measurements can be carried out in an energy range broader than the full  $2|\Delta_{\text{UTe}_2}|$  gap, in the measurement shown below we vary the bias voltage from  $-500\mu\text{V}$  to  $500\mu\text{V}$  in steps of  $25\mu\text{V}$  while recording a  $\frac{dI}{dV}$  measurement at each bias voltage step. After the  $\frac{dI}{dV}$  map has been completed we then aim to extract the energy of coherence peak maxima. To do so, we fit the energy interval  $-400\mu\text{eV}$  to  $-75\mu\text{eV}$  for the negative coherence peak, and  $125\mu\text{eV}$  to  $350\mu\text{eV}$  for the positive coherence peak with a polynomial of the form

$$g(V) = aV^2 + bV + c \quad (\text{B.1})$$

An example polynomial fit for the normal tip positive coherence peak is shown in Fig. Ba. To visualize the fitting quality of the positive and negative coherence peaks over the entire experimental FOV we introduce the fitting quality coefficient

$$R^2(\mathbf{r}) = 1 - \frac{\sum_{i=1}^N [g(\mathbf{r}, V_i) - dI/dV(\mathbf{r}, V_i)]^2}{\sum_{i=1}^N [g(\mathbf{r}, V_i) - \bar{g}(\mathbf{r})]^2} \quad (\text{B.2})$$

where  $dI/dV(\mathbf{r}, V_i)$  is the measured spectrum at position  $\mathbf{r}$  and voltage  $V_i$ ,  $g(\mathbf{r}, V_i)$  is the fitted spectrum at the same position and voltage, and  $\bar{g}(\mathbf{r})$  is the average fitted spectrum. We calculate this coefficient at every pixel in our normal tip gap map. The resulting normal tip  $R^2$  map for the positive coherence peak is shown in Fig. B.1b and the same map for the negative

coherence peak is shown in Fig. B.1c. Clearly, the normal tip gap map data is poorly fitted by this polynomial fit. To estimate the fit quality over the whole FOV we calculate  $R_{\text{RMS}}^2$  of the  $R^2$  map for this normal tip data and find  $R_{\text{RMS}+}^2 = 0.94$  and  $R_{\text{RMS}-}^2 = 0.94$  for the positive and negative coherence peaks, respectively. Not only is this fitting quality insufficient, but the poor fitting is distributed broadly around the map due to the poor spectral resolution. This explains the weak signal-to-noise ratio of the PDW peaks  $\mathbf{P}_1, \mathbf{P}_2, \mathbf{P}_3$  seen in Fig. 4.1d.

After registration of superconducting tip positive and negative coherence peak maps, we can fit this data with the same polynomial function as above. An example fit for the combined positive coherence peak  $\Delta_{\text{Nb+UTe}_2}$  is shown in Fig. Bd. The data is much more closely fitted by this polynomial and this can be seen clearly over the entire FOV in Fig. B.1e and Fig. B.1f for the positive and negative coherence peaks, respectively. The predominance of white pixels is indicative of excellent fit quality. The positive and negative superconducting tip coherence peak maps exhibit  $R_{\text{RMS}}^2$  values of 0.98 and 0.99, respectively. From this analysis, it is clear that the pronounced coherence peaks and low noise of the combined Nb-UTe<sub>2</sub> spectra allow PDW detection with energy resolution in the  $10\mu\text{eV}$  range.

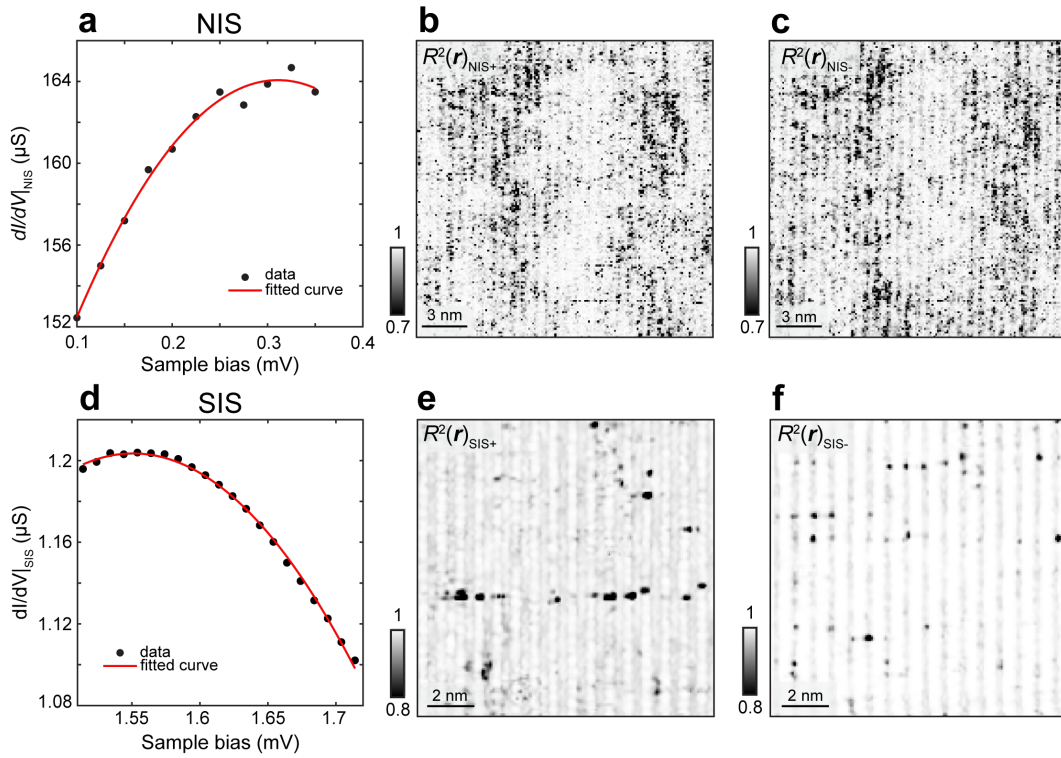


Figure B.1: **a.** Example spectrum showing the positive coherence peak of  $\text{UTe}_2$  detected by normal tip tunnelling spectroscopy (NIS). Data is shown in black dots and a second order polynomial fit is shown overlaid in red. **b.** Fitting quality coefficient,  $R^2(\mathbf{r})_{\text{NIS}+}$  for the positive coherence peak, calculated at each pixel in the normal tip FOV. **c.**  $R^2(\mathbf{r})_{\text{NIS}-}$  calculated at each pixel for the negative coherence peak. **d.** Example spectrum showing the positive coherence peak of the combined Nb- $\text{UTe}_2$  superconducting energy gap. Data is shown by black dots and the polynomial fit is overlaid as a red line. **e.** Fitting quality coefficient,  $R^2(\mathbf{r})_{\text{SIS}+}$  for the positive combined coherence peak, calculated at each pixel. **e**  $R^2(\mathbf{r})_{\text{SIS}-}$  for the negative coherence peak. The dominance of white pixels in both **e** and **f** is indicative of the improved fitting resulting from the use of a superconducting scan tip.

# Appendix C

## Josephson versus Andreev Tunnelling

Crucial to the interpretation of the results presented in Section 6, is that the zero-energy peak in differential conductance is the result of Andreev tunnelling between the  $s$ -wave scan tip and  $p$ -wave sample. As discussed in Section 2.4.2, Josephson tunnelling may also produce peaks in differential conductance centred at zero bias voltage therefore, to distinguish between the Josephson and Andreev effects, we study the behaviour of our zero-energy peak.

Firstly, we note that the zero-energy peak observed is significantly larger than that expected from the Josephson effect at equivalent tip-sample distances. This can be demonstrated clearly by plotting the measured zero-energy Andreev conductance  $a(0)$  against that of a typical SJTM measurement. For comparison, we plot the Josephson conductance measured for a Nb - NbSe<sub>2</sub> tunnel junction. Such a junction, between two  $s$ -wave superconductors, with energy gap magnitudes several times that of UTe<sub>2</sub>, is expected to allow Josephson currents much larger than those of an  $s$ -wave to  $p$ -wave tunnel junction [134]. This plot is presented in Fig. C.1a. At high junction resistance  $R_N \sim 3 \text{ M}\Omega$ , the Andreev conductance between UTe<sub>2</sub> and Nb is already an order of magnitude larger than that measured for Josephson coupling between  $s$ -wave superconductors. As the junction resistance is reduced, the Andreev conductance (blue) and Josephson conductance (red) behave entirely differently. The Andreev conductance increases quasi-linearly while the Josephson conductance grows as  $g(0) \propto 1/R_N^2$  as expected from Eq. 2.40. At low junction,  $R_N \sim 1.5 \text{ M}\Omega$ , the Andreev conductance at zero-energy begins to drop, as this intensity splits into two energy-symmetric maxima which further diverge with decreas-

ing junction resistance. The Josephson conductance, by contrast, continues to increase as  $1/R_N^2$ .

Lastly, we note that even the shape of the unsplit Andreev conductance peak provides indications that it is not the result of Josephson tunnelling. Equation 2.37 can be used to estimate the magnitude of the Josephson current in the phase-diffusive regime. Differentiation of this quantity with respect to the applied bias voltage  $V$  then yields

$$\frac{dI_P(V)}{dV} = \frac{I_J^2 Z (V_c^2 - V^2)}{2(V_c^2 + V^2)} \quad (\text{C.1})$$

Here  $I_J$  is the Josephson critical current,  $V_c = 2eZk_B T/\hbar$  is the Josephson critical voltage, and  $Z$  is the high-frequency impedance in series with the voltage source. The critical current and voltage can be extracted from  $I(V)$  measurements performed simultaneously with differential conductance mapping and is shown as inset in Fig. C.1. Attempting to fit this quantity to the measured zero-energy peak yields poor fitting values  $R^2 = 0.57$  and moreover, produces a characteristic feature of the Josephson peak, negative differential conductance at the Josephson critical voltage. This negative differential conductance is the result of the downturn in the slope of the phase-diffusive Josephson current which occurs after the maximum supercurrent  $I_P$  is realized at  $V_c$ . The absence of this downturn around the measured zero-energy peak is therefore a strong indication that the tunnelling effect producing this peak is unrelated to the Josephson effect.

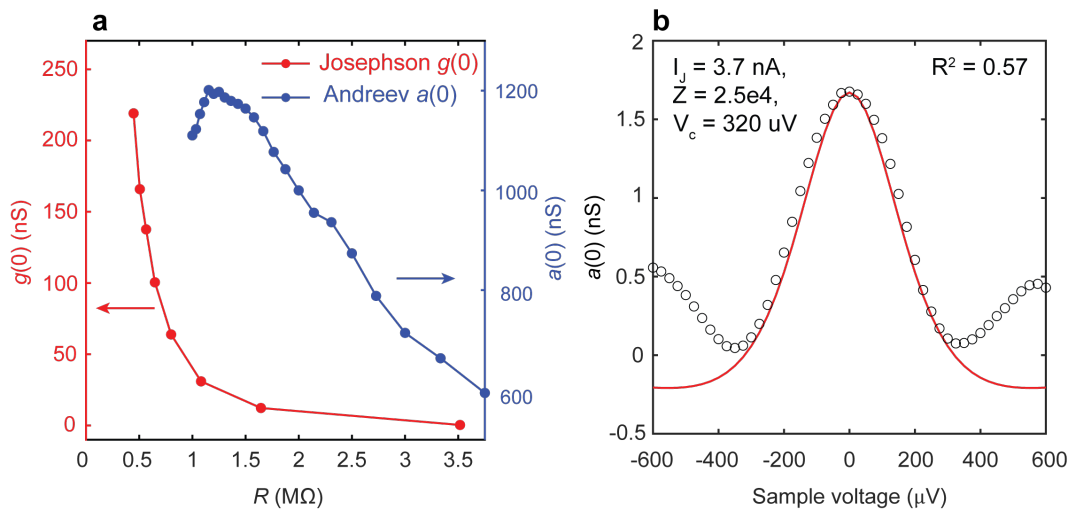


Figure C.1: **a**. Zero-energy differential conductance versus junction resistance for the Andreev zero-energy peak discovered in Ref. [109] and for the Josephson zero-energy peak measured in Ref. [28]. Josephson conductance grows as  $g(0) \propto 1/R_N^2$  while the Andreev conductance increases quasi-linearly until it begins to split due to proximity of the  $p$ -wave superconductor **b** Fitting the zero-energy Andreev conductance peak with the expression for the differential Josephson conductance above yields very poor fitting values ( $R^2 = 0.57$ ) due to the difference in their characteristic spectral shapes

# Appendix D

## Phase Fluctuations in the SIP Model

These data and SIP model raise the issue of fluctuations in the relative phase  $\delta\phi$  between the Nb and UTe<sub>2</sub> order parameters when interacting predominantly by Andreev coupling. Recall, that if UTe<sub>2</sub> is an odd-parity superconductor with a nodal, non-chiral, time-reversal conserving state  $\Delta_k$ , the minimum energy SIP relative phase is  $\delta\phi = \pi/2$  due to proximity of the s-wave electrode. This effect will split the zero-bias Andreev conductance as shown in Fig. 6.9. To evaluate if thermal fluctuations in  $\delta\phi$  should wipe out the peak splitting effect for the realistic parameterization of  $\Delta_k$  of UTe<sub>2</sub>, temperature  $T$ , and junction resistance  $R$ , we calculate the TSB density-of-states,  $N(E)$ , when  $\delta\phi = \pi/2$ , and when  $N(E)$  is averaged over the whole range  $0 < \delta\phi < \pi$ . The result, as presented in Fig. D.1, demonstrates that realistic phase fluctuations will not wipe out s-wave tip-induced  $N(E)$  splitting, thus preserving the Andreev  $a(V)$  conductance splitting.

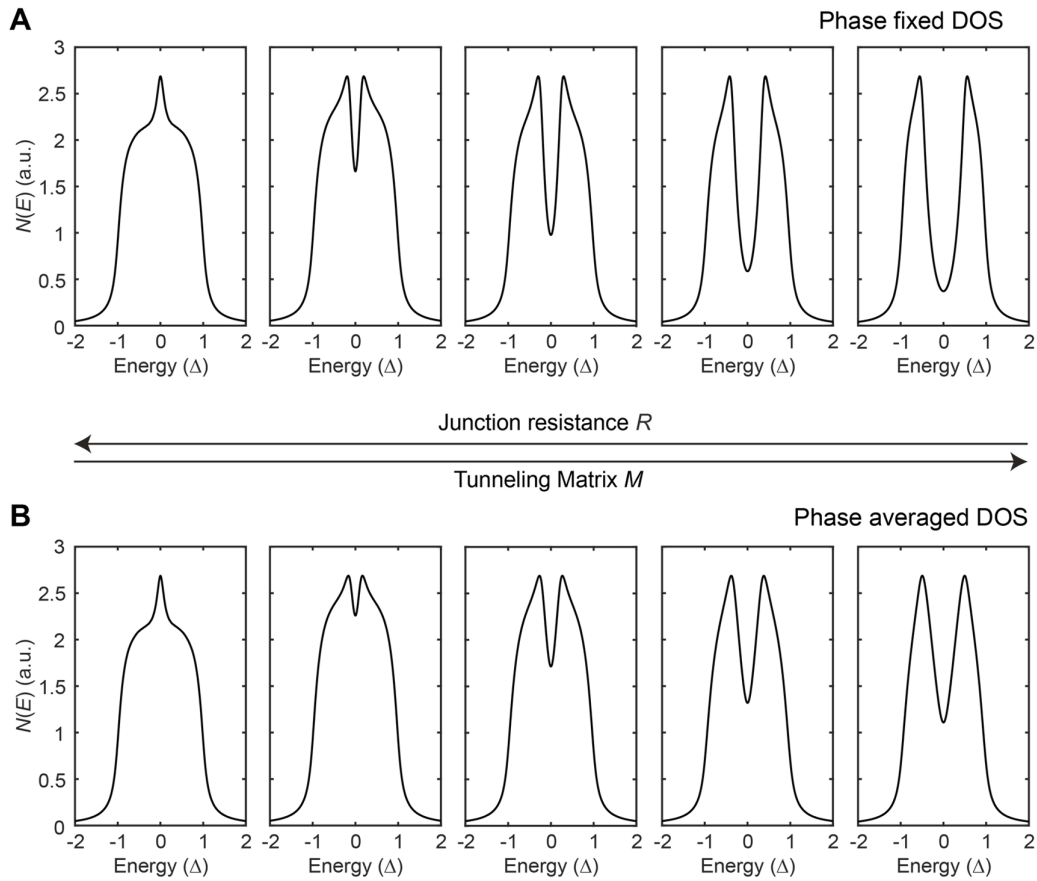


Figure D.1: **a.** Calculated TSB density of states (DOS)  $N(E)$  for phase difference  $\delta\phi$  between Nb and  $\text{UTe}_2$  with increasing tunnelling matrix  $|M|$  to the right. For a fixed phase increasing proximity of the s-wave tip to the p-wave sample splits the TSB and zero-energy peak to finite energy. **b.** Calculated DOS for  $\delta\phi$  averaged with equal probability in the range  $0 < \delta\phi < \pi$ . Despite averaging the phase difference between the s-wave and p-wave superconductor the TSB splitting, and thus, the zero-energy peak splitting, is still observed with increasing tunnelling matrix  $|M|$ . Finite phase fluctuations do not therefore alter the conclusion that zero-energy peak splitting is characteristic of a time-reversal symmetry conserving order parameter in  $\text{UTe}_2$

# Appendix E

## Normal vs. Superconducting Tip QSB QPI Detection

Motivated by the presence of dominant finite density of states at zero-energy as  $T \rightarrow 0$  and by the consequent hypothesis that a QSB exists in this material, we search for its signatures using a non-superconductive tip, at voltages within the superconducting energy gap, and identify unique features resulting from QSB scattering interference. The typical NIS tunnelling conductance of the  $\text{UTe}_2$  superconducting state, measured using a non-superconductive tip, is exemplified in the inset to Fig. E.1a. At the (0-11) surface of superconducting  $\text{UTe}_2$  crystals almost all states inside the superconducting gap  $E < |\Delta_{\mathbf{k}}|$  show residual, ungapped density of states. To visualize the scattering interference of QSB quasiparticles, we focus on a 40 nm square FOV (Fig. E.1a) for conventional differential conductance  $dI/dV|_{\text{NIS}}(\mathbf{r}, E)$  at  $T = 280$  mK and at a junction resistance of  $R = 5$  M $\Omega$ . Although the QPI inside the superconducting gap shows encouraging evidence of the QSB in  $\text{UTe}_2$ , its weak signal-to-noise ratio owing to the dominant finite density of states for  $E < |\Delta_{\mathbf{k}}|$  implies that conventional  $dI/dV|_{\text{NIS}}(\mathbf{r}, E)$  measurements are inadequate for precision application of detecting and quantifying the QPI of the QSB in  $\text{UTe}_2$ .

Thus, we turned to a new technique by using superconductive tips to increase the signal-to-noise ratio of QSB quasiparticle scattering. Theory for the tunnel junction formed between an  $s$ -wave superconductive scan-tip and a  $p$ -wave superconductor with a QSB within the interface, reveals that the high density of QSB quasiparticles allows efficient creation/annihilation of Cooper pairs in both superconductors, thus generating intense Andreev differential conductance  $a(\mathbf{r}, V) \equiv dI/dV|_{\text{SIS}}(\mathbf{r}, E)$  [109]. This is precisely what is ob-

---

served when  $\text{UTe}_2$  is studied by superconductive Nb-tip STM at  $T = 280$  mK, as evidenced by the large zero-energy conductance peak around  $a(r, V = 0)$  (inset to Fig. E.1d). Visualization of  $a(\mathbf{r}, V = 0)$  and its Fourier transform  $a(\mathbf{q}, V = 0)$  as shown in Fig. E.1, reveals intense conductance modulations and a distinct QPI pattern. Comparing  $g(\mathbf{q}, V = 0)$  in Fig. E.1b and  $a(\mathbf{q}, V = 0)$  in Fig. E.1d reveals numerous common characteristics thus demonstrating that use of  $a(\mathbf{q}, V)$  imaging yields equivalent QPI patterns as  $g(\mathbf{q}, V)$  imaging, but with greatly enhanced signal-to-noise ratio. This is as expected since spatial variations in the intensity of  $a(\mathbf{r}, V)$  are controlled by the amplitude of QSB quasiparticle wavefunctions, so that spatial interference patterns of the QSB quasiparticles will become directly observable in  $a(\mathbf{r}, V)$ . Thus, spatial variations in  $a(\mathbf{r}, V)$  and their Fourier transforms  $a(\mathbf{q}, V)$  now allow efficient, high signal-to-noise ratio, exploration of QSB quasiparticle scattering interference phenomena at the surface of  $\text{UTe}_2$ .

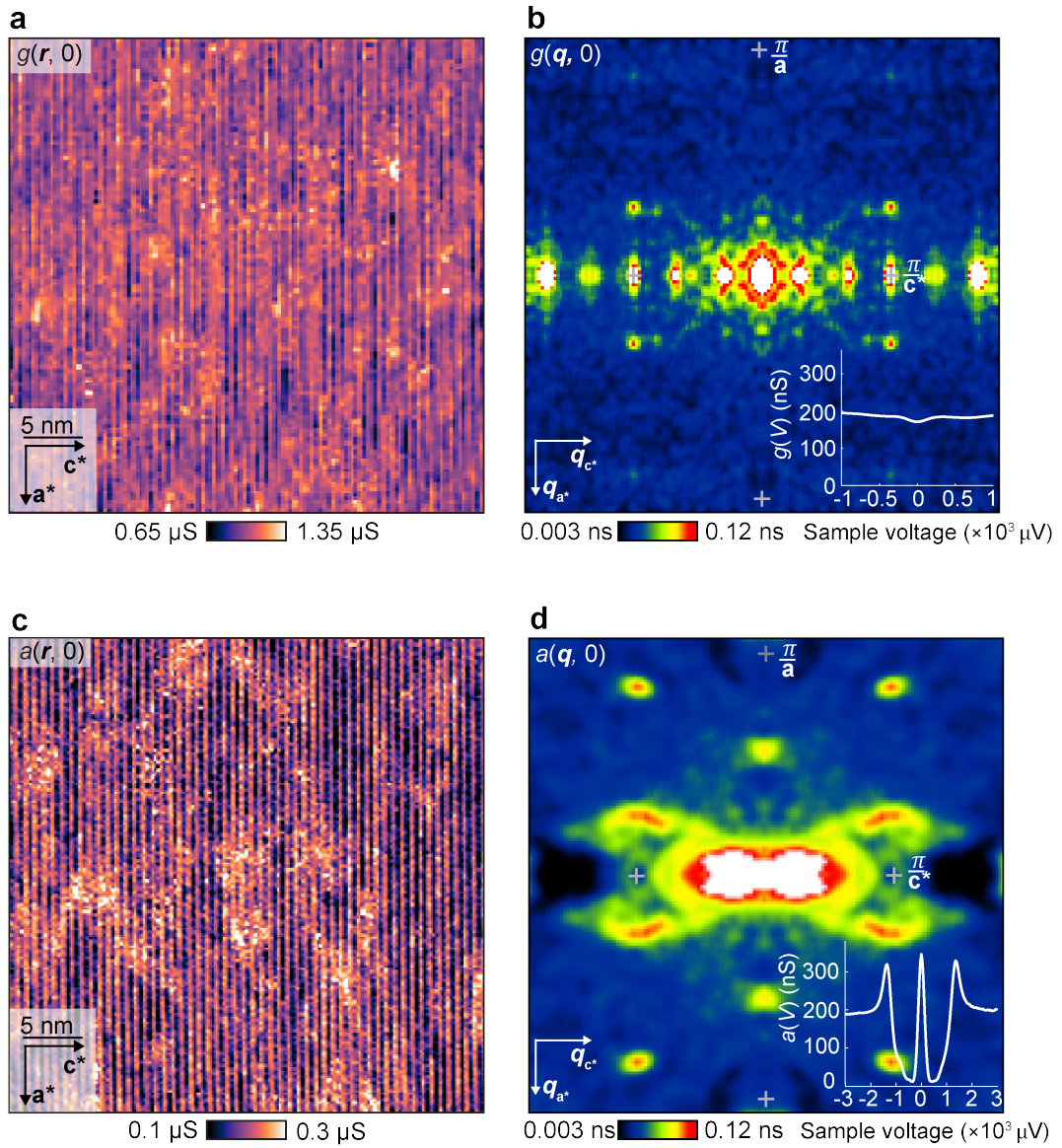


Figure E.1: **a.** Measured normal tip  $g(\mathbf{r}, V = 0)$  at  $T = 280$  mK. **b.** Measured normal tip  $g(\mathbf{q}, V = 0)$  at  $280$  mK. Inset: Normal tip single-electron tunnelling spectrum  $g(V)$ . **c.** Measured superconducting tip  $a(\mathbf{r}, V)$  at  $280$  mK. **d.** Measured superconducting tip  $a(\mathbf{q}, V = 0)$  at  $280$  mK. Inset: Superconducting tip Andreev tunnelling spectrum  $a(V)$  as described in detail in Ref. [109]

# Appendix F

## QSB QPI Repeated Measurements

To confirm that the QPI of the QSB is present in several FOVs we show two additional examples of the Fourier transformed zero-energy Andreev conductance  $a(\mathbf{q}, 0)$  from two different FOVs in Fig. F.1. Both new datasets, feature five of the six scattering wavevectors of the sextet  $\mathbf{q}_i$ ,  $i = 1 - 6$  discussed in Chapter 7 and further confirm the signatures of a  $B_{3u}$  QSB at the (0 -1 1) surface of  $\text{UTe}_2$ . Particularly repeated measurement of  $\mathbf{q}_1$  only at energies within the superconducting gap and at temperatures  $T < T_c$  supports the presence of a superconducting order parameter of  $B_{3u}$  symmetry, as this is the only order parameter which allows spin-conserved scattering at this wavevector.

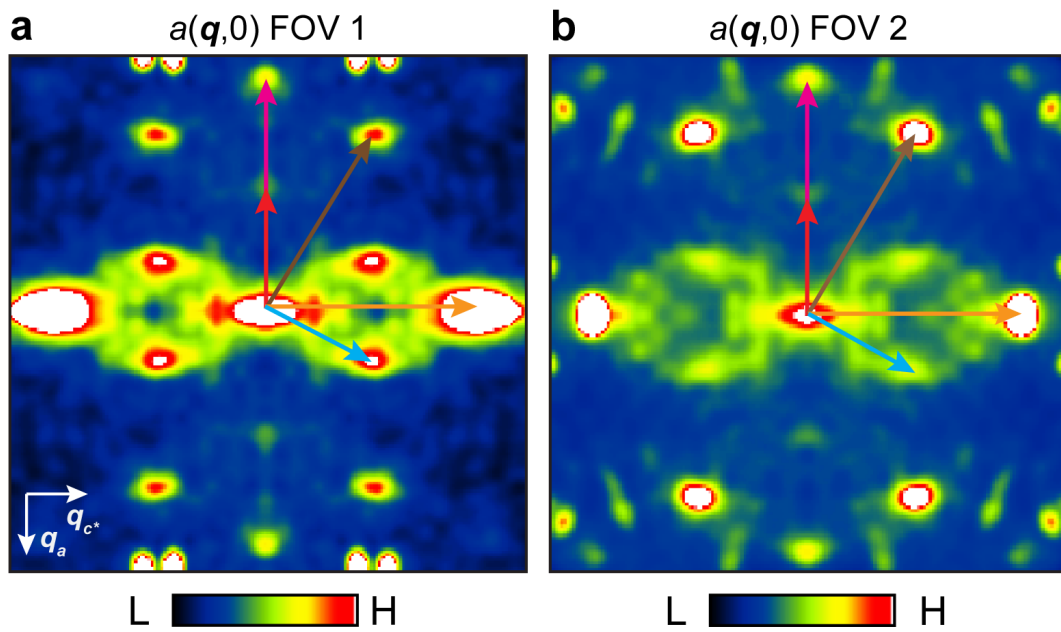


Figure F.1: Two independent measurements of  $a(\mathbf{q}, 0)$  at  $T = 0.28\text{K}$  confirms the repeatability of the sextet of scattering wavevectors for the  $B_{3u}$  QSB.

# Bibliography

- [1] W. Heisenberg. “Über quantentheoretische Umdeutung kinematischer und mechanischer Beziehungen”. In: *Z. Phys.* 33 (1925), pp. 879–893.
- [2] M.H. Anderson et al. “Observation of Bose-Einstein Condensation in a Dilute Atomic Vapor”. In: *Science* 269 (1995), pp. 198–201. DOI: 10.1126/science.269.5221.198.
- [3] T.H. Maiman. “Stimulated optical radiation in ruby”. In: *Nature* 187 (1960), pp. 493–494. DOI: 10.1038/187493a0.
- [4] D. Monaldi. “Fritz London and the scale of quantum mechanisms”. In: *Studies in History and Philosophy of Science Part B: Studies in History and Philosophy of Modern Physics* 60 (2017), pp. 35–45. DOI: 10.1016/j.shpsb.2017.07.001.
- [5] H. Fröhlich. “Theory of the Superconducting State. I. The Ground State at the Absolute Zero of Temperature”. In: *Phys. Rev.* 79 (1950), pp. 845–856. DOI: 10.1103/PhysRev.79.845.
- [6] L.N. Cooper. “Bound Electron Pairs in a Degenerate Fermi Gas”. In: *Phys. Rev.* 104 (1956), pp. 1189–1190. DOI: 10.1103/PhysRev.104.1189.
- [7] J. Bardeen, L.N. Cooper, and J.R. Schrieffer. “Microscopic Theory of Superconductivity”. In: *Phys. Rev.* 106 (1957), pp. 162–164. DOI: 10.1103/PhysRev.106.162.
- [8] M.Tinkham. *Introduction to superconductivity*. Courier Corporation, 2004.
- [9] D.R. Tilley. *Superfluidity and superconductivity*. Routledge, 2019.
- [10] E. Maxwell. “Isotope Effect in the Superconductivity of Mercury”. In: *Phys. Rev.* 78 (1950), pp. 477–477. DOI: 10.1103/PhysRev.78.477.

- 
- [11] N. N. Bogoliubov. “A NEW METHOD IN THE THEORY OF SUPERCONDUCTIVITY I”. In: *Journal of Experimental and Theoretical Physics* (1958).
- [12] R.E. Glover and M. Tinkham. “Transmission of Superconducting Films at Millimeter-Microwave and Far Infrared Frequencies”. In: *Phys. Rev.* 104 (1956), pp. 844–845. DOI: 10.1103/PhysRev.104.844.
- [13] M. Sigrist. “Introduction to Unconventional Superconductivity”. In: *AIP Conference Proceedings* 789 (2005), pp. 165–243. DOI: 10.1063/1.2080350.
- [14] K. Fujita et al. “Spectroscopic Imaging Scanning Tunneling Microscopy Studies of Electronic Structure in the Superconducting and Pseudogap Phases of Cuprate High-Tc Superconductors”. In: *Journal of the Physical Society of Japan* 81 (2012), p. 011005. DOI: 10.1143/JPSJ.81.011005.
- [15] O. Penrose and L. Onsager. “Bose-Einstein Condensation and Liquid Helium”. In: *Phys. Rev.* 104 (1956), pp. 576–584. DOI: 10.1103/PhysRev.104.576.
- [16] C.N.Yang. “Concept of Off-Diagonal Long-Range Order and the Quantum Phases of Liquid He and of Superconductors”. In: *Rev. Mod. Phys.* 34 (1962), pp. 694–704. DOI: 10.1103/RevModPhys.34.694.
- [17] Q. Chen et al. “When superconductivity crosses over: From BCS to BEC”. In: *Rev. Mod. Phys.* 96 (2024), p. 025002. DOI: 10.1103/RevModPhys.96.025002.
- [18] M. Greiter. “Is electromagnetic gauge invariance spontaneously violated in superconductors?” In: *Annals of Physics* 319 (2005), pp. 217–249. DOI: 10.1016/j.aop.2005.03.008.
- [19] M. R. Norman. “The Challenge of Unconventional Superconductivity”. In: *Science* 332 (2011), pp. 196–200. DOI: 10.1126/science.1200181.
- [20] J. T. Mäkinen, K. Zhang, and V. B. Eltsov. “Vortex-bound solitons in topological superfluid  $^3\text{He}$ ”. In: *Journal of Physics: Condensed Matter* 35 (2023), p. 214001. DOI: 10.1088/1361-648X/acc227.
- [21] D.M.Lee. “The extraordinary phases of liquid  $^3\text{He}$ ”. In: *Rev. Mod. Phys.* 69 (1997), pp. 645–666. DOI: 10.1103/RevModPhys.69.645.

- 
- [22] M. Leijnse and K. Flensberg. “Introduction to topological superconductivity and Majorana fermions”. In: *Semiconductor Science and Technology* 27 (2012), p. 124003. DOI: 10.1088/0268-1242/27/12/124003.
- [23] G. Dresselhaus M. Dresselhaus and A. Jorio. *Group Theory: Applications to the physics of condensed matter*. Springer Berlin, Heidelberg, 2007.
- [24] P. Fulde and R. A. Ferrell. “Superconductivity in a Strong Spin-Exchange Field”. In: *Phys. Rev.* 135 (1964), A550–A563. DOI: 10.1103/PhysRev.135.A550.
- [25] A.I. Larkin and Y.N Ovchinnikov. “Nonuniform state of superconductors”. In: *Zh. Eksp. Teor. Fiz.* 47 (1964), pp. 1136–1146.
- [26] R. Beyer and J. Wosnitzer. “Emerging evidence for FFLO states in layered organic superconductors (Review Article)”. In: *Low Temperature Physics* 39 (2013), pp. 225–231. DOI: 10.1063/1.4794996.
- [27] Y. Matsuda and H. Shimahara. “Fulde–Ferrell–Larkin–Ovchinnikov State in Heavy Fermion Superconductors”. In: *Journal of the Physical Society of Japan* 76 (2007), p. 051005. DOI: 10.1143/JPSJ.76.051005.
- [28] X. Liu et al. “Discovery of a Cooper-pair density wave state in a transition-metal dichalcogenide”. In: *Science* 372 (2021), pp. 1447–1452. DOI: 10.1126/science.abd4607.
- [29] M. Hamidian, S. Edkins, and S. Joo. “Detection of a Cooper-pair density wave in  $\text{Bi}_2\text{Sr}_2\text{CaCu}_2\text{O}_{8+x}$ ”. In: *Nature* 532 (2016), pp. 343–347. DOI: 10.1038/nature17411.
- [30] Q. Gu et al. “Detection of a pair density wave state in  $\text{UTe}_2$ ”. In: *Nature* 618 (2023), pp. 921–927. DOI: 10.1038/s41586-023-05919-7.
- [31] H.-D. Chen et al. “Pair Density Wave in the Pseudogap State of High Temperature Superconductors”. In: *Phys. Rev. Lett.* 93 (2004), p. 187002. DOI: 10.1103/PhysRevLett.93.187002.
- [32] Y. Wang, D.F. Agterberg, and A. Chubukov. “Coexistence of Charge-Density-Wave and Pair-Density-Wave Orders in Underdoped Cuprates”. In: *Phys. Rev. Lett.* 114 (2015), p. 197001. DOI: 10.1103/PhysRevLett.114.197001.

- 
- [33] E. Fradkin, S.A. Kivelson, and J.M. Tranquada. “Colloquium: Theory of intertwined orders in high temperature superconductors”. In: *Rev. Mod. Phys.* 87 (2015), pp. 457–482. DOI: 10.1103/RevModPhys.87.457.
- [34] C. Setty, L. Fanfarillo, and P.J. Hirschfeld. “Mechanism for fluctuating pair density wave”. In: *Nature Communications* 14 (2023), p. 3181. DOI: 10.1038/s41467-023-38956-x.
- [35] V.L. Ginzburg and L.D. Landau. “On the Theory of superconductivity”. In: *Zh. Eksp. Teor. Fiz.* 20 (1950), pp. 1064–1082. DOI: 10.1016/b978-0-08-010586-4.50078-x.
- [36] D.F. Agterberg et al. “The Physics of Pair-Density Waves: Cuprate Superconductors and Beyond”. In: *Annual Review of Condensed Matter Physics* 11 (2020), pp. 231–270. DOI: <https://doi.org/10.1146/annurev-conmatphys-031119-050711>.
- [37] G. Binnig et al. “Tunneling through a controllable vacuum gap”. In: *Applied Physics Letters* 40 (1982), pp. 178–180. DOI: 10.1063/1.92999.
- [38] K. M. Bastiaans et al. “Direct evidence for Cooper pairing without a spectral gap in a disordered superconductor above TC”. In: *Science* 374 (2021), pp. 608–611. DOI: 10.1126/science.abe3987.
- [39] M. Bode. “Spin-polarized scanning tunnelling microscopy”. In: *Reports on Progress in Physics* 66 (2003), p. 523. DOI: 10.1088/0034-4885/66/4/203.
- [40] J. Bardeen. “Tunnelling from a Many-Particle Point of View”. In: *Phys. Rev. Lett.* 6 (1961), pp. 57–59. DOI: 10.1103/PhysRevLett.6.57.
- [41] J. C. Chen. *Introduction to Scanning Tunneling Microscopy*. Oxford University Press, Sept. 2007. ISBN: 9780199211500. DOI: 10.1093/acprof:oso/9780199211500.001.0001.
- [42] S. Lounis. *Theory of Scanning Tunneling Microscopy*. 2014. arXiv: 1404.0961 [cond-mat.mes-hall].
- [43] P. A.M. Dirac. “The quantum theory of the emission and absorption of radiation”. In: *Proc. R. Soc. Lond. A* 114 (1927), pp. 243–265.
- [44] B.D. Josephson. “Possible new effects in superconductive tunnelling”. In: *Physics Letters* 1 (1962), pp. 251–253. DOI: [https://doi.org/10.1016/0031-9163\(62\)91369-0](https://doi.org/10.1016/0031-9163(62)91369-0).

- 
- [45] Y. Harada, H. Takayanagi, and A.A. Odintsov. “Cooper-pair tunneling in small junctions with tunable Josephson coupling”. In: *Phys. Rev. B* 54 (1996), pp. 6608–6613. DOI: 10.1103/PhysRevB.54.6608.
- [46] X. Liu et al. “Discovery of a Cooper-pair density wave state in a transition-metal dichalcogenide”. In: *Science* 372 (2021), pp. 1447–1452. DOI: 10.1126/science.abd4607.
- [47] H. Pirie et al. “Visualizing the atomic-scale origin of metallic behavior in Kondo insulators”. In: *Science* 379 (2023), pp. 1214–1218. DOI: 10.1126/science.abq5375.
- [48] S. Ran et al. “Nearly ferromagnetic spin-triplet superconductivity”. In: *Science* 365 (2019), pp. 684–687. DOI: 10.1126/science.aav8645.
- [49] A.M. Clogston. “Upper Limit for the Critical Field in Hard Superconductors”. In: *Phys. Rev. Lett.* 9 (1962), pp. 266–267. DOI: 10.1103/PhysRevLett.9.266.
- [50] S. K Lewin et al. “A review of UTe<sub>2</sub> at high magnetic fields”. In: *Reports on Progress in Physics* 86 (2023), p. 114501. DOI: 10.1088/1361-6633/acfb93.
- [51] L.C. Hebel and C.P. Slichter. “Nuclear Spin Relaxation in Normal and Superconducting Aluminum”. In: *Phys. Rev.* 113 (1959), pp. 1504–1519. DOI: 10.1103/PhysRev.113.1504.
- [52] D.D. Osheroff et al. “New Magnetic Phenomena in Liquid He<sup>3</sup> below 3 mK”. In: *Phys. Rev. Lett.* 29 (1972), pp. 920–923. DOI: 10.1103/PhysRevLett.29.920.
- [53] T. Imai et al. “Anomalous Temperature Dependence of Cu Nuclear Spin-Lattice Relaxation in YBa<sub>2</sub>Cu<sub>3</sub>O<sub>6.91</sub>”. In: *Journal of the Physical Society of Japan* 57 (1988), pp. 2280–2283. DOI: 10.1143/JPSJ.57.2280.
- [54] G. Nakamine et al. “Superconducting Properties of Heavy Fermion UTe<sub>2</sub> Revealed by <sup>125</sup>Te-nuclear Magnetic Resonance”. In: *Journal of the Physical Society of Japan* 88 (2019), p. 113703. DOI: 10.7566/JPSJ.88.113703.
- [55] D. Aoki et al. “Unconventional superconductivity in UTe<sub>2</sub>”. In: *Journal of Physics: Condensed Matter* 34 (2022), p. 243002. DOI: 10.1088/1361-648X/ac5863.

- 
- [56] R.H. Hammond and G.M. Kelly. “Vanishing Knight Shift in Superconducting Aluminum”. In: *Phys. Rev. Lett.* 18 (1967), pp. 156–158. DOI: 10.1103/PhysRevLett.18.156.
- [57] H. Fujibayashi et al. “Superconducting Order Parameter in  $\text{UTe}_2$  Determined by Knight Shift Measurement”. In: *Journal of the Physical Society of Japan* 91 (2022), p. 043705. DOI: 10.7566/JPSJ.91.043705.
- [58] H. Matsumura et al. “Large Reduction in the a-axis Knight Shift on  $\text{UTe}_2$  with  $T_C = 2.1$  K”. In: *Journal of the Physical Society of Japan* 92 (2023), p. 063701. DOI: 10.7566/JPSJ.92.063701.
- [59] H. Sakai et al. “Single crystal growth of superconducting  $\text{UTe}_2$  by molten salt flux method”. In: *Phys. Rev. Mater.* 6 (2022), p. 073401. DOI: 10.1103/PhysRevMaterials.6.073401.
- [60] D. Aoki. “Molten Salt Flux Liquid Transport Method for Ultra Clean Single Crystals  $\text{UTe}_2$ ”. In: *Journal of the Physical Society of Japan* 93.4 (2024), p. 043703. DOI: 10.7566/JPSJ.93.043703.
- [61] P.F.S Rosa, A. Weiland, and S.S Fender. “Single thermodynamic transition at 2 K in superconducting  $\text{UTe}_2$  single crystals.” In: *Commun Mater* 3 (2022), p. 33. DOI: 10.1038/s43246-022-00254-2.
- [62] G. Nakamine et al. “Inhomogeneous Superconducting State Probed by  $^{125}\text{Te}$  NMR on  $\text{UTe}_2$ ”. In: *Journal of the Physical Society of Japan* 90 (2021), p. 064709. DOI: 10.7566/JPSJ.90.064709.
- [63] G. Nakamine et al. “Anisotropic response of spin susceptibility in the superconducting state of  $\text{UTe}_2$  probed with  $^{125}\text{Te}$  NMR measurement”. In: *Phys. Rev. B* 103 (2021), p. L100503. DOI: 10.1103/PhysRevB.103.L100503.
- [64] “Erratum for the Research Article: Evidence for a pressure-induced antiferromagnetic quantum critical point in intermediate-valence  $\text{UTe}_2$ ”. In: *Science Advances* 7 (2021), eabn1403. DOI: 10.1126/sciadv.abn1403.
- [65] S. Kittaka et al. “Orientation of point nodes and nonunitary triplet pairing tuned by the easy-axis magnetization in  $\text{UTe}_2$ ”. In: *Phys. Rev. Res.* 2 (2020), p. 032014. DOI: 10.1103/PhysRevResearch.2.032014.

- 
- [66] T. Metz et al. “Point-node gap structure of the spin-triplet superconductor  $\text{UTe}_2$ ”. In: *Phys. Rev. B* 100 (2019), p. 220504. DOI: 10.1103/PhysRevB.100.220504.
- [67] S. Suetsugu et al. “Fully gapped pairing state in spin-triplet superconductor  $\text{UTe}_2$ ”. In: *Science Advances* 10 (2024), eadk3772. DOI: 10.1126/sciadv.adk3772.
- [68] K. Ishihara et al. “Chiral superconductivity in  $\text{UTe}_2$  probed by anisotropic low-energy excitations”. In: *Nature Communications* 14 (2023), p. 2966.
- [69] Y. Iguchi et al. “Microscopic Imaging Homogeneous and Single Phase Superfluid Density in  $\text{UTe}_2$ ”. In: *Phys. Rev. Lett.* 130 (2023), p. 196003. DOI: 10.1103/PhysRevLett.130.196003.
- [70] S. Bae et al. “Anomalous normal fluid response in a chiral superconductor  $\text{UTe}_2$ ”. In: *Nature communications* 12 (2021), p. 2644. DOI: 10.1038/s41467-021-22906-6.
- [71] E. Puchkaryov and K. Maki. “Impurity scattering in P-wave superconductors;  $\text{Sr}_2\text{RuO}_4$ ”. In: *Physica C: Superconductivity* 341-348 (2000), pp. 727–728. DOI: 10.1016/S0921-4534(00)00663-8.
- [72] P.W. Anderson. “Theory of dirty superconductors”. In: *Journal of Physics and Chemistry of Solids* 11 (1959), pp. 26–30. DOI: 10.1016/0022-3697(59)90036-8.
- [73] A. Aishwarya et al. “Magnetic-field-sensitive charge density waves in the superconductor  $\text{UTe}_2$ ”. In: *Nature* 618 (2023), pp. 928–933. DOI: 10.1038/s41586-023-06005-8.
- [74] P.F.S Rosa et al. “Single thermodynamic transition at 2 K in superconducting  $\text{UTe}_2$  single crystals”. In: *Nature Communications* 3 (2022), p. 33. DOI: 10.1038/s43246-022-00254-2.
- [75] R. Balian and N.R. Werthamer. “Superconductivity with Pairs in a Relative p Wave”. In: *Phys. Rev.* 131 (1963), pp. 1553–1564. DOI: 10.1103/PhysRev.131.1553.
- [76] K. J. Franke, G. Schulze, and J. I. Pascual. “Competition of Superconducting Phenomena and Kondo Screening at the Nanoscale”. In: *Science* 332 (2011), pp. 940–944. DOI: 10.1126/science.1202204.

- 
- [77] I. Tamir et al. “Direct observation of intrinsic surface magnetic disorder in amorphous superconducting films”. In: *Phys. Rev. B* 105 (2022), p. L140505. DOI: 10.1103/PhysRevB.105.L140505.
- [78] M. Lawler et al. “Intra-unit-cell electronic nematicity of the high- $T_C$  copper-oxide pseudogap states”. In: *Nature* 466 (2010), pp. 347–351. DOI: 10.1038/nature09169.
- [79] Y. Liu et al. “Pair density wave state in a monolayer high- $T_C$  iron-based superconductor”. In: *Nature* 618 (2023), pp. 934–939. DOI: 10.1038/s41586-023-06072-x.
- [80] G. Deutscher. “Andreev–Saint-James reflections: A probe of cuprate superconductors”. In: *Rev. Mod. Phys.* 77 (2005), pp. 109–135. DOI: 10.1103/RevModPhys.77.109.
- [81] A.V. Balatsky, I. Vekhter, and J.-X. Zhu. “Impurity-induced states in conventional and unconventional superconductors”. In: *Rev. Mod. Phys.* 78 (2006), pp. 373–433. DOI: 10.1103/RevModPhys.78.373.
- [82] I. Chenn and I.M. Sigal. “Vortex lattices and the Bogoliubov-de Gennes equations”. In: *Advances in Mathematics* 380 (2021), p. 107546. DOI: <https://doi.org/10.1016/j.aim.2020.107546>.
- [83] P.G. de Gennes. *Superconductivity Of Metals And Alloys*. CRC Press, 1999. DOI: <https://doi.org/10.1201/9780429497032>.
- [84] Y. Asano. “Andreev reflection in superconducting junctions”. In: *Springer-Briefs in Physics* (2021). DOI: 10.1007/978-981-16-4165-7.
- [85] G.E. Blonder, M. Tinkham, and T.M. Klapwijk. “Transition from metallic to tunneling regimes in superconducting microconstrictions: Excess current, charge imbalance, and supercurrent conversion”. In: *Phys. Rev. B* 25 (1982), pp. 4515–4532. DOI: 10.1103/PhysRevB.25.4515.
- [86] S. Kashiwaya and Y. Tanaka. “Tunnelling effects on surface bound states in”. In: *Reports on Progress in Physics* 63 (2000), p. 1641. DOI: 10.1088/0034-4885/63/10/202.
- [87] R. Landauer. “Conductance determined by transmission: probes and quantised constriction resistance”. In: *Journal of Physics: Condensed Matter* 1 (1989), p. 8099. DOI: 10.1088/0953-8984/1/43/011.
- [88] I.O. Kulik. “Macroscopic quantization and the proximity effect in S-N-S junctions”. In: *Soviet Physics JETP* 30 (1969), pp. 944–950.

- 
- [89] S. Misra et al. “Formation of an Andreev bound state at the step edges of  $\text{Bi}_2\text{Sr}_2\text{CaCu}_2\text{O}_{8+\delta}$  surface”. In: *Phys. Rev. B* 66 (2002), p. 100510. DOI: 10.1103/PhysRevB.66.100510.
- [90] M. Sato et al. “Topology of Andreev bound states with flat dispersion”. In: *Phys. Rev. B* 83 (2011), p. 224511. DOI: 10.1103/PhysRevB.83.224511.
- [91] D.J. Thouless et al. “Quantized Hall Conductance in a Two-Dimensional Periodic Potential”. In: *Phys. Rev. Lett.* 49 (1982), pp. 405–408. DOI: 10.1103/PhysRevLett.49.405.
- [92] M.Z. Hasan and C.L. Kane. “Colloquium: Topological insulators”. In: *Rev. Mod. Phys.* 82 (2010), pp. 3045–3067. DOI: 10.1103/RevModPhys.82.3045.
- [93] A. Bernevig et al. “Recent Progress in the Study of Topological Semimetals”. In: *Journal of the Physical Society of Japan* 87 (2018), p. 041001. DOI: 10.7566/JPSJ.87.041001.
- [94] M. Sato and Y. Ando. “Topological superconductors: a review”. In: *Reports on Progress in Physics* 80 (2017), p. 076501. DOI: 10.1088/1361-6633/aa6ac7.
- [95] B. Yan and C. Felser. “Topological Materials: Weyl Semimetals”. In: *Annual Review of Condensed Matter Physics* 8 (2017), pp. 337–354. DOI: 10.1146/annurev-conmatphys-031016-025458.
- [96] T. Mizushima et al. “Symmetry-Protected Topological Superfluids and Superconductors —From the Basics to  $^3\text{He}$ —”. In: *Journal of the Physical Society of Japan* 85 (2016), p. 022001. DOI: 10.7566/JPSJ.85.022001.
- [97] M. Sato et al. “Topology of Andreev bound states with flat dispersion”. In: *Phys. Rev. B* 83 (2011), p. 224511. DOI: 10.1103/PhysRevB.83.224511.
- [98] A. Stern. “Fractional Topological Insulators: A Pedagogical Review”. In: *Annual Review of Condensed Matter Physics* 7 (2016), pp. 349–368. DOI: <https://doi.org/10.1146/annurev-conmatphys-031115-011559>.

- 
- [99] P. Heinzner, A. Huckleberry, and M.R. Zirnbauer. “Symmetry Classes of Disordered Fermions”. In: *Communications in Mathematical Physics* 257.3 (2005), pp. 725–771. DOI: 10.1007/s00220-005-1330-9.
- [100] A.P. Schnyder et al. “Classification of topological insulators and superconductors in three spatial dimensions”. In: *Phys. Rev. B* 78 (2008), p. 195125. DOI: 10.1103/PhysRevB.78.195125.
- [101] A. P. Schnyder and P. M. R. Brydon. “Topological surface states in nodal superconductors”. In: *Journal of Physics: Condensed Matter* 27 (2015), p. 243201. DOI: 10.1088/0953-8984/27/24/243201.
- [102] S. Simon, M. Geier, and P.W. Brouwer. “Higher-order topological semimetals and nodal superconductors with an order-two crystalline symmetry”. In: *Phys. Rev. B* 106 (2022), p. 035105. DOI: 10.1103/PhysRevB.106.035105.
- [103] C.-K. Chiu and A.P. Schnyder. “Classification of reflection-symmetry-protected topological semimetals and nodal superconductors”. In: *Phys. Rev. B* 90 (2014), p. 205136. DOI: 10.1103/PhysRevB.90.205136.
- [104] T. Machida, Y. Nagai, and T. Hanaguri. “Zeeman effects on Yu-Shiba-Rusinov states”. In: *Phys. Rev. Res.* 4 (2022), p. 033182. DOI: 10.1103/PhysRevResearch.4.033182.
- [105] A.W. Kleinsasser et al. “Observation of multiple Andreev reflections in superconducting tunnel junctions”. In: *Phys. Rev. Lett.* 72 (1994), pp. 1738–1741. DOI: 10.1103/PhysRevLett.72.1738.
- [106] J.C. Cuevas and W. Belzig. “Full Counting Statistics of Multiple Andreev Reflections”. In: *Phys. Rev. Lett.* 91 (2003), p. 187001. DOI: 10.1103/PhysRevLett.91.187001.
- [107] W. Ko, J.L. Lado, and P. Maksymovych. “Noncontact Andreev Reflection as a Direct Probe of Superconductivity on the Atomic Scale”. In: *Nano Letters* 22 (2022), pp. 4042–4048. DOI: 10.1021/acs.nanolett.2c00697.
- [108] W. Ko, E.F. Dumitrescu, and P. Maksymovych. “Statistical detection of Josephson, Andreev, and single quasiparticle currents in scanning tunneling microscopy”. In: *Phys. Rev. Res.* 3 (2021), p. 033248. DOI: 10.1103/PhysRevResearch.3.033248.

- 
- [109] Q. Gu et al. “Pair Wavefunction Symmetry in  $\text{UTe}_2$  from Zero-Energy Surface State Visualization”. In: *Science* (2024).
- [110] S.-I. Fujimori et al. “Electronic Structure of  $\text{UTe}_2$  Studied by Photoelectron Spectroscopy”. In: *Journal of the Physical Society of Japan* 88 (2019), p. 103701. DOI: 10.7566/JPSJ.88.103701.
- [111] L. Miao et al. “Low Energy Band Structure and Symmetries of  $\text{UTe}_2$  from Angle-Resolved Photoemission Spectroscopy”. In: *Phys. Rev. Lett.* 124 (2020), p. 076401. DOI: 10.1103/PhysRevLett.124.076401.
- [112] Y.S. Eo et al. “c-axis transport in  $\text{UTe}_2$ : Evidence of three-dimensional conductivity component”. In: *Phys. Rev. B* 106 (2022), p. L060505. DOI: 10.1103/PhysRevB.106.L060505.
- [113] R. Sharma et al. “Momentum-resolved superconducting energy gaps of  $\text{Sr}_2\text{RuO}_4$  from quasiparticle interference imaging”. In: *Proceedings of the National Academy of Sciences* 117 (2020), pp. 5222–5227. DOI: 10.1073/pnas.1916463117.
- [114] P. O. Sprau et al. “Discovery of orbital-selective Cooper pairing in  $\text{FeSe}$ ”. In: *Science* 357 (2017), pp. 75–80. DOI: 10.1126/science.aal1575.
- [115] D. Aoki et al. “First Observation of the de Haas–van Alphen Effect and Fermi Surfaces in the Unconventional Superconductor  $\text{UTe}_2$ ”. In: *Journal of the Physical Society of Japan* 91 (2022), p. 083704. DOI: 10.7566/JPSJ.91.083704.
- [116] A.G. Eaton et al. “Quasi-2D Fermi surface in the anomalous superconductor  $\text{UTe}_2$ ”. In: *Nature Communications* 15 (2024), p. 223. DOI: 10.1038/s41467-023-44110-4.
- [117] T. I. Weinberger et al. *Quantum interference between quasi-2D Fermi surface sheets in  $\text{UTe}_2$* . 2023. arXiv: 2307.00568 [cond-mat.supr-con].
- [118] J. Ishizuka et al. “Insulator-Metal Transition and Topological Superconductivity in  $\text{UTe}_2$  from a First-Principles Calculation”. In: *Phys. Rev. Lett.* 123 (2019), p. 217001. DOI: 10.1103/PhysRevLett.123.217001.
- [119] H. C. Choi, S. H. Lee, and B.-J. Yang. “Correlated normal state fermiology and topological superconductivity in  $\text{UTe}_2$ ”. In: *Communications Physics* 7 (2024), p. 273. DOI: 10.1038/s42005-024-01708-4.

- 
- [120] J. Ishizuka and Y. Yanase. “Periodic Anderson model for magnetism and superconductivity in  $UTe_2$ ”. In: *Phys. Rev. B* 103 (2021), p. 094504. DOI: 10.1103/PhysRevB.103.094504.
- [121] B.D. White, J.D. Thompson, and M.B. Maple. “Unconventional superconductivity in heavy-fermion compounds”. In: *Physica C: Superconductivity and its Applications* 514 (2015), pp. 246–278. DOI: 10.1016/j.physc.2015.02.044.
- [122] T. I. Weinberger et al. *Pressure-enhanced  $f$ -electron orbital weighting in  $UTe_2$  mapped by quantum interferometry*. 2024. arXiv: 2403.03946 [cond-mat.supr-con]. URL: <https://arxiv.org/abs/2403.03946>.
- [123] R. Ohashi et al. *Anisotropic paramagnetic response of topological Majorana surface states in the superconductor  $UTe_2$* . 2024. arXiv: 2405.07593 [cond-mat.supr-con]. URL: <https://arxiv.org/abs/2405.07593>.
- [124] J. Tei, T. Mizushima, and S. Fujimoto. “Possible realization of topological crystalline superconductivity with time-reversal symmetry in  $UTe_2$ ”. In: *Phys. Rev. B* 107 (2023), p. 144517. DOI: 10.1103/PhysRevB.107.144517.
- [125] A. P. Schnyder and P. M. R. Brydon. “Topological surface states in nodal superconductors”. In: *Journal of Physics: Condensed Matter* 27 (2015), p. 243201. DOI: 10.1088/0953-8984/27/24/243201.
- [126] S. Pinon, V. Kaladzhyan, and C. Bena. “Surface Green’s functions and boundary modes using impurities: Weyl semimetals and topological insulators”. In: *Phys. Rev. B* 101 (2020), p. 115405. DOI: 10.1103/PhysRevB.101.115405.
- [127] A. Aishwarya et al. “Melting of the charge density wave by generation of pairs of topological defects in  $UTe_2$ ”. In: *Nature Physics* 20.6 (2024), pp. 964–969. DOI: 10.1038/s41567-024-02429-9.
- [128] A. LaFleur et al. “Inhomogeneous high temperature melting and decoupling of charge density waves in spin-triplet superconductor  $UTe_2$ ”. In: *Nature Communications* 15.1 (2024), p. 4456. DOI: 10.1038/s41467-024-48844-7.

- 
- [129] F. Theuss et al. “Absence of a bulk thermodynamic phase transition to a density wave phase in  $UTe_2$ ”. In: *Phys. Rev. B* 110 (14 2024), p. 144507. DOI: 10.1103/PhysRevB.110.144507.
- [130] C.S. Kengle et al. “Absence of bulk charge density wave order in the normal state of  $UTe_2$ ”. In: *Nature Communications* 15.1 (2024), p. 9713. DOI: 10.1038/s41467-024-53739-8.
- [131] C.S. Kengle et al. “Absence of a bulk signature of a charge density wave in hard x-ray measurements of  $UTe_2$ ”. In: *Phys. Rev. B* 110 (14 2024), p. 145101. DOI: 10.1103/PhysRevB.110.145101.
- [132] P. Dai et al. “Synthesis and neutron powder diffraction study of the superconductor  $HgBa_2Ca_2Cu_3O_{8+\delta}$  by Tl substitution”. In: *Physica C: Superconductivity* 243 (1995), pp. 201–206. DOI: 10.1016/0921-4534(94)02461-8.
- [133] S. H. Pan, E.W. Hudson, and J.C. Davis. “ $^3He$  refrigerator based very low temperature scanning tunneling microscope”. In: *Review of Scientific Instruments* 70 (1999), pp. 1459–1463. DOI: 10.1063/1.1149605.
- [134] Z. Li et al. *Observation of odd-parity superconductivity in  $UTe_2$* . 2023. arXiv: 2309.08668 [cond-mat.supr-con].